University of Alberta

A three-dimensional sharp phase front-based theory and application to shape memory alloy wires and thin films

by
Vesselin Stoilov ©

A thesis submitted to the Faculty of Graduate Studies and Research in partial fulfillment of the requirements for the degree of Doctor of Philosophy

Department of Mechanical Engineering

Edmonton, Alberta
Fall 2002

National Library
of Canada

Acquisitions and
Bibliographic Services

395 Wellington Street
Ottawa ON K1A 0N4
Canada

Bibliothèque nationale
du Canada

Acquisitions et
services bibliographiques

395, rue Wellington
Ottawa ON K1A 0N4
Canada

Your file Votre référence

Our file Notre référence

The author has granted a non-exclusive licence allowing the National Library of Canada to reproduce, loan, distribute or sell copies of this thesis in microform, paper or electronic formats.

L'auteur a accordé une licence non exclusive permettant à la Bibliothèque nationale du Canada de reproduire, prêter, distribuer ou vendre des copies de cette thèse sous la forme de microfiche/film, de reproduction sur papier ou sur format électronique.

The author retains ownership of the copyright in this thesis. Neither the thesis nor substantial extracts from it may be printed or otherwise reproduced without the author's permission.

L'auteur conserve la propriété du droit d'auteur qui protège cette thèse. Ni la thèse ni des extraits substantiels de celle-ci ne doivent être imprimés ou autrement reproduits sans son autorisation.

0-612-81271-5

Canada

University of Alberta

Library Release Form

Name of Author: **Vesselin Stoilov**

Title of Thesis: **A three-dimensional sharp phase front-based theory and application to shape memory alloy wires and thin films**

Degree: **Doctor of Philosophy**
Year this Degree Granted: **2002**

Permission is hereby granted to the University of Alberta Library to reproduce single copies of this thesis and to lend or sell such copies for private, scholarly or scientific research purposes only.

The author reserves all other publication and other rights in association with the copyright in the thesis, and except as herein provided, neither the thesis nor any substantial portion thereof may be printed or otherwise reproduced in any material form whatever without the author's prior written permission.

519C Michener Park
Edmonton , Alberta
Canada, T6H4M5

Date: Oct 1 2002

University of Alberta

Faculty of Graduate Studies and Research

The undersigned certify that they have read, and recommend to the Faculty of Graduate Studies and Research for acceptance, a thesis entitled *A three-dimensional sharp phase front–based theory and application to shape memory alloy wires and thin films* submitted by *Vesselin Stoilov* in partial fulfillment of the requirements for degree of *Doctor of Philosophy*

Dr. Jeff Yokota (Supervisor)

Dr. Andrew Mioduchowski

Walied Moussa
Dr. Walied Moussa

Dr. Jozef Szymanski

Gary Faulkner
Dr. Gary Faulkner

For Dr. Carman
Dr. Greg Carman (external examiner)

Date: Oct 1 2002

Abstract

This dissertation presents a complete theoretical framework for a three-dimensional (3D) sharp phase front-based model for phase transformations in shape memory alloys. The phases of austenite and martensite are taken to be separated by a phase front, and the phase transformation is taken to occur when the phase front moves. The usual balance laws (for conservation of mass, linear momentum and energy) are written for the bulk phases and the interface. Equality of the chemical potential at the interface leads to a generalized formulation of the Clausius-Clapeyron equation, which then gives the condition for the evolution of the interface during phase transformation. The theoretical framework is general enough to incorporate any Helmholtz free energy function. Specific results are then given in the context of the quasistatic, small strain approximation and a trilinear Helmholtz free energy function.

The developed theoretical framework was used to model the phase transformations in SMA thin wires(1D) and thin films(2D). In both studies the predictions of the theory were calculated and compared with available experimental data. The obtained results demonstrate the ability of the suggested theory to adequately model different types of phase transformations in SMA (pseudoelasticity, shape memory effect and reorientation). The simulations were performed by applying two separate numerical algorithms, developed for solving 1D and 2D problems of phase transformations in SMA. A moving boundary finite element method (MBFEM)-based numerical approach was proposed to solve one-dimensional (1D) thermomechanical problem. The Newton-Raphson method and recursive iterations, respectively, are used to address the non-linearity and coupling in the system of equations. In two dimensions, the 2D finite element-based method implements a front tracking, which is realized by mesh update at each time step. Nonoscillatory interpolation(SuperBee) was used to transfer data between the "old" and the "new" mesh.

Acknowledgements

Many people have contributed their ideas, support and time to help make this research possible. First, I would like to thank my supervisor Dr. Abhijit Bhattacharyya for his encouragement and support. Without his guidance and constructive criticism this work could not be as complete as it is now.

I also wish to thank Dr. Jeffrey Yokota for his help, especially during the final stages of this work.

Last but not least I would like to thank my wife Vesselina Roussinova for her love, support and understanding.

This study was possible, thanks to the financial assistance from Natural Sciences and Engineering Research Council, Canada(NSERC) and University of Alberta Dissertation Fellowship.

Preface

This dissertation is a compilation of chapters that have been published, accepted for publication or presented at conferences.

- Chapter 2: V. Stoilov, O. Iliev, and A. Bhattacharyya, "A moving boundary finite element method-based approach for the solution of one-dimensional problems in shape memory alloys," *Computer Methods in Applied Mechanics and Engineering* **190**, pp. 1741–1762, 2000.

- Chapter 3: A. Bhattacharyya, V. Stoilov, and O. Iliev, "Evaluation of structural influence of shape memory alloys linear actuators by sharp phase front-based constitutive models," *Computational Materials Science* **18**, pp. 269–282, 2000.

- Chapter 4: V. Stoilov and A. Bhattacharyya, "A theoretical framework of one-dimensional sharp phase fronts in shape memory alloys," *accepted in Acta Materialia*, 2002.

- Chapter 5: V. Stoilov, A. Bhattacharyya and J. Yokota, "A 3D sharp phase front-based model and its application to pseudoelasticity in SMA single crystals," *NATO Conference on martensitic transformations*, April 23-26, 2002, Metz, France.

All other chapters are specific only to this thesis.

Contents

1 Introduction **1**

1.1 Thermoelastic martensitic phase transformation 1

1.2 SMA models 5

1.2.1 Review of continuum modeling 7

1.3 Numerical methods for moving boundary problems 12

1.4 Thesis objectives and outline 14

2 The Moving Boundary Finite Element Method(MBFEM) **26**

2.1 Introduction 26

2.2 A one-dimensional moving boundary value problem in shape memory alloys 31

2.3 The temporal discretization and the MBFEM-based numerical approach 40

2.3.1 The temporal discretization 41

2.3.2 MBFEM-based numerical approach 43

2.4 The spatial discretization with moving boundary finite element method 45

2.4.1 The spatial discretization 46

2.4.2 The Newton-Raphson method 50

2.5 An analytical solution 52

2.6 Numerical results 54

2.6.1 Accuracy and stability of MBFEM 54

2.6.2 Effect of kinetic relation 57

2.6.3 Effect of the Newton-Raphson method and stress-induced transformations 60

2.7 Conclusions 62

3 Linear Shape Memory Alloy Actuators **78**

3.1 Introduction 78

3.2 Boundary value problem for a shape memory alloy bar with a sharp austenite-martensite interface 82

3.2.1 Thermomechanical governing equations 84

3.2.2 Initial conditions 86

3.2.3 Boundary conditions 86

3.3 Motion of the sharp austenite-martensite interface during phase transformation 88

3.3.1 The B-L-R model 90

3.3.2 The A-K model 91

3.4 Performance measures of SMA actuators in an active structure 93

3.4.1 Energy output per unit volume of SMA (or specific energy output) 94

3.4.2 Energy efficiency 95

3.5 The computational approach and parametric studies 95

3.5.1 The computational approach 95

3.5.2 The moving boundary finite element method 98

3.5.3 Parametric studies 100

3.6 Conclusions 105

4 A One-dimensional Theoretical Framework for Sharp Phase Fronts in Shape Memory Alloys 116

4.1 Introduction 116

4.2 The sharp phase front-based theoretical framework 120

4.2.1 Conservation Laws 120

4.2.2 Constitutive Equations 122

4.2.3 The Generalized Clausius-Clapeyron equation 123

4.2.4 Second Law of Thermodynamics 127

4.3 The quasistatic, small strain approximation and the SMA hysteresis 128

4.3.1 The quasistatic, small strain approximation 128

4.3.2 The SMA hysteretic response 131

4.4 Results and Discussion 134

4.5 Conclusions 142

5 A Three-dimensional Theoretical Framework for Sharp Phase Fronts in Shape Memory Alloys 155

5.1 Introduction 155

5.2 The 3D theory for sharp phase fronts in shape memory alloys 158

5.2.1 Conservation laws and entropy production 158

5.2.2 Constitutive equations 160

5.2.3 Generalized Clausius-Clapeyron equation 161

5.3 The 3D theory, based on a quasistatic, small strain approximation 162

5.4 The generalized Clausius-Clapeyron equation in the quasistatic, infinitesimal strain theory with a trilinear Helmholtz free energy function 164
  5.4.1 Variant selection criterion 166
5.5 The finite element method and the numerical approach 167
  5.5.1 The governing equations in a Cartesian reference frame 167
  5.5.2 Variant selection 169
  5.5.3 Numerical algorithm 170
  5.5.4 Mechanical Equilibrium Equation 172
  5.5.5 Energy Conservation Equation 176
  5.5.6 Energy Conservation at the Phase Boundary 180
  5.5.7 Finite element selection and spatial integration 181
  5.5.8 Interpolation 183
  5.5.9 Linear Algebraic Equations 187
  5.5.10 Preconditioning 190
5.6 Algorithm Validation 193
  5.6.1 Verification problems 194
  5.6.2 Accuracy and stability of the algorithm 203

5.7 Simulation and prediction of the pseudoelasticity and reorientation in SMA thin films 208
5.7.1 Material Parameters 208
5.7.2 Results and discussion 210

6 Conclusions 258

A MBFEM 263
A.1 Non-dimensional variables 263
A.2 Discretization of Eq. 2.29 in absence of the jump condition, Eq. 2.30 265
A.3 Modification of Eq. 2.40 due to the jump condition, Eq. 2.30 . 266
A.3.1 Phase boundary lies between two nodes 266
A.3.2 Phase boundary lies on node 268
A.4 The components of the Jacobian, $\mathbf{J}^{i(m)}$ 268
A.4.1 Phase boundary lies between two nodes 269
A.4.2 Phase boundary lies on a node 270

B Linear SMA Actuators 271
B.1 List of relevant non-dimensional parameters 271

C A 3D Theoretical Framework **273**

C.1 3D state of stress 273

C.2 2D state of stress 276

C.3 Maxwell Relations 278

C.4 von Neumann stability analysis 279

List of Tables

2.1 List of dimensional parameters. 67

2.2 Numerical values of θ_{pb} vs. x_{pb} obtained from the analytical solution, MBFEM and FDM-based approaches. 68

2.3 Numerical values of $\theta(x,t)$ vs. x when $x_{pb} = 0.5$. Results of the analytical solution, MBFEM and FDM-based approaches. 69

2.4 Numerical values of θ_{pb} vs. x_{pb} obtained from the analytical solution, and also computed by MBFEM when Eq. 2.60 is used for phase boundary velocity. 70

2.5 Numerical values of $\theta(x,t)$ vs. x when $x_{pb} = 0.5$. Results of the analytical solution are given, and also those from MBFEM when Eq. 2.60 is used for phase boundary velocity. 71

2.6 The effect of the Newton-Raphson method at different strain rates. 72

3.1 List of all material and computational parameters. 106

4.1 List of material, geometric, numerical and input parameters. . 150

5.1 Numerical and analytical values of the temperature, θ(deg C), in circular cylinder with time dependent boundary conditions . 219

5.2 Numerical and analytical values of the temperature, θ(deg C), in circular cylinder with time dependent heat source 221

5.3 Numerical and analytical values of T_{rr}(Pa) at three different locations of the heat source. 225

5.4 List of material, geometric, numerical and input parameters. . 228

5.5 Transformation strains of the 24 variants [1] 229

List of Figures

2.1 A schematic of a SMA bar in a deformation-controlled phase transformation process. 63

2.2 A plot θ_{pb} vs. x_{pb} during an M→A transformation, obtained from the analytical solution. 63

2.3 A plot $\theta(x, t)$ vs. x during an M→A transformation, at $x_{ph} =$ 0.5, obtained from the analytical solution. 64

2.4 The simulation of a constant phase boundary velocity vs. time, by the numerical approach of Eq. 2.60 64

2.5 A pseudoelastic stress-strain curve computed by MBFEM and FDM at $d\delta(1,t)/dt = 0.084$. 65

2.6 A pseudoelastic stress-strain curve computed by MBFEM and FDM at $d\delta(1,t)/dt = 0.84$. 65

2.7 Phase boundary temperature vs. position when $d\delta(1,t)/dt = 0.84$. 66

2.8 $\theta(x,t)$ vs. x when $x_{pb} = 0.5$ during A→M transformation, with $d\delta(1,t)/dt = 0.84$. 66

3.1 A schematic of linear SMA actuator. 107

3.2 A flowchart depicting the decision process for the phase transformation based on Leo et. al. [1] approach. 108

3.3 A flowchart outlining the MBFEM-based numerical approach of Stoilov et. al. [2] adapted to implement Leo et. al. [1] theoretical model. 109

3.4 A flowchart depicting the decision process for the phase transformation based on Abeyaratne and Knowles' [3] approach. . . . 110

3.5 Non-dimensional phase boundary position, $\bar{s}$, with respect to non-dimensional time, $\bar{t}$. 111

3.6 Non-dimensional stress, $\bar{\sigma}$, with respect to non-dimensional time, $\bar{t}$. 111

3.7 Non-dimensional phase boundary velocity, $\dot{\bar{s}}$, with respect to non-dimensional time, $\bar{t}$. 112

3.8 Non-dimensional specific energy output of SMA actuator, $\bar{W}_{act}$, with respect to non-dimensional spring stiffness, $\bar{K}_s$. 112
3.9 Energy efficiency of SMA actuator, η, with respect to non-dimensional spring stiffness, $\bar{K}_s$. 113

4.1 A schematic of the spatially one-dimensional (1D) phase transformation. 144
4.2 The decision-making process based on which either of Eq. 4.24 is used. 145
4.3 The flowchart in Fig. 4.2 requires the calculation of the field variables using the MBFEM-based numerical approach. This calculation is summarized in this flowchart. 146
4.4 Simulation of an experimental pseudoelastic stress-strain curve of a CuAlNi single crystal, uniaxial test specimen tested at $\theta_{amb} = 282K$ [1]. 147
4.5 Prediction of an experimental pseudoelastic stress-strain curve of a CuAlNi single crystal, uniaxial test specimen tested at $\theta_{amb} = 274K$ [1]. 147

4.6 Prediction of an experimental shape memory stress-strain curve of a CuAlNi single crystal, uniaxial test specimen tested at $\theta_{amb} = 243K$ [1]. 148

4.7 Prediction of the temperature-time response at the center of a NiTi SMA polycrystalline wire undergoing a thermal transformation while subjected to a constant load [2]. 149

5.1 Schematic of a thermoelastic system undergoing phase transformation 217

5.2 Numerical simulation of the temperature field θ in circular cylinder with time dependent boundary conditions 218

5.3 Numerical simulation of the temperature field θ in circular cylinder with time dependent heat source 220

5.4 Numerical simulation of the stress, T_{rr}, and temperature $\Delta\theta$ distribution within a hollow disc with heat source at $c = 0.35\ m$ 222

5.5 Numerical simulation of the stress, T_{rr}, and temperature $\Delta\theta$ distribution within a hollow disc with heat source at $c = 0.4\ m$ .223

5.6 Numerical simulation of the stress, T_{rr}, and temperature $\Delta\theta$ distribution within a hollow disc with heat source at $c = 0.45\ m$ 224

5.7 The averaged computational error as a function of the magnitude of the time step, τ ($N_{elm} = 2404$). 226

5.8 The averaged computational error as a function of the number of elements, N_{elm} ($\tau = 0.12s$). 227

5.9 Average stress, $\bar{\sigma}_{xx}$, vs. average strain, $\bar{\varepsilon}_{xx}$, comparison with experimental data [1], $\bar{\sigma}_{yy} = 0\ MPa$. 230

5.10 Martensitc volume fraction, V_m/V_{tot} as a function of the average stress, $\bar{\sigma}_{xx}$, $\bar{\sigma}_{yy} = 0\ MPa$. 231

5.11 Average stress, $\bar{\sigma}_{xx}$, evolution, $\bar{\sigma}_{yy} = 0\ MPa$. 232

5.12 Average stress, $\bar{\sigma}_{xx}$, vs. average strain, $\bar{\varepsilon}_{xx}$, comparison with experimental data [1], $\bar{\sigma}_{yy} = 40\ MPa$. 233

5.13 Martensitc volume fraction, V_m/V_{tot} as a function of the average stress, $\bar{\sigma}_{xx}$, $\bar{\sigma}_{yy} = 40\ MPa$. 234

5.14 Average stress, $\bar{\sigma}_{xx}$, evolution, $\bar{\sigma}_{yy} = 40\ MPa$. 235

5.15 Shape of the martensitic inclusion when $\bar{\varepsilon}_{xx} = 1.0\%$ during A→M transformation, $\bar{\sigma}_{yy} = 40\ MPa$. 236

5.16 Shape of the martensitic inclusion when $\bar{\varepsilon}_{xx} = 3.5\%$ during A→M transformation, $\bar{\sigma}_{yy} = 40\ MPa$. 237

5.17 Distribution of σ_{xx}(MPa) when $\bar{\varepsilon}_{xx} = 1.0\%$ during A→M transformation, $\bar{\sigma}_{yy} = 40\ MPa$. 238

5.18 Cross-sectional profiles of σ_{xx} when $\bar{\varepsilon}_{xx} = 1.0\%$ during A→M transformation, $\bar{\sigma}_{yy} = 40\ MPa$. 239

5.19 Distribution of σ_{yy}(MPa) when $\bar{\varepsilon}_{xx} = 1.0\%$ during A→M transformation, $\bar{\sigma}_{yy} = 40\ MPa$. 240

5.20 Cross-sectional profiles of σ_{yy} when $\bar{\varepsilon}_{xx} = 1.0\%$ during A→M transformation, $\bar{\sigma}_{yy} = 40\ MPa$. 241

5.21 Distribution of σ_{xy}(MPa) when $\bar{\varepsilon}_{xx} = 1.0\%$ during A→M transformation, $\bar{\sigma}_{yy} = 40\ MPa$. 242

5.22 Cross-sectional profiles of σ_{xy} when $\bar{\varepsilon}_{xx} = 1.0\%$ during A→M transformation, $\bar{\sigma}_{yy} = 40\ MPa$. 243

5.23 Temperature, θ, distribution when $\bar{\varepsilon}_{xx} = 1.0\%$ during A→M transformation, $\bar{\sigma}_{yy} = 40\ MPa$. 244

5.24 Cross-sectional profiles of the temperature, θ, when $\bar{\varepsilon}_{xx} = 1.0\%$ during A→M transformation, $\bar{\sigma}_{yy} = 40\ MPa$. 245

5.25 Distribution of σ_{xx}(MPa) when $\bar{\varepsilon}_{xx} = 3.5\%$ during A→M transformation, $\bar{\sigma}_{yy} = 40\ MPa$. 246

5.26 Cross-sectional profiles of σ_{xx} when $\bar{\varepsilon}_{xx} = 3.5\%$ during A→M transformation, $\bar{\sigma}_{yy} = 40\ MPa$. 247

5.27 Distribution of σ_{yy}(MPa) when $\bar{\varepsilon}_{xx} = 3.5\%$ during A→M transformation, $\bar{\sigma}_{yy} = 40\ MPa$. 248

5.28 Cross-sectional profiles of σ_{yy} when $\bar{\varepsilon}_{xx} = 3.5\%$ during A→M transformation, $\bar{\sigma}_{yy} = 40\ MPa$. 249

5.29 Distribution of σ_{xy}(MPa) when $\bar{\varepsilon}_{xx} = 3.5\%$ during A→M transformation, $\bar{\sigma}_{yy} = 40\ MPa$. 250

5.30 Cross-sectional profiles of σ_{xy} when $\bar{\varepsilon}_{xx} = 3.5\%$ during A→M transformation, $\bar{\sigma}_{yy} = 40\ MPa$. 251

5.31 Average stress, $\bar{\sigma}_{xx}$, vs. average strain, $\bar{\varepsilon}_{xx}$, comparison with experimental data [1], $\bar{\sigma}_{yy} = 160\ MPa$. 252

Chapter 1

Introduction

1.1 Thermoelastic martensitic phase transformation

Of the several solid state phase transformations occurring in alloy systems, martensitic transformations have had a very special interest to researchers. In the early years this interest arose out of the extraordinary hardness that iron-carbon martensite possessed. Soon it was realized that a number of alloy systems, both ferrous and nonferrous, exhibited martensitic transformations and these have been the subject of innumerable investigations. Special emphasis was laid on the fact that the resultant martensite phase had an interface with the parent phase. Extensional and shear strains on this plane are essentially zero. The corresponding strain field in the 3D domain is commonly referred in the materials literature as "Invariant plane strain"'[1]. This led to the emergence of the phenomenological theories to account for the observed crystallography of the parent-product relationship. However, the observed overall characteristics of the martensitic transformations have been used by Wayman [2] to define a martensitic transformation as one where (a) there is a lattice deformation with an accompanying shape change, (b) diffusion is not required and (c) the kinetics and morphology during the transformation are dominated by the transformation strain energy. Therefore, martensitic transformations can be induced by the application of stress as well as by changes in temperature and they are crystallographically reversible. Usually, the shape deformation of a martensitic transformation is so large relative to the stiffness and strength of the surrounding parent phase that plastic accommodation takes place during the growth process. In this sense, the interfacial motions are not reversible. Alternatively, in those instances where the shape deformation can be accommodated elastically, the interfacial motions take on reversible features. In this thesis we will consider the latter case only, so that no plastic deformation is induced during the transformation. Then the characteristics of martensitic transformation that are mentioned can sometimes lead to some interesting effects: thermoelasticity, pseudoelasticity, shape memory effect and two-way shape memory effect. A thermoelastic martensitic transformation is realized if martensite forms and grows continuously as temperature is lowered, and shrinks and vanishes continuously as temperature is raised. In their experiments with an In-TI single crystal alloy, Burkart and Read [3] observed a single interface separating the parent phase and the product phase. On slow cooling, the specimen transformed from the face-centered cubic structure to the face-centered tetragonal structure at the martesite start temperature M_s. by the motion of a single plane interface which traversed the specimen from one end to the other. Upon heating, the interface moved back in the reverse direction. Other alloys which exhibit thermoelastic transformation are AgCd, CuAlNi, NiTi, CuZn, CuSn, InTi, and so on. Alloy systems which undergo a thermoelastic transformation on cooling can be made to transform in a similarly reversible manner, even at temperatures above M_s by applying an increasing stress. This type of stress-induced transformation is an example of pseudoelasticity in view of the relatively large deformation that can be manifested ($\sim$ 8%) by the induced transformation, and yet this strain is "elastically" recoverable on unloading due to the reversal of the transformation. Many interesting features of the pseudoelastic behavior have been found. The shape of the stress-strain curve depends heavily on temperature and the stress necessary for transformation is found to increase with temperature (see Horikawa et. al. [4], Shaw et. al. [5], Fang et. al. [6], Chumlyakov et.al. [7]). The shape memory effect arises if a macroscopic deformation is accompanied, as before, by a martensitic transformation at a temperature lower than the transformation temperature; in a second step the reverse transformation and a concomitant reversal of the macroscopic deformation are induced by heating up to a temperature higher than the austenite finish temperature A_f. The system recovers its original shape after heating.

Up to this point we have implied that pseudoelasticity and the shape memory effect were associated with a martensitic transformation. The same phenomena can occur even when the specimen is fully martensitic at the outset [8]. In this case the macroscopic deformation is induced by reorientation of martensites. Thus, pseudoelasticity and the shape memory effect may be associated with a martensitic transformation, a reorientation of a martensitic structure or a combination of both. The shape memory effect just considered is one-way, i.e. no appreciable change in specimen shape occurs during the martensitic transformation on cooling; instead, a change in shape takes place during the reverse transformation on heating above A_f which cancels the prior change of shape introduced by deforming the specimen. In the two-way shape memory effect, an overall change of specimen shape operates during the cooling and heating transformations. The condition can be brought about in two ways: either after pseudoelastically cycling by loading and unloading several times above the transformation temperature or by going through the one-way shape memory effect a number of times. It appears that both of the above "training" methods, i.e. by stress induced martensite (SIM) cycling or by shape memory effect (SME) cycling, involve the preferential formation of lattice defects or micro-stresses which favor selected variants during the thermoelastic transformation on cooling.

1.2 SMA models

Constitutive models, of which there is a rich literature (see [9] for a review), can be primarily categorized into three groups: 1. Phenomenological models based on homogenization principles, 2. micromechanical models, and 3. continuum models or also known as sharp phase front-based constitutive models. The need to incorporate the SMA material behavior in engineering design of SMA-based structures probably motivated the development of the phenomenological models. These are built on phenomenological thermodynamics and/or directly curve fitting experimental data. The volume fraction of the martensite is typically used as the internal variable and different mathematical functions are used to describe the transformation procedure (Sato and Tanaka [10], Liang and Rogers [11, 12], Boyd and Lagoudas [13], Bekker and Brinson [14]). Most of the models in this group only work on uniaxial loading or are simple yet unverified extensions of these models to 2D and 3D. On the other hand, the micromechanical models sought to bridge the SMA response at the microscopic level to the SMA macroscopic response. They use thermodynamics laws to describe the transformation and micromechanics to estimate the interaction energy due to the transformation in the material, which is a key factor in the transformation mechanism (Patoor et. al. [15], Sun and Hwang [16, 17], Goo and Lexcellent [18], Lu and Wang [19], Huang and Brinson [20]). While these models are quite elaborate and computationally expensive to implement, they incorporate a significant amount of the physics of the transformation. Both types of models use an internal variable approach that allows the material state at a continuum point to exist as a mixture of the two phases of austenite and martensite. Lastly, the continuum/sharp phase front-based constitutive models incorporate the very basic feature that the SMA phase transformation is often accompanied by the motion of a phase boundary (or multiple phase boundaries) between the old and the new phase. Thus, the material state at a continuum point, within the context of such models, is either in an austenitic state or martensitic state but never both.

1.2.1 Review of continuum modeling

Various continuum-level issues related to martensitic phase transformation in crystalline solids have been successfully studied using the theory of finite thermoelasticity. For a thermoelastic material, the Helmholtz free-energy function ψ depends only on the deformation gradient tensor $\mathbf{F}$ and the temperature θ : $\psi = \psi(\mathbf{F}, \theta)$. If the stress-free material can exist in two or more phases, then the Helmholtz free-energy function ψ must have two or more energy wells. One corresponds to austenite, the other martensititic variants. In the presence of stress $\mathbf{T_R}$, one must consider the energy function $\psi = \psi(\mathbf{T_R}(\mathbf{F}, \theta), \theta)$ involving the energy wells, where $\mathbf{T_R}$ is the first Piola-Kirchhoff stress tensor. Now the material can have different stable phases coresponding to different combinations of applied stress and temperature.

Ericksen [21] studied energy minimizing deformations for a two-phase material within the one-dimensional mechanical setting of a tensile bar. He showed, in particular, that for certain values of prescribed displacement, the stable equilibrium configurations of the bar involve coexistent phases. The analogous issue in higher dimensions is more complicated: typically, deformation gradient tensors $\mathbf{F_A}$ and $\mathbf{F_M}$ corresponding to the austenite and martensite energy minima are not kinematically compatible with each other. Therefore an energy minimizing deformation cannot correspond to homogeneously deformed states of austenite and martensite separated by a phase boundary. In fact, an energy minimizer usually does not even exist, and one must contend with minimizing sequences. The deformation pattern associated with such a sequence characterizes the underlying microstructure of the material; in Cu-Al-Ni for example, an austenite-martensite phase boundary separates a homogeneous state of austenite from a fine mixture of twinned martensite. These ideas were put forward by Khachaturian [1] using a geometrically linear theory, and by Ball and James [22] for the finite deformation theory. Ball and James [22] studied an austenite/twinned martensite interface in detail, and showed that the consequences of their theory are in agreement with the crystallographic theory of martensite. Needle-like microstructures and self-accommodating microstructures have been explored by Bhattacharya [23] using similar ideas.

It has been noted by many researchers that the characteristics of thermoelastic martensitic phase transformation are changed when the transformation is repeated many times by thermal and stress cycling. This is because, during thermomechanical cycling, phase boundaries travel forward and backward in the specimen and some microstructural defects such as dislocations are generated and distributed in the alloy; for example, see Melton and Mercier [24], Miyazaki et al. [25, 26], and so on. A continuum model to describe the cyclic behavior of shape memory alloys was proposed by Tanaka et al. [27, 28]. They took the point of view that the dislocations generated are a primary cause of the accumulation of a microscopic residual stress and strain in the alloy. They introduced three internal variables, i.e. the microscopic residual stress and strain and the volume fraction of the residual martensite.

A number of studies have been concerned with developing explicit constitutive models. Ericksen [29] and Silling [30] have constructed three- dimensional Helmholtz free-energy functions for modeling specific crystals. Falk [31] has studied a one-dimensional polynomial free-energy function.

Later Falk and Konopka[32] generalized the one-dimensional approach to three dimensional free-energy function based on the Landau theory of phase transformations.

The usual continuum theory of thermoelasticity, though adequate for characterizing phase energy minimization, does not characterize the dynamic processes of a body involving transitions from one phase to another. In order to achieve an accurate dynamical response, Abeyaratne and Knowles [33] expanded the constitutive model developed by Falk [31] with the basic conservation laws: conservation of mass, linear momentum, angular momentum and energy. The resulting model, though defines one-parametric family of solutions. This lack of uniqueness of solution to particular initial-value problems has been illustrated in the works of Abeyaratne and Knowles [34]. In order to solve this uniqueness problem they adopted the view that the lack of uniqueness in the conventional formulations arose from a constitutive deficiency associated with particles on the phase interface and they supplemented the theory with further constitutive information, which were a kinetic relation and a nucleation criterion. The kinetic relation controls the progress of the phase transition once it has commenced and the nucleation criterion signals the initiation of a transition. Thus a complete constitutive theory which is capable of modeling processes involving thermoelastic phase transitions consists of a Helmholtz free-energy function, conservation laws(mass, linear momentum, angular momentum, energy) a kinetic relation, and a nucleation criterion.

Leo, Shield and Bruno [35] adapted different approach to eliminate the lack of uniqueness. They completed the constitutive model with additional constitutive equation, which is an experimentally determined relation between the stress and the temperature at the phase transformation interface. Bruno et. al. [36] and Shield et. al. [37] showed that the particular initial-value problem has unique solution when studied in this broadening setting.

Recently, Stoilov at. el. [38] have suggested a complete, explicit one-dimensional model for describing the thermoelastic phase transformations. The lack of uniqueness is eliminated by introducing a fundamental conservation law; the conservation of the chemical potential at the phase boundary. The general form of the derivation makes the approach as general as possible and applicable to any physical system capable of 1st order phase transformation. The suggested model reduces to any of the two approaches described above at the corresponding conditions. For example, using the simplified three-linear approximation of the Falk's Helmholtz free energy function, the conservation of the chemical potential results in an analytical relation between the stress and the temperature at the phase boundary, identical to the experimental one used by Leo at. el. [35].

1.3 Numerical methods for moving boundary problems

During the processes of phase transformation in thermoelastic materials (SMAs), a boundary separating two different phases develops. In these problems, the position of the boundary is not known a priori, but has to be determined as an integral part of the solution. The class of problems known as Moving Boundary Problems (MBP) is associated with time-dependent boundary problems, where the position of the Moving Boundary (MB) has to be determined as function of time and space. Moving boundary problems, also known as Stefan problems, were studied as early as 1831 by Lame and Clapeyron. However, J. Stefan was given the major credit due to a sequence of papers, which resulted from his study of the melting of the polar ice cap around 1890.

Finite Difference Methods (FDMs) are the most popular choice for numerical solution of MBPs; however, in recent years, Finite Element Methods (FEMs) and Boundary Elements Methods (BEMs) have been introduced. The advantage of FEMs and BEMs is their ability to handle complex geometries. The numerical methods for solving MBPs can be classified into: Fixed grid methods [39, 40] and Variable grid methods [41, 42, 43, 44, 45, 46, 47]. The formulation of the classical Stefan problem requires not only the initial and boundary conditions to be known, as in boundary value problems, but one more condition is needed on the moving boundary; e.g. the temperature of the boundary during freezing of water/melting of ice. In contrast the temperature of the phase boundary during phase transformation in SMAs is not prescribed, and instead is a function of the local stress. Due to this extra dependence, an additional condition is required to render a unique solution of the problem. From a mathematical point of view, the two approaches for completing the system, outlined in Sec. 1.2.1, are representative of two separate classes of problems. In the case of Leo et. al. [35] approach, the experimental correlation between the phase transformation temperature and the local stress constitutes a boundary condition at the MB. The velocity of propagation of the phase boundary is then found as part of the problem solution. This class of problems, where a boundary condition at the MB is prescribed, is referred to as "forward" problems. In the case of Abeyaratne and Knowles' [33] approach, a kinetic relation prescribing the velocity of propagation of the phase boundary completes the system. In this case the velocity is known and the temperature at the phase boundary can be determined as a function of the position. We shall refer to this class of problems as "inverse" problems. Each of these classes of problems requires a separate numerical approach.

1.4 Thesis objectives and outline

The objective of this thesis is to develop a multiaxial continuum model that includes several important features of the austenite (A) to martensite (M) phase transformation in shape memory alloys (SMA) : (i) significant hysteresis between the $A \rightarrow M$ and $M \rightarrow A$ transformation, (ii) strong thermomechanical coupling, (iii) significant difference in material properties of the two phases (this is atleast true for the Nickel-Titanium system (Faulkner, Amalraj and Bhattacharyya[48]), (iv) motion of phase boundaries, and (v) the initial microstructure and its influence on the phase transformation. Availability of such a model gives us the capability to study fundamental issues involved in the micro-macro transition in the SMA response, e.g. the correlation between the first-order transition at the micro-level (transformation at a single stress-dependent temperature) to the transformation at the macro-level over a temperature range (even in absence of external stress). The model may also be used as a computational tool to guide experiments and the development of phenomenological multiaxial models for engineering design.

This thesis is divided into five parts: A Moving Boundary Finite Element Method(MBFEM), Linear SMA actuators, a complete one dimensional theoretical framework for thermoelastic phase transformations, complete 3D theoretical model for thermoelastic phase transformations, and numerical implementation in two-dimensional domain.

Chapter 2 is entirely devoted to a Moving Boundary Finite Element Method (see Stoilov, Iliev and Bhattacharyya [49]) developed for spatially 1D phase transformation in SMAs. In Chapter 3, the MBFEM is generalized to allow a numerical solution for the approach introduced by Leo, Shield and Bruno [35]. The modified MBFEM is then used to compare the two existing sharp phase front models (Abeyaratne and Knowles [33] and Leo, Shield and Bruno [35]) in the context of linear SMA based actuators(see

Bhattacharyya, Stoilov and Iliev [50]). In Chapter 4 we propose a new sharp phase front model and the general theoretical framework for one-dimensional SMA phase transformations(see Stoilov and Bhattacharyya [38]). In Chapter 5 the general three-dimensional form of the continuum model for sharp phase fronts is presented, followed by a numerical analysis and implementation of moving boundary problems in 2-D SMA domains. In the same chapter we present the predictions for pseudoelastic behavior and reorientation in SMA thin films under biaxial loading as well as a comparison with the experimental data of Fang et. al. [6] on SMA thin films. The conclusion are given in Chapter 6.

Bibliography

[1] A. Khachaturyan, *Theory of structural transformations in solids*, John Wiley & Sons, New York, 1983.

[2] C. Wayman, *Physical Metallurgy*, North-Holland, New York, 1983.

[3] M. Burkart and T. Read, "Diffusionless phase change in indium-thallium system," *Trans. ASME - Journal of Metals* **197**, pp. 1516–1524, 1953.

[4] H. Horikawa and S. Miyazaki, "Orientation dependence of $\beta_1 \rightarrow \beta_1'$ stress-induced martensitic transformation in Cu-Al-Ni alloy," *Metallurgical Transaction A* **19**, pp. 915–923, 1988.

[5] J. A. Shaw and S. Kyriakides, "Thermomechanical aspects of NiTi," *J. Mech. Phys. Solids* **43**, pp. 1243–1281, 1995.

[6] D. Fang, W. Lu, W. Yan, T. Inoue and K. Hwang, "Stress-strain relation of CuAlNi SMA single crystal under biaxial loading-constitutive model and experiments," *Acta Materialia* **47**, pp. 269–280, 1999.

[7] Yu. Chumlyakov, I. Kireeva, A. Lysuk, A. Bhattacharyya and V. Stoilov, "Shape memory effect and superelasticity in Ti-30%Ni-20%Cu single crystals," *Proceedings of the 38th Annual Conference of Metallurgists, August 22-26, Quebec City, Quebec, Canada* , 1999.

[8] J. Ball, C. Chu and R. James, "Hysterisis during stress-induced variant rearrangement," *Journal de Physique IV* **5**, pp. 245–251, 1995.

[9] D. C. Lagoudas and A. Bhattacharyya, "On the correspondence between micromechanical models for isothermal pseudoelastic response of shape memory alloys and the preisach model for hysteresis," *Mathematics and Mechanics of Solids* **2**, pp. 405–440, 1997.

[10] Y. Sato and K. Tanaka, "Estimation of energy dissipation in alloys due to stress-induced martensitic transformation," *RES MECHANICA* **23**, pp. 381–393, 1988.

[11] C. Liang and C. Rogers, "One-dimensional thermomechanical constitutive relations for shape memory materials," *J. of Intell. Mater. Syst. and Struct.* **1**, pp. 207–234, 1990.

[12] C. Liang and C. Rogers, "A multidimensional constitutive model for shape memory alloys," *J. Eng. Math.* **26**, pp. 429–443, 1992.

[13] J. Boyd and D. Lagoudas, "Thermomechanical response of shape-memory composites," *J. Intell. Mater. Syst and Struct.* **5**, pp. 333–346, 1994.

[14] A. Bekker and L. Brinson, "Temperature-induced phase transformation in shape memory alloy: phase diagram based kinetic approach," *J. Mech. Phys. Solids* **45**, pp. 949–988, 1997.

[15] E. Patoor, A. Eberhadt and M. Bervellier, "Micromechanical modeling of the superelastic behavior," *JOURNAL DE PHYSIQUE IV* **5**, pp. 501–506, 1995.

[16] Q. Sun and K. Hwang, "Micromechanics modeling for the constitutive behavior of polycrystalline shape memory alloys. 1. Derivation of general relations," *J. Mech. Phys. Solids* **41**, pp. 1–17, 1993.

[17] Q. Sun and K. Hwang, "Micromechanics modeling for the constitutive behavior of polycrystalline shape memory alloys. 1. Study of the individual phenomena," *J. Mech. Phys. Solids* **41**, pp. 19–33, 1993.

[18] B. Goo and C. Lexcellent, "Micromechanics-based modeling of two-way memory effect of a single crystalline shape-memory alloy," *Acta Mater.* **45**, pp. 727–737, 1997.

[19] Z. Lu and G. Weng, "Martensitic transformation and stress-strain relations of shape-memory alloys," *J. Mech. Phys. Solids* **45**, pp. 1905–1928, 1997.

[20] M. Huang and L. Brinson, "A multivariant model for single crystal shape memory alloy behavior," *Journal of the Mechanics and Physics of Solids* **46**, pp. 1379–1409, 1998.

[21] J. Ericksen, "Equilibrium of bars," *Journal of elasticity* **5**, pp. 191–201, 1975.

[22] J. Ball and R. James, "Fine phase mixtures as minimazers of energy," *Archive for rational mechanics and analysis* **100**, pp. 13–52, 1987.

[23] K. Bhattacharyya, "Wedge like microstructure in martensite," *Acta Metall. Mater.* **39**, pp. 2431–2444, 1991.

[24] K. Melton and O. Mercier, "Fatigue of NiTi martensites," *Acta Metall.* **27**, pp. 137–143, 1979.

[25] S. Miyazaki, T. Imai, Y. Igo and K. Otsuka, "Effect of cyclic deformation on the pseudoelasticity characteristics of Ti-Ni alloys," *Metall. Trans.* **17A**, pp. 115–120, 1986.

[26] S. Miyazaki, Y. Igo and K. Otsuka, "Effect of thermal cycling on the transformation temperatures of Ti-Ni alloys," *Acta Metall.* **34**, pp. 2045–2051, 1986.

[27] K. Tanaka, T. Hayashi, Y. Itoh and H. Tobushi, "Analysis of thermomechanical behavior of shape memory alloys," *Mech. Mater.* **13**, pp. 207–215, 1992.

[28] K. Tanaka, F. Nashimura, T. Hayashi, H. Tobushi and C. Lexcellent, "Phenomenological analysis on subloops and cyclic behavior in shape memory alloys under mechanical and/or thermal loads," *Mech. Mater.* **19**, pp. 281–292, 1995.

[29] J. Ericksen, "Constitutive theory for constrained elastic crystals," *International Journal of Solids and Structures* **22**, pp. 951–964, 1986.

[30] S. Silling, "Phase-changes induced by deformation in isothermal elastic crystals," *Journal of the mechanics and physics of solids* **37**, pp. 293–316, 1989.

[31] F. Falk, "Model free energy, mechanics , and thermodynamics of shape memory alloys," *Acta Metallurgica* **28**, pp. 1773–1780, 1980.

[32] F. Falk and P. Konopka, "Three-dimensional Landau theory describing the martensitic phase transformation of shape-memory alloys," *J. Phys.: Condens. Matter* **2**, pp. 61–77, 1990.

[33] R. Abeyaratne and J. Knowles, "On the driving traction acting on the surface of strain discontinuity in a continuum," *J. Mech. Phys. Solids* **38**, pp. 345–360, 1990.

[34] R. Abeyaratne and J. Knowles, "Dynamics of propagating phase boundaries: adiabatic theory for thermoelastic solids," *Physica D* **79**, pp. 269–288, 1994.

[35] P. H. Leo, T. W. Shield, and O. P. Bruno, "Transient heat transfer effects on the pseudoelastic behavior of shape memory alloy wires," *Acta Metallurgica Materialia* **41**, pp. 2477–2485, 1993.

[36] O. P. Bruno, P. H. Leo, and F. Reitich, "Free boundary conditions at austenite-martensite interfaces," *Phys. Rev. Lett.* **74**, pp. 746–749, 1995.

[37] T. Shield, P. Leo, and C. Grebner, "Quasi-static extension of shape memory wires under constant load," *Acta Materialia* **45**, pp. 67–74, 1997.

[38] V. Stoilov and A. Bhattacharyya, "A theoretical framework of one-dimensional sharp phase fronts in shape memory alloys," *to appear in Acta Materialia* .

[39] J. Crank, "Two methods for the numerical solution of moving boundary problems in diffusion and heat flow," *J. Mech. Appl. Math.* **10**, pp. 220–231, 1957.

[40] L. Ehrlich, "A numerical method of solving a heat flow problem with phase boundary," *J. Assn. Comp. Math* **5**, pp. 161–176, 1958.

[41] N. Asaithambi, "On a variable time-step method for the one-dimensional stefan problem," *Comput. Meth. Appl. Mech. Eng* **71**, pp. 1–13, 1988.

[42] R. Gupta and D. Kumar, "A modified variable time step method for one dimensional stefan problem," *Comput. Meth. Appl. Mech. Eng.* **23**, pp. 101–109, 1980.

[43] R. Gupta and D. Kumar, "Variable time step methods for one dimensional stefan problem with mixed boundary conditions," *J. Heat and Mass Transfer* **24**, pp. 251–259, 1981.

[44] W. Murray and F. Landis, "Numerical and machine solutions of transient heat conduction problems involving melting or freezing," *J. Heat and Mass Transfer* **81**, pp. 106–112, 1959.

[45] J. Crank and R. Gupta, "A method for solving moving boundary value problems in heat flow using cubic splines or polynomials," *J. Inst. Math. Appl.* **10**, pp. 296–304, 1972.

[46] R. Gupta, "Moving grid method without interpolations," *Comput. Meth. Appl. Mech. Eng.* **4**, pp. 143–152, 1974.

[47] M. Djomehri and J. George, "Application of the moving finite element method to moving boundary stefan problems," *Comput. Meth. Appl. Mech. Eng.* **71**, pp. 125–136, 1987.

[48] M. G. Faulkner, J. J. Amalraj, and A. Bhattacharyya, "Experimental determination of thermal and electrical properties of ni-ti shape memory wires," *Smart Mater. Struct.* **9**, pp. 632–639, 2000.

[49] V. Stoilov, O. Iliev, and A. Bhattacharyya, "A moving boundary finite element method-based approach for the solution of one-dimensional problems in shape memory alloys," *Computer Methods in Applied Mechanics and Engineering* **190**, pp. 1741–1762, 2000.

[50] A. Bhattacharyya, V. Stoilov, and O. Iliev, "Evaluation of structural influence of shape memory alloys linear actuators by sharp phase front-based constitutive models," *Computational Materials Science* **18**, pp. 269–282, 2000.

Chapter 2

The Moving Boundary Finite Element Method(MBFEM)

2.1 Introduction

The phase transformation process in SMAs is often accompanied by the motion of a boundary between the "old" phase and the "new" phase that is being created [1, 2]. Traditionally, problems involving a moving boundary have been encountered in processes involving melting, solidification or diffusion, and are commonly referred to as the Stefan problems[3]. The moving boundary in a Stefan problem has two key features: (1) The temperature (or "concentration" for problems in diffusion) at the phase boundary is prescribed. (2) The heat flux (or concentration gradient) at the phase boundary has a jump, and this jump is proportional to the unknown velocity of the phase boundary. The velocity is then found as a part of the problem solution. In contrast, the temperature at the moving boundary in a phase transformation process in SMAs is not prescribed. However, similar to a Stefan problem, there is a jump in the heat flux at the moving boundary. This jump is proportional to the phase boundary velocity, which is also sometimes known as the "kinetic relation" [4]. The kinetic relation has to be developed from phenomenological considerations, and in general, is a function of the unknown temperature and stress at the phase boundary. These then have to be found as part of the problem solution. Numerical methods that address the Stefan problem may be classified in two categories [5]:

1. Fixed grid methods in which the spatial domain is discretized into elements of fixed length and the time stepping is based on a constant time increment. Therefore, at any given time, the moving boundary may lie on a grid node or between two nodes [6, 7].

2. Variable grid methods in which the discretization is fixed either in the spatial or the temporal domain. If the spatial discretization is fixed for

all time, then the incremental time step is adjusted so that the moving boundary always coincides with a grid node [8, 9, 10]. On the other hand, if the incremental time step is held fixed for all time, then the spatial discretization is adjusted over time such that a grid node always coincides with the moving boundary [11, 12, 13, 14].

The evolution in the thermal field during phase transformation was determined by a variable grid approach, referred as the moving boundary finite element method (MBFEM). While the MBFEM has been used to model Stefan problems in melting/solidification [11, 14] and diffusion[12, 13], to the best of our knowledge, it was used for the first time in problems involving phase transformation in SMAs by Stoilov et al. [15]. Issues involving stability and accuracy of the MBFEM-based numerical approach have been also addressed.

In this chapter, a MBFEM-based numerical approach used to solve a system of non-linear, coupled equations with a moving phase boundary in a 1-D domain, will be analyzed. An SMA bar, initially in the austenitic state and at a uniform temperature is considered. The bar is subjected to uniaxial mechanical loading. This is accompanied by a phase transformation of the bar from austenite to martensite, and the motion of a phase boundary between the two phases; see Fig. 2.1. Due to the strong coupling between the thermal and mechanical fields during phase transformation in SMAs [4, 16, 17, 18, 19], the effect of the mechanical loading is to induce a non-uniform temperature field in the bar. In the 1-D setting to which we restrict ourselves in this chapter, the entire problem is described by a system of four equations: (1) An equation relating the deformation rate to the stress rate (i.e. rate form of Hooke's law for a thermoelastic material). (2) The heat conduction equation (i.e. conservation of energy) for both phases. (3) A condition involving the jump in the heat flux at the moving boundary, proportional to the phase boundary velocity. (4) An expression for the phase boundary velocity, also known as a "kinetic relation" [4]. This expression has to be "assumed" based on phenomenological considerations. The heat conduction equation is non-linear in the temperature field whereas the system of equations is strongly coupled in the temperature and the stress field (also referred as "thermomechanical coupling").

This work addresses the solution of the aforementioned equations as a "system". The non-linear heat conduction equation is addressed by a Newton-Raphson technique whereas the thermomechanical coupling is addressed by an iterative procedure. Discretization of the spatial domain is done by introducing an extra grid node in a 1-D mesh, which otherwise remains unchanged from one time step to another. The extra node at a given time step is positioned such that it coincides with the phase boundary position at that instant. Our approach differs from the following approaches: (i) Murray and Landis[11] re-meshed the entire domain such that a grid node coincides with the phase boundary. (ii) Crank and Gupta[12] suggested a grid that moves with the phase boundary , such that the phase boundary always coincides with a grid node; the method requires the use of interpolation functions. (iii) Gupta [13] suggested avoiding the interpolations by employing a Taylor's series expansion in space and time. (iv) Djomehri and George [14] suggested the use of time-dependent basis functions in approximating the field variable (e.g. temperature).

The accuracy and stability of the proposed MBFEM-based numerical approach are demonstrated for the special case of a thermally induced phase transformation (the uniaxial stress is zero, and hence there is no thermomechanical coupling) that admits an analytical solution. For completeness, we also compare the current approach with a finite difference method (FDM)-based numerical approach, originally used by Kim and Abeyaratne [4]. Noting that the kinetic relation (i.e. the expression for the phase boundary velocity) is an "assumed" one, we compare the predictions of both approaches within the context of the analytical solution when the kinetic relation is "pathological" in nature. Subsequently, we compare predictions of both approaches for a phase transformation induced by mechanical loading (i.e. thermomechanical coupling is present).

The chapter is organized in the following sections. Section 2.2 introduces the 1-D BVP and Section 2.3 gives the temporal discretization and MBFEM-based numerical approach. Section 2.4 describes the spatial discretization with the MBFEM, Section 2.5 gives an analytical solution and Section 2.6 presents the numerical results. The conclusions are outlined in Section 2.7.

2.2 A one-dimensional moving boundary value problem in shape memory alloys

Consider an SMA bar of length 2L, shown in Fig. 2.1. The phase transformation in a bar is often accompanied by the motion of a boundary between the new and old phase. As in [4], we assume that during the A→M transformation (M→A transformation) for an initially austenitic (martensitic) bar, the martensite (austenite) nucleates at the center of the bar (at the end of the bar). The motion of the phase boundary is stress and temperature dependent, and their values at the phase boundary are not prescribed, in general. We consider the simplest situation in which two moving boundaries may be observed, wherein we restrict the BVP such that the motion of the two boundaries (see Fig. 2.1) is symmetric with respect to the center of the bar. Experimentally, this has been observed in Copper-Aluminium-Nickel SMA single crystals by Salzbrenner and Cohen [20]. Admittedly, a more common scenario is where multiple phase boundaries are observed (e.g. see the work of Leo et al. [1], Shaw and Kyriakides [2]). The numerical approach proposed herein will have to be modified appropriately to reflect such a situation; this is outside the scope of this chapter. Choosing the origin at the center of the bar, we focus on the domain, $0 \leq x \leq L$, for our analysis. The location of the phase boundary in that domain is denoted as $x_{pb}(t)$.

Phase transformations in the 1-D SMA bar are considered such that the time-dependent uniaxial stress is spatially uniform whereas the temperature field is x-dependent and time-dependent. Thus

$$\sigma \equiv \sigma(t) \quad \text{and} \quad \theta \equiv \theta(x,t) \; . \tag{2.1}$$

Defining $\delta(L,t)$ as the total deformation at the end of the bar, it is given as [21]

$$\delta(L.t) = \frac{L}{E}\sigma(t) + \alpha \int_0^L \left[\theta(x,t) - \theta_{amb}\right] dx + \varepsilon_T x_{pb}(t) \ , \qquad (2.2)$$

where the three terms on the right represent deformation in the bar due to elastic strains, thermal strains and strains due to phase transformation. The parameter L is the half-length of the bar, E the Young's modulus of SMA (assumed identical for both austenite and martensite), α the coefficient of thermal expansion and θ_{amb} is the ambient temperature. The parameter ε_T is the inelastic phase transformation strain and is defined as the deformation (or change in length) introduced in a unit length of SMA bar as it changes from austenite to martensite. The strain ε_T can have a value as high as 8% [22, 23]. In such cases and also in a situation where multiple stress-free configurations of the martensite can exist (i.e. ε_T will have different values depending on the corresponding martensite configuration or variant), an additive split of the total deformation in the bar (Eq. 2.2) may not be valid. Herein, the theory is restricted to one stress-free martensitic variant. Moreover, it is recommended that the theory and the developed numerical approach are used to simulate/predict experimental results only when ε_T is "small", and at best, used with considerable caution if the observed ε_T is as high as 8%. We now define an average temperature in the bar as

$$\bar{\theta} = \frac{1}{L}\int_0^L \theta(x,t)dx \ , \tag{2.3}$$

based on which, Eq. 2.2 may be written in a rate form as

$$\frac{d\delta}{dt}(L,t) = \frac{L}{E}\frac{d\sigma}{dt}(t) + L\alpha\frac{d\bar{\theta}}{dt}(x,t) + \varepsilon_T\frac{dx_{pb}}{dt}(t) \ . \tag{2.4}$$

The first law of thermodynamics provides the heat conduction equation for SMAs. It is [4, 21]

$$\begin{aligned} k\frac{\partial^2\theta}{\partial x^2}(x,t) + \rho r(x,t) = \left[\rho c + E\alpha^2\theta(x,t)\right]\frac{\partial\theta}{\partial t}(x,t) + \\ \alpha\theta(x,t)\frac{d\sigma}{dt}(t) \quad \text{for} \quad x \neq x_{pb}(t) \ , \end{aligned} \tag{2.5}$$

valid at all points on the 1-D bar, except at the phase boundary. The parameter k is the thermal conductivity, ρ the mass density, $r(x;t)$ a heat source and c is the specific heat. The heat source term $\rho r(x,t)$ (second term in Eq. 2.5) is taken as

$$\rho r(x,t) = \rho_E J^2 - \frac{hP}{A}\left[\theta(x,t) - \theta_{amb}\right] \ , \tag{2.6}$$

where the first term on the right represents joule heating of the SMA bar; ρ_E is the electrical resistivity (assumed identical for A and M) and J is the electric current density in the bar. Purely thermal transformations induced by joule heating within the context of this model has an analytical solution (as we shall see in Section 2.5); that is why the joule heating term has been included. The second term represents convection along the length of the bar and has been approximately included as a heat source [4, 21]. The parameter h is the convection coefficient along the length of the bar, P the perimeter of the bar cross-section and A is the cross-sectional area.

At the phase boundary, the heat flux has a jump. This condition is stated as

$$-k\left(\frac{\partial\theta}{\partial x}\left(x_{pb}^{+}(t),t\right)-\frac{\partial\theta}{\partial x}\left(x_{pb}^{-}(t),t\right)\right)=(\sigma(t)\varepsilon_T+\rho\lambda_T)\frac{dx_{pb}}{dt}\quad\text{for}\quad x=x_{pb}(t)\,, \tag{2.7}$$

where $\frac{\partial\theta}{\partial x}\left(x_{pb}^{+}(t),t\right)$ and $\frac{\partial\theta}{\partial x}\left(x_{pb}^{-}(t),t\right)$ are the temperature gradients on the right-hand side and the left-hand side of the phase boundary, respectively. In particular, the term λ_T ($\lambda_T \geq 0$) represents the magnitude of the latent heat that is evolved or absorbed at the moving boundary during an A→ M or M→A transformation, respectively. The term $\frac{dx_{pb}(t)}{dt}$ represents the velocity of the moving boundary. It is usually specified based on phenomenological considerations [4], and will be given at the end of this section.

Adiabatic boundary conditions at the ends of the half-length of the bar are assumed, thus

$$\frac{\partial\theta}{\partial x}(0,t) = 0 \quad \text{and} \quad \frac{\partial\theta}{\partial x}(L,t) = 0 \ , \tag{2.8}$$

where the first condition follows from symmetry considerations, whereas the latter has been found to be a reasonable assumption [4] in simulating the effects of "end grips" in a laboratory experiment.

The initial conditions of the stress and phase boundary position are denoted as

$$\sigma(0) = \sigma_0 \quad \text{and} \quad x_{pb}(0) = s_0 \ , \tag{2.9}$$

where σ_0 and s_0 are parameters to be specified in the numerical implementation. The initial value of the temperature field is taken to be spatially uniform, and set equal to a parameter, θ_0 (which may be different from the ambient temperature, θ_{amb}). Therefore

$$\theta(x,0) = \theta_0 \ . \tag{2.10}$$

The motion of the phase boundary occurs when a driving force, f, at the phase boundary attains a critical value. The driving force is dependent on the stress and the temperature at the phase boundary. Defining the latter as $\theta_{pb} = \theta(x_{pb}, t)$, we have [4]

$$f \equiv f(\sigma\theta_{pb}) = \left[\sigma - \frac{\rho\lambda_T}{\varepsilon_T\theta_T}(\theta_{pb} - \theta_T)\right]\varepsilon_T \ , \tag{2.11}$$

where θ_T is a parameter known as the equilibrium temperature. The phase transformation occurs when the driving force, $f(\sigma, \theta_{pb})$, satisfies the following criteria:

$$f \geq f_1 \quad \text{and} \quad f \leq f_2 \ , \tag{2.12}$$

where the first condition pertains to the A→M transformation and the second condition corresponds to the M →A transformation. The parameters f_1 and f_2 are defined as

$$f_1 = \frac{\rho\lambda_T}{\theta_T}(\theta_T - M_s) \quad , \quad f_2 = \frac{\rho\lambda_T}{\theta_T}(\theta_T - A_s) \ , \tag{2.13}$$

where M_s and A_s are the experimentally measured stress-free martensitic start and austenitic start temperatures, respectively. The velocity, $\frac{dx_{pb}(t)}{dt}$, of the phase boundary is taken as[4, 24]

$$\frac{dx_{pb}}{dt} = 2R\exp\left(-\frac{f^2 + \frac{E^2g^4}{4}}{2rEg^2K\theta_{pb}}\right)\sinh\left(\frac{f}{2rK\theta_{pb}}\right) \ , \tag{2.14}$$

where R is known as the mobility coefficient, $g = \frac{E\alpha}{\rho c}$ called Gruneisen's constant [4], r the number of atoms per unit volume and K is the Boltzmann's constant. The statement of the 1-D BVP is now complete.

For a specified deformation rate, $\frac{d\delta}{dt}(L, t)$, the problem, then, is to find the temperature distribution, $\theta(x, t)$, in the austenitic and martensitic phases of the bar, the uniaxial stress, $\sigma(t)$, and the position, $x_{pb}(t)$, of the phase boundary. These quantities may be found by solving the system of equations, Eqs. 2.4, 2.5, 2.7 and 2.14, subject to thermal boundary conditions (Eq. 2.8) and initial conditions (Eqs. 2.9 and 2.10).

Before attempting a solution, these equations are now given in a non-dimensional form. Non-dimensionalization is carried out by the application of the Buckingham π theorem[25]. The non-dimensional variables are given in Appendix A. As the non-dimensional equations only will be used in the rest of the chapter, we omit the "tilde" when we give the non-dimensional equations next. Eq. 2.4 becomes

$$\frac{d\delta}{dt} = \frac{d\sigma}{dt} + \alpha\frac{d\bar{\theta}}{dt} + \varepsilon_T\frac{dx_{pb}}{dt} \,. \qquad (2.15)$$

We incorporate Eq. 2.6 in Eq. 2.5 and give the non-dimensional form of the latter as

$$\frac{\partial^2\theta}{\partial x^2} + J^2 - h(\theta - 1) = (1 + g\alpha\theta)\,\frac{\partial\theta}{\partial t} + g\theta\frac{d\sigma}{dt} \quad \text{for} \quad x \neq x_{pb}(t)\,. \qquad (2.16)$$

The jump condition Eq. 2.7, becomes

$$\frac{\partial\theta}{\partial x}\left(x^+_{pb}(t), t\right) - \frac{\partial\theta}{\partial x}\left(x^-_{pb}(t), t\right) = -\frac{g}{\alpha}(\sigma\varepsilon_T + \lambda_T)\frac{dx_{pb}}{dt} \quad \text{for} \quad x = x_{pb}(t)\,. \qquad (2.17)$$

The velocity of the moving boundary follows from Eq. 2.14 as:

$$\frac{dx_{pb}}{dt} = 2R\exp\left(-\frac{f^2 + \frac{g^4}{4}}{2g^2K\theta_{pb}}\right)\sinh\left(\frac{f}{2K\theta_{pb}}\right) \,, \qquad (2.18)$$

where f follows from Eq. 2.11 as:

$$f = \sigma\varepsilon_T - \lambda_T\left(\frac{\theta_{pb}}{\theta_T} - 1\right) . \tag{2.19}$$

The parameters f_1 and f_2 may be derived from Eq. 2.13 as

$$f_1 = \lambda_T\left(1 - \frac{M_s}{\theta_T}\right) \quad , \quad f_2 = \lambda_T\left(1 - \frac{A_s}{\theta_T}\right) , \tag{2.20}$$

The thermal boundary conditions follow from Eq. 2.8 as:

$$\frac{\partial\theta}{\partial x}(0,t) = 0 \quad \text{and} \quad \frac{\partial\theta}{\partial x}(1,t) = 0 . \tag{2.21}$$

The initial conditions of the stress and phase boundary position in their non-dimensional forms follow from Eq. 2.9:

$$\sigma(0) = \sigma_0 \quad \text{and} \quad x_{pb}(0) = s_0 , \tag{2.22}$$

whereas the initial non-dimensional temperature distribution follows from Eq. 2.10 as:

$$\theta(x,0) = \theta_0 . \tag{2.23}$$

We now outline the temporal discretization and the MBFEM-based numerical approach in the next section.

2.3 The temporal discretization and the MBFEM-based numerical approach

In this section, we describe the temporal discretization of Eqs. 2.15-2.18. This is followed by the description of the MBFEM-based numerical approach to solve the aforementioned system of non-linear, coupled equations subject to the appropriate initial and boundary conditions.

Eqs. 2.15-2.18 are a system of non-linear, coupled equations. The non-linearity arises in the heat conduction equation, Eq. 2.16, due to the term $1 + g\alpha\theta$. On the other hand, the coupling in the equations originates from various sources. In absence of a stress-induced transformation, $\sigma(t) = 0$, Eq. 2.17 is coupled with Eqs. 2.15 and 2.16 as the phase boundary velocity is dependent on θ_{pb}. Moreover, when $\sigma(t) \neq 0$, there is an additional coupling between the thermal and mechanical fields. This thermomechanical coupling originates from two sources: (1) The last term in Eq.2.16, $g\theta\frac{d\sigma}{dt}$, represents the well-known thermomechanical coupling for a thermoelastic material. This coupling is weak when the stress rate (or strain rate) is low, i.e. loading is quasistatic in nature [26], as is the case in this work. (2) During the phase transformation, (i.e. $\frac{dx_{pb}}{dt} \neq 0$ in Eq. 2.17), the term on the right of Eq. 2.17 represents an additional thermomechanical coupling; this effect is quite strong even at quasistatic loading rates [4]. To summarize, since the aforementioned system of equations is non-linear and has a strong thermomechanical coupling, any numerical approach attempting to solve the equations should, ideally, solve them as a system. This is the objective of the MBFEM-based numerical approach that we address in this chapter.

2.3.1 The temporal discretization

Before we discuss the numerical approach, it is convenient to introduce the temporal discretization (or time stepping) of Eqs. 2.15-2.18. This is done based on a constant time increment, τ. At the end of the ith increment, the total elapsed time is

$$t_i = i\tau \ , \quad i \geq 1 \ , \tag{2.24}$$

where i is an integer. The values of the parameters $\sigma(t)$, $\theta(x,t)$ and $x_{pb}(t)$ at the end of the ith increment are defined as

$$\sigma^i \equiv \sigma(t_i) \ , \quad \theta^i \equiv \theta(x,t_i) \ , \quad x^i_{pb} \equiv x_{xp}(t_i) \ , \tag{2.25}$$

where their partial time derivatives at the end of the *i*th step are defined by forward differencing as

$$\frac{d\sigma^i}{dt} \equiv \frac{d\sigma}{dt}(t_i) \approx \frac{\sigma^i - \sigma^{i-1}}{\tau} \quad , \quad \frac{d\theta^i}{dt}(x) \equiv \frac{d\sigma}{dt}(x, t_i) \approx \frac{\theta^i(x) - \theta^{i-1}(x)}{\tau} \ ,$$

$$\frac{dx^i_{pb}}{dt} \equiv \frac{x_{pb}}{dt}(t_i) \approx \frac{x^i_{pb} - x^{i-1}_{pb}}{\tau} \ . \qquad (2.26)$$

With Eqs. 2.25 and 2.26, Eqs. 2.18 and 2.15-2.17 are written at the end of the *i*th time step as

$$\frac{dx^i_{pb}}{dt} = \frac{dx_{pb}}{dt}\left(\sigma^*, \theta^*_{pb}\right) \ , \qquad (2.27)$$

$$\frac{d\delta^i}{dt} = \frac{d\sigma^i}{dt} + \alpha\frac{d\bar{\theta}^*}{dt} + \varepsilon_T\frac{dx^i_{pb}}{dt} \ . \qquad (2.28)$$

$$\frac{\partial^2\theta^i}{\partial x^2} + J^2 - h(\theta^i - 1) = (1 + g\alpha\theta^*)\frac{\partial\theta^i}{\partial t} + g\theta^i\frac{d\sigma^i}{dt} \quad \text{for} \quad x \neq x_{pb}(t_i) \ . \qquad (2.29)$$

$$\frac{\partial\theta^i}{\partial x}\left(x^{+^i}_{pb}(t), t_i\right) - \frac{\partial\theta^i}{\partial x}\left(x^{-^i}_{pb}(t), t_i\right) = -\frac{g}{\alpha}(\sigma^i\varepsilon_T + \lambda_T)\frac{dx^i_{pb}}{dt} \quad \text{for} \quad x = x_{pb}(t_i) \ . \qquad (2.30)$$

The reader will notice that some of the terms are written with a superscript "*". This is to indicate that the numerical approach makes a "guess" of these values in order to compute σ^i, $\theta^i(x)$ and x^i_{pb} at the *i*th time step; we shall return to this point soon.

2.3.2 MBFEM-based numerical approach

Eqs. 2.27-2.30 are a coupled system of equations that need to be solved as a system. The numerical approach involves a spatial discretization of Eqs. 2.29 and 2.30 by the moving boundary finite element method; this is described in Section 2.4. For now, we assume that the aforementioned equations may be replaced by the system of equations

$$\mathbf{A}^*\vec{\Theta}^i = \vec{B}^* \ , \tag{2.31}$$

where $\mathbf{A}^*$ is a global mass matrix, $\vec{\Theta}^i$ the vector of nodal temperatures and $\vec{B}^*$ is the global force vector. $\mathbf{A}^*$ and $\vec{B}^*$ have been written with the superscript, "*", as their components contain the term, $g\alpha\theta^*$ (originally in Eq. 2.29). Their components are derived in Section 2.4. We now give the solution of Eqs. 2.27, 2.28 and 2.31 next.

The recursive iteration

In order to calculate σ^i, $\theta^i(x)$ and x^i_{pb} at the end of the ith time step, a recursive iteration procedure is implemented within that time step. Specifically, we calculate $\frac{dx^i_{pb}}{dt}$ from Eq. 2.27 by setting the starred quantities identical to their values at end of the previous time step, t_{i-l}. Therefore

$$\frac{dx^i_{pb}}{dt} = \frac{dx_{pb}}{dt}\left(\sigma^{i-1}, \theta^{i-1}_{pb}\right) . \tag{2.32}$$

Since, $\frac{dx^i_{pb}}{dt}$ is now known, x^i_{pb} follows by the third of Eq. 2.26. The stress rate, $\frac{d\sigma^i}{dt}$ is calculated from Eq. 2.28 by replacing $\frac{d\bar{\theta}^*}{dt}$ with $\frac{d\bar{\theta}^{i-1}}{dt}$. Thus

$$\frac{d\delta^i}{dt} = \frac{d\sigma^i}{dt} + \alpha\frac{d\bar{\theta}^{i-1}}{dt} + \varepsilon_T\frac{dx^i_{pb}}{dt} . \tag{2.33}$$

may be solved for $\frac{d\sigma^i}{dt}$ since $\frac{d\delta^i}{dt}$ is assumed to be known, and $\frac{dx^i_{pb}}{dt}$ has been computed by Eq. 2.32. With $\frac{d\sigma^i}{dt}$ now known, σ^i follows from the first of Eq. 2.26. The term, $g\alpha\theta^*$, in Eq. 2.29 is replaced with $g\alpha\bar{\theta}^{i-1}$ and thus we can write Eq. 2.31 as

$$\mathbf{A}^{i-1}\vec{\Theta}^i = \vec{B}^{i-1} , \tag{2.34}$$

which is a set of linear algebraic equations in the nodal temperatures, that may be easily solved. Next, the "starred" quantities in Eqs. 2.27, 2.28 and 2.31 are updated by setting them equal to their corresponding newly determined values. With this update, Eqs. 2.27, 2.28 and 2.31 are solved again to get a new set of values for σ^i, $\theta^i(x)$ and x^i_{pb}. This recursive iteration is continued until the relative change in values of the stress and phase boundary temperature from one iteration to the next occurs by an amount less than a small prescribed parameter, ξ_a , i.e.

$$\left|\frac{\sigma^i - \sigma^*}{\sigma^*}\right| \leq \xi_a \quad , \quad \left|\frac{\theta^i_{pb} - \theta^*_{pb}}{\theta^*_{pb}}\right| \leq \xi_a \, , \tag{2.35}$$

where $\xi_a << 1$. The iteration within the ith time step is then terminated.

The recursive iteration coupled with Newton-Raphson method

The numerical approach here is identical to the one in the previous section except the manner in which the nodal temperatures are computed. We set the non-linear term, $g\alpha\theta^*$, in Eq. 2.29 equal to $g\alpha\theta^i$, so that Eq. 2.31 becomes

$$\mathbf{A}^i\vec{\Theta}^i = \vec{B}^i \, . \tag{2.36}$$

Since $\mathbf{A}^i$ and $\vec{B}^i$ are now functions of the current nodal temperatures, Eq. 2.36 is a set of non-linear algebraic equations in the nodal temperatures. The system is solved by the Newton-Raphson method, outlined in Section 2.4.2.

2.4 The spatial discretization with moving boundary finite element method

The governing equation, Eq. 2.29, and the jump condition, Eq. 2.30, will be solved for $\theta^i(x)$ using the MBFEM. Eq. 2.29 is first discretized without taking the jump condition, Eq. 2.30, into consideration. At this stage, the spatial discretization is done uniformly. The global stiffness and mass matrices, and the force vector are developed. In the second-step, these global quantities are augmented to include the effect of the jump condition, after an additional grid node, coinciding with the phase boundary (the location of which is already determined; see Section 2.3.2), is introduced in the spatial discretization of the first-step. This approach is different and somewhat simpler than those suggested by Murray and Landis[11], Crank and Gupta[12], Gupta [13] and Djomehri and George[14]; see Section 2.1 for discussion.

2.4.1 The spatial discretization

Discretization of Eq. 2.29 in absence of the jump condition, Eq. 2.30

We weigh Eq. 2.29 with a probe function, $\nu = nu(x)$ and write it (i.e. Eq. 2.29) in a weak form

$$
\begin{aligned}
-\int_0^1 \frac{d\nu}{dx}\frac{\partial\theta^i}{\partial x}dx = \frac{1}{\tau}\int_0^1 \nu(1+g\alpha\theta^*)(\theta^i-\theta^{i-1})dx + \\
\left(g\frac{d\sigma^i}{dt}+h\right)\int_0^1 \nu\theta^i dx - (h+J^2)\int_0^1 \nu dx \quad \text{for} x \neq x_{pb}(t_i)\ , \qquad (2.37)
\end{aligned}
$$

where the boundary conditions, Eqs. 2.21, and the second of Eq. 2.26 have been used.

The normalized half-length of the bar is discretized into N elements of equal length, $\Delta L = \frac{1}{N}$. The elements are numbered 1 to N from the left to the right, whereas the nodes are numbered 1 to $N+1$. The co-ordinates of the nodes are denoted with the parameter, $x_i (1 \leq i \leq N+1)$. The time-dependent temperature field in the bar is approximated by the following function:

$$\theta^i(x) = \sum_{j=1}^{2} \phi_j^{(q)}(x)\theta^i_{q+j-1} \ , \quad x_q \leq x \leq x_{q+1} \ , \quad i \geq 1 \ , \quad 1 \leq q \leq N \ , \qquad (2.38)$$

where $\phi_1^{(q)}$ and $\phi_2^{(q)}$ are basis functions for the qth element. They are taken to be linear functions in x, as below

$$\phi_1^{(q)}(x) = \frac{x_{q+1} - x}{x_{q+1} - x_q} \quad \text{and} \quad \phi_2^{(q)}(x) = \frac{x - x_q}{x_{q+1} - x_q} \ , \qquad 1 \leq q \leq N \ . \qquad (2.39)$$

The parameter θ^i_q represents the value of the temperature at the qth node and at the end of the ith time step. Eq. 2.37 is now discretized after identifying the probe function as a two-component vector function, where the components are taken identical to the basis functions in Eq. 2.39. We shall not give the details of the discretization procedure. Here, we give the end result

$$\mathbf{A}^{*}_{UN}\vec{\Theta}^{i}_{UN} = \vec{B}^{*}_{UN} \ , \qquad (2.40)$$

where $\mathbf{A}^{*}_{UN}$ is a $(N+1) \times (N+1)$ global stiffness matrix, $\vec{\Theta}^{i}_{UN}$ is a $(N+$

1) × 1 column matrix with the nodal temperatures as its components (i.e. $\vec{\Theta}^{i}_{UN,k} = \vec{\theta}^{i}_{k}$) and $\vec{B}^{*}_{UN}$ is the force vector, represented as a $(N+I) \times 1$ column matrix. The subscript "UN" has been used to indicate that Eq. 2.40 has been developed without taking the jump condition (Eq. 2.30) into account. Moreover, the matrices $\mathbf{A}^{*}_{UN}$ and $\vec{B}^{*}_{UN}$ include the term, $g\alpha\theta^{*}$, and therefore have been written with a superscript, "*". The global stiffness matrix, $\mathbf{A}^{*}_{UN}$, is given by

$$\mathbf{A}^{*}_{UN} = \tau\mathbf{K} + \mathbf{M} + \tau\left(g\frac{d\sigma^{i}}{dt} + h\right)\mathbf{M} + \alpha g\bar{\mathbf{M}}^{*} , \tag{2.41}$$

where the components of **K**, **M** and $\bar{\mathbf{M}}^{*}$ are given in Section A.2 of Appendix A. The global force vector, $\vec{B}^{*}_{UN}$ is

$$\vec{B}^{*}_{UN} = \left(\mathbf{M} + \alpha g\bar{\mathbf{M}}^{*}\right)\vec{\Theta}^{i-1}_{UN} + \tau(h + J^{2})\vec{F} , \tag{2.42}$$

where the components of $\vec{F}$ are given in Section A.2 of Appendix A.

Modification of Eq. 2.40 in view of the jump condition Eq. 2.30

We shall now modify Eq. 2.40 to reflect the effect of the jump condition, Eq. 2.30. Noting that the new position of the phase boundary may fall between two nodes or on an existing node, the following two cases must be considered.

Phase boundary lies between two nodes

If the new phase boundary position is within the pth element (or between the pth and $(p+1)$th nodes), the original pth element may be replaced by two elements, referred henceforth as elements $p-$ and $p+$, respectively. These elements will have lengths, w_{p-} and w_{p+}, defined, respectively, as

$$w_{p-} = x^i_{pb} - x_p \quad \text{and} \quad w_{p+} = x_{p+1} - x^i_{pb} \ . \tag{2.43}$$

The contribution to the global stiffness matrix and the force vector due to the discretization for the pth element done in the previous section is now dropped, and Eqs. 2.29 and 2.30 will be used to determine the appropriate temperature discretization in the two newly defined elements. Specifically, Eq. 2.29 is written at the pth and $(p+l)$th node, and Eq. 2.30 is written for the extra node introduced at the phase boundary, wherein the spatial derivatives and the temporal derivatives are approximated by central differencing and forward differencing, respectively. The discretization procedure results in

$$\mathbf{A}^* \vec{\Theta}^i = \vec{B}^* \ , \tag{2.44}$$

where now that we have one extra node (at the phase boundary), $\mathbf{A}^*$ is a $(N+2) \times (N+2)$ matrix, $\vec{\Theta}^i$ and $\vec{B}^*$ are $(N+2) \times 1$ column matrices; the components of $\mathbf{A}^*$, $\vec{\Theta}^i$ and $\vec{B}^*$ are given in of Appendix A (Section A.2).

Eq. 2.44 was first introduced as Eq. 2.31 in Section 2.3.2.

Phase boundary lies on a node

In the event that the phase boundary position lies on an existing node (e.g. the $(p+1)$ node), Eq. 2.30 is used to find the new temperature at the $(p+1)$th node. With this modification, we have

$$\mathbf{A}^{*}\vec{\Theta}^{i} = \vec{B}^{*} \ , \tag{2.45}$$

Since the number of nodes remain unchanged, $\mathbf{A}^{*}$is a $(N+1) \times (N+1)$ matrix, and $\vec{\Theta}^{i}$ and $\vec{B}^{*}$ are $(N+1) \times 1$ column matrices, whose components are given in Section A.3.2. When the phase boundary lies on a node, we use Eq. 2.45 instead of Eq. 2.44 in the MBFEM-based numerical approach.

2.4.2 The Newton-Raphson method

We set the non-linear term $g\alpha\theta^{*}$ (refer Eq. 2.29) equal to $g\alpha\theta^{i}$ (as it should be), by which Eq. 2.44 or Eq. 2.45 becomes

$$\mathbf{A}^{i}\vec{\Theta}^{i} = \vec{B}^{i} \ . \tag{2.46}$$

Eq. 2.46 was originally introduced as Eq. 2.36 in Section 2.3.2; it is a system of non-linear algebraic equations in the nodal temperatures, which is solved by the Newton-Raphson method, briefly described below. We define a vector $\vec{f}^i$ at the ith time step as

$$\vec{f}^i = \mathbf{A}^i \vec{\Theta}^i - \vec{B}^i \, . \tag{2.47}$$

The non-linear system of equations represented by Eq. 2.46 is then tantamount to setting

$$\vec{f}^i = 0 \, . \tag{2.48}$$

The solution for the temperature vector is obtained when the condition, Eq. 2.48, is met. The Newton- Raphson method is an iterative process, by which a trial solution for the temperature vector, $\vec{\Theta}^{i(m+1)}$, at the $(m+1)$th iteration is calculated from the trial solution at the mth iteration, i.e. $\vec{\Theta}^{i(m)}$. This iterative process is based on

$$\vec{\Theta}^{i(m+1)} = \vec{\Theta}^{i(m)} - \left(\mathbf{J}^{i(m)}\right)^{-1} \vec{f}^{i(m)} \, , \quad m \geq 1 \, , \tag{2.49}$$

where $\mathbf{J}^{i(m)}$ is the Jacobian; its components are given in Section A.4. This iterative process continues until the component of the vector, $\vec{\Theta}^{i(m+1)} - \vec{\Theta}^{i(m)}$, with the maximum magnitude is less than a small prescribed parameter, ξ_b; thus

$$\max_{1 \leq j \leq \tilde{N}} \left| \frac{\theta_j^{i(m+1)} - \theta_j^{i(m)}}{\theta_j^{i(m)}} \right| \leq \xi_b \, , \tag{2.50}$$

where the index "j "represents the jth component of the considered vector, $\bar{N} = N+1$ if the phase boundary lies on anode and $N+2$ if it lies between two nodes, and $\xi_b << 1$.

2.5 An analytical solution

In order to assess the accuracy of the MBFEM, we shall compare its predictions with an analytical solution for the special case of a purely thermal transformation i.e. $\sigma(t) = 0$. The physical problem corresponds to an initially martensitic bar that undergoes a stress-free transformation to austenite on joule heating. The BVP is summarized below. The governing equation (Eq. 2.16) becomes

$$\frac{\partial^2\theta}{\partial x^2} + J^2 - h(\theta - 1) = \frac{\partial \theta}{\partial t} \quad \text{for} \quad x \neq x_{pb}(t)\ , \tag{2.51}$$

where we have made the assumption that the non-linear term in Eq. 2.16, $g\alpha\theta \approx 0$; this was shown to be true by Bhattacharyya et al. [21]. The jump condition (Eq. 2.17) is

$$\frac{\partial\theta}{\partial x}\left(x^+_{pb}(t), t\right) - \frac{\partial\theta}{\partial x}\left(x^-_{pb}(t), t\right) = -\frac{g}{\alpha}\lambda_T\frac{dx_{pb}}{dt} \quad \text{for} \quad x = x_{pb}(t)\ , \tag{2.52}$$

where the velocity, $\frac{dx_{pb}}{dt}$, of the moving boundary will be specified later. The boundary conditions follow from Eq. 2.21 and the initial conditions from

Eqs. 2.22 and 2.23 wherein we set $\sigma(t) = 0$.

Eqs. 2.51 and 2.52 with their associated boundary and initial conditions may be solved by the Green's function approach [27] after using the substitution, $\theta(x,t) = 1 + \varphi(x,t)\exp(-ht)$, and then incorporating the transformed Eq. 2.52 into Eq. 2.51 using a Dirac-delta function. The solution for the temperature fields turns out to be

$$\theta(x,t) = 1 + \frac{J^2}{h}(1 - \exp(-ht)) - \frac{g\lambda_T}{\alpha}\int_0^1 \frac{dx_{pb}}{dt}(\tau)\exp(-h(t-\tau)) \\ \times \left(1 + \sum_{m=1}^{\infty} \exp(-(m\pi)^2(t-\tau))\cos(m\pi x)\cos(m\pi x_{pb}(\tau))\right) d\tau \ . \quad (2.53)$$

If the phase front velocity is constant, i.e.

$$\frac{dx_{pb}}{dt}(t) = A \ , \quad (2.54)$$

where A is a prescribed constant parameter, Eq. 2.53 reduces to

$$\theta(x,t) = 1 + \frac{1}{h}\left(J^2 - \frac{g\lambda_T A}{\alpha}\right)(1 - \exp(-ht)) - \frac{g\lambda_T A}{\alpha}\sum_{m=1}^{\infty} \frac{cos(m\pi x)}{((m\pi)^2 + h)^2 + A^2(m\pi)^2} \\ \times \left[\left((m\pi)^2 + h\right)\left(\cos(m\pi At) - \exp\left(-\left((m\pi)^2 + h\right)t\right)\right) + Am\pi h\sin(m\pi At)\right] (2.55)$$

Since Eq. 2.55 is an infinite series, the number of terms used to calculate $\theta(x,t)$ is decided by the following criterion. We retain only the first N terms in the infinite series in Eq. 2.55 if

$$\left|\frac{\theta_{N+1}(x,t) - \theta_N(x,t)}{\theta_N(x,t)}\right| \le \xi_c \ , \quad (2.56)$$

where $\theta_j(x,t)$ is the temperature computed by including the first j terms, and $\xi_c << 1$.

2.6 Numerical results

The ingredients involved in the proposed numerical approach outlined in Section 2.3, i.e. the MBFEM, the recursive iteration technique and the Newton-Raphson method, will be studied and wherever appropriate, we shall also include a comparison with the FDM-based numerical approach of Kim and Abeyaratne [4]. This section will conclude with a brief parametric study on stress-induced transformations.

In all the computations to follow, the dimensional parameters that are consistently used have been listed in Table 2.1. The parameters that do change from one computation to another will be introduced below.

2.6.1 Accuracy and stability of MBFEM

The accuracy and stability of MBFEM are addressed by simulating the analytical solution developed in Section 2.5. We recall that the solution corresponds to an SMA bar, that is initially martensitic and at a uniform initial temperature. The bar undergoes the $M \rightarrow A$ transformation when it is heated electrically, in absence of stress. In line with Kim and Abeyaratne's [4] work, we take the phase boundaries to originate at the ends of the bar and move to the center. We assume that the phase boundary velocity is constant, so that the analytical solution may be used. For these conditions, $\sigma(t) = 0$, and the dimensional values of the initial stress, phase boundary position and the temperature are taken as 0, L and $370K$ (or $97°C$), respectively. The corresponding non-dimensional values are

$$\sigma_0 = 0 \ , \quad s_0 = 1 \ , \quad \theta(x,0) = 1.23 \ .$$

The constant velocity of the phase boundary is taken as $-1.28mm/s$ and the dimensional electric current density is taken as $2A/mm^2$. Thus, the non-dimensional parameter A (refer Eq. 2.54) and the non-dimensional current density are respectively

$$A = -7 \quad \text{and} \quad J = 0.7 \ .$$

Recall that in the analytical solution, the non-linear term, $g\alpha\theta \approx 0$, (refer Eq. 2.16), has been dropped. Therefore, the issue of using the Newton-Raphson method does not arise. On the other hand, since the transformation is purely thermal (no thermomechanical coupling) and the phase boundary velocity is explicitly known (as a function of time), the recursive iteration becomes unnecessary. Hence, the simulation of the analytical solution will serve to demonstrate the accuracy and stability of the MBFEM.

The numerical results of the phase boundary location, x_{pb}, vs. the phase boundary temperature, θ_{pb}, are given in Table 2.2 for $A = -7$. The first column gives x_{pb} and the second column gives θ_{pb} calculated by the analytical solution. We use $\xi_c = 1 \times 10^{-12}$(see Eq. 2.56) to calculate θ_{pb}. A plot of θ_{pb} vs. x_{pb} is given in Fig. 2.2. Note that the temperature at the phase boundary, as it moves during the transformation, is not constant (unlike classical Stefan problems). In any case, the predictions by MBFEM and a finite difference method (FDM) proposed by Kim and Abeyaratne [4] are given in column 3 of Table 2.2 where the spatial domain has been discretized into 70 elements (i.e. element length $\Delta L = 0.014$) and the time increment, $\tau = 0.0001$. We see that both approaches closely approximate the analytical solution and, in fact, the FDM does it somewhat better. Due to the known conditional stability of the FDM, Kim [24] had suggested the relation, $\tau \leq 0.1(pc/k)(\Delta L)^2$, between the element length and the time increment. This is confirmed when ΔL is reduced by 50% in the fourth column and τ has been reduced in keeping with the recommendation. The predictions of both methods are very satisfactory.

However, when ΔL is reduced further without an accompanying reduction in τ (see fifth column), the FDM fails to yield meaningful results whereas the MBFEM does. This demonstrates the conditional stability of the FDM and the unconditional stability of the MBFEM.

Corresponding results are given for the spatial distribution of the temperature, θ_{pb} when the phase boundary has moved mid-way to the center of the half-length of the bar, i.e $x_{pb} = 0.5$. The plot of θ_{pb} vs. x has been given in Fig. 2.3 and the numerical results given in Table 2.3.

2.6.2 Effect of kinetic relation

In the previous section, the recursive iteration was not necessary as the phase boundary velocity was taken as a known constant, and thus was independent of the temperature. In reality, the phase boundary velocity has to be developed from phenomenological considerations and is usually a function of the phase boundary temperature (and also the stress in stress-induced transformations). In such a case, a recursive iteration approach is desirable. The iteration may be all the more necessary if the expression for the phase boundary velocity has a "complicated" dependence on the temperature. We consider an extreme or "pathological" case by starting with the analytical expression of the temperature field (Eq. 2.55) and deriving an alternative form of the constant phase boundary velocity assumption from it. Since $\theta_{pb} = \theta(x_{pb}, t)$ and due to the constant velocity assumption, by which $t = (x_{pb}(t) - x_{pb}(0))/A$, we have

$$\theta_{pb} = \theta(x_{pb}, t) = \theta\left(x_{pb}, \frac{x_{pb}(t) - x_{pb}(0)}{A}\right) . \tag{2.57}$$

We identify the last of Eq. 2.57 as the function $F(x_{pb})$, therefore

$$\theta_{pb} = F(x_{pb}(t)) = \theta\left(x_{pb}, \frac{x_{pb}(t) - x_{pb}(0)}{A}\right) . \tag{2.58}$$

With Eq. 2.58, we may write

$$\frac{dx_{pb}}{dt} = \left[\frac{dF}{dx_{pb}}(x_{pb})\right]^{-1} \frac{d\theta_{pb}}{dt} . \tag{2.59}$$

Also from the first of Eq. 2.58, we have $x_{pb} = F^{-1}(\theta_{pb})$, and Eq. 2.59 becomes

$$\frac{dx_{pb}}{dt} = \left[\frac{dF}{dx_{pb}}(F^{-1}(\theta_{pb}))\right]^{-1} \frac{d\theta_{pb}}{dt} . \tag{2.60}$$

Eq. 2.60 is a more complicated representation of the constant velocity assumption, and will be used to "test" the recursive iteration procedure. The phase boundary velocity in its present form, Eq. 2.60, is used along with the problem defined in Eqs. 2.51 and 2.52 to simulate the analytical solution with the MBFEM-based numerical approach. Recursive iteration is now needed to accommodate Eq. 2.60; this is done by replacing θ_{pb} and

$d\theta_{pb}/dt$ in Eq. 2.60 by θ_{pb}^{*} and $d\theta_{pb}^{*}/dt$, respectively. Also note that the inversion of F, i.e. $F^{-1}(\theta_{pb})$, has to be done by numerically solving Eq. 2.55, for which the bisection method is used. For the recursive iteration, we use $\xi_a = 5 \times 10^{-6}$. The comparison of the analytical solution with the results of the MBFEM approach is shown in Tables 2.4 and 2.5. We also tried to carry out the same computation with the FDM-based numerical approach but failed to get convergence. This is probably due to the fact that the FDM-based approach does not include a recursive iteration to address the coupling. The outcome of this exercise is that while a recursive iteration is always desirable to solve a coupled system of equations, it becomes all the more necessary when the coupling is "pathological" in nature, as represented by the complicated kinetic relation in Eq. 2.60. In closing, we note that the numerical implementation of Eq. 2.60 is shown in Fig. 2.4; it is seen that it simulates the constant velocity assumption ($A = -7$) quite well except at the start and end of transformation.

2.6.3 Effect of the Newton-Raphson method and stress-induced transformations

We now address the general problem of stress-induced transformations. An austenitic SMA bar is subjected to a deformation rate, $\dot{\delta}(L,t)$ (see Fig. 2.1). When the A→M transformation sets in, the phase boundaries move from the center of the bar to its ends. After the completion of the A→M transformation, unloading (or a decreasing strain rate) causes the initiation of the reverse M→A transformation (if the ambient temperature is high enough). The reverse transformation is complete when the stress reduces to zero, leading to the so-called pseudoelastic effect. The dimensional values of initial stress, phase boundary position and temperature are taken as 0, 0 and $300K$ (or $27°C$), respectively. The corresponding non- dimensional values are

$$\sigma_0 = 0 \ , \quad s_0 = 1 \ , \quad \theta(x,0) = 1 \ .$$

Since the bar is not subjected to joule heating, we set $J = 0$. The solution of the problem follows from Eqs. 2.15-2.18. We point out that we now retain the non-linear term, $g\alpha\theta$, in Eq. 2.16 even though this non- linearity is known to be weak [21]. To address this non-linearity, the recursive iteration coupled with the Newton-Raphson method is used, for which we take $\xi_b = 1 \times 10^{-6}$.

The effect of the non- linearity is shown in Table 2.6. The first column has different strain rates. It is seen that irrespective of the strain rate, the average number of recursive iterations within a time step is always lower when the Newton- Raphson method is used. Note that in spite of the weakness of the non-linearity, the difference is not negligible.

The pseudoelastic response of the SMA bar is shown at two different deformation rates in Figs. 2.5 and 2.6; computations by the MBFEM-based and FDM-based approaches are shown. It is only at a high strain rate (Fig. 2.7) that there is a noticeable difference between the two approaches. Fig. 2.7 shows the temperature evolution at the phase boundary during the A→M (and M→A) transformation when $\dot{\delta}(1,t) = 0.84$. It is obvious that, unlike a classical Stefan problem, the temperature at the interface during a stress-induced transformation is not constant. Fig. 2.8 shows the spatial distribution of temperature when the phase boundary has moved mid-way along the half-length of the bar during the A→M transformation.

2.7 Conclusions

In summary, the MBFEM-based numerical approach suggested to address 1-D moving BVPs in SMAs has been found to be accurate and unconditionally stable when compared to an analytical solution for a purely thermal transformation and robust enough to give accurate solutions even when a "pathological" kinetic relation is adopted. While we cannot claim that the MBFEM approach is accurate when applied to stress-induced transformations (as there is no analytical solution to compare it with), we have checked (by the same procedure as for the purely thermal problem) that it is indeed unconditionally stable during stress- induced transformations also.

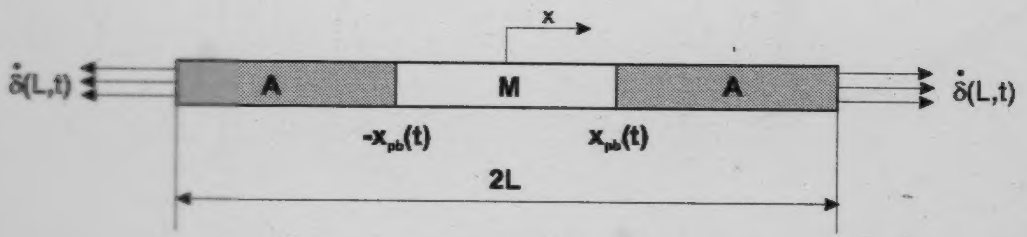
x
δ̇(L,t)
A
M
A
δ̇(L,t)
-x_pb(t)
x_pb(t)
2L

Figure 2.1: A schematic of a SMA bar in a deformation-controlled phase transformation process.

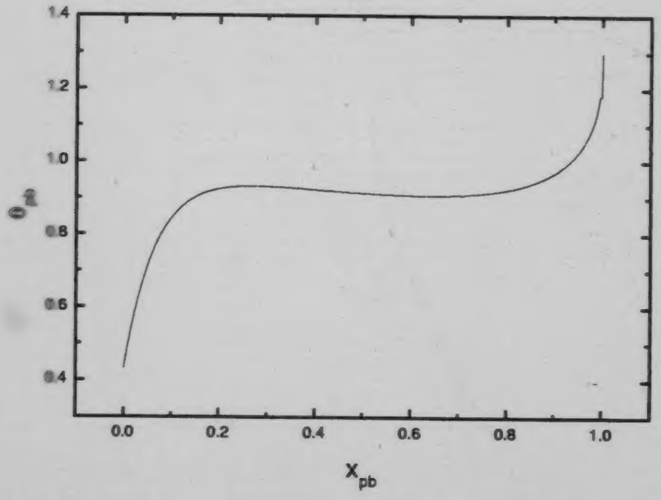

Figure 2.2: A plot θ_{pb} vs. x_{pb} during an M→A transformation, obtained from the analytical solution.

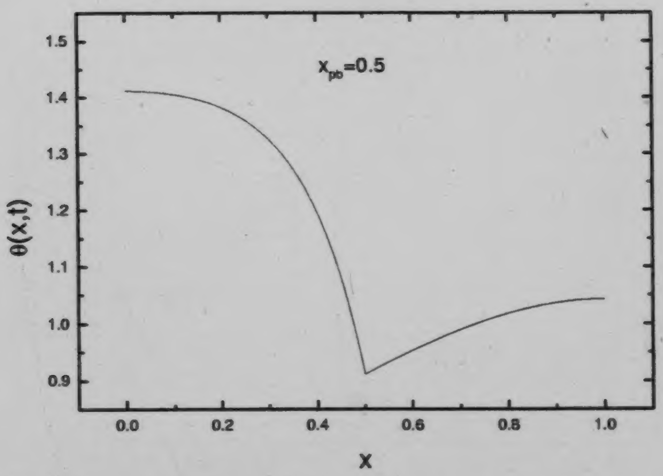

Figure 2.3: A plot $\theta(x,t)$ vs. x during an M→A transformation, at $x_{ph} = 0.5$, obtained from the analytical solution.

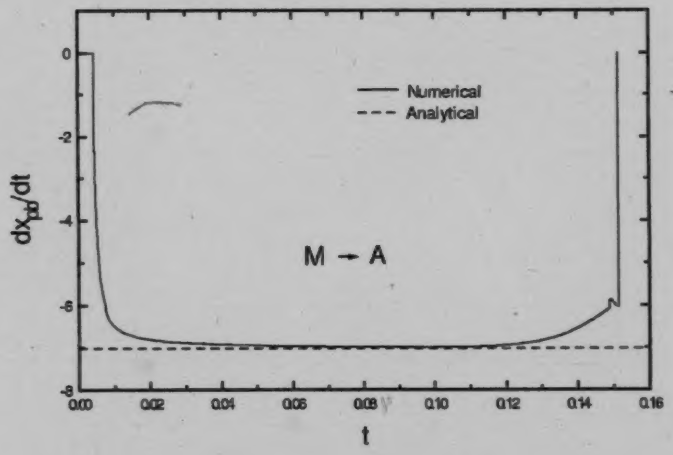

Figure 2.4: The simulation of a constant phase boundary velocity vs. time, by the numerical approach of Eq. 2.60

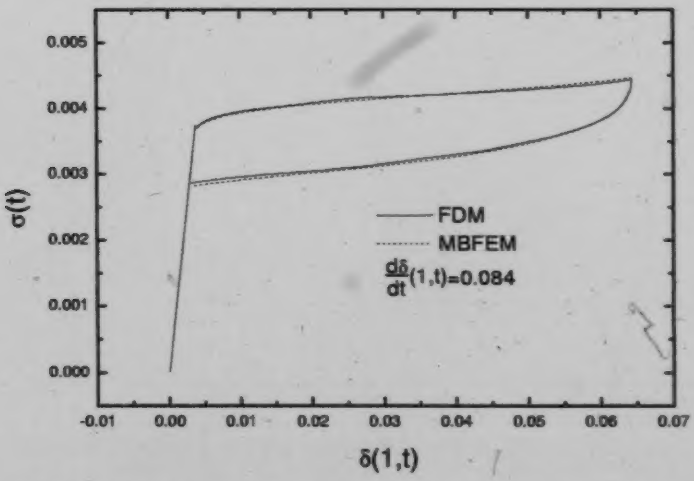

Figure 2.5: A pseudoelastic stress-strain curve computed by MBFEM and FDM at $d\delta(1,t)/dt = 0.084$.

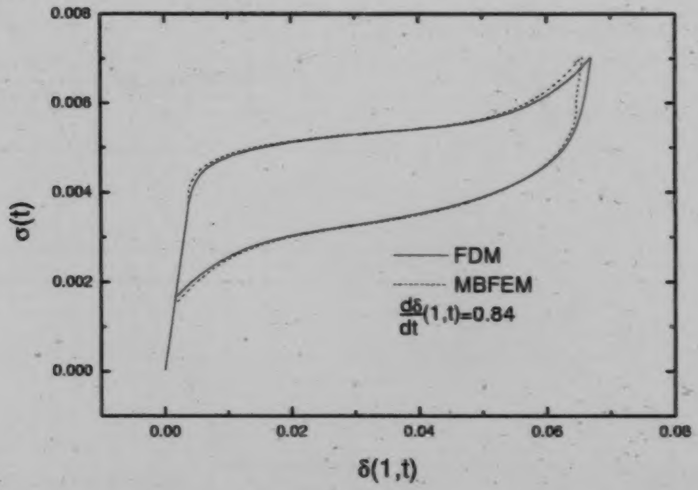

Figure 2.6: A pseudoelastic stress-strain curve computed by MBFEM and FDM at $d\delta(1,t)/dt = 0.84$.

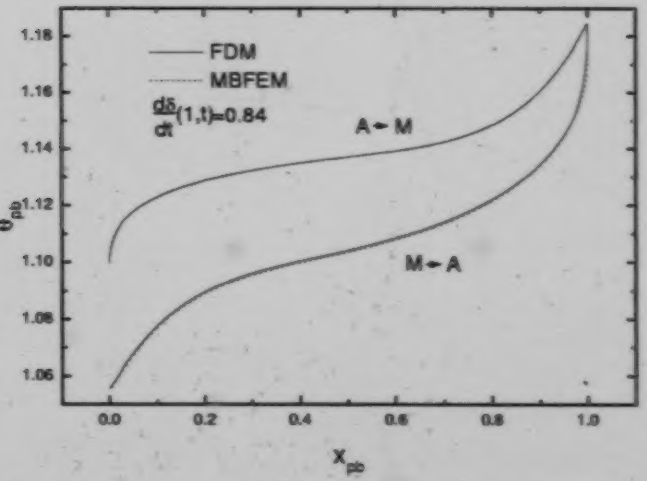

Figure 2.7: Phase boundary temperature vs. position when $d\delta(1,t)/dt = 0.84$.

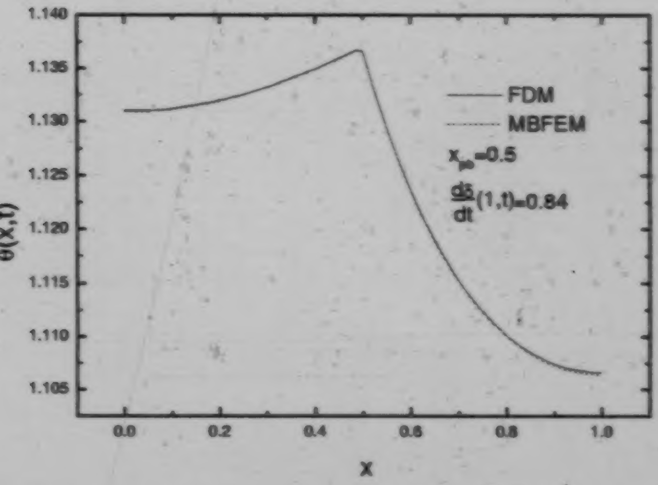

Figure 2.8: $\theta(x,t)$ vs. x when $x_{pb} = 0.5$ during A→M transformation, with $d\delta(1,t)/dt = 0.84$.

Description	Simbol	Value
Length of the bar	L	$31.75 \times 10^{-3} m$
Perimeter of bar cross-section	P	$3.3528 \times 10^{-3} m$
Area of bar cross-section	A	$0.8942 \times 10^{-6} m^2$
Mass density	ρ	$6450 kg/m^3$
Specific heat	c	$465 J/(kgK)$
Coefficient of thermal expansion	α	$10^{-5} K^{-1}$
Young's modulus	E	$51.6 GPa$
Uniaxial phase transformation strain	ε_T	0.06
Latent heat of phase transformation	λ_T	$1.8733 \times 10^7 J/kg$
Thermal conductivity	k	$17.4 W/(mK)$
Ambient temperature	θ_{amb}	$300 K$
Mobility coefficient	R	$0.0509 m/s$
Atoms per unit volume	r	$7.785 \times 10^{28} m^{-3}$
A→M starting temperature	M_s	$283.81 K$
M→A starting temperature	A_s	$286.01 K$
Convective coefficient	h	$5.3757 W/(m^2 K)$
Equilibrium temperature	θ_T	$284.95 K$
Electrical resistivity	ρ_E	$6.3242 \times 10^{-4} \Omega mm$

Table 2.1: List of dimensional parameters.

	Temperature of the phase boundary, θ_{pb}						
Phase boundary position, x_{pb}	Analytical solution	$\Delta L = 0.014$, $\tau = 0.0001$		$\Delta L = 0.007$, $\tau = 0.00001$		$\Delta L = 0.0035$, $\tau = 0.00001$	
		FDM	MBFEM	FDM	MBFEM	FDM	MBFEM
0.9	0.9681	0.9559	0.9441	0.9631	0.9557	-	0.9609
0.8	0.9221	0.9142	0.9020	0.9186	0.9117	-	0.9159
0.7	0.9079	0.9016	0.8895	0.9049	0.8986	-	0.9023
0.6	0.9071	0.9015	0.8903	0.9043	0.8984	-	0.9017
0.5	0.9120	0.9082	0.8977	0.9102	0.9054	-	0.9086
0.4	0.9221	0.9170	0.9056	0.9194	0.9134	-	0.9167
0.3	0.9295	0.9250	0.9142	0.9275	0.9215	-	0.9246
0.2	0.9244	0.9196	0.9046	0.9213	0.9138	-	0.9175
0.1	0.8450	0.8396	0.8203	0.8422	0.8384	-	0.8401
0.0	0.4300	0.4189	0.4055	0.4206	0.4124	-	0.4207

Table 2.2: Numerical values of θ_{pb} vs. x_{pb} obtained from the analytical solution, MBFEM and FDM-based approaches.

	$\theta(x,t)$ when $x_{pb} = 0.5$						
x	Analytical solution	$\Delta L = 0.014$, $\tau = 0.0001$		$\Delta L = 0.007$, $\tau = 0.00001$		$\Delta L = 0.0035$, $\tau = 0.00001$	
		FDM	MBFEM	FDM	MBFEM	FDM	MBFEM
0.9	1.0367	1.0304	1.0205	1.0342	1.0271	-	1.0311
0.8	1.0183	1.0123	1.0088	1.0159	1.0124	-	1.0131
0.7	0.9897	0.9841	0.9724	0.9875	0.9811	-	0.9848
0.6	0.9533	0.9483	0.9367	0.9513	0.9452	-	0.9487
0.5	0.9120	0.9082	0.8977	0.9102	0.9054	-	0.9086
0.4	1.1972	1.1954	1.1891	1.1971	1.1938	-	1.1955
0.3	1.3259	1.3251	1.3217	1.3258	1.3242	-	1.3250
0.2	1.3825	1.3821	1.3801	1.3824	1.3815	-	1.3819
0.1	1.4056	1.4054	1.4039	1.4054	1.4048	-	1.4051
0.0	1.4118	1.4116	1.4097	1.4116	1.4108	-	1.4112

Table 2.3: Numerical values of $\theta(x,t)$ vs. x when $x_{pb} = 0.5$. Results of the analytical solution, MBFEM and FDM-based approaches.

	Temperature of the phase boundary, θ_{pb}			
Phase boundary position, x_{pb}	Analytical solution	$\Delta L = 0.014$, $\tau = 0.0001$	$\Delta L = 0.007$, $\tau = 0.00001$	$\Delta L = 0.0035$, $\tau = 0.00001$
0.9	0.9681	0.9440	0.9555	0.9605
0.8	0.9221	0.9020	0.9115	0.9157
0.7	0.9079	0.8894	0.8986	0.9023
0.6	0.9071	0.8903	0.8984	0.9017
0.5	0.9120	0.8973	0.9054	0.9086
0.4	0.9221	0.9053	0.9134	0.9167
0.3	0.9295	0.9140	0.9214	0.9246
0.2	0.9244	0.9045	0.9136	0.9172
0.1	0.8450	0.8203	0.8382	0.8400
0.0	0.4300	0.4054	0.4122	0.4205
Averaged number of iterations per time step		2.120	1.990	1.853

Table 2.4: Numerical values of θ_{pb} vs. x_{pb} obtained from the analytical solution, and also computed by MBFEM when Eq. 2.60 is used for phase boundary velocity.

x	$\theta(x,t)$ when $x_{pb} = 0.5$			
	Analytical solution	$\Delta L = 0.014$, $\tau = 0.0001$	$\Delta L = 0.007$, $\tau = 0.00001$	$\Delta L = 0.0035$, $\tau = 0.00001$
0.9	1.0367	1.0201	1.0270	1.0310
0.8	1.0183	1.0084	1.0123	1.0131
0.7	0.9897	0.9722	0.9810	0.9847
0.6	0.9533	0.9362	0.9452	0.9487
0.5	0.9120	0.8974	0.9051	0.9086
0.4	1.1972	1.1892	1.1935	1.1955
0.3	1.3259	1.3211	1.3240	1.3250
0.2	1.3825	1.3801	1.3814	1.3818
0.1	1.4056	1.4035	1.4046	1.4050
0.0	1.4118	1.4092	1.4106	1.4110

Table 2.5: Numerical values of $\theta(x,t)$ vs. x when $x_{pb} = 0.5$. Results of the analytical solution are given, and also those from MBFEM when Eq. 2.60 is used for phase boundary velocity.

$d\delta(1,t)/dt$	Average iterations per time step (without Newton-Raphson)	Average iterations per time step (with Newton-Raphson)
0.84	5.0	4.3
0.42	4.4	3.9
0.084	1.8	1.5
0.042	1.3	1.3
0.0084	1.3	1.2

Table 2.6: The effect of the Newton-Raphson method at different strain rates.

Bibliography

[1] P. H. Leo, T. W. Shield, and O. P. Bruno, "Transient heat transfer effects on the pseudoelastic behavior of shape memory alloy wires," *Acta Metallurgica Materialia* **41**, pp. 2477–2485, 1993.

[2] J. A. Shaw and S. Kyriakides, "Thermomechanical aspects of NiTi," *J. Mech. Phys. Solids* **43**, pp. 1243–1281, 1995.

[3] H. Carslaw and S. Jaeger, *Conduction of Heat in Solids*, Oxford University Press, UK, 1959.

[4] S. Kim and R. Abeyaratne, "On the effect of the heat generated during a stress-induced thermoelastic phase transformation," *Continuum Mechanics and Thermodynamics* **7**, pp. 311–332, 1995.

[5] J. Crank, *Free and Moving Boundary Problems*, Clarendon Press, Oxford, 1984.

[6] J. Crank, "Two methods for the numerical solution of moving boundary problems in diffusion and heat flow," *J. Mech. Appl. Math.* **10**, pp. 220–231, 1957.

[7] L. Ehrlich, "A numerical method of solving a heat flow problem with phase boundary," *J. Assn. Comp. Math* **5**, pp. 161–176, 1958.

[8] N. Asaithambi, "On a variable time-step method for the one-dimensional stefan problem," *Comput. Meth. Appl. Mech. Eng* **71**, pp. 1–13, 1988.

[9] R. Gupta and D. Kumar, "A modified variable time step method for one dimensional stefan problem," *Comput. Meth. Appl. Mech. Eng.* **23**, pp. 101–109, 1980.

[10] R. Gupta and D. Kumar, "Variable time step methods for one dimensional stefan problem with mixed boundary conditions," *J. Heat and Mass Transfer* **24**, pp. 251–259, 1981.

[11] W. Murray and F. Landis, "Numerical and machine solutions of transient heat conduction problems involving melting or freezing," *J. Heat and Mass Transfer* **81**, pp. 106–112, 1959.

[12] J. Crank and R. Gupta, "A method for solving moving boundary value problems in heat flow using cubic splines or polynomials," *J. Inst. Math. Appl.* **10**, pp. 296–304, 1972.

[13] R. Gupta, "Moving grid method without interpolations," *Comput. Meth. Appl. Mech. Eng.* **4**, pp. 143–152, 1974.

[14] M. Djomehri and J. George, "Application of the moving finite element method to moving boundary stefan problems," *Comput. Meth. Appl. Mech. Eng.* **71**, pp. 125–136, 1987.

[15] V. Stoilov, O. Iliev, and A. Bhattacharyya, "A moving boundary finite element method-based approach for the solution of one-dimensional problems in shape memory alloys," *Computer Methods in Applied Mechanics and Engineering* **190**, pp. 1741–1762, 2000.

[16] D. C. Lagoudas and A. Bhattacharyya, "Modeling of thin layer extensional thermoelectric sma actuators," *Int. J. Solids Struct.* **35**, pp. 331–362, 1998.

[17] F. Oberaigner, K. Tanaka and F. Fischer, "Investigation of the damping behavior of a vibrating shape memory alloy rod using a micromechanical model," *J. Smart Mater. Struct.* **3**, pp. 456–463, 1996.

[18] A. Bekker and L. Brinson, "Temperature-induced phase transformation in shape memory alloy: phase diagram based kinetic approach," *J. Mech. Phys. Solids* **45**, pp. 949–988, 1997.

[19] Z. Bo, "Constitutive modeling of shape memory alloys," *PhD thesis, Texas A & M University, College Station, Texas* , 1996.

[20] R. Salzbenner and M. Cohen, "On the thermodynamics of thermoelastic martensitic transformations," *Acta Metall.* **27**, pp. 739–748, 1979.

[21] A. Bhattacharyya, V. Stoilov, and O. Iliev, "Evaluation of structural influence of shape memory alloys linear actuators by sharp phase front-based constitutive models," *Computational Materials Science* **18**, pp. 269–282, 2000.

[22] C. Jackson, H. Wagner and R. Wasilewski, "55-nitinol the alloy with a memory: its physical metallurgy, properties and applications," *NASA-SP 5110 Washington, DC* , 1972.

[23] H. Funakubo, *Shape Memory Alloys*, Gordon and Breach, New York, 1984.

[24] S. Kim, "A continuum model for phase transitions in thermoelastic solids and its application to shape memory alloys," *PhD thesis, MIT, USA* , 1995.

[25] E. Buckingham, "On physically similar system illustrations of the use of the dynamical equations," *Phys. Rev.* **4**, pp. 345–376, 1914.

[26] B.A. Boley and J.H. Weiner, *Theory of Thermal Stresses*, Krieger, New York,USA, 1960.

[27] M. Ozisik, *Heat Conduction*, Wiley, New York, 1980.

Chapter 3

Linear Shape Memory Alloy Actuators

3.1 Introduction

Two issues that are of central importance in actuator design with shape memory alloys (SMAs) are: 1. Availability of an appropriate constitutive model to characterize the response of shape memory alloys, 2. evaluation of SMA actuator response based on a certain commonly accepted definitions of actuator performance. The first issue is complicated by the fact that the phase transformations in shape memory alloys are accompanied by a strong coupling between the thermal and mechanical fields in the SMA actuator. Another important fact is that the phase transformation is largely inhomogeneous in nature, accompanied by the presence of multiple phase boundaries that move during the progression of the transformation itself. Motion of phase boundaries has been observed in experiments on tensile loading of Copper-Aluminum-Nickel (CuAlNi) single crystals [4] or in Nickel- Titanium (NiTi) wires [1, 5]. The former paper reported the motion of one phase boundary whereas the latter two reported the motion of multiple phase boundaries during the phase transformation. In particular, modeling of such experiments may be done by the theoretical approaches proposed by Abeyaratne and Knowles [6, 3] on the one hand and Leo et al. [1] on the other hand. The latter approach was further elucidated by Bruno et al. [7]. Both approaches are similar in most aspects but differ somewhat in how they propose to describe the motion of the phase boundary during phase transformation. We shall henceforth refer to Abeyaratne and Knowles' [3] model as the A-K approach whereas the model of Bruno, Leo and Reitich [7] will be referred to as the B-L-R approach.

Another issue that is central to SMA actuator design is the actuator performance. There are two commonly accepted measures of SMA actuator performance: 1. Energy efficiency, and 2. specific energy output (or energy output per unit volume of actuator material). These performance measures have to be viewed in the light of the type of SMA actuator being designed -linear (wire, rod or thin film configuration) and rotatory -as also the structural situation in which these actuators will be employed. The simplest scenario that can be anticipated is when such an active actuator is incorporated into a structure having a single passive element (which may be taken as elastic). This was recognized by Lagoudas and Bhattacharyya [8] when they analyzed a thin plate actuator subjected to a spring-loaded mechanical boundary condition. The thin plate actuator was activated by the thermoelectric effect and they determined the performance measures of such an actuator. Motivated by the assumption of free convection thermal boundary conditions and the thinness of the film, they could make the reasonable assumption that the temperature field in the film was spatially uniform, leading to a drastic simplification in the numerical implementation of the problem.

This chapter has two objectives and addresses them in the context of an SMA linear actuator (an SMA rod or a wire) actuated electrically and subjected to spring-loaded boundary conditions at its ends (see Fig. 3.1): 1. The first objective is to address the question as to how different is the response of an SMA linear actuator as predicted by the A-K and B-L-R constitutive models, 2. the second objective is to analyze the SMA linear actuator, and determine the influence on the actuator performance due to the structural stiffness (modeled here by the stiffness of the spring). In contrast to Lagoudas and Bhattacharyya's [8] analysis, we allow the temperature field to be spatially non-uniform. These aforementioned issues can only be addressed after the thermomechanical field in the SMA actuator is carefully modeled. Analytical solutions are usually not available for spatially non-uniform thermal fields, and thus we use the MBFEM-based numerical approach proposed by Stoilov et al. [2] and given in Chapter 2. While they demonstrated their numerical approach using the A-K model, we suitably adapt their approach here so that the B-L-R model may also be used.

The chapter is organized in five sections. Section 3.2 discusses the boundary value problem of the spring-loaded SMA linear actuator. Section 3.3 addresses the issue of phase transformation in the linear actuator in the context of the two different constitutive models. Section 3.4 defines the performance measures of the SMA actuator in the context of the specific boundary value problem outlined in Section 3.2. Section 3.5 discusses the computational approach and gives the parametric studies. The chapter ends with the conclusions of the study, summarized in Section 3.6. The entire analysis will be restricted to a quasistatic loading situation such that inertia effects may be ignored.

3.2 Boundary value problem for a shape memory alloy bar with a sharp austenite-martensite interface

We begin this section with a description of the schematic in Fig. 3.1. An SMA bar of length $2L$, is shown with initially pre-stretched linear springs attached at its ends. The schematic shows a martensitic phase separating two austenitic phases. We consider the class of problems wherein at any given time t, the two-phase boundaries between martensite and austenite are always symmetrically situated with respect to the center of the bar. The location of these two phase boundaries are denoted by the parameter, $s(t)$ and $-s(t)$, where $s(t)$ lies within the range, $0 \leq s(t) \leq L$. Each continuum point along the bar will be either in a purely austenitic state or purely martensitic state but never a mixture of both. The phase boundary therefore defines the location where there is a sharp transition from one phase into another. This is in contrast to phenomenological theories of phase transformation based on homogenization principles where the material at a continuum point is allowed to exist as a mixture of both phases. Based on that approach, phase fronts in such problems can possibly represent a transition from purely one phase to a mixture of two phases. In that context, such phase fronts will not be referred as "sharp". The theories we shall focus on in this work belong to the former class, i.e., they allow only sharp phase fronts.

We consider thermomechanical phase transformations in which the uniaxial stress field, σ, is time dependent and spatially uniform whereas the temperature field, θ, is time dependent and spatially non-uniform along the length of the bar (i.e., along the x-direction). Therefore

$$\sigma \equiv \sigma(t) \quad \text{and} \quad \theta \equiv \theta(x,t) \ . \tag{3.1}$$

Due to the spatial symmetry of the thermomechanical problem, only one-half of the bar ($0 \leq x \leq L$) will be considered in the sequel. In this context, only one phase boundary is involved in the problem. While such a situation has been observed in experiments on CuAlNi SMAs [4], the issue of multiple phase boundaries may also be addressed within the context of the theory to be discussed here. However, we shall restrict the paper in addressing a single-phase boundary problem, so that we can maintain a focus on the issues we intend to address in this paper.

3.2.1 Thermomechanical governing equations

The constitutive response of the austenite and martensite phases in the bar is taken to be thermoelastic. Excluding rigid body displacements, the deformation, $\delta(L,t)$, at the end of the bar ($x = L$) is

$$\delta(L.t) = \frac{L}{E}\sigma(t) + \alpha \int_0^L \left[\theta(x,t) - \theta_0\right] dx + \varepsilon_T s(t) \ , \tag{3.2}$$

where E is the Young's modulus, α the linear coefficient of thermal expansion (for simplicity, E and α have been assumed identical for both phases), θ_0 the ambient temperature and ε_T is the uniaxial phase transformation strain in the martensite phase. We note that the three terms on the right-hand side of Eq. 3.2 correspond to contributions to the overall deformation of the bar due to elastic strains, thermal strains and phase transformation strains, respectively. Often, the rate form of Eq. 3.2 is useful; it is

$$\dot{\delta}(L,t) = \frac{L}{E}\dot{\sigma}(t) + \alpha \int_0^L \dot{\theta}(x,t) dx + \varepsilon_T \dot{s}(t) \ , \tag{3.3}$$

where a superimposed dot denotes the time derivative. The conservation of energy in either phase (but away from the phase boundary) will now be given. We shall assume that the SMA bar is heated electrically. Convection along the length of the bar is approximately included as a heat sink. The energy equation can then be written as

$$k\frac{\partial^2\theta}{\partial x^2}(x,t) - \frac{h_L P}{A}\left[\theta(x,t) - \theta_0\right] + \rho_E J^2 =$$
$$\left[\rho c + E\alpha^2\theta(x,t)\right]\frac{\partial\theta}{\partial t}(x,t) + \alpha\theta(x,t)\frac{d\sigma}{dt}(t) \quad \text{for} \quad x \neq s(t)\ , \tag{3.4}$$

where k is the thermal conductivity, h_L the convection coefficient along the length of the bar, P and A are the perimeter and area of the bar cross-section, respectively, ρ_E the electrical resistivity, J the electrical current density, ρ the mass density and c is the specific heat. The parameters -k, ρ_E and c -have been taken identical for both phases. At the phase boundary, the heat flux has a jump, given as

$$-k\left(\frac{\partial\theta}{\partial x}\left(s^+(t),t\right) - \frac{\partial\theta}{\partial x}\left(s^-(t),t\right)\right) = (\sigma(t)\varepsilon_T + \rho\lambda_T)\dot{s} \quad \text{for} \quad x = s(t)\ , \tag{3.5}$$

where λ_T is the magnitude of the latent heat released (or absorbed) per unit mass of austenite as it transforms into martensite (or vice versa) during cooling (or heating). The parameters, $s^+(t)$ and $s^-(t)$ are respectively defined as $s^{\pm}(t) = \lim_{\Delta\to 0}(s(t) \pm \Delta),\ \Delta > 0$.

3.2.2 Initial conditions

The initial conditions for the stress, temperature and the position of the phase boundary are defined as

$$\sigma(0) = \sigma_0 \ , \quad \theta(x,0) = \theta_0 \ , \quad s(0) = s_0 \ , \tag{3.6}$$

corresponding respectively to a stressed initial state, spatially uniform initial temperature (identical to the ambient) and an initial co-existence of martensite and austenite. The initial stress state, σ_0 (given by the first of Eq. 3.6) will follow from the condition that the springs have an initial pre-stretch when they are attached to the bar. We shall find this stress in Section 3.2.3.

3.2.3 Boundary conditions

The thermal boundary conditions are taken as

$$\frac{\partial \theta}{\partial x}(0,t) = 0 \ , \quad k\frac{\partial \theta}{\partial x}(L,t) = h_b(\theta(L,t) - \theta_0) \ , \tag{3.7}$$

where the former is a statement of the symmetry condition at $x = 0$ and the latter states that the heat conduction at $x = L$ (i.e., the end grips in a laboratory experiment) is approximately simulated by a convective-type boundary condition with a linear temperature dependence; the parameter,

h_b, represents the ability of the end grips to conduct heat. If it is so desired, a more complicated end boundary condition may always be adopted.

The mechanical boundary conditions are now given. It is assumed that the ends of the SMA bar (of length $2L$) are connected to linear springs of identical stiffness, K_s (see Fig. 3.1), and that the springs are pre-stretched by an amount, δ_s, before connecting them to the SMA bar. Therefore, for the half-length of the SMA bar, $0 \leq x \leq L$, we have

$$\sigma(t) = \frac{K_s}{A}[\delta_s - (\delta(L,t) - \epsilon_T s_0)] \ , \quad \delta(0,t) = 0 \ , \tag{3.8}$$

where the former state the stress-displacement relationship of the SMA bar at $x = L$ due to the spring with stiffness, K_s, whereas the latter of Eq. 3.8 is instrumental in removing rigid body displacements (and has already been accounted for, in developing Eq. 3.2). Using Eqs. 3.2 and 3.6, the initial value of the stress, σ_0 (the first of Eq. 3.6) follows as:

$$\sigma(0) = \frac{K_s}{A + \frac{K_s L}{E}} \delta_s \ . \tag{3.9}$$

In summary, the boundary value problem seeks a solution for $\sigma(t)$, $\delta(L,t)$, $\theta(x,t)$ and $s(t)$ from the Eqs. 3.3-3.5 and the first of Eq. 3.8. Since Eqs. 3.4 and 3.5 may be viewed as one single equation (this may be realized by incorporating the heat source, represented by Eq. 3.5 into Eq. 3.4, using a delta function), there are really three available equations. Since the number of unknown parameters exceeds the number of equations by one, one additional equation is required to allow for a complete and unique solution for the unknown parameters. The two different approaches -the B-L-R and the A-K models -primarily differ in how they obtain the fourth equation; this is what we turn to next.

3.3 Motion of the sharp austenite-martensite interface during phase transformation

Phase transformation with a slow (or quasistatic) motion of phase boundaries in thermoelastic materials is a dissipative process. Abeyaratne and Knowles [6] have demonstrated that the dissipation results in the following inequality arising out of the second law of thermodynamics

$$f\dot{s} \geq 0 \, , \tag{3.10}$$

where f is identified as the driving traction at the phase boundary and can be shown to be identical to a jump in the Gibbs free energy per unit volume, g, at the phase boundary at any instant in time, i.e., $f = g(s^+(t), t) - g(s^-(t), t)$. For the boundary value problem defined in Section 3.2, it can be shown that [3]

$$f = [\sigma - \sigma_M(\theta_s)]\varepsilon_T \ , \tag{3.11}$$

where $\theta_s = \theta(s(t), t)$ is the temperature at the phase boundary and $\sigma_M(\theta_s)$ is the value of the stress at which the driving force vanishes at a given phase boundary temperature; $\sigma_M(\theta_s)$ is known as the Maxwell stress. Any additional equation that is proposed to complete the system of equations introduced in Section 3.2 will have to be such that Eq. 3.10 is not violated.

Note that while Eq. 3.10 specifies the condition for dissipation, it does not address the issue of hysteresis that is a key feature of phase transformation in SMAs. To incorporate hysteresis into the aforementioned theory while satisfying the second law inequality (Eq. 3.10), the A-K model proposed that [3]

$$\begin{aligned} f \geq f_1, &\quad \text{where } \ f_1 > 0 \ \text{ and } \dot{s} > 0 \ , \\ -f_2 < f < f_1, &\quad \text{where } \ f_1, f_2 > 0 \ \text{ and } \dot{s} = 0 \ , \\ f \leq -f_2, &\quad \text{where } \ f_2 > 0 \ \text{ and } \dot{s} < 0 \ , \end{aligned} \tag{3.12}$$

where f_1 and f_2 are the threshold values of the driving traction during the A→M transformation ($\dot{s} > 0$) and the M→A transformation ($\dot{s} < 0$), respectively. Eq. 3.12 assures hysteresis in the SMA response as long as f_1 and f_2

are not simultaneously zero. In the context of the above framework, the B-L-R model's [7] approach is to choose the driving traction, f, appropriately so that Eq. 3.12 is satisfied, whereas the A-K model suggests an expression for the phase front velocity, $\dot{s}$, so that Eq. 3.12 is satisfied. We briefly discuss these two approaches next.

3.3.1 The B-L-R model

Motivated by experimental observations, Bruno et al.'s [7] approach is to assume that $f_1 = f_2$ and postulate that during the A→M transformation ($\dot{s} > 0$), $f = f_1$, whereas, during the M→A transformation ($\dot{s} < 0$), $f = -f_1$. These choices assure that Eq. 3.12 (and thereby Eq. 3.10 is satisfied). Denoting $\sigma \equiv \sigma_{A\to M}(\theta_s)$ during the A→M transformation and $\sigma \equiv \sigma_{M\to A}(\theta_s)$ during the M→A transformation, the aforementioned conditions, along with Eq. 3.11, may be written as

$$\begin{aligned} \sigma_{A\to M}(\theta_s) &= \sigma_M(\theta_s) + \frac{f_1}{\varepsilon_T}, \text{ where } f_1 > 0 \text{ and } \dot{s} > 0 \,, \\ \sigma_{M\to A}(\theta_s) &= \sigma_M(\theta_s) - \frac{f_1}{\varepsilon_T}, \text{ where } \dot{s} < 0 \,, \\ \sigma_{M\to A}(\theta_s) &< \sigma < \sigma_{A\to M}(\theta_s), \text{ where } \dot{s} = 0 \,, \end{aligned} \tag{3.13}$$

where a linear dependence of the Maxwell stress, $\sigma_M(\theta_s)$, on θ_s is assumed by Bruno et al. [7] (as was also done in the A-K model; see Section 3.3.2). The term, f_1/ϵ_T, in Eq. 3.13 is referred by Bruno et al. [7] as σ_{hyst}, and is a measure of the hysteresis inherent in the phase transformation. The evolution of the phase front velocity, $\dot{s}$, will then emerge as a solution to the problem.

3.3.2 The A-K model

The approach of Abeyaratne and Knowles [3] is to specify an initiation criterion for the start of the A→M (or M→ A) transformation. During the subsequent transformation, they prescribe $\dot{s}$ in a manner such that Eq. 3.12 is satisfied. This prescribed expression is referred by them as the kinetic relation.

Initiation criterion

The initiation criterion is the condition that is used to determine the initiation of the phase transformation, i.e., the criterion based on which the phase front velocity changes from $\dot{s} = 0$ to $\dot{s} \neq 0$. Abeyaratne and Knowles [3] propose that during the A→M transformation, $f = f_1$, whereas during the

M→ A transformation, $f = -f_2$. These conditions coincide with those of the B-L-R model when $f_1 = f_2$. Using Eq. 3.11, the initiation criterion of the phase transformation at some time $t = t_1$ is written as

$$
\begin{aligned}
\sigma = \sigma_M(\theta_s) + \frac{f_1}{\varepsilon_T}, \text{ where } f_1 > 0, \quad & \dot{s}(t_1) > 0 \, , \\
\sigma = \sigma_M(\theta_s) - \frac{f_2}{\varepsilon_T}, \text{ where } f_2 > 0, \quad & \dot{s}(t_1) < 0 \, , \\
\sigma_M(\theta_s) - \frac{f_2}{\varepsilon_T} < \sigma < \sigma_M(\theta_s) + \frac{f_1}{\varepsilon_T}, \quad & \dot{s}(t_1) = 0 \, , \\
\lim_{\Delta \to 0} \dot{s}(t_1 - \Delta t) = 0 \, , \quad & \Delta t > 0 \, , \qquad (3.14)
\end{aligned}
$$

where the first of Eq. 3.14 corresponds to initiation of the A→M transformation whereas the second of Eq. 3.14 corresponds to the initiation of the M→A transformation. The parameters $\sigma_M(\theta_s)$, f_1, f_2 are [3]:

$$
\begin{aligned}
\sigma_M &= \frac{\rho\lambda_T}{\varepsilon_T}\left(\frac{\theta_s}{\theta_T} - 1\right) \, , \\
f_1 &= \frac{\rho\lambda_T}{\theta_T}\left(\theta_T - M_s^0\right) \, , \\
f_2 &= \frac{\rho\lambda_T}{\theta_T}\left(\theta_T - A_s^0\right) \, , \qquad (3.15)
\end{aligned}
$$

where θ_T is known as the equilibrium temperature (i.e., the temperature at which the Maxwell stress vanishes), M_s^0 and A_s^0 are the respective temperatures at which a stress-free A→M or a M→A transformation initiates.

The kinetic relation

Once the phase transformation has initiated, the expression for the phase front velocity has to be chosen appropriately so that Eq. 3.12 is satisfied. An example of such relation, motivated by experimental observations on a CuAINi SMA [4], was proposed by Kim [9] as

$$\dot{s} = \begin{cases} R_1(f - f_1) & \text{for } f \geq f_1 \;,\; R_1 > 0 \;, \\ 0 & \text{for } -f_2 < f < f_1 \;, \\ R_2(f + f_2) & \text{for } f \leq -f_2 \;,\; R_2 > 0 \;, \end{cases} \tag{3.16}$$

where R_1 and R_2 are experimentally determined material parameters.

3.4 Performance measures of SMA actuators in an active structure

The shape memory effect (SME) of an SMA actuator may be advantageously used for actuation by integrating the SMA actuator into a structure. Therefore, even if all the other structural components may not possess the SME and hence, in that context, are passive, the structure, as a whole, may display some SME, due to the SMA actuator itself. Such a structure is referred to as "active". It is often of interest to determine how the performance of the SMA actuator is influenced by the interaction of the actuator with the rest of the structure itself. In that context, two performance measures for the SMA actuator may be used: energy output per unit volume and energy efficiency [8, 10]. In the context of the boundary value problem defined in Section 3.2 for the simple SMA bar-linear spring active structure, we define the two performance measures below.

3.4.1 Energy output per unit volume of SMA (or specific energy output)

The energy stored in the spring during its extension (or actuation) will be defined as the energy output of the actuator. Denoting the energy output of the SMA actuator per unit volume (or specific energy output) of the SMA material as $W_{act}(t)$, we have

$$W_{act}(t) = \frac{A}{2K_s L}[\sigma^2(t) - \sigma^2(t_0)] \ , \tag{3.17}$$

where $\sigma(t_0)$ is the stress at time $t = t_0$, when the M→A transformation commences, leading to the contraction of the SMA bar and extension of the spring.

3.4.2 Energy efficiency

The energy efficiency of the actuator during actuation is defined as the ratio of useful mechanical energy, $W_{act}(t)$, obtained to the electrical energy input, $W_{elec}(t)$, both defined per unit volume of SMA material. If the actuation commences at $t = t_0$, the electrical energy input per unit SMA volume during $t \geq t_0$ is defined simply as $W_{elec}(t) = \rho_E J^2(t - t_0)$. Therefore

$$\eta_{act}(t) = \frac{W_{act}(t)}{W_{elec}(t)} = \frac{A}{2K_s L} \frac{\sigma^2(t) - \sigma^2(t_0)}{\rho_E J^2(t - t_0)} . \tag{3.18}$$

3.5 The computational approach and parametric studies

3.5.1 The computational approach

The system of equations presented in Section 3.3 does not, in general, have an analytical solution, and must therefore be solved by an appropriate computational approach. The key parameters for which we seek a solution are $\sigma(t)$, $\delta(L,t)$, $\theta(x,t)$ and $s(t)$. A total of 4 equations are needed; these are Eqs. 3.3 and 3.4 (combined with Eq. 3.5), the first of Eq. 3.8, and any of Eq. 3.13 (when the B-L-R model is under consideration), or the kinetic relation given by Eq. 3.16 (when the A-K model is under consideration). Any numerical approach will have to address the issue of a moving phase boundary (characterized by $\dot{s} \neq 0$), a coupling between the thermal and mechanical fields (evident in Eq. 3.5 and the last term of Eq. 3.4 and a non-linearity of the thermal field in the energy equation (represented by the first term on the right-hand side of Eq. 3.4). All these ingredients were addressed in the context of the A-K model for stress-induced transformations in an SMA bar subjected to constant deformation rates by Stoilov et al. [2] when they proposed an MBFEM-based numerical approach to deal with such problems. The key feature of the MBFEM proposed by them was to introduce a grid node (at the phase boundary and moving with it) in a one-dimensional (1D) mesh, which otherwise remains unchanged from one step to another. Additionally, the non-linearity in the system of equations is addressed by the Newton- Raphson method and the coupling by an iterative procedure within a given time step. They demonstrated the MBFEM to be accurate, unconditionally stable and robust when compared to an analytical solution for purely thermal transformations. They also found that the MBFEM-based numerical approach to be unconditionally stable in the context of stress-induced transformations during a constant deformation rate process. Their approach is equally applicable here, with some modification, wherein the mechanical boundary condition is dictated by linear springs instead of a constant deformation rate process. While the reader is referred to Stoilov et al. [2] for details of the numerical approach, we summarize it here in the context of a spring-loaded boundary condition and the B-L-R model. An efficient way to present the numerical process in a compact, yet easily understandable form is to present it in the form of two flowcharts, described below.

The entire numerical approach will be based on a temporal discretization with a constant time increment, τ .The total time elapsed at the end of the kth increment is defined as $t_k = k\tau$ ($k \geq 1$, where k is an integer, and not to be confused with the same symbol used for the thermal conductivity). The values of $\sigma(t)$, $\delta(L,t)$, $\theta(x,t)$ and $s(t)$ at the end of the kth increment will be denoted as σ^k, δ^k, $\theta^k(x)$ and s^k .Time derivatives of these parameters $\dot{\sigma}(t)$, $\dot{\delta}(L,t)$, $\dot{\theta}(x,t)$ and $\dot{s}(t)$ -at the end of the kth increment will be denoted as $\dot{\sigma}^k$, $\dot{\delta}^k$, $\dot{\theta}^k(x)$ and $\dot{s}^k$ using forward differencing. Thus, for example

$$\dot{\sigma}^k = \begin{cases} 0, & k = 0, \\ \frac{\sigma^k - \sigma^{k-1}}{\tau}, & k > 1. \end{cases} \tag{3.19}$$

Based on the spatial and temporal discretization, the flowchart in Fig. 3.2 outlines the process based on which a decision is taken as to which of Eq. 3.13

is applicable. Once that is decided, the flowchart in Fig. 3.3 gives the process by which all the necessary field variables are calculated in the context of the B-L-R model. For the sake of completeness, we have also included a third flowchart (see Fig. 3.4) that summarizes the MBFEM- based numerical approach in the context of the A-K model. This flowchart summarizes the decision-making process based on which of Eq. 3.14 should be used to initiate the transformation.

3.5.2 The moving boundary finite element method

The flowcharts (Figs. 3.2-3.4) summarize the decision-making process involved in evolving the phase transformation by the B-L-R and the K-A models, and the accompanying numerical approach. An integral part of the numerical approach is how to solve for the spatial temperature field, $\theta(x,t)$, from Eqs. 3.4 and 3.5 at a given time assuming that all other quantities in those equations are known. This is precisely the MBFEM that was proposed by Stoilov et al. [2]. This is briefly described in two steps below.

The first step in the process is to spatially discretize Eq. 3.4 without taking the jump condition Eq.3.5, into consideration. For simplicity, a uniform spatial grid of N elements is adopted, based on which the global stiffness and mass matrices as well as the force vector are developed. We write it as

$$\mathbf{A}_{UN}\vec{\Theta}_{UN} = \vec{B}_{UN} \ , \tag{3.20}$$

where $\mathbf{A}_{UN}$ is an $(N+1) \times (N+1)$ global stiffness matrix, $\vec{\Theta}_{UN}$ is an $(N+1) \times 1$ column matrix with the nodal temperatures as its components and $\vec{B}_{UN}$ is the force vector, and is an $(N+1) \times 1$ column matrix. The subscript "UN" has been used to indicate that the jump condition Eq.3.5, has not yet been used. We point out that due to the non-linear temperature term in Eq. 3.4 (the first term on the right of Eq. 3.4), the temperature in that term, i.e., in $E\alpha^2\theta(x,t)$, will be taken from the previous iteration in a Newton-Raphson scheme that is implemented within a given time step (see Section 4.2 of Stoilov et al. [2] for details).

In the second step, we account for Eq.3.5 by choosing an additional grid node that is taken to coincide with the location of the phase boundary at the end of the current time step. With this additional grid node (assuming that it is positioned between two successive nodes of the fixed grid) and Eqs.3.5 and 3.15 is augmented to read

$$\mathbf{A}\vec{\Theta} = \vec{B} \ , \tag{3.21}$$

where $\mathbf{A}$ is an $(N+2) \times (N+2)$ matrix, $\vec{\Theta}$ and $\vec{B}$ are $(N+2) \times 1$ column matrices. In the eventuality that the phase boundary falls on anyone of the fixed nodes, an additional grid node is not necessary, and the number of nodes based on which Eq. 3.16 is written is still $N + 1$. The details of the MBFEM approach may be found in Stoilov et al. [2].

3.5.3 Parametric studies

For the parametric study, we focus on phase transformation in an SMA bar that is initially in the fully martensitic condition. It is connected to initially pre-stretched springs, as shown in Fig. 3.1. The SMA bar is heated electrically until the M→A transformation initiates. It is assumed that the phase boundary will start moving from the ends of the bar towards its center. To complete a cycle of transformation, the heating is stopped after sometime, and free convection cools the bar until the A→M transformation initiates (i.e., the phase boundary now moves towards the ends of the bar). All parameters used in the computation are listed in Table 3.1. In the study to follow, we first give a comparison of the B-L-R and A-K approaches, followed by some performance characteristics of the SMA linear actuator. The results are presented in non-dimensional form. The relevant non-dimensional parameters involved in Figs. 3.5-3.9 are listed in Appendix B.

Fig. 3.5 is a plot of the phase boundary position with respect to time for $\bar{K}_s = 0.413$ (or the dimensional value of $K_s = 600N/mm$). At this value of $\bar{K}_s$, the transformation from martensite to austenite (characterized by a decreasing s) during heating slows considerably after 60% of the bar has transformed to austenite (or $s = 0.4$). Therefore the data shown in Fig. 3.5 is for 60% transformation of the initially martensitic bar to austenite. It is seen that the B-L-R model predicts a somewhat faster transformation from martensite to austenite than the A-K model. Subsequently, the cooling of the bar initiates the A→M transformation after about $\bar{t} = 0.4$, which occurs somewhat faster by the B-L-R approach (until about $\bar{t} = 0.7$). The evolution of stress is shown in Fig. 3.6. The contraction of the SMA actuator during the M→A transformation during heating is instrumental in extending the spring, and increasing the stress on the bar. Surprisingly, the stress calculated by both approaches are almost identical during the M→A transformation. The curves plateau when the heating is stopped at the end of the 60% transformation from martensite to austenite. The stress level attained by the B-L-R model at the end of the heating is seen to be somewhat lower than that calculated by the A-K approach. We have found this difference to be about 3.3% (since at the end of the heating, $\bar{\sigma} = 0.1990$ and 0.206, respectively, as computed by the B-L-R and A-K approaches). In spite of the small difference, it is somewhat instructive to examine the sources of the difference. We can infer from Eq. 3.2 and the first of Eq. 3.8 that, if we ignore the thermal strains (i.e., set $\alpha = 0$ in Eq. 3.2), then there is an unique relation between the stress, σ, and the phase boundary position, s. This implies that for a given amount of transformation, there is a unique value of stress operative in the SMA actuator, regardless of the model used to compute that stress. For this special case (i.e., $\alpha = 0$), we recomputed the non-dimensional stress at the end of the 60% M → A transformation to be 0.2102 and 0.2118, respectively, as computed by the B-L-R and A-K approaches; this is a difference of about 0.76%. This difference, which should be ideally zero, is necessarily due to the numerical approach (in principle, the difference may be reduced by refining the mesh and reducing the time step). Therefore the remainder of the difference, $3.3\% - 0.76\% = 2.54\%$, is necessarily due to the thermal strains in the SMA bar. The evolution of the phase boundary velocity is shown in Fig. 3.7. It is seen that while the qualitative trend as predicted by both models are very similar, the magnitude of the velocity predicted by the B-L-R approach is higher than that predicted by the A-K model, during the M →A transformation. Figs. 3.5-3.7 demonstrate that the two approaches do give somewhat different results. They would however have coincided exactly if it was possible to write an analytical expression for the phase front velocity predicted by the B-L-R model, and then that the expression was adopted as the kinetic relation in the A-K model. Nonetheless, within the context of the present results, we would not like to indicate a preference of one model over the other. A more pragmatic approach will be to test each model against experiments for a specific SMA linear actuator, and decide which one is more appropriate. On the other hand (in reference to Figs. 3.5-3.7), we observe that while the predictions by the two approaches are noticeably different, their quantitative values are close enough and their qualitative trend are similar enough so that either model may be equally preferred when experiments need to be simulated.

We now turn to the performance measures of the SMA linear actuator, as predicted by both models. The results given in Figs. 3.8 and 3.9 have been calculated based on a complete transformation of an initially martensitic bar to austenite. Fig. 3.8 gives the non-dimensional mechanical work output, $\bar{W}_{act}$, with respect to the non-dimensional stiffness, $\bar{K}_s$, of the spring. It is seen that the work output of the SMA actuator changes from about 1×10^{-4} to 5.5×10^{-4} as the stiffness changes from about 1×10^{-2} to 8×10^{-2}. As the

B-L-R approach has predicted a lower stress level at the end of the M→A transformation (see Fig. 3.6), expectedly, it predicts a lower $\bar{W}_{act}$ as compared to the A-K model (see Fig. 3.8). Another feature is that within the considered range of spring stiffness, the change in $\bar{W}_{act}$ is monotonic. Fig. 3.9 gives the energy efficiency, η, vs. $\bar{K}_s$. While the B-L-R model predicts a somewhat lower η, interestingly both models predict a non-monotonic change in η with respect to increasing $\bar{K}_s$. These results therefore imply that there is an optimum stiffness of the passive component (spring) of the SMA actuator- linear spring structure that will deliver the most energetically efficient response of the active structural component (the SMA actuator). Fig. 3.9 indicates that the most efficient SMA actuator response, predicted by both models occurs at about $\bar{K}_s = 3 \times 10^{-2}$ (the corresponding dimensional spring stiffness is $K_s = 43.6N/mm$). This points to the possibility that when an SMA actuator is integrated into a structure, the passive components of the structure may play a key role in determining the optimum energy efficiency with which the active component (i.e., the actuator) will activate the structure.

3.6 Conclusions

This paper has considered a specific boundary value problem of an electrically actuated SMA linear actuator, subjected to a spring-loaded boundary condition at its ends. Within the context of this boundary value problem, the SMA actuator response has been evaluated based on two sharp phase front-based constitutive models proposed by Abeyaratne and Knowles [3] and Bruno et al. [7] and the differences due to the two models have been analyzed. The computational component of the work has been completed using the MBFEM-based numerical approach proposed by Stoilov et al. [2]. The paper has also analyzed the performance specific work output and the energy efficiency of the actuator by both models. Interestingly, both models predict an optimum spring stiffness corresponding to which the efficiency of the actuator is at its maximum. This raises the possibility that when an SMA actuator is integrated into a structure, the passive components of the structure may play a key role in determining the optimum energy efficiency with which the active component (i.e., the actuator) will activate the structure.

Description	Simbol	Value
Length of the bar	L	$31.75 \times 10^{-3} m$
Perimeter of bar cross-section	P	$3.3528 \times 10^{-3} m$
Area of bar cross-section	A	$0.8942 \times 10^{-6} m^2$
Mass density	ρ	$6450 kg/m^3$
Specific heat	c	$465 J/(kgK)$
Coefficient of thermal expansion	α	$10^{-5} K^{-1}$
Young's modulus	E	$51.6 GPa$
Uniaxial phase transformation strain	ε_T	0.06
Latent heat of phase transformation	λ_T	$1.8733 \times 10^7 J/kg$
Convective coefficients	h_L	$5.3757 W/(m^2 K)$
	h_b	0
Thermal conductivity	k	$17.4 W/(mK)$
Ambient temperature	θ_0	$27C$
Equilibrium temperature	θ_T	$12C$
Mobility coefficient A→M	R_1	$2.1058269 \times 10^{-10} m^3/(Ns)$
Mobility coefficient M→A	R_2	$4.7381105 \times 10^{-10} m^3/(Ns)$
Driving force, A→M	f_1	$8791125 N/m^2$
Driving force, M→A	f_2	$6722625 N/m^2$
Initial pre-stretch of the spring	δ_s	$0.13 mm$
Initial phase boundary position	s_0	L
Electric current density	J	$2 A/mm^2 K$
Electrical resistivity	ρ_E	$6.3242 \times 10^{-4} \Omega mm$
Time increment	τ	$1.73 \times 10^{-3} s$
Number of elements	N	100
Tolerance	ε_{tol}	10^{-5}

Table 3.1: List of all material and computational parameters.

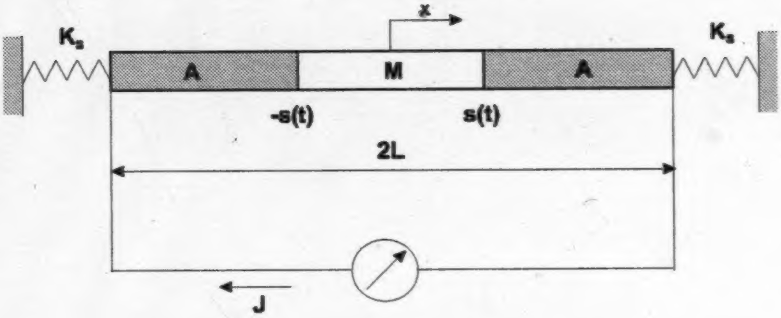
x
K_s
K_s
A
M
A
-s(t)
s(t)
2L
J

Figure 3.1: A schematic of linear SMA actuator.

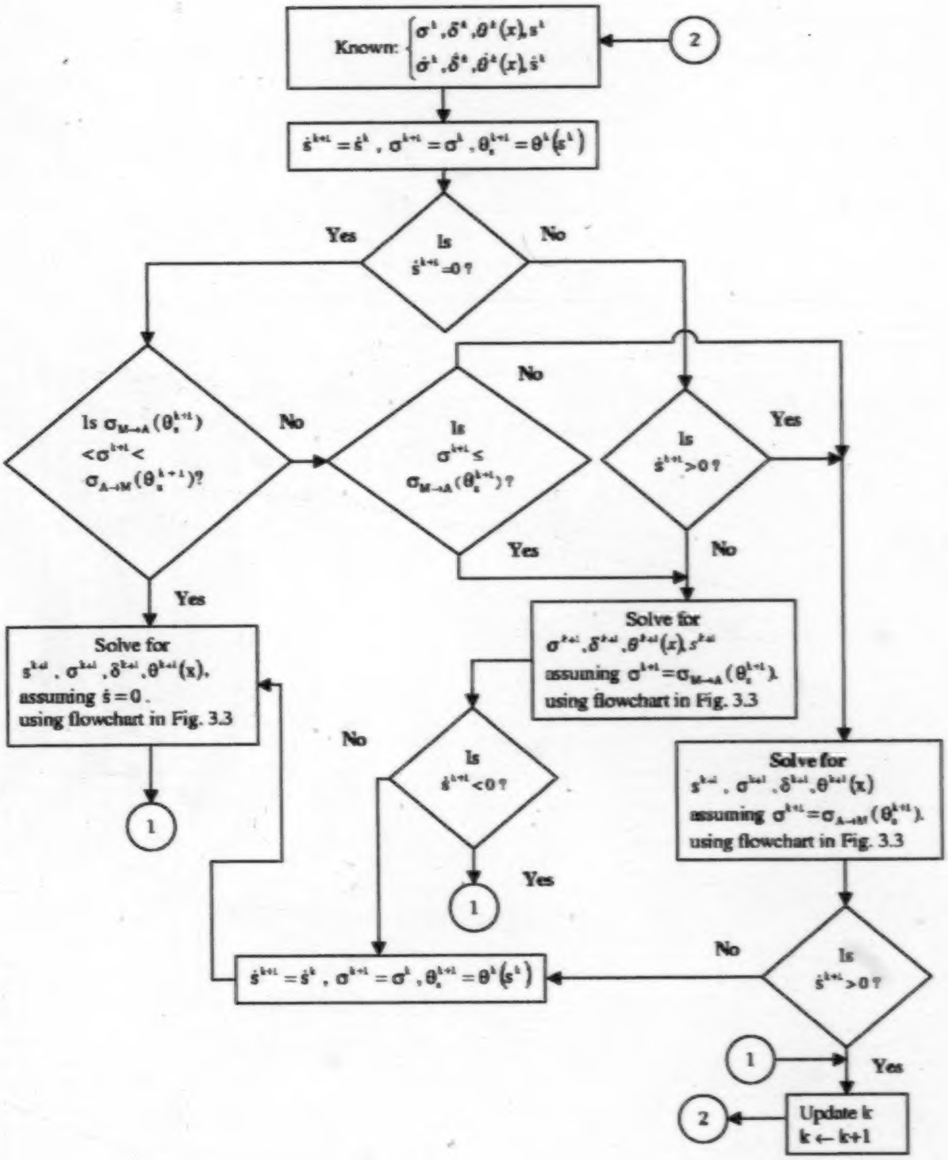
Known: $\begin{cases} \sigma^k, \delta^k, \theta^k(x), s^k \\ \dot{\sigma}^k, \dot{\delta}^k, \dot{\theta}^k(x), \dot{s}^k \end{cases}$
2
$\dot{s}^{k+1} = \dot{s}^k$, $\sigma^{k+1} = \sigma^k$, $\theta_s^{k+1} = \theta^k(s^k)$
Yes
Is $\dot{s}^{k+1} = 0$?
No
Is $\sigma_{M\to A}(\theta_s^{k+1}) < \sigma^{k+1} < \sigma_{A\to M}(\theta_s^{k+1})$?
No
Is $\sigma^{k+1} \le \sigma_{M\to A}(\theta_s^{k+1})$?
No
Is $\dot{s}^{k+1} > 0$?
Yes
Yes
No
Yes
Solve for s^{k+1} , σ^{k+1}, δ^{k+1}, $\theta^{k+1}(x)$, assuming $\dot{s} = 0$. using flowchart in Fig. 3.3
1
Solve for $\sigma^{k+1}, \delta^{k+1}, \theta^{k+1}(x), s^{k+1}$ assuming $\sigma^{k+1} = \sigma_{M\to A}(\theta_s^{k+1})$, using flowchart in Fig. 3.3
No
Is $\dot{s}^{k+1} < 0$?
Yes
1
Solve for s^{k+1} , σ^{k+1}, δ^{k+1}, $\theta^{k+1}(x)$ assuming $\sigma^{k+1} = \sigma_{A\to M}(\theta_s^{k+1})$, using flowchart in Fig. 3.3
No
Is $\dot{s}^{k+1} > 0$?
$\dot{s}^{k+1} = \dot{s}^k$, $\sigma^{k+1} = \sigma^k$, $\theta_s^{k+1} = \theta^k(s^k)$
1
Yes
Update k
$k \leftarrow k+1$
2

Figure 3.2: A flowchart depicting the decision process for the phase transformation based on Leo et. al. [1] approach.

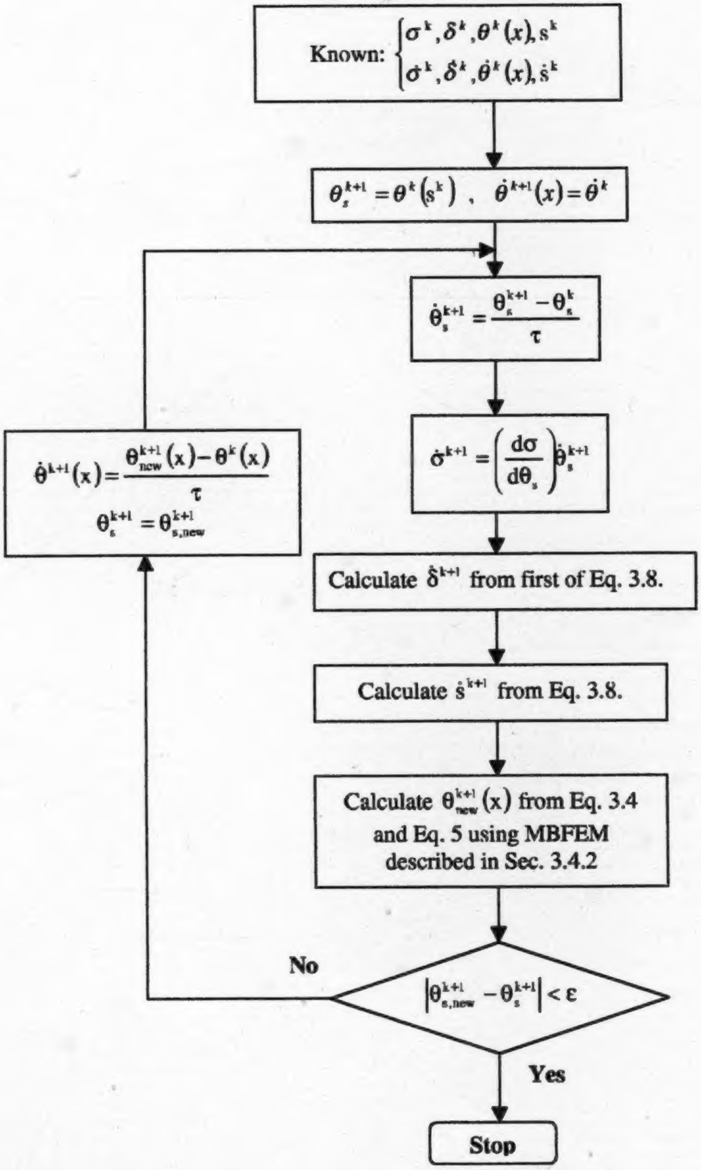

Known: $\begin{cases}\sigma^k, \delta^k, \theta^k(x), s^k \\ \dot\sigma^k, \dot\delta^k, \dot\theta^k(x), \dot s^k\end{cases}$
$\theta_s^{k+1} = \theta^k(s^k)$, $\dot\theta^{k+1}(x) = \dot\theta^k$
$\dot\theta_s^{k+1} = \frac{\theta_s^{k+1} - \theta_s^k}{\tau}$
$\dot\sigma^{k+1} = \left(\frac{d\sigma}{d\theta_s}\right)\dot\theta_s^{k+1}$
Calculate $\dot\delta^{k+1}$ from first of Eq. 3.8.
Calculate $\dot s^{k+1}$ from Eq. 3.8.
Calculate $\theta_{new}^{k+1}(x)$ from Eq. 3.4 and Eq. 5 using MBFEM described in Sec. 3.4.2
$\left|\theta_{s,new}^{k+1} - \theta_s^{k+1}\right| < \varepsilon$
No
Yes
Stop
$\dot\theta^{k+1}(x) = \frac{\theta_{new}^{k+1}(x) - \theta^k(x)}{\tau}$
$\theta_s^{k+1} = \theta_{s,new}^{k+1}$

Figure 3.3: A flowchart outlining the MBFEM-based numerical approach of Stoilov et. al. [2] adapted to implement Leo et. al. [1] theoretical model.

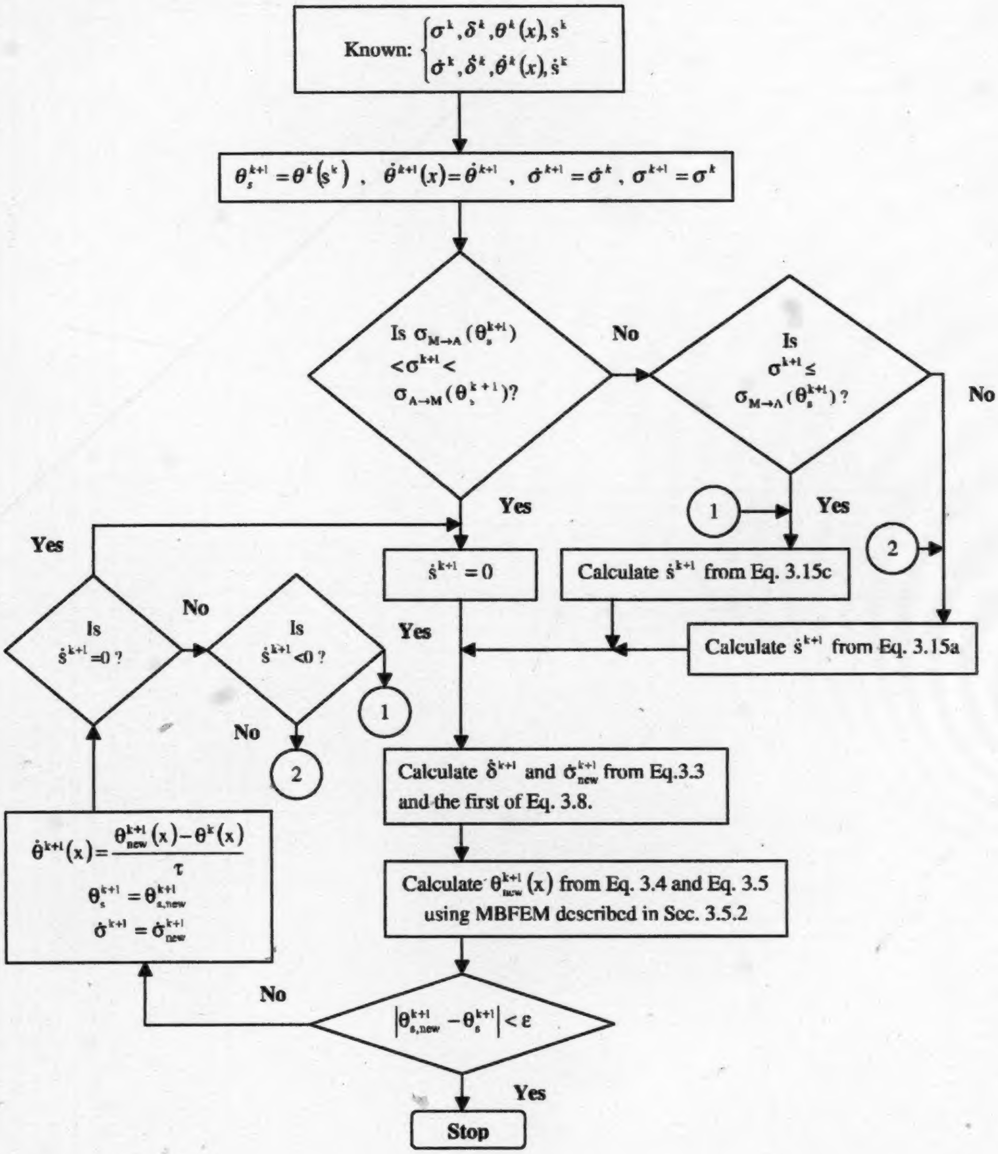
Known: $\sigma^k, \delta^k, \theta^k(x), s^k$; $\dot\sigma^k, \dot\delta^k, \dot\theta^k(x), \dot s^k$
$\theta_s^{k+1} = \theta^k(s^k)$, $\dot\theta^{k+1}(x) = \dot\theta^{k+1}$, $\dot\sigma^{k+1} = \dot\sigma^k$, $\sigma^{k+1} = \sigma^k$
Is $\sigma_{M\to A}(\theta_s^{k+1}) < \sigma^{k+1} < \sigma_{A\to M}(\theta_s^{k+1})$?
No
Is $\sigma^{k+1} \le \sigma_{M\to A}(\theta_s^{k+1})$?
No
Yes
1
Yes
2
$\dot s^{k+1} = 0$
Calculate $\dot s^{k+1}$ from Eq. 3.15c
Calculate $\dot s^{k+1}$ from Eq. 3.15a
Yes
Is $\dot s^{k+1} = 0$?
No
Is $\dot s^{k+1} < 0$?
Yes
1
No
2
Calculate $\dot\delta^{k+1}$ and $\dot\sigma_{new}^{k+1}$ from Eq.3.3 and the first of Eq. 3.8.
Calculate $\theta_{new}^{k+1}(x)$ from Eq. 3.4 and Eq. 3.5 using MBFEM described in Sec. 3.5.2
$\dot\theta^{k+1}(x) = \frac{\theta_{new}^{k+1}(x) - \theta^k(x)}{\tau}$
$\theta_s^{k+1} = \theta_{s,new}^{k+1}$
$\dot\sigma^{k+1} = \dot\sigma_{new}^{k+1}$
No
$\left|\theta_{s,new}^{k+1} - \theta_s^{k+1}\right| < \varepsilon$
Yes
Stop

Figure 3.4: A flowchart depicting the decision process for the phase transformation based on Abeyaratne and Knowles' [3] approach.

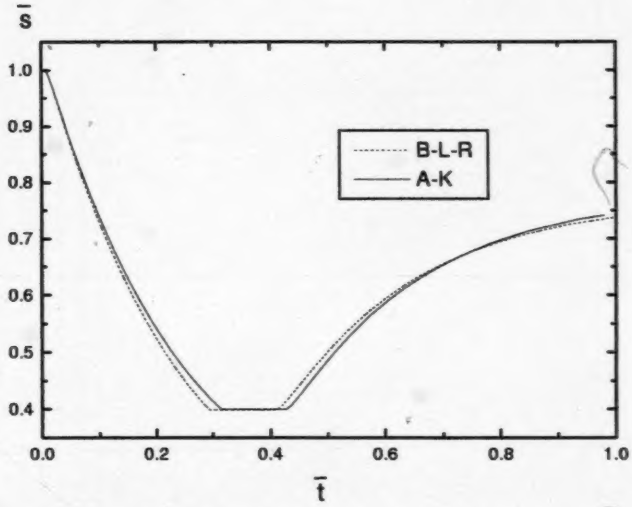

Figure 3.5: Non-dimensional phase boundary position, $\bar{s}$, with respect to non-dimensional time, $\bar{t}$.

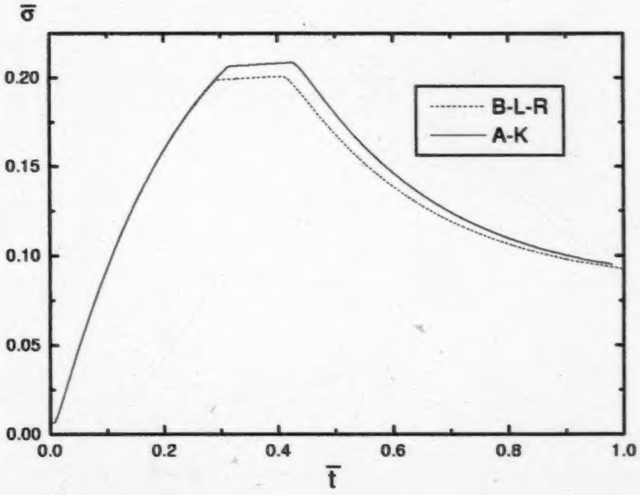

Figure 3.6: Non-dimensional stress, $\bar{\sigma}$, with respect to non-dimensional time, $\bar{t}$.

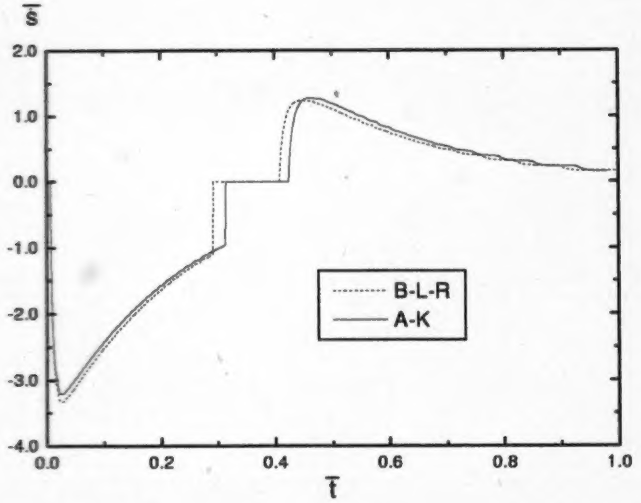

Figure 3.7: Non-dimensional phase boundary velocity, $\bar{\dot{s}}$, with respect to non-dimensional time, $\bar{t}$.

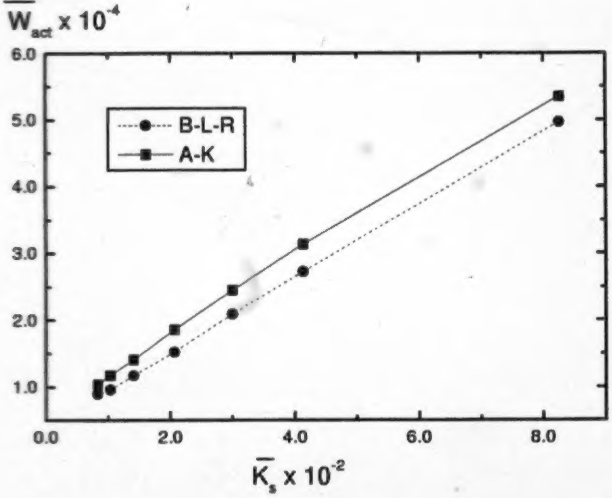

Figure 3.8: Non-dimensional specific energy output of SMA actuator, $\bar{W}_{act}$, with respect to non-dimensional spring stiffness, $\bar{K}_s$.

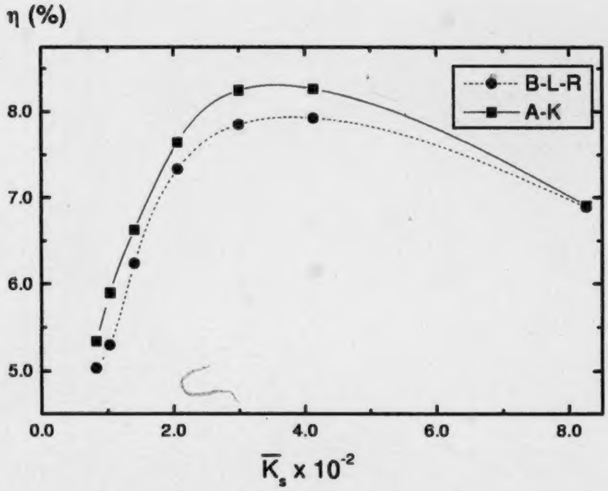

Figure 3.9: Energy efficiency of SMA actuator, η, with respect to non-dimensional spring stiffness, $\bar{K}_s$.

Bibliography

[1] P. H. Leo, T. W. Shield, and O. P. Bruno, "Transient heat transfer effects on the pseudoelastic behavior of shape memory alloy wires," *Acta Metallurgica Materialia* **41**, pp. 2477–2485, 1993.

[2] V. Stoilov, O. Iliev, and A. Bhattacharyya, "A moving boundary finite element method-based approach for the solution of one-dimensional problems in shape memory alloys," *Computer Methods in Applied Mechanics and Engineering* **190**, pp. 1741–1762, 2000.

[3] R. Abeyaratne and J. Knowles, "A continuum model of a thermoelastic solid capable of undergoing phase transitions," *J. Mech. Phys. Solids* **41**, pp. 541–571, 1993.

[4] R. Salzbrenner and M. Cohen, "Thermodynamics of thermoelastic martensitic transformations," *Acta Metallurgica* **27**, pp. 739–748, 1979.

[5] J. A. Shaw and S. Kyriakides, "Thermomechanical aspects of NiTi," *J. Mech. Phys. Solids* **43**, pp. 1243–1281, 1995.

[6] R. Abeyaratne and J. Knowles, "On the driving traction acting on the surface of strain discontinuity in a continuum," *J. Mech. Phys. Solids* **38**, pp. 345–360, 1990.

[7] O. P. Bruno, P. H. Leo, and F. Reitich, "Free boundary conditions at austenite-martensite interfaces," *Phys. Rev. Lett.* **74**, pp. 746–749, 1995.

[8] D. C. Lagoudas and A. Bhattacharyya, "Modeling of thin layer extensional thermoelectric sma actuators," *Int. J. Solids Struct.* **35**, pp. 331–362, 1998.

[9] S. Kim, "A continuum model for phase transitions in thermoelastic solids and its application to shape memory alloys," *PhD thesis, MIT, USA* , 1995.

[10] V. Giurgiutiu, Z. Chaudhry and C. Rogers, "Energy based comparison of solid state actuators," *Technical Report, Center for intelligent materials and structures,* **VPI-SU, Blacksburg, VA**, 1995.

Chapter 4

A One-dimensional Theoretical Framework for Sharp Phase Fronts in Shape Memory Alloys

4.1 Introduction

One-dimensional (1D) phase front-based continuum models(Abeyaratne and Knowles[3, 4], Bruno,Leo and Reitich[5]) assume that a phase front in the 1D domain always separates a fully austenitic phase from a fully martensitic phase. Abeyaratne and Knowles[3, 4] proposed an initiation criterion for the phase boundary motion and a kinetic relation for its evolution, which is then determined from experiments (by tracking the motion of phase boundaries in SMA wires). On the other hand, Bruno, Leo and Reitich[5] proposed an empirical equation (relating the phase boundary stress and temperature) for the phase boundary motion. Experimentally tracking 1D phase boundary motion is a direct but difficult approach and will definitely become more challenging if 2D phase boundary motion needs to be tracked. Using an empirical relation is a somewhat indirect but easier approach as it involves start and finish transformation temperatures that are more easily measurable. In view of these difficulties and in order to satisfy the objectives outlined in Section 1.4, we have proposed a complete 3D theoretical framework and the numerical approach for 2D phase front computational models of SMA phase transformation in Chapter 5. The key ingredient in that development is the assumption that the chemical potential of either phase is identical at the phase boundary, from which a generalized Clausius-Clapeyron equation may be derived. Such an approach will then render unneccessary the need to determine phase front velocities from experiments. It is however essential to demonstrate that the 1D implementation recover some of the known features of the 1D SMA phase transformation before the 2D implementation is attempted.

In this chapter, we propose a theoretical framework for modeling 1D sharp phase fronts in SMAs. The formulation is based on finite deformations, includes inertia (leading to a stress jump at the phase front), assumes the continuity of temperature and chemical potential at the phase front. The continuity of chemical potential is reducible to an identity that relates the stresses and temperature to a jump in entropy at the phase front. We refer to the resulting identity as the generalized Clausius-Clapeyron equation. The formulation is based on the Helmholtz free energy of each phase and thus is general enough to incorporate the constituent material response. The advantage of this approach is that if the Helmholtz free energy of each phase is explicitly known (and its parameters completely determined), the complete framework (including the generalized Clausius-Clapeyron equation) reduces to an explicit system of equations with completely characterized parameters. The velocity of the phase front does not have to be determined from experiments. Such an approach can then be generalized to the 2D case, and still be tractable. Analytical results are given for two sample Helmholtz free energy functions: a sixth order polynomial [6] and a trilinear function [3]. The framework is then specialized to small deformations, deformation gradients and negligible inertia. In that context, we demonstrate that for the special case of a trilinear Helmholtz free energy function with identical material properties for both phases (except the inelastic transformation strain), the generalized Clausius-Clapeyron equation reduces to a form similar to the empirical one used by Leo, Shield and Bruno [7]. The entire system of equations resulting from the theoretical framework are coupled and nonlinear, the solution of which is obtained by using the MBFEM - based numerical approach developed by Stoilov, Iliev and Bhattacharyya[8] and given in Chapter 2 . The numerical solution is then used to predict experimental data on SMA single and polycrystals subjected to uniaxial loading. The chapter is organized into five sections. Section 4.2 introduces the sharp phase front-based theoretical framework for shape memory alloys, Section 4.3 gives the quasistatic, small strain approximation and the SMA hysteretic response whereas Section 4.4 gives the results and discussions. Conclusions are given in Section 4.5.

4.2 The sharp phase front-based theoretical framework

We shall focus on phase transformations in a spatially 1D shape memory alloy bar subjected to uniaxial loading; see schematic in Fig. 4.1. The interface in the deformed configuration separating the austenite and martensite is taken to be located at $x = x_s(t)$. Quantities that are defined per unit volume of the reference configuration will be referred to as "specific", i.e. "specific entropy" will mean "entropy per unit volume of the reference configuration".

4.2.1 Conservation Laws

In absence of body forces, the conservation of linear momentum at all locations away from the phase boundary is written as

$$\frac{\partial \sigma}{\partial X} = \rho_0 \frac{dV}{dt} \qquad \text{at} \qquad x \neq x_s(t) \ , \tag{4.1}$$

where the co-ordinate, X, is the location of a particle in the reference configuration, t is time, $\sigma \equiv \sigma(X,t)$ is the uniaxial first Piola-Kirchoff stress (also referred sometimes as the "nominal stress"), $\rho_0 \equiv \rho_0(X)$ is the mass density in the reference configuration, and V is the particle velocity. The material derivative of V is dV/dt which, in turn, is related to its partial derivative through $dV/dt = \partial V/\partial t + V\partial V/\partial x$ (where x is the co-ordinate in the deformed configuration of a particle that was at X in the reference configuration). The conservation of energy is

$$\frac{\partial q}{\partial X} + \sigma\frac{dF}{dt} + \rho_0 r = \frac{du}{dt} \qquad \text{at} \qquad x \neq x_s(t)\ , \tag{4.2}$$

where q is the heat flux, F is the deformation gradient (defined below), $r \equiv r(X,t)$ is the heat source per unit mass and u is the internal energy per unit volume of the reference configuration. In particular, we define

$$F = 1 + \frac{\partial w}{\partial X}, \quad \text{where} \quad w = x - X\ , \tag{4.3}$$

w being the displacement of a particle from its reference configuration. The conservation of mass is stated as

$$\frac{d\rho}{dt} + \rho\frac{\partial V}{\partial x} = 0 \qquad \text{at} \qquad x \neq x_s(t)\ , \tag{4.4}$$

where ρ is the mass density in the deformed configuration. Denoting a jump in a quantity, $\mathcal{A}$, at the phase boundary as $[\mathcal{A}]$ and defining it as $[\mathcal{A}] = \lim_{\triangle\to 0}\mathcal{A}(x_s + \triangle, t) - \lim_{\triangle\to 0}\mathcal{A}(x_s - \triangle, t)$, where $\triangle > 0$, the conservation of linear momentum, energy and mass at the phase boundary ($x = x_s(t)$) respectively imply the following jumps

$$[\sigma] = -\rho_0[V]V_s \quad , \quad [q] = -[u + \frac{1}{2}\rho_0 V^2]V_s - [V\sigma] \quad , \quad [V] = -V_s[F]\ , \tag{4.5}$$

where $V_s = \partial x_s/\partial t$ is the phase boundary velocity.

4.2.2 Constitutive Equations

We shall focus on the class of materials for which the stress, σ, the specific entropy, η, and the specific internal energy, u, are dependent on the Lagrangian strain, ϵ, and the temperature, θ, while the heat flux, q, is given by the Fourier's law of heat conduction. These relations are respectively stated as

$$\sigma \equiv \sigma(\epsilon,\theta) \;\;,\;\; \eta \equiv \eta(\epsilon,\theta) \;\;,\;\; u \equiv u(\epsilon,\theta) \;\;,\;\; q = -k\frac{\partial\theta}{\partial X} \;, \tag{4.6}$$

where the Lagrangian strain follows from the deformation gradient, F, as

$$\epsilon = \frac{1}{2}\left(F^2 - 1\right) \;, \tag{4.7}$$

and the parameter, k, in the last of Eq.4.6 is the thermal conductivity. In particular, the stress, entropy and the internal energy may be derived from a specific Helmholtz free energy function, $\psi \equiv \psi(\epsilon,\theta)$, as [9]

$$\sigma = \left(\frac{\partial\psi}{\partial\epsilon}\right)_\theta \quad , \quad \eta = -\left(\frac{\partial\psi}{\partial\theta}\right)_\epsilon \quad , \quad u = \psi + \theta\eta \;, \tag{4.8}$$

where the subscript "θ" in the first of Eq.4.8 implies that the partial derivative, $\frac{\partial\psi}{\partial\epsilon}$, has been taken while keeping θ fixed. The condition for the phase boundary evolution is given next.

4.2.3 The Generalized Clausius-Clapeyron equation

For two phases to co-exist in thermodynamic equilibrium, the stress (σ), the temperature (θ) and the chemical potential (μ), have to be continuous at their interface [9]. Here, we propose that for irreversible processes not too far away from thermodynamic equilibrium, the latter two quantities remain continuous at the phase boundary, or equivalently, their jumps vanish. Thus

$$[\theta] = 0 \quad , \quad [\mu\,(\sigma,\theta)] = 0 \qquad \text{at} \qquad x = x_s(t) \ . \tag{4.9}$$

Denoting $\theta(x_s(t)) = \theta_s$, the latter of Eq. 4.9 is differentiated with respect to θ_s, resulting in

$$\left[\left(\frac{\partial\mu}{\partial\sigma}\right)_{\theta_s}\frac{\partial\sigma}{\partial\theta_s} + \left(\frac{\partial\mu}{\partial\theta_s}\right)_{\sigma}\right] = 0 \ . \tag{4.10}$$

The partial derivatives of the chemical potential with respect to the phase boundary temperature and stress are given by the Maxwell relations([9])

$$\left(\frac{\partial\mu}{\partial\sigma}\right)_{\theta_s} = -\epsilon v_p \quad , \quad \left(\frac{\partial\mu}{\partial\theta_s}\right)_{\sigma} = -\eta_p \quad , \tag{4.11}$$

where ϵ, v_p and η_p are the strain, volume and entropy per particle respectively. The phase transformation in most SMAs is primarily a shear process[10]. Therefore it is reasonable to assume that there is no volume change between the two phases, thus $[v_p] = 0$. Using this assumption alongwith Eq. 4.11,

Eq. 4.10 becomes

$$\left[\epsilon \frac{\partial \sigma}{\partial \theta_s}\right] = -[\eta] \qquad \text{at} \qquad x = x_s(t) \ , \tag{4.12}$$

where we have used the relation, $\eta = \eta_p/v_p$ in arriving at Eq.4.12. We shall refer to Eq.4.12 as the generalized Clausius-Clapeyron equation. The commonly used empirical relation of a one-to-one correspondence between the stress and temperature at the phase front (represented by the classical Clausius-Clapeyron equation) cannot be obtained. Note that if the Helmholtz free energy is completely characterized, so is the entropy, η, (second of Eq.4.8), and the Clausius-Clapeyron equation too (Eq.4.12). Experimentally tracking the 1D phase boundary motion to characterize a constitutive relation for phase boundary motion is thus not necessary. This 1D approach is useful not only in its own right but also as a precursor to a 2D generalization of the theory. In the next two sections, we give explicit forms of Eq.4.12 corresponding to two sample Helmholtz free energy functions.

A sixth order Helmholtz free energy polynomial

Based on the Landau-Devonshire theory of the phase transformations, Falk[6] suggested the following explicit definition of a sixth order Helmholtz free energy polynomial

$$\psi(\epsilon,\theta) = \alpha\epsilon^6 - \beta\epsilon^4 + (\delta\theta - \gamma)\,\epsilon^2 + \psi_0\,(\theta)\ \ , \tag{4.13}$$

where α, β, γ and δ are positive constants and $\psi_0\,(\theta)$ is the chemical free energy. For the special case of a material having identical material parameters, the chemical free energy can be derived from the definition of the heat capacity, C_ϵ, at constant strain[11] as

$$\psi_0\,(\theta) = C_\epsilon\theta\left(1 - ln\frac{\theta}{\theta_0}\right) + \bar{\psi}_0\ , \tag{4.14}$$

where we have assumed that C_ϵ is temperature-independent, θ_0 is referred as the equilibrium temperature (i.e. at which the driving force vanishes in absence of stress, or $f(0,\theta_0) = 0$) and $\bar{\psi}_0$ is a constant parameter. Using Eq.4.13, the explicit expressions for stress, entropy and internal energy (Eq.4.8) and the generalized Clausius-Clapeyron equation (Eq.4.12) as

$$\begin{aligned} &\sigma = 6\alpha\epsilon^5 - 4\beta\epsilon^3 + 2\,(\delta\theta - \gamma)\,\epsilon \quad , \quad \eta = -\delta\epsilon^2 + C_\epsilon ln\frac{\theta}{\theta_0}\ , \\ &u = \alpha\epsilon^6 - \beta\epsilon^4 - \gamma\epsilon^2 + C_\epsilon\theta + \bar{\psi}_0\ , \\ &\left[\epsilon\frac{\partial\sigma}{\partial\theta_s}\right] = \delta[\epsilon^2] \qquad \text{at} \qquad x = x_s(t)\ . \end{aligned} \tag{4.15}$$

A trilinear Helmholtz free energy function

In this section, we derive the explicit form of the generalized Clausius-Clapeyron equation based on Abeyaratne & Knowles's[3] formulation of the Helmholtz free energy function, which qualitatively is the trilinear approximation of the sixth order polynomial discussed in the previous section. The reader is referred to Abeyaratne and Knowles'[3] Eq.32 for the expression of the Helmholtz free energy that leads to the intermediate (unstable) portion of the σ-ϵ curve. The low strain and high strain segments of the trilinear Helmholtz free energy function can be collectively represented by

$$\psi = \frac{1}{2}E\left(\epsilon - \epsilon_T\right)^2 - E\alpha\left(\epsilon - \epsilon_T\right)\left(\theta - \theta_0\right) + C_\epsilon\theta\left(1 - ln\frac{\theta}{\theta_0}\right) + \lambda_T\left(\frac{\theta}{\theta_0} - 1\right) + \psi_0 \tag{4.16}$$

where E, α, C_ϵ and ψ_0 are the Young's modulus, coefficient of volumetric thermal expansion, heat capacity and a reference Helmholtz free energy respectively. These will take different values depending on whether the considered phase is austenite or martensite. As well, the parameters, ϵ_T and λ_T, will take the following phase-dependent values

$$\epsilon_T = \begin{cases} 0 & \text{Austenite} \\ \epsilon_{ph} & \text{Martensite} \end{cases}, \quad \lambda_T = \begin{cases} 0 & \text{Austenite} \\ \lambda_{ph} & \text{Martensite} \end{cases}, \tag{4.17}$$

in terms of the transformation strain, ϵ_{ph}, and the latent heat of phase transformation, λ_{ph}, respectively. Using Eq.4.16, the expressions for stress, entropy and internal energy (Eq. 4.8) and the generalized Clausius-Clayperon equation (Eq.4.12) follow as

$$
\begin{aligned}
&\sigma = E\left\{(\epsilon - \epsilon_T) - \alpha\,(\theta - \theta_0)\right\} \quad , \quad \eta = E\alpha\,(\epsilon - \epsilon_T) + C_\epsilon ln\frac{\theta}{\theta_0} - \frac{\lambda_T}{\theta_0} \ , \\
&u = \frac{1}{2}E(\epsilon - \epsilon_T)^2 + E\alpha\,(\epsilon - \epsilon_T)\,\theta_0 + C_\epsilon\theta - \lambda_T + \psi_0 \ , \\
&\left[\epsilon\frac{\partial\sigma}{\partial\theta_s}\right] = -\left[E\alpha(\epsilon - \epsilon_T)\right] - [C_\epsilon]\, ln\frac{\theta_s}{\theta_0} + \frac{[\lambda_T]}{\theta_0} \quad \text{at} \quad x = x_s(t) \ . \qquad (4.18)
\end{aligned}
$$

4.2.4 Second Law of Thermodynamics

The second law of thermodynamics stipulates that the rate of entropy production during a dissipative process like the phase transformation in SMA will always be non-negative, resulting in (Abeyaratne and Knowles[4])

$$
fV_s \geq 0 \quad , \quad \text{where} \quad f = [g] \quad \text{and} \quad g = \psi - \sigma\epsilon \ ; \qquad (4.19)
$$

The quantity, $[g]$, is the jump of the specific Gibbs free energy at the interface. Abeyaratne and Knowles [4] proposed a constitutive relation for V_s in such a way that Eq.4.19 is always satisfied. Since we do not make an explicit choice here, the inequality (Eq.4.19) should always be verified numerically.

4.3 The quasistatic, small strain approximation and the SMA hysteresis

4.3.1 The quasistatic, small strain approximation

While the formulation based on finite deformations and inertia is the complete one, often a practical and reasonable approach is the quasistatic, small strain approximation. However, the sequence of assumptions that lead from the complete to the approximate theory is not always obvious nor have we found those explicitly stated in the literature. We state these assumptions here clearly. These are: (i) uniform and identical density for both phases, i.e. $d\rho/dt = 0$ (refer Eq.4.4) (reasonable for most SMAs), (ii) negligible inertia, i.e. $|\rho_0 dV/dt| << |\partial\sigma/\partial X|$ (refer Eq.4.1), (iii) small particle velocity, V, such that $dV/dt \approx \partial V/\partial t$, (iv) small deformations such that $\partial\sigma/\partial X \approx \partial\sigma/\partial x$, (v) small deformation gradients (i.e. $\frac{\partial w}{\partial x} << 1$), using which, Eqs.4.3 and 4.7 can be used to show that $F \approx 1 + \epsilon$. With these assumptions, the conservation equations (Eqs.4.1, 4.2, 4.4) in the domain $(x \neq x_s(t))$ become

$$\frac{\partial\sigma}{\partial x} = 0 \quad \rightarrow \quad \sigma \equiv \sigma(t) \ , \ \frac{\partial q}{\partial x} + \sigma\frac{\partial\epsilon}{\partial t} + \rho_0 r = \frac{\partial u}{\partial t} \ , \ \frac{\partial V}{\partial x} = 0 \ . \quad (4.20)$$

The simplifications in the jump conditions are: (i) The small strain approximation ($F \approx 1 + \epsilon$) is invoked, such that $[F] = [\epsilon]$, (ii) the last of Eq.4.5 in the first of Eq.4.5 yields $[\sigma] = \rho_0 V_s^2 [F]$; we assume that the inertia term, $\rho_0 V_s^2 [F]$, is substantially smaller than the stress on either side of the phase boundary, i.e. $|\rho_0 V_s^2 [F]| << |\sigma(x_s^+, t)|, |\sigma(x_s^-, t)|$ where $x_s^+ = \lim_{\Delta \to 0} (x_s + \Delta)$, $x_s^- = \lim_{\Delta \to 0} (x_s - \Delta)$ and $\Delta > 0$. With this assumption, the jump in the stress at the phase boundary vanishes, i.e. $[\sigma] = 0$, (iii) the outcome of the assumption (ii) may be used to write the second of Eq.4.5 as $[q] = -([u] + \rho_0 [V^2]/2 - \sigma[F]) V_s$. We assume that the particle velocities are small enough such that $|\rho_0 [V^2]/2| << |\sigma[F]|$. To summarize, Eqs.4.5 reduce to

$$[\sigma] = 0 \quad , \quad [q] = (-[u] + \sigma[\epsilon]) V_s \quad , \quad [V] = -V_s [\epsilon] \ . \tag{4.21}$$

Eqs.4.20-4.21 constitute the quasistatic, small strain approximation. Note that the first of Eq.4.20 and 4.21 assure that the stress is spatially uniform. With this outcome, the generalized Clausius-Clapeyron equation reduces from Eq.4.12 to

$$\frac{\partial \sigma}{\partial \theta_s} = -\frac{[\eta]}{[\epsilon]} \qquad \text{at} \qquad x = x_s(t) \ , \tag{4.22}$$

from which one can derive a one-to-one correspondence between σ and θ_s for the phase front evolution. For the sixth order and trilinear Helmholtz free energy functions, the right hand side of Eq.4.22 has the following explicit forms

$$\frac{[\eta]}{[\epsilon]} = \begin{cases} -\delta\frac{[\epsilon^2]}{[\epsilon]} & \text{for a sixth order Helmholtz free energy polynomial} \\ \frac{[E\alpha(\epsilon-\epsilon_T)]}{[\epsilon]} + \frac{[C_\epsilon]}{[\epsilon]}\ln\frac{\theta_s}{\theta_0} - \frac{[\lambda_T]}{[\epsilon]\theta_0} & \text{for a trilinear Helmholtz free energy function} \end{cases} \tag{4.23}$$

The first of Eq.4.23 follows from Eq.4.15, and the second of Eq.4.23 follows from Eq.4.18. The σ vs. θ_s relation that follows from the integration of Eq.4.22 will be, in general, non-linear and therefore is qualitatively similar to experimental observations; see Horikawa et al.[1] for SMA single crystals and Shaw and Kyriakides[12] for SMA polycrystals. Eq.4.22 may be integrated for the $A \rightarrow M$ and the $M \rightarrow A$ transformation respectively as

$$\sigma_{A\rightarrow M}(\theta_s) = \sigma_0 - \int_{M_s(\sigma_0)}^{\theta_s} \frac{[\eta]}{[\epsilon]} d\tilde{\theta}_s \ , \quad \sigma_{M\rightarrow A}(\theta_s) = \sigma_0 - \int_{A_s(\sigma_0)}^{\theta_s} \frac{[\eta]}{[\epsilon]} d\tilde{\theta}_s \ , \tag{4.24}$$

where $M_s(\sigma_0)$ and $A_s(\sigma_0)$ are the start temperatures for the A → M and the M → A transformations respectively, at the stress, σ_0. For a material with a trilinear Helmholtz free energy function and identical material properties for both phases, Eq.4.18 may be written as $[\sigma] = E\{[\epsilon - \epsilon_T] - \alpha[\theta - \theta_0]\}$ at the phase boundary; this equation simplifies to $[\epsilon - \epsilon_T] = 0$ (or $[\epsilon] = [\epsilon_T]$) due to the first of Eq.4.9 and the first of Eq.4.21. Therefore, the second of Eq.4.23

reduces to

$$\frac{\partial \sigma}{\partial \theta_s} = \frac{\lambda_{ph}}{\epsilon_{ph}\theta_0} \qquad \text{at} \qquad x = x_s(t) \ . \tag{4.25}$$

Eq.4.25 is a linear σ vs. θ_s relation and, in that sense, such an outcome is similar to Bruno et al.'s[5] approach (see Eq.8 of their paper). They propose that the linear stress-temperature equation be determined directly from experiments. The difference is that in our case, the right hand side of Eq.4.25 is already known as long as the material parameters of Eq.4.16 are known.

4.3.2 The SMA hysteretic response

The SMA response during a closed cycle of thermomechanical loading is hysteretic. The resulting entropy generation, Γ_s, for the entire bar is [4]

$$\Gamma_s = A \oint \frac{f V_s}{\theta_s} dt \ , \tag{4.26}$$

where A is the area of cross-section of the 1D bar under consideration. While an explicit evaluation of Eq.4.26 is not possible in general, it reduces to simple explicit expressions, derived below for a SMA with a trilinear Helmholtz free energy function and identical material properties (i.e. $[E] = 0$, $[\alpha] = 0$, $[C_\epsilon] = 0$) during a – (i) constant temperature, stress-induced phase transformation, and (ii) constant stress, temperature-induced phase transformation. These outcomes will now be demonstrated for a 1D bar with length, L, having a phase distribution where austenite always exists in the domain, $0 \leq x < x_s(t)$, and martensite exists in the remainder of the bar. Even if the phase distribution was reversed, the outcome of the analysis will remain unchanged. The driving force, f, follows from Eqs.4.16, 4.18 and 4.19 as

$$f = -\sigma\epsilon_{ph} + \lambda_{ph}\left(\frac{\theta_s}{\theta_0} - 1\right) , \tag{4.27}$$

whereas Eqs.4.24 result in

$$\sigma_{A\to M}(\theta_s) = \frac{\lambda_{ph}}{\theta_0\epsilon_{ph}}(\theta_s - M_s^0) \quad , \quad \sigma_{M\to A}(\theta_s) = \frac{\lambda_{ph}}{\theta_0\epsilon_{ph}}(\theta_s - A_s^0) \, . \tag{4.28}$$

Constant temperature, stress-induced phase transformation

Consider the pseudoelastic response of the 1D bar initially in a fully austenitic state and at an uniform temperature, identical to that of the environment. We shall also assume that the temperature of the environment, θ_{amb}, is greater than A_s^0 (to assure a pseudoelastic response on loading and unloading). At all times, the deformation rate is slow enough such that the temperature of the bar practically does not change from that of the environment, θ_{amb}; thus, $\theta(x,t) \approx \theta_{amb}$, and therefore $\theta_s \approx \theta_{amb}$. Note that Eq.4.27 and the first of Eq.4.28 can be used to demonstrate that $f = \lambda_{ph}(M_s^0/\theta_0 - 1)$

and $f = \lambda_{ph}(A_s^0/\theta_0 - 1)$ during the $A \rightarrow M$ and $M \rightarrow A$ transformations respectively. As well, Eq.4.19 dictates that $V_s < 0$ during the $A \rightarrow M$ transformation (since $f < 0$) and vice-versa. Thus, Eq.4.26 becomes $\Gamma_s \theta_{amb}/A = f_{A\rightarrow M}\int_L^0 dx_s + f_{M\rightarrow A}\int_0^L dx_s$. This outcome, along with Eq.4.28, results in the specific entropy

$$\frac{\Gamma_s}{AL} = \frac{[\sigma_{A\rightarrow M}(\theta_{amb}) - \sigma_{M\rightarrow A}(\theta_{amb})]\, \epsilon_{ph}}{\theta_{amb}}, \tag{4.29}$$

in terms of the specific mechanical work done on the bar (numerator on right of Eq.4.29); it is identical to the area enclosed by the closed loop of an isothermal, pseudoelastic uniaxial stress-overall strain curve of the SMA bar. Note that if $M_s^0 = A_s^0$, it implies that $\sigma_{A\rightarrow M}(\theta_{amb}) = \sigma_{M\rightarrow A}(\theta_{amb})$ (by Eq.4.28), and the specific entropy (and hence the dissipation) vanishes.

Constant stress, temperature-induced phase transformation

Consider a SMA bar initially in a fully martensite state, subjected to a constant stress, σ_{amb} ($< \sigma_{M\rightarrow A}(\theta_{amb})$) and at an initially uniform temperature identical to that of the environment, θ_{amb}. This restriction guarantees that the $M \rightarrow A$ transformation will not set in at the chosen initial stress and temperature, σ_{amb} and θ_{amb}, respectively. The temperature of the environment is gradually raised until the $M \rightarrow A$ transformation is complete and then decreased until the $A \to M$ transformation is complete. At all times, the temperature rate (at which the environmental temperature is changed) is kept low enough so that temperature gradients along the bar are also low, to the extent that $\theta(x,t) \approx \theta_{amb}$, and therefore $\theta_s \approx \theta_{amb}$, is an excellent approximation. Within this context, Eqs.4.26-4.28 reduce to

$$\frac{\Gamma_s}{AL} = \lambda_{ph} \left(\frac{\frac{A_s^0}{\theta_0} - 1}{M_s^0 + \frac{\sigma_{amb}\theta_0\epsilon_{ph}}{\lambda_{ph}}} - \frac{\frac{M_s^0}{\theta_0} - 1}{A_s^0 + \frac{\sigma_{amb}\theta_0\epsilon_{ph}}{\lambda_{ph}}} \right) , \tag{4.30}$$

The specific entropy (Eq.4.30), and hence the dissipation, vanishes when $M_s^0 = A_s^0$.

4.4 Results and Discussion

In this section, we use the theory to predict two experiments: (i) stress-induced phase transformation at constant deformation rate of a SMA single crystal uniaxial test specimen, and (ii) constant stress, temperature-induced phase transformation of a SMA polycrystal wire. The boundary value problems (BVPs) corresponding to both experiments are based on the quasistatic, small strain approximation with a trilinear Helmholtz free energy function. The governing equations reduce from the second of Eq.4.20 and the second of Eq.4.21

$$
\begin{aligned}
k\frac{\partial^2\theta}{\partial x^2} - \alpha\theta\frac{\partial\sigma}{\partial t} - \frac{h_L P}{A}(\theta - \theta_{amb}) + \rho_E J^2 = \left(C_\epsilon + E\alpha^2\theta\right)\frac{\partial\theta}{\partial t}\ , \\
-\left[k\frac{\partial\theta}{\partial x}\right] = -\left(\frac{1}{2}\left[E(\epsilon - \epsilon_T)^2\right] + \left[E\alpha\left(\epsilon - \epsilon_T\right)\right]\theta_0\right)V_s - \\
\left(\left[C_\epsilon\right]\theta_s - \left[\lambda_T\right] - \sigma[\epsilon]\right)V_s\ , \qquad (4.31)
\end{aligned}
$$

for a trilinear free energy function and either of Eq.4.24. Note that the heat source term $(\rho_o r)$ in the second of Eq.4.20 has been replaced by the third and fourth term on the left side of the first of Eq.4.31. The third term represents the heat that is exchanged between the environment and the SMA specimen along its length whereas the fourth term represents the fact that the $M \rightarrow A$ transformation may be driven by electrical (or joule) heating. The parameter, h_L, is a convection coefficient, P and A are the perimeter and the area of the specimen cross-section respectively, ρ_E is the electrical resistivity of the considered phase and J is the density of the electrical current, I, flowing along the length of the specimen (defined as $J = I/A$). The mechanical boundary conditions are now given. The left end of the bar is always taken to be fixed (thus excluding rigid body displacements) and, motivated by the experiments to be modeled, either one of two boundary conditions (deformation or load control) will be imposed at $x = L$. These are

$$w(0,t) = 0 \quad , \quad \dot{w}(L,t) = \dot{w}_L(t) \quad \text{or} \quad \sigma(L,t) = \sigma_L(t) \; . \tag{4.32}$$

An adiabatic boundary condition and a temperature-dependent linear boundary condition are taken at $x = 0$ and $x = L$ respectively, i.e.

$$q(0,t) = 0 \quad , \quad q(L,t) = -h_B(\theta(L,t) - \theta_{amb}) \; . \tag{4.33}$$

The initial conditions are taken as

$$\sigma(0) = \sigma^I \quad , \quad \theta(x,0) = \theta^I(x) \quad , \quad x_s(0) = x_s^I \; , \tag{4.34}$$

where σ^I, $\theta^I(x)$ and x_s^I are parameters to be specified for a given simulation. The first and second of Eq.4.32 are invoked for the first BVP whereas the first and third of Eq.4.32 are invoked for the second BVP. The BVPs are solved using a moving boundary finite element method (MBFEM)-based numerical approach outlined in Chapter 2 [8].

The uniaxial stress-strain response during a phase transformation of a Copper-Aluminium-Nickel (CuAlNi) single crystal from the β_1 austenitic phase to the γ_1' martensitic phase [1] is modeled here. The mass percent of Aluminium and Nickel are 14.1 and 3.9 respectively. The specimen is 2 cm. in length with a rectangular cross-section (2 mm. by 3 mm.). The numerical approach to address this problem is summarized in the flowcharts of Figs. 4.2 and 4.3 respectively. Note that the parameter, σ_k, used in these figures represent the value of $\sigma(t)$ at the end of the kth time increment of the temporal discretization (a similar correspondence for the remaining parameters in the flow charts is implied). Three sets of experiments have been modeled and in all these cases, the initial conditions (Eq.4.34) of the problem are taken as $\sigma^I = 0$, $\theta^I(x) = 282$ K (Fig. 4.4), 274 K (Fig. 4.5), 243 K (Fig. 4.6) and $x_s^I = 0$. Based on the experimental data, the Young's modulus was taken to be identical for both phases. All necessary material, geometric, numerical and input parameters of the problem have been summarized in Table 4.1. Among the necessary parameters given in Table 4.1, a total of five had to be determined - these are h_L, h_B, E and k (for both phases). Ideally, the determination of five parameters from a limited set of experimental data often turns out to be a non-trivial optimization problem. For simplicity, we have set $h_B = 0$ (a reasonable assumption for end grips in a laboratory experiment) and determined by trial and error a combination of the remaining four parameters that gave a reasonable *simulation* of the $\sigma - \epsilon$ curve at $\theta_{amb} = 282\ K$. This has been shown in Fig. 4.4. With the determined parameters, the *predictions* of the single crystal SMA pseudoelastic response at $\theta_{amb} = 274\ K$ and the shape memory response at $\theta_{amb} = 243\ K$ have been shown in Figs. 4.5 and 4.6 respectively. A common feature in the results is the failure of the model to capture stress peaks during loading (Figs. 4.4, 4.5 and 4.6) and the valleys during unloading (Figs. 4.4 and 4.5). These features in the experimental data are believed to be due to the relative absence of defects in a single crystal as opposed to a polycrystal [13]. Defects act as sites for local stress concentration; thus, for example, a relative absence of defects will make it difficult for the $A \to M$ transformation to initiate (and hence the stress peak during the loading process). These peaks are usually not observed in polycrystals. In the context of the current model, the implication is that one will have to come up with a Helmholtz free energy function that reflects the stress peaks (and valleys) for stress-induced transformations more appropriately.

Next, we model the temperature-time response during a cycle of heating and cooling of a polycrystalline Nickel-Titanium (NiTi) SMA wire subjected to a constant load of 2 kg (and the stress will be assumed to be constant and spatially uniform). The material properties are given in Table 4.1, and the Clausius-Clapeyron equation is linear (Eq.4.25). With a constant stress, Eqs.4.25 will give the constant temperature, θ_s, at which the phase boundary needs to be at, for the $A \rightarrow M$ or the $M \rightarrow A$ phase transformation to occur. Due to this reason, the numerical approach is considerably simpler. The issue reduces to the determination of the velocity, V_s, of the phase boundary during either transformation. At every time instant, the spatial temperature profile in either phase can be calculated separately using the first of Eq.4.31 since θ_s is known and then the second of Eq.4.31 is used to calculate V_s. Further details of the numerical approach are not being given here for brevity. The experiment, reported by Faulkner, Amalraj and Bhattacharyya[2], was done in air while the SMA wire was exposed to free convection. The heating of the wire was done electrically. The electrical current was switched off during the cooling portion of the cycle and the free convection of air was allowed to cool the wire back to the ambient temperature. The experiment was carried out to reasonably ensure the symmetry of the problem about the center of the wire. It is at the center that the origin of the 1D co-ordinate system is taken. All necessary parameters are given in Table 4.1. The initial conditions (Eqs.4.34) for this problem are taken as $\sigma^I = 173.86$ MPa, $\theta^I(x) = 294\ K$ and $x_s^I = L$. The first and third of Eq.4.32 represent the mechanical boundary conditions (where we set $\sigma_L(t) = 173.86$ MPa). Since the material state of a SMA wire is usually non-uniform during a phase transformation, Faulkner, Amalraj and Bhattacharyya[2] developed experimental procedures to determine the thermal conductivity and electrical resistivity of the austenite and martensite phase of the SMA wire. The heat capacities of either phase were determined using a differential scanning calorimeter (DSC) experiment. The experimental data given in Fig. 4.7 was not used by Faulkner, Amalraj and Bhattacharyya[2] in the determination of the phase-dependent material properties; hence, any model that uses their properties to predict the data in Fig. 4.7 (discussed in the next paragraph) is truly a prediction.

The temperature, $\theta(0,t)$, of the wire at its center, $x = 0$, is given with respect to time, t, in Fig. 4.7; the experimental data points have been shown as the "squares". Notice the distinctive "plateaus" in the experimental curve during the heating and cooling. Each plateau corresponds to the latent heat evolution during the phase transformation. An obvious item of interest is that the phenomenological model (dotted line) predicts the experiment far better than the current sharp phase front-based model (solid line); especially, notice how "well" the plateaus have been modeled by the phenomenological model. This contrast is due to a fundamental difference in the way the conservation of energy is written in the two models. We shall high-light this difference for the special case of a SMA with identical material properties undergoing a thermally induced transformation at constant stress ($\partial\sigma/\partial t = 0$). After invoking these assumptions, the second of Eq.4.31 is incorporated into the first of Eq.4.31 using a delta function, $\delta(x - x_s)$, defined as $\int_{-\infty}^{+\infty} \delta(x - x_s)g(x)dx = g(x_s)$, where $g(x)$ is any arbitrary function. Further, approximating $E\alpha^2\theta \approx E\alpha^2\theta_0$, "order-of-magnitude" calculations show that $C_\epsilon/(E\alpha^2\theta_0) \approx 3902$ (using austenitic values for material parameters). As a consequence, we write

$$k\frac{\partial^2\theta}{\partial x^2} + \rho_0 r = C_\epsilon\frac{\partial\theta}{\partial t} + (\lambda_{ph} + \sigma\epsilon_{ph})\, V_s\ \delta(x - x_s)\ . \tag{4.35}$$

On the other hand, Lagoudas, Bo and Bhattacharyya [14] represent the material state using an internal variable known as the martensite volume fraction, ξ $(= \lim_{\Delta V\to 0} \Delta V_M/\Delta V)$ where ΔV is the volume of material around a continuum point and ΔV_M is the component of ΔV that is in the martensitic state. For the current problem, their conservation of energy reduces to[14]

$$k\frac{\partial^2\theta}{\partial x^2} + \rho_0 r = C_\epsilon\frac{\partial\theta}{\partial t} - \lambda_{ph}\frac{\partial\xi}{\partial t}\ , \tag{4.36}$$

where the last term, $\partial\xi/\partial t = -p(\theta)\partial\theta/\partial t$ for $(\partial\theta/\partial t > 0)$ and $\partial\xi/\partial t = g(\theta)\partial\theta/\partial t$ for $(\partial\theta/\partial t < 0)$. The functions, $p(\theta)$ and $g(\theta)$, can be determined from DSC measurements of the latent heat evolution in a stress-free SMA undergoing the $M \rightarrow A$ and the $A \rightarrow M$ transformation respectively. Now compare Eqs.4.35 and 4.36. Both are identical except the second term on the right side of either equation. Thus, these terms are responsible for the significant contrast in the predictions by the phenomenological model and the current sharp phase-front model based on the trilinear Helmholtz free energy function. An improvement in the predictions of both sets of experimental data by the current theory may be attempted by using candidate Helmholtz free energy functions other than the trilinear one.

4.5 Conclusions

In this chapter, a one-dimensional (1D) sharp phase front-based theoretical framework for shape memory alloys has been given. The assumption of an equality of the chemical potential at the interface leads to a generalized Clausius-Clapeyron equation. The theoretical framework is general enough to incorporate any Helmholtz free energy function, and if this function is completely characterized, then so is the system of equations including the condition for the evolution of the phase front. The small strain, quasistatic approximation of the general framework in conjunction with a trilinear Helmholtz free energy function has been used to predict the following two experiments: (i) Constant deformation-rate phase transformation in a SMA single crystal, and (ii) Constant load, temperature-induced transformation in a SMA polycrystalline wire.

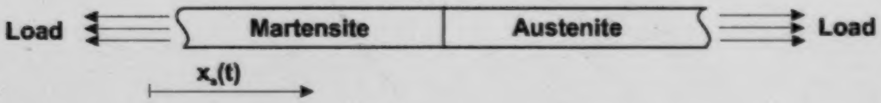
Load
Martensite
Austenite
Load
$x_s(t)$

Figure 4.1: A schematic of the spatially one-dimensional (1D) phase transformation.

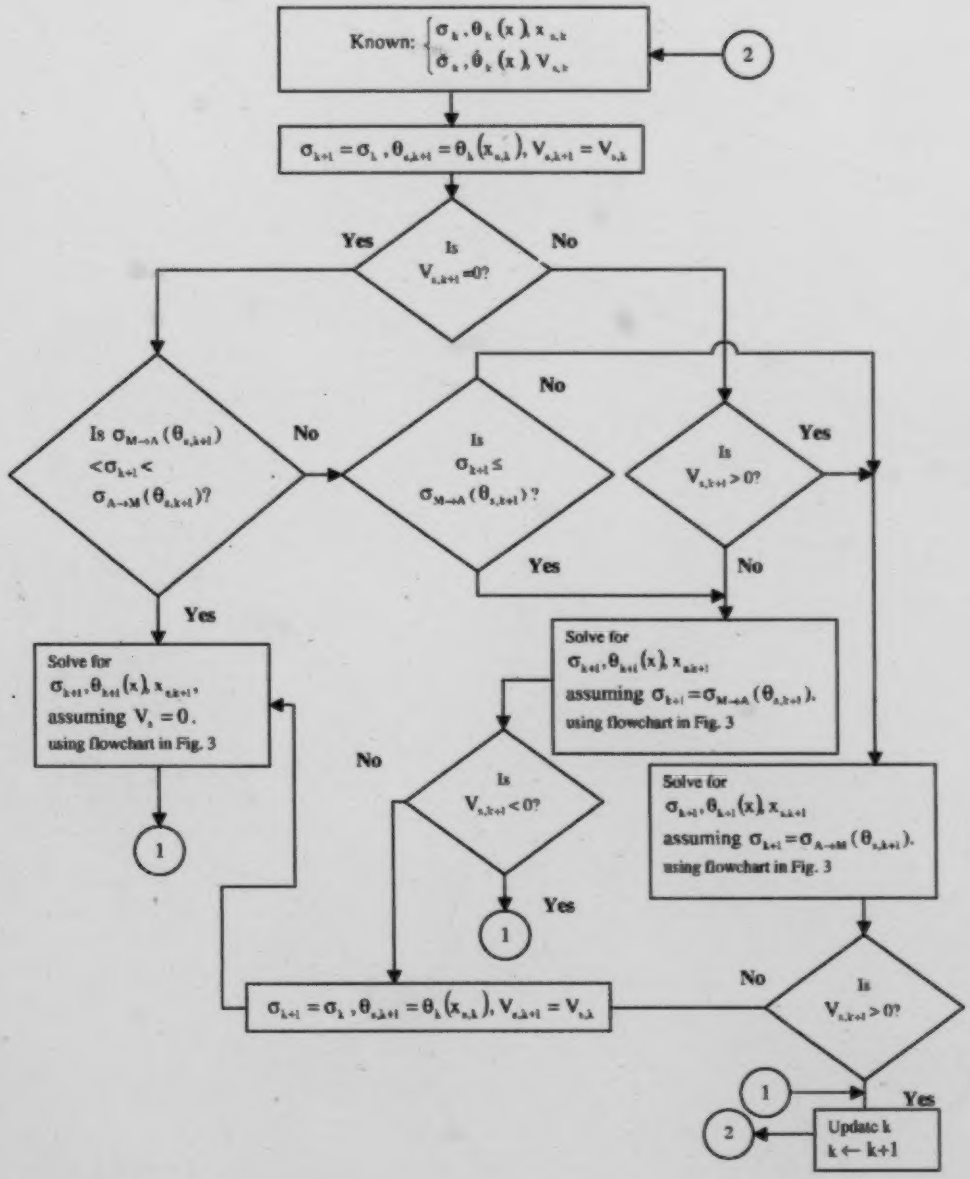

Known: $\sigma_k, \theta_k(x), x_{s,k}$; $\dot{\sigma}_k, \dot{\theta}_k(x), V_{s,k}$
2
$\sigma_{k+1} = \sigma_k, \theta_{s,k+1} = \theta_k(x_{s,k}), V_{s,k+1} = V_{s,k}$
Is $V_{s,k+1} = 0$?
Yes
No
Is $\sigma_{M \to A}(\theta_{s,k+1}) < \sigma_{k+1} < \sigma_{A \to M}(\theta_{s,k+1})$?
No
Is $\sigma_{k+1} \le \sigma_{M \to A}(\theta_{s,k+1})$?
No
Yes
Is $V_{s,k+1} > 0$?
Yes
No
Yes
Solve for $\sigma_{k+1}, \theta_{k+1}(x), x_{s,k+1}$, assuming $V_s = 0$. using flowchart in Fig. 3
1
Solve for $\sigma_{k+1}, \theta_{k+1}(x), x_{s,k+1}$ assuming $\sigma_{k+1} = \sigma_{M \to A}(\theta_{s,k+1})$. using flowchart in Fig. 3
No
Is $V_{s,k+1} < 0$?
Yes
1
Solve for $\sigma_{k+1}, \theta_{k+1}(x), x_{s,k+1}$ assuming $\sigma_{k+1} = \sigma_{A \to M}(\theta_{s,k+1})$. using flowchart in Fig. 3
$\sigma_{k+1} = \sigma_k, \theta_{s,k+1} = \theta_k(x_{s,k}), V_{s,k+1} = V_{s,k}$
No
Is $V_{s,k+1} > 0$?
Yes
1
2
Update k
k ← k+1

Figure 4.2: The decision-making process based on which either of Eq. 4.24 is used.

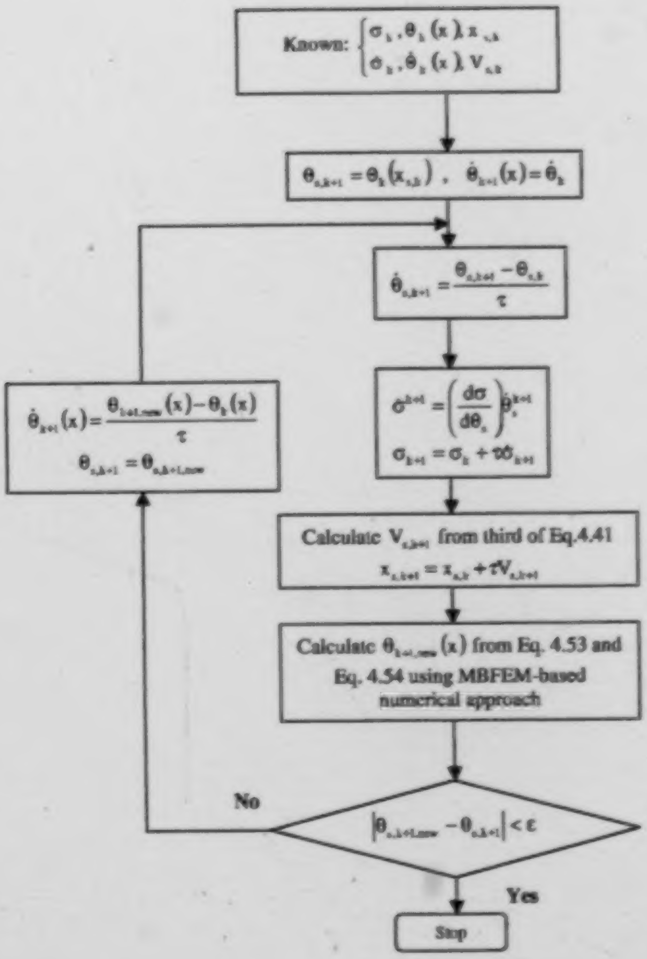

Known:
Calculate $V_{s,k+1}$ from third of Eq.4.41
Calculate $\theta_{k+1,new}(x)$ from Eq. 4.53 and Eq. 4.54 using MBFEM-based numerical approach
No
Yes
Stop

Figure 4.3: The flowchart in Fig. 4.2 requires the calculation of the field variables using the MBFEM-based numerical approach. This calculation is summarized in this flowchart.

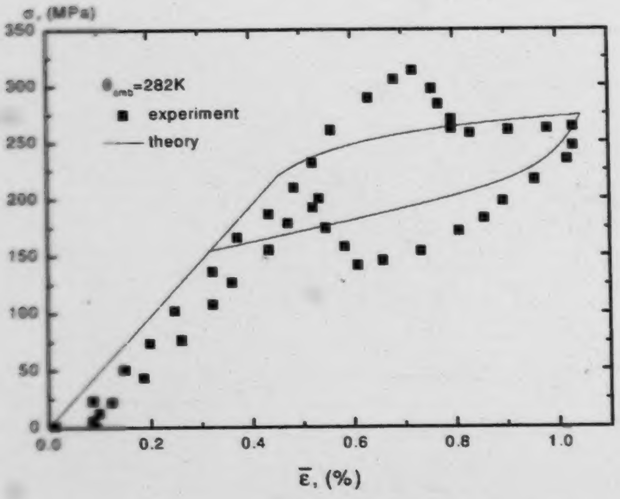

Figure 4.4: Simulation of an experimental pseudoelastic stress-strain curve of a CuAlNi single crystal, uniaxial test specimen tested at $\theta_{amb} = 282K$ [1].

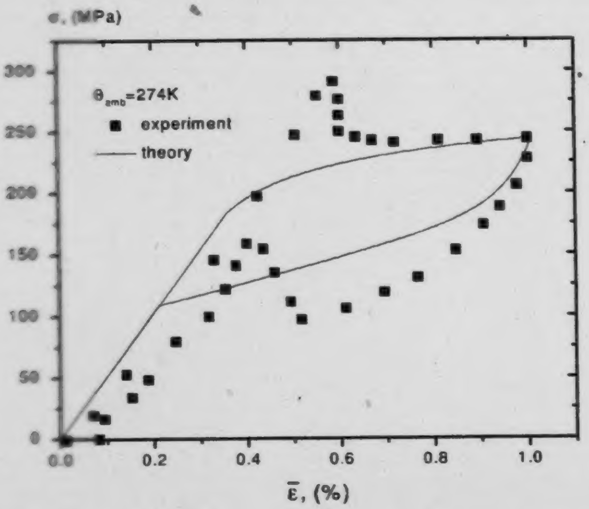

Figure 4.5: Prediction of an experimental pseudoelastic stress-strain curve of a CuAlNi single crystal, uniaxial test specimen tested at $\theta_{amb} = 274K$ [1].

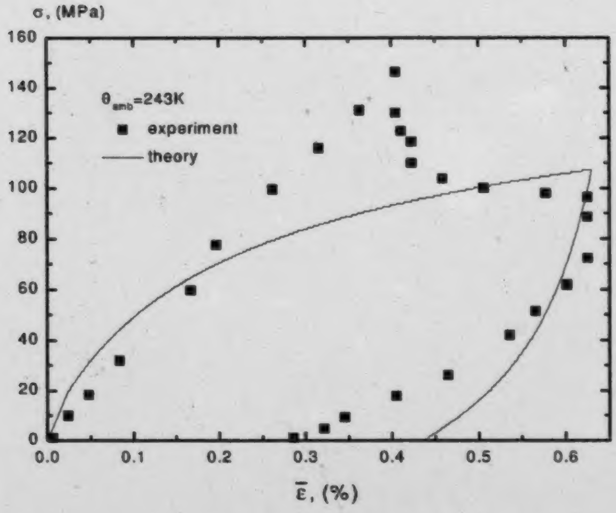

Figure 4.6: Prediction of an experimental shape memory stress-strain curve of a CuAlNi single crystal, uniaxial test specimen tested at $\theta_{amb} = 243K$ [1].

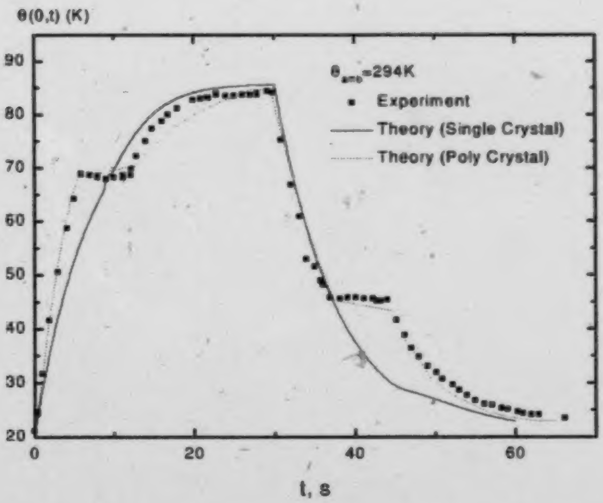

Figure 4.7: Prediction of the temperature-time response at the center of a NiTi SMA polycrystalline wire undergoing a thermal transformation while subjected to a constant load [2].

Parameter	Symbol	NiTi Polycrystalline wire		CuAlNi Single crystal specimen	
		Value	Ref.	Value	Ref.
Length	L	0.08m	[15]	0.02m	[1]
Perimeter of the cross-section	P	0.0012m	[15]	0.001m	[1]
Area of the cross-section	A	$1.14 \times 10^{-7} m^2$	[15]	$0.003 \times 0.003 m^2$	[1]
Mass density	ρ_0	$6450 kg/m^3$	[11]	$7120 kg/m^3$	[16]
Heat capacity	$C_{Austenite}$	$5.92 \times 10^6 J/(m^3 K)$	[15]	$2.797 \times 10^6 J/(m^3 K)$	[17]
	$C_{Martensite}$	$4.50 \times 10^6 J/(m^3 K)$	[15]	$2.819 \times 10^6 J/(m^3 K)$	[17]
Coefficient of thermal expansion	α	$10^{-5} K^{-1}$	[11]	$10^{-5} K^{-1}$	[11]
Young's modulus	E	$51.6 GPa$	[11]	$47.5 GPa$	*
Uniaxial phase transformation strain	ϵ_{ph}	0.06	[15]	0.06	[1]
Latent heat of phase transformation	λ_{ph}	$0.121 GJ/m^3$	[15]	$0.063 GJ/m^3$	[18]
Thermal conductivity	$k_{Austenite}$	$14 W/(mK)$	[15]	$43 W/(mK)$	*
	$k_{Martensite}$	$28 W/(mK)$	[15]	$30 W/(mK)$	*
Equilibrium temperature	θ_0	$326.4 K$	[15]	$217.5 K$	[1]
Ambient temperature	θ_{amb}	$294 K$	[15]	$282 K$, $274 K$, $343 K$	[1]
Convective coefficients	h_L	$77 W/(m^2 K)$	[15]	$110 W/(m^2 K)$	*
	h_b	$450 W/(m^2 K)$	[15]	0	*
Applied load	σ_L	$173.86 MPa$	[15]	-	-
Applied deformation rate	$\dot{u}$	-	-	$8.4 \times 10^{-6} m/s$	[1]
Electric current	I	0.9	[15]	-	-
Electrical resistivity	$\rho E_{Austenite}$	$8.371 \times 10^{-4} \Omega mm$	[15]	-	-
	$\rho E_{Martensite}$	$9.003 \times 10^{-4} \Omega mm$	[15]	-	-
Time increment	τ	$8.1 \times 10^{-4} s$	-	$3.2 \times 10^{-4} s$	-
Number of elements	N	110	-	144	-
Tolerance	ϵ_{tol}	10^{-5}	-	10^{-5}	-

Table 4.1: List of material, geometric, numerical and input parameters. The symbol, '*', indicates that the corresponding parameters follow from the simulation in Fig. 4.4

Bibliography

[1] H. Horikawa and S. Miyazaki, "Orientation dependence of $\beta_1 \rightarrow \beta_1'$ stress-induced martensitic transformation in Cu-Al-Ni alloy," *Metallurgical Transaction A* **19**, pp. 915–923, 1988.

[2] M. G. Faulkner, J. J. Amalraj, and A. Bhattacharyya, "Experimental determination of thermal and electrical properties of ni-ti shape memory wires," *Smart Mater. Struct.* **9**, pp. 632–639, 2000.

[3] R. Abeyaratne and J. Knowles, "A continuum model of a thermoelastic solid capable of undergoing phase transitions," *J. Mech. Phys. Solids* **41**, pp. 541–571, 1993.

[4] R. Abeyaratne and J. Knowles, "On the driving traction acting on the surface of strain discontinuity in a continuum," *J. Mech. Phys. Solids* **38**, pp. 345–360, 1990.

[5] O. P. Bruno, P. H. Leo, and F. Reitich, "Free boundary conditions at austenite-martensite interfaces," *Phys. Rev. Lett.* **74**, pp. 746–749, 1995.

[6] F. Falk, "Model free energy, mechanics , and thermodynamics of shape memory alloys," *Acta Metallurgica* **28**, pp. 1773–1780, 1980.

[7] P. H. Leo, T. W. Shield, and O. P. Bruno, "Transient heat transfer effects on the pseudoelastic behavior of shape memory alloy wires," *Acta Metallurgica Materialia* **41**, pp. 2477–2485, 1993.

[8] V. Stoilov, O. Iliev, and A. Bhattacharyya, "A moving boundary finite element method-based approach for the solution of one-dimensional problems in shape memory alloys," *Computer Methods in Applied Mechanics and Engineering* **190**, pp. 1741–1762, 2000.

[9] L. D. Landau and E. M. Lifshitz, *Statistical physics*, Oxford University, New York, 1990.

[10] K. Bhattacharyya and R. Kohn, "Symmetry, texture and recoverable strain of shape-memory alloy polycrystals," *Acta Metallurgica Materialia* **44**, pp. 529–542, 1995.

[11] S. Kim, "A continuum model for phase transitions in thermoelastic solids and its application to shape memory alloys," *PhD thesis, MIT, USA* , 1995.

[12] J. A. Shaw and S. Kyriakides, "Thermomechanical aspects of NiTi," *J. Mech. Phys. Solids* **43**, pp. 1243–1281, 1995.

[13] S. Miyazaki and C. Wayman, "The r-phase transition and associated shape memory mechanism in ti–ni single crystals," *Acta Metallurgica* **36**, pp. 181–192, 1988.

[14] D. C. Lagoudas, Z. Bo, and A. Bhattacharyya, "A thermodynamic constitutive model for gradual phase transformation of sma materials," *Proc. Math and Control in Smart Structures* **2715**, pp. 482–493, 1996.

[15] J. Amalraj, "Effect of the variable material properties on purely thermal phase transformation in shape memory alloys wire-modeling and experiments," *MSc thesis, University of Alberta, Canada* , 1999.

[16] T. Duerig, K. Meiton, D. Stockel, and C. Wayman, *Engineering aspects of shape memory alloys*, Butterworth-Heinemann, New York, 1990.

[17] Q. Jiang, J. Li and J. Tong, "C_p measurements around the martensitic transformation temperature of CuAlNi alloy," *Mat. Science and Engineering A* **196**, pp. 165–169, 1995.

[18] R. Salzbrenner and M. Cohen, "Thermodynamics of thermoelastic martensitic transformations," *Acta Metallurgica* **27**, pp. 739–748, 1979.

Chapter 5

A Three-dimensional Theoretical Framework for Sharp Phase Fronts in Shape Memory Alloys

5.1 Introduction

The theory presented here is a natural extension of the 1D theory developed in Chapter 4. The suggested theoretical framework is based on three main components: conservation laws, constitutive equations and continuity of the chemical potential on the interface between the different phases. The conservation laws represent the fundamental balance relations valid for any physical system undergoing fist order phase transformation. The constitutive equations introduce the characteristics of the specific material into the model. The combination of the conservation laws and the constitutive equations is the basis of all known theoretical models of phase transformations in thermoelastic solids. However, as it was shown by Abeyaratne and Knowles [2], a model based only on conservation laws and constitutive relations do not render a unique solution of the phase transformation problem. Different approaches have been suggested to complete the model.

Abeyaratne and Knowles[3, 4] suggested the introduction of a semiempirical relation between the phase boundary velocity and the intensive thermodynamical quantities(stress, temperature). The semiempirical nature of the approach requires fitting experimental data. An alternative to the Abeyaratne and Knowles' approach was developed by Bruno,Leo and Reitich[5]. They completed the model with an experimentally determined relation between the stress and phase transformation temperature. Both approaches, although applied successfully to 1D problems, are practically inapplicable to problems in two and three dimensions. The third component of the model is the introduction of the continuity of the chemical potential on the phase boundary - representing an equilibrium condition in systems close to phase equilibrium. This formulation of the model renders a complete description of the physical problem of the first order phase transformations. The formulation is general enough to accept any form of constitutive equation.

In the following section we present a detailed derivation of the general 3D theory of phase transformation. Later the derived model will be applied to 2D problem of biaxial loading of SMA thin film and the simulation results will be compared to the experimental data obtained by Fang et. al. [1] for similar system. In the chapter we also introduce a description of a novel numerical algorithm developed for the implementation of the proposed model to the 2D problem. The developed algorithm is based on 2D FEM for solving the coupled thermo-mechanical problem. The algorithm is second order accurate in time and space. The phase front tracking is accomplished by constant update of the spatial discretization(mesh) and the computational data is transferred from the "old" mesh to the "new" mesh by non-oscillatory 2D interpolation. The accuracy and stability of the suggested algorithm were validated by comparing the results of the simulations to two thermal and one mechanical test problems with analytical solution.

5.2 The 3D theory for sharp phase fronts in shape memory alloys

5.2.1 Conservation laws and entropy production

Consider a body occupying the region $R(t)$ at time, t; see Figure 5.1. Tractions and displacements are prescribed on the surface of the body. Further, $S_p(t)$ is a regular surface in $R(t)$ across which thermomechanical and kinematic quantities may be discontinuous. The conservation laws for all particles not on $S_p(t)$ are listed below. The conservation of mass is

$$\dot{\rho} + \rho \, div \, \mathbf{v} = 0 \,, \tag{5.1}$$

where ρ is the mass density in the deformed configuration. The conservation of linear momentum is

$$div \, \mathbf{T_R} + \mathbf{b} = \rho \dot{\mathbf{v}}, \tag{5.2}$$

where $\mathbf{T_R}$ is the first Piola-Kirchhoff stress tensor and $\mathbf{b}$ is the body force. The conservation of angular momentum is

$$\mathbf{T_R}\mathbf{F}^\mathbf{T} = \mathbf{F}\mathbf{T}_\mathbf{R}^\mathbf{T}, \tag{5.3}$$

where **F** is the deformation gradient tensor. The conservation of energy is

$$tr(\mathbf{T_R}\dot{\mathbf{F}}) + div\ \mathbf{q} + \rho r = \dot{u}, \tag{5.4}$$

where **q** is the heat flux vector, r is the heat source per unit mass and u is the specific internal energy per unit volume of the reference configuration. The deformation gradient tensor , **F**, is defined as

$$\mathbf{F} = \mathbf{1} + \nabla \otimes \mathbf{w}, \tag{5.5}$$

where **w** is the displacement vector of a particle. The jump discontinuities in mass, linear momentum, energy and deformation gradient across $S_p(t)$ are given by [4]

$$[[\mathbf{v}]] = -V_n[[\mathbf{F}]]\mathbf{n}, \tag{5.6}$$

$$[[\mathbf{T_R}\mathbf{n}]] = -\rho[[\mathbf{v}]]V_n, \tag{5.7}$$

$$[[\mathbf{q}\cdot\mathbf{n}]] = -[[\mathbf{v}\cdot\mathbf{T_R}\mathbf{n}]] - \left[\left[u + \frac{1}{2}\rho|\mathbf{v}|^2\right]\right] V_n, \tag{5.8}$$

$$[[\mathbf{F}]]\mathbf{m} = 0, \tag{5.9}$$

where $[[*]]$ indicates a jump, V_n is the normal component of the interface velocity, and **n** and **m** are normal and tangential vectors at a given location on $S_p(t)$.

Any dissipative process will result in entropy production. The Clausius-Duhem inequality away from $S_p(t)$ is given by

$$div\left(\frac{\mathbf{q}}{\theta}\right) + \frac{\rho r}{\theta} \leq \dot{\eta}, \tag{5.10}$$

where θ is the temperature and η is the specific entropy. The jump in specific entropy across $S_p(t)$ has to satisfy the inequality

$$[[\eta]] \leq -\frac{1}{V_n}\left[\left[\frac{\mathbf{q}\cdot\mathbf{n}}{\theta}\right]\right]. \tag{5.11}$$

5.2.2 Constitutive equations

Based on a specific Helmholtz free energy function, ψ

$$\psi \equiv \psi(\mathbf{F}, \theta), \tag{5.12}$$

the constitutive relations for the stress, specific entropy and internal energy follow as

$$\mathbf{T_R} = \partial_{\mathbf{F}}\psi \ \ , \ \ \eta = -\partial_\theta\psi \ \ , \ \ u = \psi + \theta\eta. \tag{5.13}$$

The heat flux is given by Fourier's law of heat conduction

$$\mathbf{q} = -\mathbf{K}\nabla\theta\ , \tag{5.14}$$

where $\mathbf{K}$ is the tensor of thermal conductivity.

5.2.3 Generalized Clausius-Clapeyron equation

The coexistence of two phases in thermodynamic equilibrium requires the continuity of stress, temperature and the chemical potential at the interface [6]. Here we propose that for dissipative processes not too far away from thermodynamic equilibrium, the temperature θ and specific chemical potential (μ) remain continuous, or their jumps vanish. Therefore,

$$[[\theta]] = 0 \quad , \quad [[\mu(\mathbf{T_R}, \theta)]] = 0 \quad at \quad \mathbf{x} \subset S_p(t). \tag{5.15}$$

From the second of Eqs. 5.15,we can write

$$[[\partial_\theta \mu + tr(\partial_{\mathbf{T_R}} \mu \;\; \partial_\theta \mathbf{T_R}^T)]] = 0 \, . \tag{5.16}$$

The Maxwell relations (refer Appendix C.3) are

$$\partial_\theta \mu = -\eta_p \quad , \quad \partial_{\mathbf{T_R}} \mu = -\upsilon_p \mathbf{F} \quad . \tag{5.17}$$

Phase transformation in SMAs is primary a shear process [7]. We assume there is no difference in volume for a particle which exists either in the austenite or the martensite phase, i.e. $[[\upsilon_p]] = 0$. Using this assumption along with Eqs. 5.17, Eq. 5.16 becomes

$$[[\eta]] = -[[tr(\mathbf{F} \;\; \partial_\theta \mathbf{T}_{\mathbf{R}}^{\mathbf{T}})]] \quad at \quad \mathbf{x} \subset S_p(t), \tag{5.18}$$

where we have used the relation for specific entropy, $\eta = \frac{\eta_p}{v_p}$ in arriving at Eq. 5.18. We shall refer to Eq. 5.18 as the generalized Clausius-Clapeyron equation.

5.3 The 3D theory, based on a quasistatic, small strain approximation

The transition from the complete theory (Sec.5.2) to the simpler theory based on a quasistatic, infinitesimal strain approximation is given in this section, and is made by invoking the following assumptions: (i) constant, uniform and identical density for both phases, i.e. $\dot{\rho} = 0$, (ii) negligible inertia, i.e.$|\rho\dot{\mathbf{v}}| << |div\ \mathbf{T_R}|$, (iii) small particle velocity, $\mathbf{v}$, such that $\dot{\mathbf{v}} \approx \partial_t \mathbf{v}$, (iv) small deformation gradients (i.e.$\nabla \otimes \mathbf{w} << 1$), such that $div\ \mathbf{T_R} \approx div\ \mathbf{T}$ where $\mathbf{T}$ is the Cauchy stress tensor. Further, the Lagrangian strain tensor, $\tilde{\mathbf{E}} = \frac{1}{2}(\mathbf{F^T F} - \mathbf{1})$, reduces to the infinitesimal strain tensor, $\mathbf{E}$

$$\mathbf{E} = \frac{1}{2}\left(\mathbf{F} + \mathbf{F}^T - 1\right). \tag{5.19}$$

With these assumptions, Eqs. 5.1-5.4 become

$$div\ \mathbf{v} = 0, \tag{5.20}$$

$$div\ \mathbf{T} = 0, \tag{5.21}$$

$$\mathbf{T} = \mathbf{T}^{\mathbf{T}}, \tag{5.22}$$

$$tr(\mathbf{T}\ \partial_t \mathbf{E}) + div\ \mathbf{q} + \rho r = \partial_t u\ . \tag{5.23}$$

The jump conditions are now simplified: (i) Eq. 5.6 in Eq. 5.7 yields $[[\mathbf{T_R n}]] = \rho V_n^2[[\mathbf{F}]]n$. We assume that the inertial term, $\rho V_n^2[[\mathbf{F}]]\mathbf{n}$, is vanishingly small , leading to $[[\mathbf{T_R n}]] = 0$, (ii) with this result and Eq. 5.6, Eq. 5.8 becomes $[[\mathbf{q}\cdot\mathbf{n}]] = -[[u + \frac{1}{2}\rho|\mathbf{v}|^2 - \mathbf{Fn}\cdot\mathbf{T_R n}]]V_n$. We assume that particle velocities are small enough such that $\frac{1}{2}\rho|\mathbf{v}|^2 << \mathbf{Fn}\cdot\mathbf{T_R n}$. As well, we use the identity $\mathbf{Fn}\cdot\mathbf{T_R n} = tr(\mathbf{TF}) = tr(\mathbf{TE})$. With these assumptions, Eqs. 5.6-5.9 reduce to

$$[[\mathbf{v}]] = -V_n[[\mathbf{F}]]\mathbf{n}, \tag{5.24}$$

$$[[\mathbf{Tn}]] = 0, \tag{5.25}$$

$$[[\mathbf{F}]]\mathbf{m} = 0, \tag{5.26}$$

$$[[\mathbf{q}\cdot\mathbf{n}]] = [[u - tr(\mathbf{TE})]]V_n. \tag{5.27}$$

The generalized Clausius-Clapeyron equation Eq. 5.18 becomes

$$[[\eta]] = -tr([[\mathbf{E}]]\ \partial_\theta \mathbf{T}) \quad at \quad \mathbf{x} \subset S_p(t). \tag{5.28}$$

5.4 The generalized Clausius-Clapeyron equation in the quasistatic, infinitesimal strain theory with a trilinear Helmholtz free energy function

The generalized Clausius-Clapeyron equation (Eq. 5.28) will now be specialized for a trilinear Helmholtz free energy function. The infinitesimal strain approximation implies that Eq. 5.12 now becomes $\psi \equiv \psi(\mathbf{E}, \theta)$ in terms of the infinitesimal strain tensor. A 3D generalization of the Helmholtz free energy function available in [8] is adopted

$$\begin{aligned}\psi \equiv \psi(\mathbf{E}, \theta) = \frac{1}{2} tr(\mathbf{E_{te}} \mathcal{L} \mathbf{E_{te}}) - tr(\mathbf{E_{te}} \mathcal{L} \mathbf{A})(\theta - \theta_0) + \\ C_\varepsilon \theta \left(1 - \ln \frac{\theta}{\theta_0}\right) - \lambda_T \left(1 - \frac{\theta}{\theta_0}\right) + \text{const.}\end{aligned} \tag{5.29}$$

where $\mathbf{E_{te}}$ is the thermoelastic strain tensor, $\mathcal{L}$ is the fourth-order tensor of elastic moduli, $\mathbf{A}$ is the tensor of the coefficient of thermal expansion, θ_0 is a reference temperature, C_ε is heat capacity at constant strain and λ_T is the latent heat of transformation. The thermoelastic strain tensor is defined as

$$\mathbf{E_{te}} = \mathbf{E} - \mathbf{E_T}, \tag{5.30}$$

where $\mathbf{E_T}$ is the phase transformation strain of a product martensitic phase with respect to a parent austenitic phase. We define

$$\mathbf{E_T} = \begin{cases} 0 & \text{Austensite} \\ \mathbf{E^i_{ph}} & i\text{th variant of martensite} \end{cases} \tag{5.31}$$

$$\lambda_T = \begin{cases} 0 & \text{Austensite} \\ \lambda_{ph} & i\text{th variant of martensite} \end{cases} \tag{5.32}$$

noting that while the value of $\mathbf{E}_T$ will be different depending on the particular martensitic variant, λ_T will have the same value for any martensitic variant. With Eq. 5.29, the stress, entropy and internal energy will follow from Eq. 5.13. Note that, due to the small strain approximation, the first of Eq. 5.13 becomes $\mathbf{T_R} = \partial_{\mathbf{E}}\psi$. Thus, we have

$$\mathbf{T} = \mathcal{L}[\mathbf{E_{te}} - \mathbf{A}(\theta - \theta_0)], \tag{5.33}$$

$$\eta = tr(\mathbf{E_{te}}\mathcal{L}\mathbf{A}) + C_\varepsilon \ln\frac{\theta}{\theta_0} - \frac{\lambda_T}{\theta_0} \tag{5.34}$$

$$u = \frac{1}{2}tr(\mathbf{E_{te}}\mathcal{L}\mathbf{E_{te}}) + tr(\mathbf{E_{te}}\mathcal{L}\mathbf{A})(\theta - \theta_0) + C_\varepsilon\theta - \lambda_T + \text{const.} \tag{5.35}$$

The generalized Clausius-Clapeyron equation (Eq. 5.28) for a trilinear Helmholtz free energy function reduces to

$$-tr([[\mathbf{E}]]\ \partial_\theta\mathbf{T}) = [[tr(\mathbf{E_{te}}\mathcal{L}\mathbf{A})]] + [[C_\varepsilon]]\ln\frac{\theta}{\theta_0} - \frac{1}{\theta_0}[[\lambda_T]]\ , \tag{5.36}$$

where Eq. 5.33-5.35, have been used. Eq. 5.36, is, in essence, the stress-temperature relationship at an interface between two phases. If, in particular, the interface is between two martensitic variants, then $[[C_\varepsilon]] = 0$, $[[\lambda_T]] = 0$ and Eq. 5.36 simplifies to

$$tr([[\mathbf{E}]]\ \partial_\theta \mathbf{T}) = -tr[[\mathbf{E_{te}}\mathcal{L}\mathbf{A})]]\ . \tag{5.37}$$

5.4.1 Variant selection criterion

Different martensitic variants can be realized during the phase transformation in SMAs. The appearance of a specific martensitic variant is determined by the local value of the thermal and mechanical fields as well as the material characteristics of the variant(i.e. transformation strain, elastic moduli etc.). From thermodynamical point of view, the variant that should appear must lead to formation of a stable system at thermomechanical equilibrium. This state of equilibrium is achieved when the local thermal and mechanical fields satisfy the conditions in Section 5.2.3. Since the first two equilibriums conditions(equality of the local stress and equality of the local temperature) are trivially satisfied, the Generalized Clausius-Clapeyron equation (Eq. 5.18) is the natural choice for a variant selection criterion. Based on the reasoning above the variant selection criterion adopted in this work can be formulated as follows: The i^{th} martensitic variant appears in a system undergoing or is about to undergo phase transformation, at each location, $\vec{x}$, where the local temperature, θ, local stress, $\mathbf{T_R}$, and the i^{th} variant material properties satisfy Eq. 5.18. In the infinitesimal strain approximation Eq. 5.18 must be replaced by Eq. 5.36 and/or Eq. 5.37.

5.5 The finite element method and the numerical approach

5.5.1 The governing equations in a Cartesian reference frame

In order to prepare for the finite element implementation, the symbolic form of the governing equations presented in Section 5.4 will be converted into indicial form. A Cartesian reference frame is adopted, wherein $\mathbf{e_i}$ is the ith unit vector ($i = 1,\ 2,\ 3$). The Cartesian representation of some pertinent tensorial quantities are

$$\mathbf{T} = T_{ij}(\mathbf{e_i} \otimes \mathbf{e_j})\ ,\ \mathbf{E_{te}} = E_{te,ij}(\mathbf{e_i} \otimes \mathbf{e_j})\ ,\ \mathbf{A} = \alpha(\mathbf{e_i} \otimes \mathbf{e_j})\ ,$$
$$\mathcal{L} = L_{ijkl}(\mathbf{e_i} \otimes \mathbf{e_j} \otimes \mathbf{e_k} \otimes \mathbf{e_l})\ . \qquad (5.38)$$

With Eq. 5.38, we then make a transition to a matrix and vector formulation for finite element implementation. A second order tensor, e.g., $\mathbf{E_{te}}$, will be written as a vector, e.g. $\vec{E}_{te}$, whereas a fourth order tensor , e.g. $\mathcal{L}$, will be written as a matrix and denoted as $[\mathcal{L}]$. A dot product between two vectors, $\vec{T}$ and $\vec{E}_{te}$, will be denoted as $\vec{T} \cdot \vec{E}_{te}$. The components of $\vec{T}$, $\vec{E}_{te}$, $\vec{A}$ and $[\mathcal{L}]$ have been listed in Appendix C.1. The matrix of elastic compliances, $[\mathcal{M}]$, will follow from the inverse of $[\mathcal{L}]$, i.e.

$$[\mathcal{M}] = [\mathcal{L}]^{-1}. \tag{5.39}$$

Eq. 5.21 and Eq. 5.33 to 5.35 respectively become

$$div\ \vec{T} = 0, \tag{5.40}$$

$$\vec{E}_{te} = [\mathcal{M}]\vec{T} + \vec{A}(\theta - \theta_0), \tag{5.41}$$

$$\eta = \vec{E}_{te} \cdot [\mathcal{L}]\vec{A} + C_\varepsilon \ln \frac{\theta}{\theta_0} - \frac{\lambda_T}{\theta_0} \tag{5.42}$$

$$u = \frac{1}{2}\vec{E}_{te} \cdot [\mathcal{L}]\vec{E}_{te} + \vec{E}_{te} \cdot [\mathcal{L}]\vec{A}(\theta - \theta_0) + C_\varepsilon\theta - \lambda_T + \text{const.} \tag{5.43}$$

With Eqs. 5.41 and 5.43, Eqs. 5.23 and 5.27 become respectively

$$div\ \mathbf{q} + \rho r = \dot{\vec{T}} \cdot \vec{A}\theta + \left(\vec{A} \cdot [\mathcal{L}]\vec{A}\theta + \dot{C_\epsilon}\right)\dot{\theta}, \tag{5.44}$$

$$\begin{aligned} [[\mathbf{q} \cdot \mathbf{n}]] = V_n \left(\frac{1}{2}\vec{T} \cdot [[\ [\mathcal{M}]\ ]]\vec{T} - \vec{T} \cdot [[\vec{A}]]\theta_0 + \vec{T} \cdot [[\vec{E}_T]]\right) - \\ V_n \left(\frac{1}{2}[[\vec{A} \cdot [\mathcal{L}]\vec{A}]](\theta_s^2 - \theta_0^2) + [[C_\epsilon]]\theta_s - [[\lambda_T]]\right) . \end{aligned} \tag{5.45}$$

Finally, the generalized Clausius-Clapeyron equation (Eq. 5.28) becomes

$$-\frac{d\vec{T}}{d\theta_s} \cdot \left[\left[\vec{E}_{te}\right]\right] = \vec{T} \cdot [[\vec{A}]] + [[\vec{A} \cdot [\mathcal{L}] \vec{A}]](\theta_s - \theta_0) + [[C_\epsilon]] \; ln \frac{\theta_s}{\theta_0} - \frac{[[\lambda_T]]}{\theta_0}. \quad (5.46)$$

Phase transformation in shape memory alloy thin films may be effectively modeled by assuming a two-dimensional state of stress (in the plane of the film). The predictions using the approximation become more accurate as the thickness of the thin film decreases, and are exact in the case of vanishing film thickness. We take the plane of the thin film to coincide with the $x_1 - x_2$ plane. The components of $\vec{T}$, $\vec{E}_{te}$, $\vec{A}$ and $[\mathcal{L}]$ for the 2D plane stress problem are listed in the Appendix C.2.

5.5.2 Variant selection

The variant selection is based on the criterion outlined in Section 5.4.1 and Eq. 5.46. For each martensitic variant, the required phase transformation temperature at each location is determined using Eq. 5.46 and the known stress field. Thus, for a specific location, the obtained set of possible phase transformation temperatures is

$$\theta_s^i < \theta_s^j < \theta_s^k < \ldots , \quad (5.47)$$

where indices i, j, k represent the i^{th}, j^{th}, k^{th} variants respectively. The selection criterion implies that a variant p will appear if the local temperature, θ, is equal to the required phase transformation temperature, θ_s^p, i.e.

$$\theta = \theta_s^p \,. \tag{5.48}$$

However, due to the discrete character of the numerical solution for θ and θ_s^p, the condition in Eq. 5.48 may not be exactly attainable. Therefore, we propose that the variant p will appear if for two consecutive time increments, n and $n+1$, one of the following transitions occurs

$$\theta^n < \theta_s^p \rightarrow \theta^{n+1} \geq \theta_s^p \,,$$

$$\theta^n > \theta_s^p \rightarrow \theta^{n+1} \leq \theta_s^p \,.$$

5.5.3 Numerical algorithm

Eq. 5.40 along with Eqs. 5.44-5.46 constitute the non-linear, time-dependent, coupled system of equations describing the evolution of phase transformation in SMAs. Solving this system of equations numerically is not a trivial problem. That is mostly due to the strong coupling between the stress and temperature fields and the presence of moving heat source. The spatial discretization of the equation was perform by applying Finite Element Methods(FEM):

functional minimization and weighted residuals(Gelerkin method). Three different time discretization schemes has been implemented: first order explicit, first order implicit and second order semi-implicit(Crank-Nicholson). Time stepping in the case of explicit scheme is relatively simple but a condition of the type $\Delta t \leq C\Delta x^2$[9] must be satisfied in achieve convergence. That kind of stability problems are avoided with the implementation of implicit or semi-implicit time discretization schemes. The result of the discretization of Eq. 5.40 and Eqs. 5.44-5.46 in space and time by applying FEM and implicit/semi-implicit schemes is a system of nonlinear algebraic equations. To solve this system the following iterative sequence has been implemented. It is summarized below

1. Guess the new phase boundary velocity, V_n
2. Update the phase boundary velocity
3. Calculate the new position of the interface at the $(i+1)^{th}$ time step, based on its position at the i^{th} time step, $\vec{x}_s^{i+1} = \vec{x}_s^{i} + V_n\Delta t$
4. Update the mesh
5. Transfer(interpolate) the old θ and $\vec{T}$ onto the new mesh

6. Calculate the stress, $\vec{T}$, using Eq. 5.40 on the new mesh
7. Calculate the phase transformation temperature, θ_s, from Eq. 5.46
8. Calculate the temperature field, θ, from Eq. 5.44
9. Calculate the new phase boundary velocity
10. Check if the old velocity(step 1) and new velocity(step 9) are close enough(i.e. within a certain tolerance). If "yes" finish the iterations, otherwise go to step 2.

A detailed description of the specific numerical method used in steps 4-9 is given in the next sections.

5.5.4 Mechanical Equilibrium Equation

The finite element formulation of the mechanical equilibrium problem(Eq. 5.40) is based on the first variational theorem of elastostatics[10].

Theorem 1 *A domain occupying a region, R, has displacements and tractions prescribed on its surface, S, (see Fig. 5.1) i.e.*

$$\begin{aligned} \mathbf{w} &= \mathbf{w_0}(\mathbf{x}), \quad \text{where} \quad \mathbf{x} \in S^{(1)}, \\ \mathbf{Tn} &= \mathbf{t_0}(\mathbf{x}), \quad \text{where} \quad \mathbf{x} \in S^{(2)}, \end{aligned} \tag{5.49}$$

such that $S^{(1)} \cup S^{(2)} = S$. *For this mixed boundary value problem, the deformation field,* $\mathbf{w} = \mathbf{w_0}(\mathbf{x})$ *is a solution if and only if the first variation of the functional*

$$J(\mathbf{w}) = \Lambda - W_p \tag{5.50}$$

vanishes for all variations $\delta\mathbf{w}$ *such that* $\delta\mathbf{w} = 0$ *on* $S^{(1)}$.

In Eq. 5.50, Λ is the total elastic strain energy of the system. The parameter W_p is the work done by the applied loads, and is defined as

$$W_p = W_p^C + W_p^D + W_p^B \ , \tag{5.51}$$

where W_p^C, W_p^D and W_p^B are the work due to applied concentrated loads, applied distributed loads on the surface and the body forces respectively. The total elastic strain energy is given by

$$\Lambda = \frac{1}{2}\int_V \vec{T} \cdot \vec{E}_{el}\, dV \ , \tag{5.52}$$

where the elastic strain

$$\vec{E}_{el} = \vec{E} - \vec{E}_{tp} \quad \text{and} \quad \vec{E}_{tp} = \vec{E}_T + \vec{A}(\theta - \theta_0). \tag{5.53}$$

If the domain V is discretized into N elements, each with a volume, V_N, Eq. 5.52 becomes

$$\Lambda = \sum_{i=1}^{N} \Lambda_i = \frac{1}{2}\sum_{i=1}^{N} \int_{V_i} \vec{T} \cdot \vec{E}_{el}\, dV_i. \tag{5.54}$$

Within each element, each continuous quantity, χ, can be approximated by using its corresponding nodal values, χ_α, and the shape function, φ_k as

$$\chi = \sum_{k=1}^{N_{nodes}} \varphi_k \chi_k, \tag{5.55}$$

where N_{nodes} is the number of nodes. With Eq. 5.55, the components of the displacement, $\mathbf{w}$, can be written in terms of the nodal displacements, $\{U\}$, as

$$\mathbf{w} = \hat{N}\{U\} \tag{5.56}$$

where $\hat{N}$ is the matrix of shape functions. From Eq. 5.56 the strain, $\vec{E}$, follows by the application of Eqs. 5.5 and 5.19 as

$$\vec{E} = \hat{B}\{U\}. \tag{5.57}$$

The strain energy, Λ_i, for a single element can be written as

$$\Lambda_i = \frac{1}{2}\int_{V_i} \left(\{U\}^T \hat{B}_i^T \hat{S}_i \hat{B}_i \{U\} - 2\{U\}^T \hat{B}_i^T \hat{S}_i \{E_{tp}\} + \{E_{tp}\}^T \hat{S}_i \{E_{tp}\} \right) dV_i. \tag{5.58}$$

A node is placed at the point of action of a concentrated force on the surface. If $\{P_0\}$ denotes the vector of nodal force components, the work performed is given by

$$W_p^C = \{U\}^T \{P_0\}, \tag{5.59}$$

This definition assumes that the forces have been resolved into components parallel to the displacement components. The work done by the distributed loads that act on the surface is

$$W_p^D = \int_{S_2} \mathbf{w} \cdot \mathbf{t_0} \, dS_2. \tag{5.60}$$

With Eq. 5.56, Eq. 5.60 is rewritten as

$$W_p^D = \sum_{i=1}^{N} \int_{S_{2,i}} \{U\}^T \hat{N}_i^T \{t_0\} \, dS_{2,i}, \tag{5.61}$$

where $\{t_0\}$ is the vector of nodal components of the distributed load. The work done by the body forces is given by

$$W_p^B = \int_V \mathbf{w} \cdot \mathbf{b} \, dV, \tag{5.62}$$

which may be written as

$$W_p^B = \sum_{i=1}^{N} \int_{V_i} \{U\}^T \hat{N}_i^T \{b\} \, dV_i, \tag{5.63}$$

where $\{b\}$ is vector of the components of the body force. The Eqs. 5.59, 5.61 and 5.63 are inserted in Eq. 5.51. The Eq. 5.51 and Eq. 5.52 are then put into Eq. 5.50. The extremum value of the functional J(Eq. 5.50) in terms of displacements is found by setting its first derivative with respect to $\{U\}$ to zero

$$\frac{\partial J}{\partial \{U\}} = \hat{k}\{U\} + \{f\} = 0 \ , \tag{5.64}$$

where the stiffness matrix $\hat{k}$ is represented by the volume integral

$$\hat{k} = \sum_{i=1}^{N} \int_{V_i} \hat{B}_i^{\,T} \hat{S}_i \hat{B}_i \; dV_i \; , \tag{5.65}$$

and the force vector $\{f\}$ is the sum of the other three integrals

$$\begin{aligned} \{f\} = -\sum_{i=1}^{N} \int_{V_i} \hat{B}_i^{\,T} \hat{S}_i \{E_{tp}\} \; dV_i - \sum_{i=1}^{N} \int_{V_i} \hat{N}_i^{\,T} \{b\} \; dV_i \\ -\sum_{i=1}^{N} \int_{S_{2,i}} \hat{N}_i^{\,T} \{t_0\} \; dS_{2,i} - \{P_0\} \; . \end{aligned} \tag{5.66}$$

Once the displacements are determined, the strain field can be easily calculated by using Eq. 5.57 and the stress field will follow from Eqs. 5.41(along with Eq. 5.30).

5.5.5 Energy Conservation Equation

The spatial discretization of Eq. 5.44 is done by using Galerkin method. The reason is that no functional for the considered problem can be found due to its nonlinearity and stress coupling. If φ_k denotes the set of shape functions on the discretized region, the weak form of the Eq. 5.44(after replacing $[\mathcal{L}]$ with $[S]$) reads

$$\begin{aligned} k \int_V \varphi_k \, \nabla^2 \, \theta dV = \int_V \varphi_k \dot{T}_j A_j \theta dV + \int_V \mathcal{B} \theta \varphi_k \dot{\theta} dV + \\ C_\varepsilon \int_V \dot{\theta} \varphi_k dV + \xi \int_V \theta \varphi_k dV - \xi \theta_0 \int_V \varphi_k dV \end{aligned} \tag{5.67}$$

where $\mathcal{B} = S_{ij}A_iA_j$ and Eq. 5.14 has been invoked, assuming an isotropic solid with respect to heat conduction(i.e. the tensor **K** has been replaced with a scalar k). If the Green's theorem

$$\int_V \nabla\varphi \cdot \nabla\psi \, dV + \int_V \psi \, \nabla^2 \varphi \, dV = \int_S \psi \frac{\partial\varphi}{\partial\vec{n}} dS \tag{5.68}$$

is applied to the LHS term in Eq. 5.67 it becomes

$$-k \int_V \nabla\theta \cdot \nabla\varphi_k dV + k \int_S \varphi_k \frac{\partial\theta}{\partial\vec{n}} dS = \int_V \dot{T}_j A_j \varphi_k \theta dV + \\ \mathcal{B} \int_V \varphi_k \theta \dot{\theta} dV + C_\epsilon \int_V \dot{\theta} \varphi_k dV + \xi \int_V \varphi_k \theta dV - \xi\theta_0 \int_V \varphi_k dV \; . \tag{5.69}$$

The second term on the LHS in Eq. 5.69 represents the heat flux through the volume boundaries. In the specific problem there are two types of boundaries for each phase: external and internal (phase) boundaries. The heat flux on the external boundaries is taken as zero(thermally insulated). At this stage of implementation of FEM, the zero heat flux condition will be imposed on all volume boundaries, including the internal ones. The nonzero heat flux on the phase boundaries will be taken into account later in the matrix formulation, by imposing the phase transformation temperature calculated from Eq. 5.46 as a boundary condition, replacing the heat flux condition. By setting

$$k \int_S \varphi_k \frac{\partial\theta}{\partial\vec{n}} dS = 0$$

and utilizing Eq. 5.55, the discrete formulation of Eq. 5.69 can be rewritten as

$$\begin{aligned} -k\theta_l \sum_e \int_{V^e} \nabla\varphi_l \cdot \nabla\varphi_k dV = \\ \dot{T}_j A_j \theta_l \sum_e \int_{V^e} \varphi_k \varphi_l dV + \mathcal{B}\dot{\theta}_l \sum_e \int_{V^e} \varphi_k \varphi_l (\varphi_p \theta_p) dV + \\ C_\varepsilon \dot{\theta}_l \sum_e \int_{V^e} \varphi_l \varphi_k dV + \xi\theta_l \sum_e \int_{V^e} \varphi_k \varphi_l dV - \xi\theta_0 \sum_e \int_{V^e} \varphi_k dV \end{aligned} \tag{5.70}$$

In matrix format, Eq. 5.70 is given by

$$\begin{aligned} -k\hat{R}\{\theta\} = \{\dot{T}_j\} A_j \hat{Q}\{\theta\} \\ + \left(\mathcal{B}\hat{Q}^{(3)} + C_\varepsilon \hat{Q}\right)\{\dot{\theta}\} + \xi\hat{Q}\{\theta\} - \xi\theta_0\{F^0\} \end{aligned} \tag{5.71}$$

where the global matrices are defined as follows

$$\hat{R}_{lk} = \sum_e \int_{V^e} \nabla\varphi_l \cdot \nabla\varphi_k dV \tag{5.72}$$

$$\hat{Q}_{lk} = \sum_e \int_{V^e} \varphi_k \varphi_l dV \tag{5.73}$$

$$\hat{Q}^{(3)}_{lk} = \sum_e \int_{V^e} \varphi_k \varphi_l (\varphi_p \theta_p) dV \tag{5.74}$$

$$\{F^0\}_k = \sum_e \int_{V^e} \varphi_k dV \tag{5.75}$$

The temporal discretization of Eq. 5.71 is implemented based on constant time increment,τ. The total time elapsed at the end of the i^{th} increment is defined as

$$t_i = i\tau \qquad , \qquad i \geq 1$$

The value of an arbitrary parameter $\mathcal{A}(\vec{x},t)$ at the end of the i^{th} time increment is defined as

$$\mathcal{A}^i = \mathcal{A}(t_i) \tag{5.76}$$

whereas the time derivative of the same quantity is approximated by

$$\frac{\partial \mathcal{A}}{\partial t} = \frac{\mathcal{A}^{i+1} - \mathcal{A}^i}{\tau} . \tag{5.77}$$

Utilizing Eq. 5.77, Eq. 5.71 can be rewritten as

$$\begin{aligned} \left(\mathcal{B}\hat{Q}^{(3)} + C_\epsilon \hat{Q}\right) \frac{\{\theta\}^{i+1} - \{\theta\}^i}{\tau} = \xi\theta_0\{F^0\} - \\ (1-\varrho)\left(\frac{\{T_j\}^{i+1} - \{T_j\}^i}{\tau} A_j\hat{Q} + k\hat{R} + \xi\hat{Q}\right)\{\theta\}^i - \\ \varrho\left(\frac{\{T_j\}^{i+1} - \{T_j\}^i}{\tau} A_j\hat{Q} + k\hat{R} + \xi\hat{Q}\right)\{\theta\}^{i+1} . \end{aligned} \tag{5.78}$$

Three different time discretization schemes were tested

a) First order explicit scheme, $\varrho = 0$,

b) First order implicit scheme, $\varrho = 1$,

c) Second order semi-implicit scheme, $\varrho = 0.5$(Crank-Nicholson).

The numerical experiments carried out with the three schemes above showed that scheme c) is the most effective as regards to numerical stability and required CPU time. Therefore all numerical results obtained during the simulations are based on Crank-Nicholson time discretization scheme.

5.5.6 Energy Conservation at the Phase Boundary

The weak form of Eq. 5.45 is

$$
\begin{aligned}
-\int_S \varphi_k \vec{n} \cdot (k^M \nabla \theta^M - k^A \nabla \theta^A) dS = \\
\int_S \left(\frac{1}{2} T_i [[M_{ik}]] T_k - T_i [[A_i]] \theta_0 + T_i e_i^0 + \lambda_T \right) \varphi_k V_n dS - \\
\frac{1}{2} [[S_{ij} A_i A_j]] \left(\int_S \varphi_k V_n \theta_s^2 dS - \theta_0^2 \int_S \varphi_k V_n dS \right) - [[C_\epsilon]] \int_S \varphi_k V_n \theta_s dS
\end{aligned}
\tag{5.79}
$$

The integration is performed over the phase boundary, S, with normal vector, $\vec{n}$. The element formulation of Eq. 5.79 on the discretized boundary is obtained after applying the finite element approximation (Eq. 5.55) of the phase boundary velocity, V_n, and phase boundary temperature, θ_s.

$$
\begin{aligned}
-\vec{n} \cdot (k^M - k^A) \theta_{s,l} \sum_e \int_{S^e} \varphi_k \nabla \varphi_l dS = \\
\left(\frac{1}{2} T_i [[M_{ik}]] T_k - T_i [[A_i]] \theta_0 + T_i e_i^0 + \lambda_T \right) V_{n,l} \sum_e \int_{S^e} \varphi_k \varphi_l dS - \\
\frac{1}{2} [[S_{ij} A_i A_j]] V_{n,l} \left(\theta_{s,p} \theta_{s,m} \sum_e \int_{S^e} \varphi_k \varphi_l \varphi_p \varphi_m dS - \theta_0^2 \sum_e \int_{S^e} \varphi_k \varphi_l dS \right) - \\
[[C_\varepsilon]] V_{n,l} \theta_{s,p} \sum_e \int_{S^e} \varphi_k \varphi_l \varphi_p dS
\end{aligned}
\tag{5.80}
$$

Here the subscript "," is used to separate the summation index from the abbreviation of the variable(V_n is the normal component of the phase boundary velocity whereas $V_{n,i}$ is the normal component of the phase boundary velocity in node i). With the definition of the following matrices

$$\hat{L}_{kl} = \sum_e \int_{S^e} \varphi_k \vec{n} \cdot \nabla \varphi_l dS \tag{5.81}$$

$$\hat{P}_{kl} = \sum_e \int_{S^e} \varphi_k \varphi_l dS \tag{5.82}$$

$$\hat{P}^{(3)}_{klp} = \sum_e \int_{S^e} \varphi_k \varphi_l \varphi_p dS \tag{5.83}$$

$$\hat{P}^{(4)}_{lkpm} = \sum_e \int_{S^e} \varphi_l \varphi_k \varphi_p \varphi_m dS \tag{5.84}$$

Eq. 5.80 becomes

$$\begin{gathered}-\hat{L} \cdot \left(k^M - k^A\right) \{\theta_s\} = \left(\frac{1}{2} T_i [[M_{ik}]] T_k - T_i [[A_i]] \theta_0 + T_i e_i^0 + \lambda_T\right) \hat{P} \{V_n\} - \\ \frac{1}{2} [[S_{ij} A_i A_j]] \left(\{\theta_s\}\{\theta_s\} \hat{P}^{(4)} - \theta_0^2 \hat{P}\right) \{V_n\} - [[C_\varepsilon]] \{\theta_s\} \hat{P}^{(3)} \{V_n\} \, .\end{gathered} \tag{5.85}$$

5.5.7 Finite element selection and spatial integration

The different nature of the thermal and mechanical problem imposes strict constrains on the selection of the type of finite elements used in the numerical implementation. The discontinuity in the first derivative of the temperature (due to moving heat source) implies the use of linear (C^0) elements(i.e. slope continuity is not required). On the other hand for the thermomechanical problem such restriction does not exist. However, the extensive work done on characterization of the thin plates in structural mechanics show that the choice of suitable elements is limited. In particular, quadrilateral elements turn out to have complications related to smoothness as illustrated in Dhatt [11]. A comparison of different plate bending elements can be found in Zienkiewics and Taylor [12] and a comprehensive performance evaluation of triangular elements is summarized in Batoz et al. [13]. In the present work we adopt a linear(C^0) triangular element (Zienkiewics and Taylor [12]), which easily satisfies the specific requirements for both thermal and thermoelastic problems. The shape functions for the selected linear triangular elements are

$$\begin{aligned} \varphi_1 &= 1 - \zeta - \vartheta \,, \\ \varphi_2 &= \zeta \,, \\ \varphi_3 &= \vartheta \,. \end{aligned} \tag{5.86}$$

It was found that the spatial integrals encountered can be evaluated with sufficient accuracy by using a third order Gaussian quadrature [11]. The calculated values agreed with those obtained by direct integration. Moreover, the element and the integration scheme passed the test of uniform convergence for several problems with respect to an analytical solution(see Section 5.6.1).

5.5.8 Interpolation

The front tracking in the specified problem is achieved by refining/updating the mesh at each time step. The refining/updating the mesh is done in such a way so that the phase front always lies on mesh nodes. Because of the transient nature of the problem, the data from the previous time step should be available on the new updated mesh. The data transfer from the old mesh to the new one is accomplished by two-step interpolation sequence. From numerical point of view the interpolation on insufficiently smooth functions is difficult and some times impossible. In the considered problem the additional complication is the jump in the first derivative of the temperature(heat flux) at the phase boundary. Due to this jump the order of interpolation close to the phase boundary cannot be more than first. On the other hand the simple linear interpolation introduces artificial fluctuations close to the plane of discontinuity. A solution to this problem is the use of Nonoscillatory interpolation schemes. The first step in the interpolation sequence is Linear Finite element interpolation. The main purpose of this step is to transfer data from the unstructured triangular mesh on a structured quadrilateral one, suitable for Nonoscillatory interpolation schemes.

Finite element interpolation

The Finite Element Interpolation is based on the idea of mapping an element with irregular shape to an element with regular one. Let P_k be a set of values of the variable P at the nodes of a selected element and P_0 is the value of the same variable at (x_0, y_0) that is to be determined. Utilizing the finite element approximation (Eq. 5.55) the coordinates of P_0 can be expressed as

$$x_0 = \sum_{k=1}^{N_{nodes}} \varphi_k(\zeta_0, \vartheta_0) x_k \tag{5.87}$$

$$y_0 = \sum_{k=1}^{N_{nodes}} \varphi_k(\zeta_0, \vartheta_0) y_k \tag{5.88}$$

where φ_k is the set of shape functions for the chosen type of elements(for linear triangular elements see Eq. 5.86). The mapped coordinates of P_0, ζ_0, ϑ_0 can be determined from Eq. 5.87 and Eq. 5.88. Once the mapped coordinates are known P_0 can be calculated from

$$P_0 = \sum_{k=1}^{N_{nodes}} \varphi_k(\zeta_0, \vartheta_0) P_k \tag{5.89}$$

The order of interpolation depends on the order of the selected shape functions within the elements. For linear elements (linear shape functions) solving Eq. 5.87 and Eq. 5.88 for ζ_0, ϑ_0 is straight forward. In case of second and higher order elements the solution of the equations must be computed numerically.

Nonoscillatory Interpolation

The equations describing the phase transformation in SMAs constitute a non-linear system with moving heat source, and hence smooth initial data gives rise to data with discontinuous first and higher order derivatives in finite time during the evolution. As a consequence classical finite element methods present important deficiencies when dealing with such systems. Typically first order accurate schemes are too dissipative across discontinuities(excessive smearing), and second order(or higher) schemes produce spurious oscillations near discontinuities, which do not disappear as the grid is refined. There are two approaches to obtain high-order oscillation-free accurate representation of discontinuous solutions: Artificial damping [14, 15] and TVD(Total Variation Diminishing) schemes. The interpolation scheme used in the presented work is based on the later group of methods.

The TVD schemes utilize the concept of preventing any values being generated at location x that lie outside the range of those present in close vicinity of x. The main criterion, which determines the efficiency of the TVD schemes, is the total-variation defined as:

$$TV = \sum_{j} \left| u_{j+1} - u_j \right| . \tag{5.90}$$

A numerical scheme is said to be a TVD scheme if the total variation, TV, is bounded for any initial data. The basic ingredient of the TVD interpolation schemes is a flux splitting technique [16]. A one-dimensional interpolation in general can be written as

$$u(x_i + \delta) = u(x_i) + S_i\delta \ , \tag{5.91}$$

where S_i is the slope of a piecewise linear distribution of data over the intermediate finite element around each grid point. The slope corresponding to Roe's Superbee [17] scheme can be interpreted as:

$$S_i^{Superbee} = \frac{median\left(0, u^c_{i+1/2} - u_i, u_i - u^c_{i-1/2} u_i - u_{i-1}, u_{i+1} - u_i\right)}{h} \ , \tag{5.92}$$

where

$$u^c_{i+1/2} = \frac{1}{2}(u_i + u_{i+1}) \quad \text{and} \quad u_i = u(x_i) \ .$$

The median of three quantities is evaluated as follows

$$median(a, b, c) = a + minmod(b - a, c - a) \ , \tag{5.93}$$

$$minmod(a, b) = sign(a) max(0, sign(ab) min(|a||b|)) \ , \tag{5.94}$$

while the median of five quantities is evaluated as

$$median(a, b, c, d, e) = median(A, B, e) \ , \tag{5.95}$$

where

$$A = median(a, b, c) \ ,$$

$$B = a + b + c + d - max(a, b, c, d) - min(a, b, c, d) - A \ .$$

5.5.9 Linear Algebraic Equations

Biconjugate gradient method

The conjugate gradient methods [18] provide a general means for solving the linear system

$$\hat{A} \cdot \vec{x} = \vec{b} \ , \qquad (5.96)$$

where $\hat{A}$ is a matrix, $\vec{b}$ and $\vec{x}$ are vectors.

The attractiveness of these methods for large systems ~~is that~~ they reference $\hat{A}$ only through its multiplication of a vector, or multiplication of its transpose and a vector. These two operations can be very efficient for properly stored sparse matrix. The simplest conjugate gradient algorithm solves Eq. 5.96 only in the case that $\hat{A}$ is symmetric and positive definite($\vec{x} \cdot \hat{A} \cdot \vec{x}^T > 0$ for every nonzero $\vec{x}$). It is based on the idea of minimizing the function

$$f(\vec{x}) = \frac{1}{2}\vec{x} \cdot \hat{A} \cdot \vec{x} - \vec{b} \cdot \vec{x} \ ,$$

which is equivalent to

$$\nabla f(\vec{x}) = \hat{A} \cdot \vec{x} - \vec{b} = 0\,.$$

The minimization is carried out by generating a succession of search directions $\vec{p}_k$ and improved minimizers $\vec{x}_k$. At each iteration a quantity α_k is found that minimizes $f(\vec{x}_k + \alpha_k \vec{p}_k)$, and $\vec{x}_{k+1}$ is set equal to the new point $\vec{x}_k + \alpha_k \vec{p}_k$. The sequences of $\vec{p}_k$ and $\vec{x}_k$ are built in such a way that $\vec{x}_{k+1}$ is also a minimizer of f over the whole vector subspace of directions already taken $(\vec{p}_1, \vec{p}_2, ...\vec{p}_k)$. For the specific problem considered in the paper a generalized form of the conjugate gradient method is used, called the biconjugate gradient method. The main advantage of the biconjugate gradient method over the "ordinary" conjugate gradient methods is that it solves linear but not necessarily positive definite or symmetric equations. The biconjugate gradient algorithm can be summarized by the following iterative sequence [18]

$$\alpha_k = \frac{\tilde{\vec{r}}_k \cdot \vec{r}_k}{\tilde{\vec{p}}_k \cdot \hat{A} \cdot \vec{p}_k}$$

$$\vec{r}_{k+1} = \vec{r}_k - \alpha_k \hat{A} \cdot \vec{p}_k$$

$$\tilde{\vec{r}}_{k+1} = \tilde{\vec{r}}_k - \alpha_k \hat{A}^T \cdot \tilde{\vec{p}}_k$$

$$\beta_k = \frac{\tilde{\vec{r}}_{k+1} \cdot \vec{r}_{k+1}}{\tilde{\vec{r}}_k \cdot \vec{r}_k}$$

$$\vec{p}_{k+1} = \vec{r}_k + \beta_k \vec{p}_k$$

$$\tilde{\vec{p}}_{k+1} = \tilde{\vec{r}}_k + \beta_k \tilde{\vec{p}}_k \tag{5.97}$$

The sequence of vectors satisfies the biorthogonality condition

$$\tilde{\vec{r}}_i \cdot \vec{r}_j = \vec{r}_i \cdot \tilde{\vec{r}}_j = 0 \ , \quad j < i \tag{5.98}$$

the biconjugacy condition

$$\tilde{\vec{p}}_i \cdot \hat{A} \cdot \vec{p}_j = \vec{p}_i \cdot \hat{A}^T \cdot \tilde{\vec{p}}_j = 0 \ , \quad j < i \tag{5.99}$$

and a mutual orthogonality

$$\tilde{\vec{r}}_i \cdot \vec{p}_j = \vec{r}_i \cdot \tilde{\vec{p}}_j = 0 \ . \quad j < i \tag{5.100}$$

To use the algorithm(Eq. 5.97) to solve the system Eq. 5.96, an initial guess $\vec{x}_1$ for the solution should be made. Vector $\vec{r}_1$ is the residual

$$\vec{r}_1 = \vec{b} - \hat{A} \cdot \vec{x}_1 \tag{5.101}$$

and $\tilde{\vec{r}}_1 = \vec{r}_1$. Then the sequence of improved estimates

$$\vec{x}_{k+1} = \vec{x}_k + \alpha \vec{p}_k \tag{5.102}$$

should be formed while carrying out the recurrence Eq. 5.97.

The outlined conjugate gradient method works well for matrices that are well-conditioned, i.e., "close" to the identity matrix. This suggest applying these methods to the preconditioned form of Eq. 5.96 ,

$$(\hat{E}^{-1}\cdot\hat{A})\cdot\vec{x} = \hat{E}^{-1}\cdot\vec{b} \tag{5.103}$$

The idea is to find $\hat{E}$ close to $\hat{A}$, in which case $E^{-1}\cdot\hat{A}\approx 1$, allowing the algorithm to converge in fewer steps. The matrix $\hat{E}$ is called a preconditioner, and the following scheme is known as the preconditioned biconjugate gradient method or PBCG. For efficient implementation, the PBCG algorithm introduces an additional set of vectors $\vec{z}_k$ and $\tilde{\vec{z}}_k$ defined by

$$\hat{E}\cdot\vec{z}_k = \vec{r}_k \qquad \mathit{and} \qquad \hat{E}^T\cdot\tilde{\vec{z}}_k = \tilde{\vec{r}}_k \tag{5.104}$$

and modifies the definitions of α_k,β_k, $\vec{p}_k$ and $\tilde{\vec{p}}_k$ in Eq. 5.97.

$$\alpha_k = \frac{\tilde{\vec{r}}_k\cdot\vec{z}_k}{\tilde{\vec{p}}_k\cdot\hat{A}\cdot\vec{p}_k} \tag{5.105}$$

$$\beta_k = \frac{\tilde{\vec{r}}_{k+1}\cdot\vec{z}_{k+1}}{\tilde{\vec{r}}_k\cdot\vec{z}_k} \tag{5.106}$$

$$\vec{p}_{k+1} = \vec{z}_k + \beta_k\vec{p}_k \tag{5.107}$$

$$\tilde{\vec{p}}_{k+1} = \tilde{\vec{z}}_k + \beta_k\tilde{\vec{p}}_k \tag{5.108}$$

5.5.10 Preconditioning

Incomplete Cholesky (ILL^T) factorization is a robust, well-understood preconditioning technique, and has been extensively documented [19, 20]. We start the description of the ILL^T with the complete Cholesky factorization followed by techniques for discarding the fill-in entries.

The Cholesky factorization is an efficient, triangular decomposition of symmetric and positive definite square matrix $\hat{A}$. Instead of seeking arbitrary lower and upper triangular factors $\hat{L}$ and $\hat{U}$ as it is in LU decomposition, the Cholesky factorization constructs a lower triangular matrix $\hat{L}$ whose transpose $\hat{L}^T$ can itself serve as the upper triangular part. In other words the matrix $\hat{A}$ can presented as

$$\hat{L} \cdot \hat{L}^T = \hat{A}. \tag{5.109}$$

This factorization is sometimes referred to as "taking the square root" of the matrix $\hat{A}$. The values of the components of the factor $\hat{L}$ can be calculated using the following relations

$$L_{ii} = \left(A_{ii} - \sum_{k=1}^{i-1} L_{ik}^2 \right)^{\frac{1}{2}} \tag{5.110}$$

$$L_{ji} = \frac{1}{L_{ii}} \left(A_{ij} - \sum_{k=1}^{i-1} L_{ik} L_{jk} \right) \tag{5.111}$$

$$j = i + 1; i + 2; ...; N \tag{5.112}$$

Criteria for discarding the fill-in entries that occur during the factorization are generally based on the graph of the matrix (levels of fill) [21], the magnitudes of the entries (drop tolerance) [22], or both. There is a standard definition of a level-based ILL^T [20], whereas a drop tolerance ILL^T can vary according to the form of the dropping criterion. Dickinson et. al. [20] have shown that for linear elasticity applications, a drop tolerance ILL^T generally outperforms a level-based ILL^T having the same number of non-zero entries. The drop tolerance is also the technique that was implemented in the present work.

We denote by $\hat{A}^{(k)}$ the matrix obtained after $(k-1)$ stages of elimination. In this work, a fill-in entry $A_{ij}^{(k+1)}$ during the kth stage will be discarded if

$$|A_{ij}^{(k+1)}| < \varepsilon_{fill}|A_{ii}^{(k+1)}| \tag{5.113}$$

where $\varepsilon_{fill} \in [0,1]$ is the drop tolerance parameter. Note that using a drop tolerance of $\varepsilon_{fill} = 0$ gives a complete factorization, whereas using a value $\varepsilon_{fill} = 1$ permits very few fill-in entries to remain in the preconditioner. The appropriate value for ε_{fill} should be chosen to suit the needs of the problem; for example, solving ill-conditioned problems requires a finer drop tolerance (to ensure good convergence) than is necessary for solving well-conditioned problems.

5.6 Algorithm Validation

In this section we present a verification of the numerical algorithm developed in Section 5.5.3. There are several direct methods for investigating the accuracy and stability of a numerical scheme. Most of these method are well defined for finite difference method on a uniform mesh [23], whereas the only test method for finite element method(unstructured mesh) is the "patch test" [12]. The patch test for nonlinear problems is based on linearization of the problem to a problem, which has an analytical solution. The results from the analytical solution are compared to the numerical predictions on a very coarse mesh (set of several elements). Unfortunately for the 2D problem considered here, the linearization does not render an analytical solution. Therefore we accepted a slightly different approach based on the investigation of the behavior of three different 2D test problems, which allow derivation of a closed form solutions. Two of the selected problems are transient thermal problems and one steady state thermomechanical problem. The problems are:

a) Circular cylinder with time dependent thermal boundary conditions;

b) Circular cylinder with time dependent heat source;

c) Thermal Stresses in thin hollow disk.

The selection of the test problems listed above was done to allow validation of the following three aspects of the algorithm respectively:

a) solution of the thermal problem when strong, time dependent thermal gradients are applied close to the boundary;

b) solution of the thermal problem in the case of strong, time dependent nonlinear heat source;

c) solution of the thermoelastic problem when the applied temperature field has discontinuous first derivative(implying presence of heat source).

We start the section with a description of the test problems and the analytical methods used to obtain the corresponding close form solutions. It will be followed by discussion on the stability and accuracy of the numerical algorithm based on comparison between the analytical results and the numerical predictions.

5.6.1 Verification problems

The analytical solutions for the thermal test problems will be derived by applying the Forward Laplace transformations and the corresponding Inversion

Theorem. The forward Laplace transformation is defined as

$$L\{v(\vec{r},t)\} \equiv \bar{v} = \int_0^\infty e^{-pt} v(\vec{r},t)dt \ , \tag{5.114}$$

where p is a number whose real part is positive and large enough to make the integral defined with Eq. 5.114 convergent. Once the solution of the problem is obtained in the $\{\vec{r},p\}$ space, the Inversion Theorem(Eq. 5.115) is to be applied

$$v(\vec{r},t) = \frac{1}{2\pi i}\int_{\gamma-i\infty}^{\gamma+i\infty} e^{pt}\bar{v}(\vec{r},p)dp \ , \tag{5.115}$$

where γ is to be large enough so that all singularities of $\bar{v}$ lie to the left of the line $(\gamma - i\infty, \gamma + i\infty)$.

For both problems below consider an infinitely extended cylinder with circular cross section. Due to the symmetry of the problems, the solutions will be obtained in the cylindrical coordinate system, (r,ϕ,z), where z axis is taken along the cylinder axis, r is the radial coordinate($0 \leq r \leq a$, a is the radius of the cylinder), and ϕ is the azimuth angle.

Circular cylinder with time dependent thermal boundary conditions

Consider the thermal problem of a stress-free circular cylinder subjected to time dependent thermal boundary conditions. The conservation of energy (or heat conduction) equation is

$$\frac{\partial^2\theta}{\partial r^2} + \frac{1}{r}\frac{\partial\theta}{\partial r} = \frac{1}{\alpha}\frac{\partial\theta}{\partial t} , \tag{5.116}$$

where $\alpha = \frac{k}{C_\varepsilon}$, C_ε is the heat capacity and k is the thermal conductivity. The boundary condition is

$$\theta(a,t) = \xi t , \tag{5.117}$$

where ξ is a constant parameter. Applying the Laplace transformation(Eq. 5.114) to Eqs. 5.116 and 5.117 results into

$$\frac{\partial^2\bar{\theta}}{\partial r^2} + \frac{1}{r}\frac{\partial\bar{\theta}}{\partial r} - q^2\bar{\theta} = 0 , \tag{5.118}$$

$$\bar{\theta}(a,p) = \frac{\xi}{p^2} , \tag{5.119}$$

where $q^2 = \frac{p}{\alpha}$. The obtained Bessel equation(Eq. 5.118) has a simple solution which satisfies the inhomogeneous boundary condition(Eq. 5.119), i.e.

$$\bar{\theta}(r,p) = \frac{\xi}{p^2}\frac{I_0(qr)}{I_0(qa)}. \tag{5.120}$$

Therefore the Inversion Theorem applied to a properly chosen contour of the integration and taking into account the double pole at $p = 0$ yields

$$\theta(r,t) = \xi\left(t - \frac{a^2 - r^2}{4\alpha}\right) + \frac{2\xi}{a\alpha}\sum_{n=1}^{\infty} e^{-\alpha\beta_n^2 t}\frac{J_0(r\beta_n)}{\beta_n^3 J_1(a\beta_n)} , \tag{5.121}$$

where β_n are the positive roots of $J_0(a\beta) = 0$. The results from the numerical simulation with material data

$$a = 0.3\ m,\ \alpha = 5.4 \times 10^{-4}\ m^2/s,\ k = 21.9\ W/(mK),\ \xi = 10.0\ K/s$$

are shown in Fig. 5.2. Temperature profiles at three different instances were extracted from the numerical solution and compared(Table 5.1) to the profiles calculated analytically using Eq. 5.121. It was found that the numerical results are within $\sim$ 4.5% of the analytical predictions(N_{elm} = 618, τ = 0.12s). Also the mesh density distribution in the domain has very significant effect on the accuracy of the numerical simulation. A gradual increase of the mesh density close to the boundary with the time dependent condition(the region with the highest thermal gradients) showed an improved accuracy and stability in the numerical scheme. Based on the computational experiments on this specific problem an empirical criterion for the local mesh refinement was developed and used later in the simulations of the phase transformations in the SMA thin films(see Section 5.6.2).

Circular cylinder with time dependent heat source

Consider the thermal problem of a stress-free cylinder with circular cross-section with time dependent heat source and subjected to isothermal boundary conditions. The conservation of energy equation is

$$\frac{\partial^2\theta}{\partial r^2}+\frac{1}{r}\frac{\partial\theta}{\partial r}+\frac{A_0}{k}e^{-\lambda t}=\frac{1}{\alpha}\frac{\partial\theta}{\partial t}\ , \tag{5.122}$$

where A_0 is a constant. The isothermal boundary condition is

$$\theta(a,t)=0\ . \tag{5.123}$$

By applying the Laplace transformation(Eq. 5.114) to Eqs. 5.122 and 5.123, we obtain the corresponding ordinary differential equation in the (r,p) space

$$\frac{\partial^2\bar\theta}{\partial r^2}+\frac{1}{r}\frac{\partial\bar\theta}{\partial r}-q^2\bar\theta=-\frac{A_0}{k(p+\lambda)}\ , \tag{5.124}$$

$$\bar\theta(a,p)=0\ . \tag{5.125}$$

The solution of the inhomogeneous Eq. 5.124 which satisfies Eq. 5.125 as well is

$$\bar\theta(r,p)=\frac{\alpha A_0}{kp(p+\lambda)}\left(1-\frac{I_0(qr)}{I_0(qa)}\right). \tag{5.126}$$

The Inversion Theorem is applied to Eq. 5.126 to obtain the temperature field

$$\theta(r,t)=\frac{\alpha A_0}{k\lambda}e^{-\lambda t}\left(\frac{J_0\left(r\sqrt{\frac{\lambda}{\alpha}}\right)}{J_0\left(a\sqrt{\frac{\lambda}{\alpha}}\right)}-1\right)- \\ \frac{2A_0\alpha}{ak}\sum_{n=1}^{\infty}e^{-\alpha\beta_n^2 t}\frac{J_0(r\beta_n)}{\beta_n(\alpha\beta_n^2-\lambda)J_1(a\beta_n)}\ , \tag{5.127}$$

where β_n are the positive roots of $J_0(a\beta) = 0$. The presence of the heat source in the consider problem (Eq. 5.122), allows us to investigate the influence of a strong nonlinearity on the performance of the numerical algorithm. Several numerical experiments, for different values of the power, A_0, and time constant, λ, of the heat source, were carried out. It was found that the time step, τ, must be chosen inversely proportional to the rate of change of the heat source

$$\tau \sim \frac{1}{|\lambda| A_0 e^{-\lambda t}} ,$$

in order to obtain optimal computational performance(lowest CPU time). The material data used in the calculation is

$$a = 0.3\ m,\ \alpha = 5.4 \times 10^{-4}\ m^2/s,\ k = 21.9\ W/(mK),$$

$$\lambda = 1.0\ s^{-1},\ A_0 = 1.0\ W/m^3\ .$$

Results from the numerical simulations are presented in Fig. 5.3. The numerical solution is compared to the analytical one (Eq. 5.127) in Table 5.2. The observed averaged computational error is $\sim 4\%(N_{elm} = 618,\ \tau = 0.12s)$.

Thermal Stresses in thin hollow disk

Consider a thin hollow disk of a linearly elastic, isotropic solid with inner radius a and outer radius b. We assume an axisymmetric temperature distribution, $\theta = \theta(r)$, as well as the following mechanical boundary conditions

$$\sigma_{rr}(a,t) = T_0 \quad , \quad \sigma_{rr}(b,t) = 0 \; . \tag{5.128}$$

We shall solve the problem assuming small strain and applying the plain stress approximation. The governing law describing the static problem above is the equilibrium equation (Eq. 5.40), which in the case of axisymmetric problems can be expressed in cylindrical coordinates as

$$\frac{d\sigma_{rr}}{dr} + \frac{\sigma_{rr} - \sigma_{\phi\phi}}{r} = 0 \; . \tag{5.129}$$

Eq. 5.129 accepts a solution in the form

$$\begin{aligned} \sigma_{rr} &= \frac{\varphi}{r} \; , \\ \sigma_{\phi\phi} &= \frac{d\varphi}{dr} \; , \end{aligned} \tag{5.130}$$

where $\varphi = \varphi(r)$ is an axisymmetric stress function. Using the Hooke's law for thermoelastic isotropic solids, the strains ε_{rr} and $\varepsilon_{\phi\phi}$ are written as

$$\begin{aligned} \varepsilon_{rr} &= \frac{1}{E}(\sigma_{rr} - \nu\sigma_{\phi\phi}) + \alpha\Delta\theta \; , \\ \varepsilon_{\phi\phi} &= \frac{1}{E}(\sigma_{\phi\phi} - \nu\sigma_{rr}) + \alpha\Delta\theta \; , \end{aligned} \tag{5.131}$$

where ν is the Poisson ratio and α is the volumetric coefficient of thermal expansion. Following the definition of ε_{rr} and $\varepsilon_{\phi\phi}$

$$\varepsilon_{rr} = \frac{du_r}{dr} \; ,$$

$$\varepsilon_{\phi\phi} = \frac{u_r}{r} \,, \tag{5.132}$$

and eliminating the radial displacement u_r from Eqs. 5.132 we obtain a simplified compatibility relation

$$\frac{d}{dr}\left(r\varepsilon_{\phi\phi}\right) - \varepsilon_{rr} = 0 \,. \tag{5.133}$$

Eq. 5.133 with Eqs. 5.130 and 5.131 result in the following equation for the stress function φ.

$$\frac{d}{dr}\left(\frac{1}{r}\frac{d}{dr}\left(r\varphi\right)\right) = -\alpha E \frac{d}{dr}\left(\Delta\theta\right) \,. \tag{5.134}$$

The solution of the Eq. 5.134 is

$$\begin{aligned} \sigma_{rr} &= -\frac{\alpha E}{r^2}\int_a^r \left(\Delta\theta\right) r dr + \frac{C_1}{2} + \frac{C_2}{r^2} \,, \\ \sigma_{\phi\phi} &= \alpha E\left[-\left(\Delta\theta\right) + \frac{1}{r^2}\int_a^r \left(\Delta\theta\right) r dr\right] + \frac{C_1}{2} + \frac{C_2}{r^2} \,, \end{aligned} \tag{5.135}$$

where the constants C_1 and C_2 are determined from the boundary conditions Eqs. 5.128

$$\begin{aligned} C_1 &= \frac{2}{b^2 - a^2}\left(-a^2 T_0 + \alpha E \int_a^b \left(\Delta\theta\right) r dr\right) \,, \\ C_2 &= \frac{a^2}{b^2 - a^2}\left(b^2 T_0 - \alpha E \int_a^b \left(\Delta\theta\right) r dr\right) \,. \end{aligned} \tag{5.136}$$

The following temperature profile, $\Delta\theta$, is chosen

$$\Delta\theta = \begin{cases} \theta_{ampl}\ e^{\lambda(r-a)} & r \le c \\ \theta_{ampl}\ e^{\lambda(2c-r-a)} & r > c \end{cases} \,. \tag{5.137}$$

Notice from Eq. 5.137 that $\Delta\theta$ is a continuous function throughout the domain, $a \leq r \leq b$, whereas its first derivative suffers a jump at $r = c$. This corresponds to a possible physical problem where there is a line heat source/sink at $r = c$. The explicit form of Eqs. 5.135 is obtained after the integration of temperature distribution profiles (Eq. 5.137).

$$\int_a^r (\Delta\theta)\, r dr = \begin{cases} I_1(r) & r \leq c \\ I_2(r) & r > c \end{cases} , \tag{5.138}$$

where

$$\begin{aligned} I_1(r) &= \frac{\theta_{ampl}}{\lambda^2}\left(e^{\lambda(r-a)}(\lambda r - 1) - (\lambda a - 1)\right) , \\ I_2(r) &= I_1(r) - \frac{\theta_{ampl}}{\lambda^2}\left(e^{\lambda(c-r)}(\lambda r + 1) - (\lambda c + 1)\right) . \end{aligned} \tag{5.139}$$

The test problem described in this section is intended to verify the accuracy of the two dimensional thermoelastic part of the numerical algorithm. The selected thermal field mimics the presence of a heat source(the first derivative of the temperature suffers jump at $r = c$). The material parameters used in the calculations are

$$a = 0.3\ m,\ b = 0.5\ m,\ \alpha = 7.0 \times 10^{-6}\ K^{-1},\ E = 1.0 \times 10^{7}\ Pa,$$

$$T_0 = -500\ Pa,\ \theta_{ampl} = 100.0\ K,\ \lambda = 10.0\ m^{-1} .$$

Figures s 5.4, 5.5 and 5.6 show the numerically calculated stress/temperature distributions for three different locations of the heat source, $c = 0.35\ m, c = 0.40\ m, c = 0.45\ m$. In Table 5.3, the numerical results($N_{elm} = 618$, $\tau = 0.12s$) for the three different locations of the heat source are compared to the analytical solution defined with Eqs. 5.136, 5.135 and 5.139.

5.6.2 Accuracy and stability of the algorithm

The accuracy and stability analysis will be carried out on 2D test problems described above. Two of the problems are transient problems, and our goal is to investigate the accuracy and stability of the time stepping and space discretization schemes.

In Section 5.5.5 we defined three time discretization schemes for the heat conduction equation: explicit($\varrho = 0$); implicit($\varrho = 1$) and Crank-Nicholson(CN)($\varrho = 0.5$). For the three schemes stability conditions can be derived by applying the linear von Neumann stability analysis(see Appendix C.4). In the case of explicit scheme(($\varrho = 0$)) the stability condition is defined with Eq. C.24 in Appendix C.4. The other two cases, the implicit and the CN schemes are unconditionally stable(see Appendix C.4). Note that the CN scheme($\varrho = 0.5$) satisfies the lower limit for unconditional stability, therefore the result derived through the von Neumann linear analysis is exact only for the conditions at which it was obtained(finite differences method and uniform mesh in x and y directions). For the considered problem the stability of the CN scheme will be verified by numerical experiments on the solutions of the test problems. The results presented here are obtained using the first test problem - circular cylinder with time dependent boundary condition. This problem was selected as the transient problem closest to the real thermal problem in SMA phase transformation. To verify the order of discretization(truncation error) and the convergence of the rate of the CN scheme the average computational error, *err*, must be computed as function of the magnitude of the time step, τ, (see Fig. 5.7). The averaged error *err* is defined as

$$err = \frac{1}{N}\sum_{i}^{N}\frac{|\theta_i - \theta_i^{theo}|}{\theta_i^{theo}}\,, \tag{5.140}$$

where θ_i and θ_i^{theo} are the nodal values of the computed and theoretical temperatures and N is the total number of nodes. The computations were carried out at constant number of elements $N_{elm} = 2404$. Clearly the error decreases as the time step decreases. The obtained data was fitted with a second order polynomial represented by the solid line in Fig. 5.7.

The special discretization is the other factor that influences the accuracy and stability of the numerical algorithm. The numerical experiments performed here are intended to investigate the influence of the mesh density on the averaged computational error(Eq. 5.140). In the considered 2D problem the characteristic element size is

$$h_{el} = \sqrt{S_{el}}\,, \tag{5.141}$$

where S_{el} is the averaged area of a single element. By using the relation

$$S_{el} = \frac{S_{tot}}{N_{elm}}\,,$$

one can easily obtain

$$h \sim \frac{1}{\sqrt{N_{elm}}}\,.$$

Obviously an algorithm of order $O(h^n)$ should lead to hyperbolic error decrease as the number of elements increases. In the case of $n = 2$ should behave as $O(1/N_{elm})$. A plot of the averaged error as a function of N_{elm} is shown in Fig. 5.7. As the number of elements increases the error drops quickly until the N_{elm} reaches 1000 elements, beyond that value the error decreases rather slowly. The time step used in the calculation presented in Fig. 5.7 is $\tau = 0.12s$.

Refinement criterion

The computations involved in the test problems are relatively inexpensive, and therefore they were used for determining a criterion for mesh refinement. The derived empirical relation between the element size and the local gradients was used later as mesh refinements tool for code optimization. In an optimal mesh the distribution of the local error should be equal between all elements. Thus if the permissible error is specified, err_p, the ratio,

$$\xi_i = \frac{err_i}{err_p} \, , \tag{5.142}$$

can be used as a refinement criterion. The refinement should take place whenever

$$\xi_i > 1 \, .$$

Recall that the local error is related to the characteristic element size as

$$err_i \sim h_i^n \, , \tag{5.143}$$

where n is the order of approximation. Next, Eq. 5.142 combined with Eq. 5.143 yields [12]

$$h_i^{new} = \frac{h_i}{\xi^{\frac{1}{n}}} \tag{5.144}$$

For 2D problems the application of the criterion in Eq. 5.144 is more convenient in the form

$$S_i^{new} = \frac{S_i}{\xi^{\frac{2}{n}}} , \tag{5.145}$$

where S_i is the area of the i^{th} element. The final step in determining the refinement criterion is the derivation of an empirical correlation between the local error, err_i, and the physical fields in the specific problem. In the phase transformations in SMA, the temperature gradient close to the phase boundary is of crucial importance for the velocity of the phase front propagation. This is the physical field that is used to estimate the local error, err_i.

$$err_i = f(|\nabla\theta|) . \tag{5.146}$$

After expanding err_i into series up to a linear term, Eq, 5.146 reads

$$err_i = a|\nabla\theta| + b , \tag{5.147}$$

where the empirical constants $a = 3.7054 \times 10^{-4}\ m/K$ and $b = 0.0062$ were determined from the first test problem and invoking the following definitions of local error and temperature gradient

$$err_i = \frac{|\theta_i - \theta_i^{theo}|}{\theta_i^{theo}} \quad \text{and} \quad |\nabla\theta| = \frac{d\theta}{dr} .$$

All the simulations presented in the next section were performed by applying the criterion defined with Eqs. 5.147, 5.145 and 5.142. At each mesh regeneration an error limit of $err_p = 2.5\%$ was imposed.

5.7 Simulation and prediction of the pseudoelasticity and reorientation in SMA thin films

In this section we use the theoretical framework developed in Sections 5.2-5.4 to simulate and predict the stress-strain response of SMA thin films. The numerical solution of the resulting mathematical problem utilizes the algorithm described in Section 5.5.

5.7.1 Material Parameters

In the simulations described below, we consider a square plate of Cu-13.7%Al-4.18%Ni(wt%). A list of the material parameters used in the simulation is given in Table 5.4. The values of the components of the phase transformation strains of the 24 martensitic variants are taken from Fang et. al. [1], and are given in Table 5.5. The values in Fang et. al. [1] are specified in the coordinate system , $(\vec{e}_0)$, of the parent phase(austenite). In order to obtain the phase transformation strains in the laboratory coordinate system , $(\vec{e}_n)$, the law for transformation of second order tensors must be used

$$E'_{ij} = \beta_{ir}\beta_{js}E_{rs} \ , \tag{5.148}$$

where β_{ij} is the transformation tensor determined as

$$\beta_{ij} = \vec{e}_{n(i)} \cdot \vec{e}_{o(j)} = \begin{pmatrix} -0.0925 & 0.3698 & 0.9245 \\ 0.4268 & 0.8536 & -0.2988 \\ -0.8996 & 0.3669 & -0.2368 \end{pmatrix} , \tag{5.149}$$

and the directional cosines of the basis vectors, $\vec{e}_n$, in austenite basis , $(\vec{e}_0)$, are

$$\vec{e}_{n(1)} = (-0.0925, 0.3698, 0.9245) \ ,$$

$$\vec{e}_{n(2)} = (0.4268, 0.8536, -0.2988) \ ,$$

$$\vec{e}_{n(3)} = (-0.8996, 0.3669, -0.2368) \ .$$

The values of the austenitic and martensitic elastic constants (see Appendix C for the notation) follow from the experimental measurements of Robertson [24].

1. Austenitic Parent phase, cubic(BCC)

$$\lambda_{1111} = \Upsilon = 141 \ GPa \ , \ \lambda_{1122} = \Pi = 125 \ GPa \ , \ \lambda_{2323} = \Xi = 97 \ GPa \ .$$

2. Martensitic phase, orthorhombic

$$\lambda_{1111} = 205\ GPa\ ,\ \lambda_{2222} = 189\ GPa\ ,\ \lambda_{3333} = 141\ GPa\ ,$$

$$\lambda_{2323} = 62.6\ GPa\ ,\ \lambda_{1313} = 54.9\ GPa\ ,\ \lambda_{1212} = 19.7\ GPa\ ,$$

$$\lambda_{1122} = 45.5\ GPa\ ,\ \lambda_{1133} = 125\ GPa\ ,\ \lambda_{2233} = 124\ GPa\ .$$

The stiffness tensor for any other variant is obtained from the one above with corresponding orthogonal transformations [1]. Once the components of the stiffness tensor for each variant are calculated in the coordinate system of the parent phase, they should be transformed to the laboratory coordinate system. A detailed description of the transformation procedure of the fourth order tensor is given in Appendix C.1.

5.7.2 Results and discussion

The sequence of events underlying all of the calculations to be described below is as follows: we consider a thin plate with thermally insulated ends that is initially entirely in one phase. The initial phase is austenite in the case of pseudoelasticity(PE) due to A→M phase transformation, and predetermined variant of martensite in the case of PE due to reorientation. The initial temperature is uniform and is the same as that of the surrounding environment.

The averaged global stress on the thin film in x and y directions are denoted as

$$\bar{\sigma}_{xx} = \frac{1}{L_y} \int_0^{L_y} \sigma_{xx}(L_x, y)\, dy$$

and

$$\bar{\sigma}_{yy} = \frac{1}{L_x} \int_0^{L_x} \sigma_{yy}(x, L_y)\, dx\ ,$$

where L_x and L_y are the undeformed lengths of the edges of the thin film in x and y directions. A similar definition for the averaged strain, $\bar{\varepsilon}_{xx}$ and $\bar{\varepsilon}_{yy}$, is used. The plate is uniformly pre-stressed(tensile stress) in y direction and subjected to a constant deformation rate $\dot{\Delta} > 0$ in x direction. At some later instant Eqs. 5.40 and 5.46 are satisfied and a martensitic variant is nucleated at the center of the plate(for the implementation of the variant selection criterion see Section 5.5.2). The shape of the formed nucleus is assumed to be circular with radius 1/100 of the characteristic dimension of the plate. The formed phase boundary propagates outwards as the deformation increases. When the deformation reaches a predetermined value the unloading takes place. The unloading is carried out at constant deformation rate $-\dot{\Delta}$. The temperature of the surrounding environment remains fixed during the process.

Now we turn to the predictions of the thermomechanical response of the a single crystal CuAlNi plate by the theory developed in Sections 5.2-5.4. The presented results include calculations of the overall stress-strain curves for three different pre-stress values of $\bar{\sigma}_{yy}$. The three values of $\bar{\sigma}_{yy}$ are 0 MPa, 40 MPa and 160 MPa. At the first two values of $\bar{\sigma}_{yy}$ the SMA plate is initially in austenitic phase, whereas at $\bar{\sigma}_{yy} = 160$ MPa the plate is initially in martensitic phase(variant No. 14, see Table 5.5). Figs. 5.9 and 5.12 show comparison between the predicted and experimentally measured [1] stress-strain curves for $\bar{\sigma}_{yy} = 0$ MPa and $\bar{\sigma}_{yy} = 40$ MPa respectively. In both cases the stress increases linearly from zero to the stress at which the formation of martensite is detected. Based on the selection criterion (see Section 5.5.2) the martensitic variant, which is detected, is variant No. 9(Table 5.5). The shape of the initial inclusion is a circle, which quickly evolves into ellipse with high R_y/R_x ratio (R_x and R_y are the semimajor and semiminor axes respectively). For example, see Figs. 5.15 and 5.16 for the shape of the martensite at $\bar{\varepsilon}_{xx} = 1.0\%$ and 3.5% respectively, both at $\bar{\sigma}_{yy} = 40$ MPa. As the deformation increases, the stress remains almost constant (Figs. 5.9 and 5.12) until the phase boundary gets close to the geometrical boundaries $x = 0$ and $x = 3.0$. Because of the thermal insulation conditions applied to the boundaries the local temperature increases, which requires higher stress, in order to continue the transformation. As a result, an increase in the stress at the end of the transformation can be observed. Once the deformation is reversed the system goes through a stage of elastic relaxation, followed by reverse transformation at almost constant stress until the martensitic phase has completely transformed to austenite. For both pre-stress values, $\bar{\sigma}_{yy} = 0\ MPa$ and $\bar{\sigma}_{yy} = 40\ MPa$, the results from the numerical simulation are in a good agreement with the experimental data(see Figs. 5.9 and 5.12)). In both cases the formation of one variant of martensite, i.e. variant No 9, was detected. The formation of the same single variant at the specified conditions agrees with the analytical results reported by Fang et. al.([1]).

The martensitic volume fraction, defined as V_m/V_{tot}(V_m is the total volume of martensite, V_{tot} is the total domain volume), is presented as a function of $\bar{\sigma}_{xx}$ in Figs. 5.10 and 5.13. In both cases about 65% of the austenite was transformed to martensite. Beyond this stage, a continuation of the deformation leads to exponential increase in the stress and arrest of the phase transformation ($\Delta V_m \approx 0$). This phenomenon reflects the constraint imposed by the film edges to further transformation.

Although the presence of pre-stress($\bar{\sigma}_{yy} = 40\ MPa$) does not affect the total transformation to martensite significantly, it reduces the time for completing a loading-unloading cycle and also the stresses at which the transformations occur. In the particular case, when tensile forces are applied in y direction ($\bar{\sigma}_{yy} = 40\ MPa$) the time necessary for completing a cycle of transformation is reduced by $\sim$ 13% and the transformation stresses by $\sim 5\ MPa$ (Figs. 5.11 and 5.14).

Figures 5.17-5.30 show two series of 3D plots which depict various thermomechanical characteristics of the phase transformation of the pre-stressed thin film ($\bar{\sigma}_{yy} = 40\ MPa$) at two instances - when $\bar{\varepsilon}_{xx} = 1.0\%$ and $\bar{\varepsilon}_{xx} = 3.5\%$, during the $A \rightarrow M$ transformation. When $\bar{\varepsilon}_{xx} = 1.0\%$ the phase transformation boundary did not reach the geometrical boundaries at $y = 0$ and $y = 3.0$ (Fig. 5.15). The elliptical martensitic inclusion, strained by ε_T is accommodated by the parent phase, which creates significant concentrations of σ_{xx} within the SMA film and especially close to the top(y_{max}) and bottom(y_{min}) of the inclusion(see Fig. 5.17 and 5.18). Further, high stresses at the top and the bottom of the inclusion, induce high velocity of propagation of the phase boundary in y direction. As well, the computed distributions of σ_{yy} and σ_{xy} are presented in Figs. 5.19-5.22. We noted in Section 5.4 that the A→M phase transformation is accompanied with release of latent heat. The presence of moving heat source increases the temperature within the inclusion forming a characteristic "top hat" profile(Figs. 5.23 and 5.24). When $\bar{\varepsilon}_{xx} = 3.5\%$, the martensitic inclusion reached the geometrical boundaries at $y = 0$ and $y = 3.0$, and spans the whole film in y direction(see Fig. 5.16). For this specific shape of the inclusion, σ_{xx} is almost uniform in "y" direction (see Figs. 5.25 and 5.26). The accommodation of the strained inclusion in y direction leads to significant compression (see the plot of σ_{yy} in Figs. 5.27 and 5.28) and relatively high shear stress close to the geometrical boundaries(see Figs. 5.29 and 5.30).

In the simulations considered so far, the tensile stress, $\bar{\sigma}_{yy}$, was not high enough to induce phase transformation before $\bar{\sigma}_{xx}$ was applied. However, when $\bar{\sigma}_{yy}$ is increased up to 160 MPa, a phase transformation is observed. As a result of this phase transformation, the SMA plate is entirely in the martensitic phase(variant No. 14, Table 5.5) even before any deformation in x direction is imposed. As a deformation rate in x direction is imposed, a formation of new variant of martensite is observed. This process is known as "reorientation". The results of the simulation of the reorientation and comparison with experimental data [1] is presented in Fig. 5.31. The reorientation process starts with an appearance of a new martensitic variant - No 15. The observed $M14 \rightarrow M15$ transformation("M" implies martensitic variant) is relatively fast with small transformation strain in x direction. As the deformation increases further the appearance of another variant of martensite No 9 is detected. In the three component system $M14$, $M15$, $M9$ the transformation process $M14 \rightarrow M15$ is practically stopped and only $M15 \rightarrow M9$ transformation is observed. During unloading, the reverse transformation takes place. The transformation $M9 \rightarrow M15$ leads to disappearance of the $M9$ followed by $M15 \rightarrow M14$ and eventually the whole SMA film is restored to its initial martensitic state - variant $M14$. If the tensile deformation is reversed to compression another reorientation transformation is observed $M14 \rightarrow M5$. In this case the further increase in the deformation does not induce a third variant and the forward and backward transformations are between $M14$ and $M5$. The detected variants in the simulations coincide with the ones analytically predicted by Fang et. al. [1].

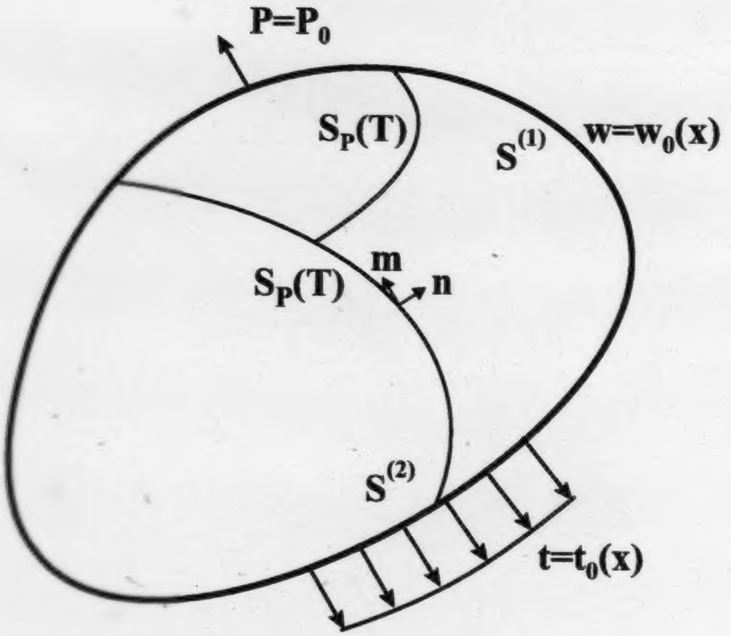
P=P_0
S_P(T)
S^(1)
w=w_0(x)
m
n
S_P(T)
S^(2)
t=t_0(x)

Figure 5.1: Schematic of a thermoelastic system undergoing phase transformation

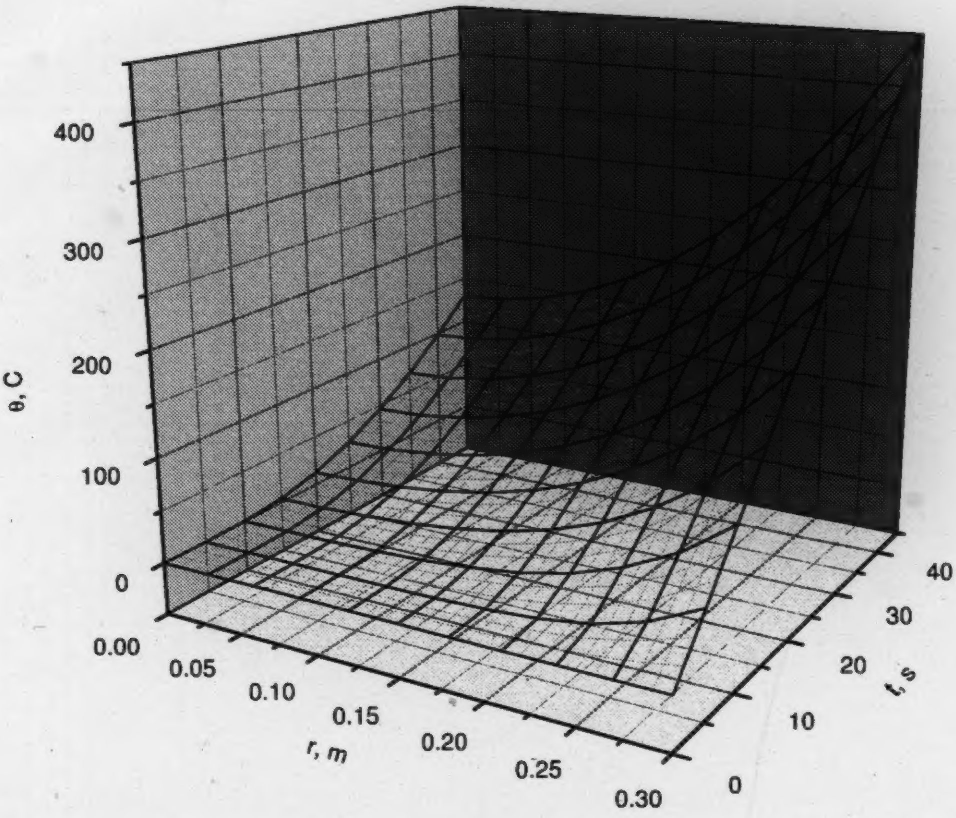

Figure 5.2: Numerical simulation of the temperature field θ in circular cylinder with time dependent boundary conditions

r, m	$t = 10s$		$t = 25s$		$t = 40s$	
	Analytical	Numerical	Analytical	Numerical	Analytical	Numerical
0.0	0.5024	0.5245	26.6390	28.1120	98.5209	102.2211
0.03	0.6305	0.6724	28.0573	29.6072	101.0305	104.8303
0.06	1.0810	1.1655	32.4227	34.1610	108.6305	112.6312
0.09	2.0705	2.2415	40.0637	42.0911	121.5306	125.8102
0.12	4.0166	4.3124	51.5164	54.0150	140.0697	144.8301
0.15	7.6103	8.2921	67.5063	70.5790	164.7001	169.9863
0.18	13.8923	15.1280	88.9215	92.7331	195.9663	201.9251
0.21	24.3031	26.1770	116.7759	121.4103	234.4796	241.1320
0.24	40.6760	43.2050	152.1641	157.7211	280.8892	288.2653
0.27	65.1501	68.5980	196.2079	202.0201	335.8516	343.0867
0.3	100.0	100.0	250.0	250.0	400.0	400.0

Table 5.1: Numerical and analytical values of the temperature, θ(deg C), in circular cylinder with time dependent boundary conditions

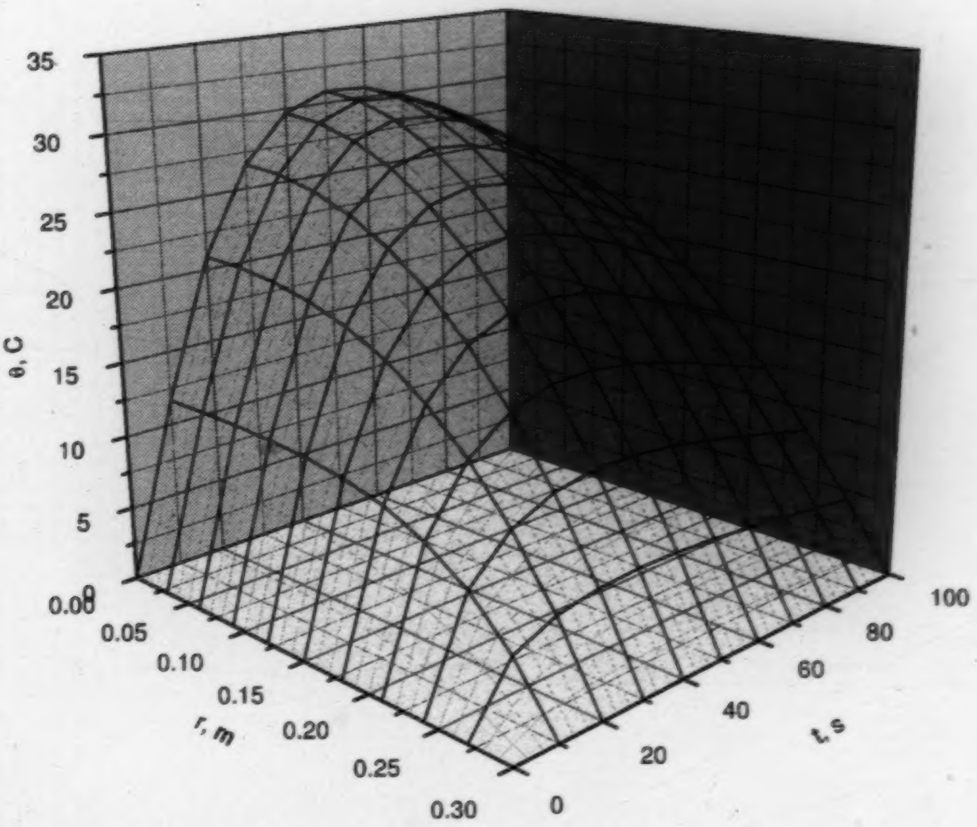

Figure 5.3: Numerical simulation of the temperature field θ in circular cylinder with time dependent heat source

r, m	$t = 30s$		$t = 60s$		$t = 90s$	
	Analytical	Numerical	Analytical	Numerical	Analytical	Numerical
0.0	26.6475	26.0150	30.6651	29.6081	26.58281	25.4861
0.03	26.4434	25.8051	30.3579	29.2992	26.2995	25.2033
0.06	25.8218	25.1712	29.4359	28.3800	25.4519	24.3672
0.09	24.7549	24.0882	27.8975	26.8521	24.0457	22.9842
0.12	23.1985	22.5041	25.7411	24.7020	22.0912	21.0551
0.15	21.0949	20.3732	22.9653	21.9460	19.6028	18.6083
0.18	18.3772	17.6220	19.5715	18.5741	16.5997	15.6511
0.21	14.9739	14.1931	15.5642	14.6053	13.1059	12.2210
0.24	10.8155	10.0163	10.9536	10.0466	9.1505	8.3408
0.27	5.8401	5.1155	5.75694	4.9948	4.7684	4.1128
0.3	0.0	0.0	0.0	0.0	0.0	0.0

Table 5.2: Numerical and analytical values of the temperature, θ(deg C), in circular cylinder with time dependent heat source

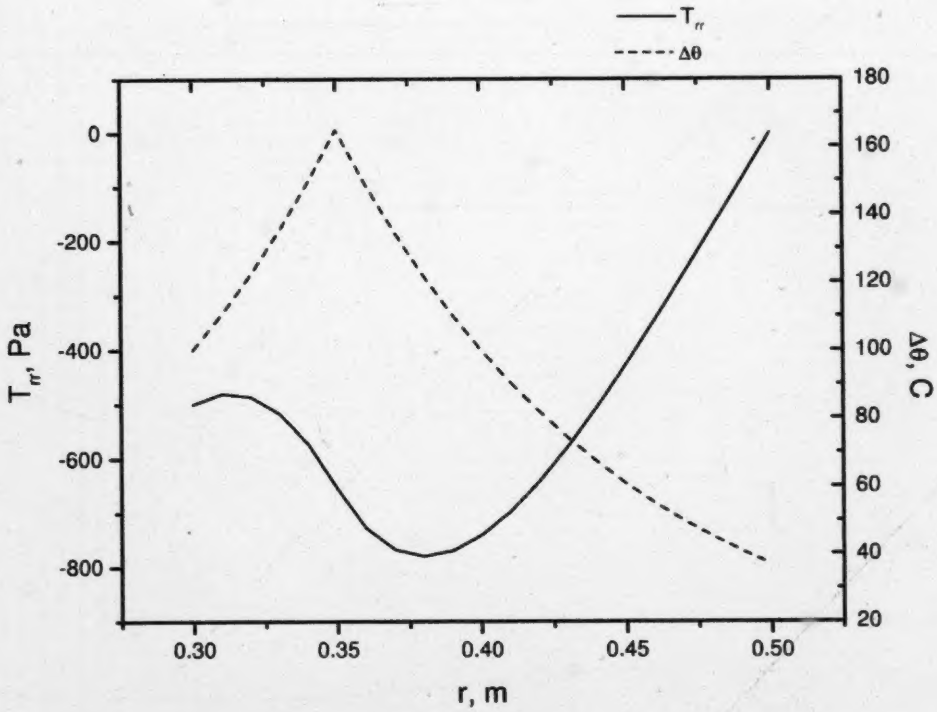

Figure 5.4: Numerical simulation of the stress, T_{rr}, and temperature $\Delta\theta$ distribution within a hollow disc with heat source at $c = 0.35\ m$.

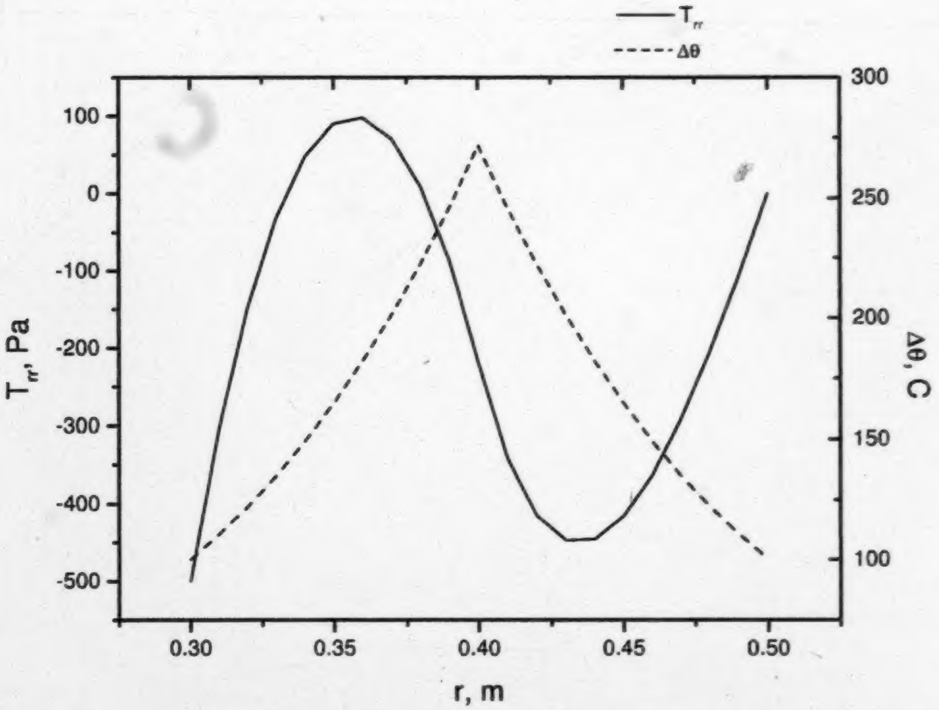

Figure 5.5: Numerical simulation of the stress, T_{rr}, and temperature $\Delta\theta$ distribution within a hollow disc with heat source at $c = 0.4\ m$.

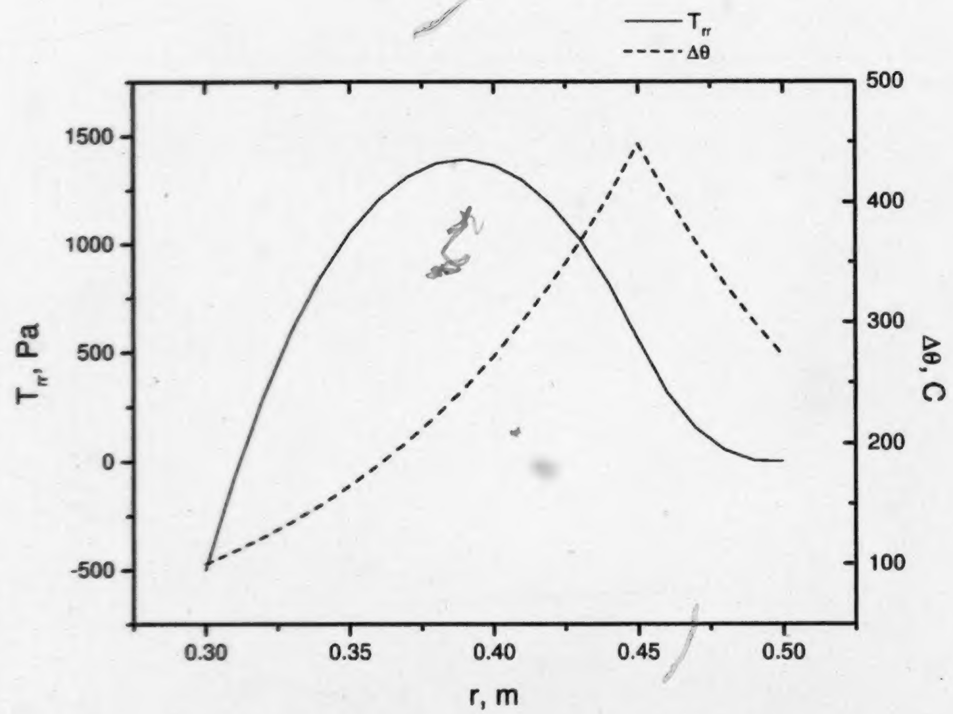

Figure 5.6: Numerical simulation of the stress, T_{rr}, and temperature $\Delta\theta$ distribution within a hollow disc with heat source at $c = 0.45\ m$.

r, m	$c = 0.35\ m$		$c = 0.40\ m$		$c = 0.45\ m$	
	Analytical	Numerical	Analytical	Numerical	Analytical	Numerical
0.3	-500.0	-500.0	-500.0	-500.0	-500.0	-500.0
0.32	-486.5509	-488.9836	-146.8271	-147.8548	291.7956	294.7205
0.34	-573.4282	-576.8687	47.8503	48.2809	849.9928	854.2427
0.36	-727.7065	-730.6173	97.7294	98.1203	1204.5050	1209.3230
0.38	-780.0437	-783.9439	8.6900	8.8334	1373.2770	1378.7701
0.4	-741.1822	-744.1469	-219.8290	-221.3678	1364.8720	1371.6963
0.42	-642.5104	-646.3654	-415.1502	-416.8108	1180.0350	1184.7551
0.44	-505.9490	-508.4787	-445.7150	-448.8350	812.5319	815.7820
0.46	-346.7986	-348.5325	-363.6191	-365.8008	317.2563	318.5253
0.48	-175.7005	-176.5790	-206.1507	-207.5937	51.6833	52.0967
0.5	0.0	0.0	0.0	0.0	0.0	0.0

Table 5.3: Numerical and analytical values of T_{rr}(Pa) at three different locations of the heat source.

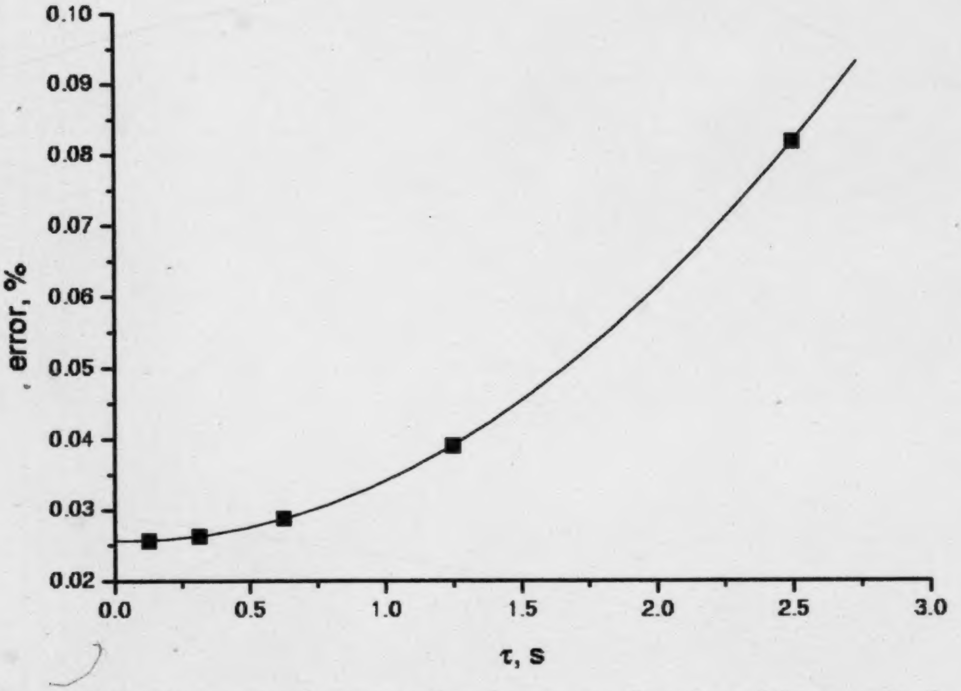

Figure 5.7: The averaged computational error as a function of the magnitude of the time step, τ ($N_{elm} = 2404$).

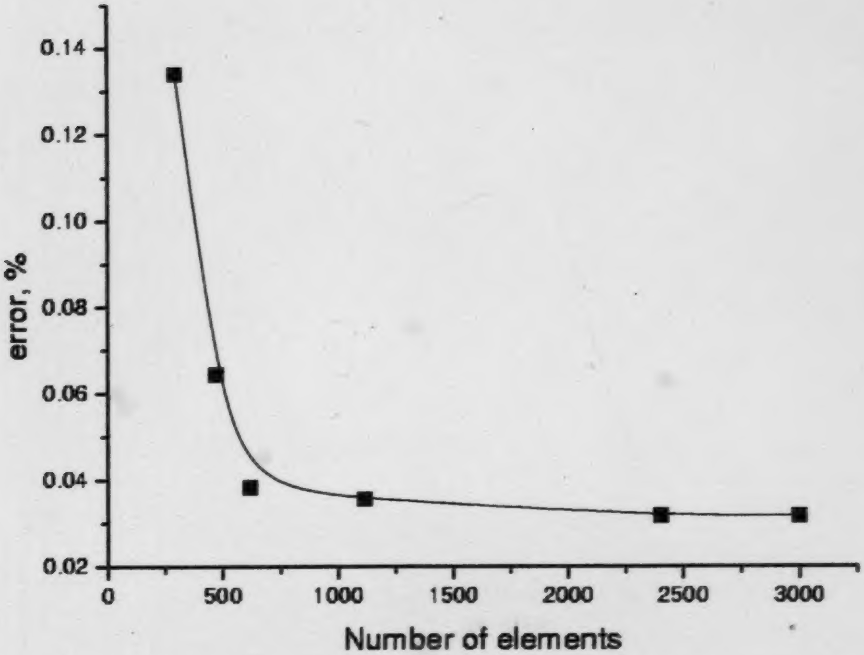

Figure 5.8: The averaged computational error as a function of the number of elements, N_{elm} ($\tau = 0.12s$).

Parameter	Symbol	Value	Ref.
Length	L_x, L_y	$0.03\ m$	-
Mass density	ρ_0	$7120\ kg/m^3$	[25]
Heat capacity	$C_{Austenite}$	$2.797 \times 10^6\ J/(m^3K)$	[26]
	$C_{Martensite}$	$2.819 \times 10^6\ J/(m^3K)$	[26]
Coefficient of thermal expansion	α	$10^{-5}\ K^{-1}$	[8]
Latent heat of phase transformation	λ_{ph}	$0.063\ GJ/m^3$	[27]
Thermal conductivity	$k_{Austenite}$	$47\ W/(mK)$	*
	$k_{Martensite}$	$35\ W/(mK)$	*
Equilibrium temperature	θ_0	$253.5\ K$	[1]
Ambient temperature	θ_{amb}	$300\ K$	-
Convective coefficients	h_L	$93\ W/(m^2K)$	*
	h_b	0	*
Applied deformation rate	$\dot{\Delta}_{PE}$	$2.1 \times 10^{-7}\ m/s$	*
	$\dot{\Delta}_{reor}$	$1.1 \times 10^{-8}\ m/s$	-
Time increment	τ	$2.2 \times 10^{-5}\ s$	-
Number of elements	N	~ 20000	-
Tolerance	ε_{tol}	10^{-5}	-

Table 5.4: List of material, geometric, numerical and input parameters. The symbol, '*', indicates that the corresponding parameters follow from the simulation in Fig. 5.12

Variant No	E_{ph11}	E_{ph12}	E_{ph22}	E_{ph13}	E_{ph23}	E_{ph33}
1	4.61625×10^{-4}	-6.86274×10^{-4}	-1.05792×10^{-1}	6.84996×10^{-3}	-8.66572×10^{-3}	1.01624×10^{-1}
2	4.61625×10^{-4}	6.86274×10^{-4}	-1.05792×10^{-1}	6.84996×10^{-3}	8.66572×10^{-3}	1.01624×10^{-1}
3	4.61625×10^{-4}	6.86274×10^{-4}	-1.05792×10^{-1}	-6.84996×10^{-3}	-8.66572×10^{-3}	1.01624×10^{-1}
4	4.61625×10^{-4}	-6.86274×10^{-4}	-1.05792×10^{-1}	-6.84996×10^{-3}	8.66572×10^{-3}	1.01624×10^{-1}
5	4.61625×10^{-4}	6.84996×10^{-3}	1.01624×10^{-1}	-6.86274×10^{-4}	-8.66572×10^{-3}	-1.05792×10^{-1}
6	4.61625×10^{-4}	-6.84996×10^{-3}	1.01624×10^{-1}	-6.86274×10^{-4}	8.66572×10^{-3}	-1.05792×10^{-1}
7	4.61625×10^{-4}	-6.84996×10^{-3}	1.01624×10^{-1}	6.86274×10^{-4}	-8.66572×10^{-3}	-1.05792×10^{-1}
8	4.61625×10^{-4}	6.84996×10^{-3}	1.01624×10^{-1}	6.86274×10^{-4}	8.66572×10^{-3}	-1.05792×10^{-1}
9	-1.05792×10^{-1}	-6.86274×10^{-4}	4.61625×10^{-4}	-8.66572×10^{-3}	6.84996×10^{-3}	1.01624×10^{-1}
10	-1.05792×10^{-1}	6.86274×10^{-4}	4.61625×10^{-4}	-8.66572×10^{-3}	-6.84996×10^{-3}	1.01624×10^{-1}
11	-1.05792×10^{-1}	6.86274×10^{-4}	4.61625×10^{-4}	8.66572×10^{-3}	6.84996×10^{-3}	1.01624×10^{-1}
12	-1.05792×10^{-1}	-6.86274×10^{-4}	4.61625×10^{-4}	8.66572×10^{-3}	-6.84996×10^{-3}	1.01624×10^{-1}
13	-1.05792×10^{-1}	-8.66527×10^{-3}	1.01624×10^{-1}	-6.86274×10^{-4}	6.84996×10^{-3}	4.61625×10^{-4}
14	-1.05792×10^{-1}	8.66527×10^{-3}	1.01624×10^{-1}	-6.86274×10^{-4}	-6.84996×10^{-3}	4.61625×10^{-4}
15	-1.05792×10^{-1}	8.66527×10^{-3}	1.01624×10^{-1}	6.86274×10^{-4}	6.84996×10^{-3}	4.61625×10^{-4}
16	-1.05792×10^{-1}	-8.66527×10^{-3}	1.01624×10^{-1}	6.86274×10^{-4}	-6.84996×10^{-3}	4.61625×10^{-4}
17	1.01624×10^{-1}	6.84996×10^{-3}	4.61625×10^{-4}	-8.66572×10^{-3}	-6.86274×10^{-4}	-1.05792×10^{-1}
18	1.01624×10^{-1}	-6.84996×10^{-3}	4.61625×10^{-4}	-8.66572×10^{-3}	6.86274×10^{-4}	-1.05792×10^{-1}
19	1.01624×10^{-1}	-6.84996×10^{-3}	4.61625×10^{-4}	8.66572×10^{-3}	-6.86274×10^{-4}	-1.05792×10^{-1}
20	1.01624×10^{-1}	6.84996×10^{-3}	4.61625×10^{-4}	8.66572×10^{-3}	6.86274×10^{-4}	-1.05792×10^{-1}
21	1.01624×10^{-1}	-8.66572×10^{-3}	-1.05792×10^{-1}	6.84996×10^{-3}	-6.86274×10^{-4}	4.61625×10^{-4}
22	1.01624×10^{-1}	8.66572×10^{-3}	-1.05792×10^{-1}	6.84996×10^{-3}	6.86274×10^{-4}	4.61625×10^{-4}
23	1.01624×10^{-1}	8.66572×10^{-3}	-1.05792×10^{-1}	-6.84996×10^{-3}	-6.86274×10^{-4}	4.61625×10^{-4}
24	1.01624×10^{-1}	-8.66572×10^{-3}	-1.05792×10^{-1}	-6.84996×10^{-3}	6.86274×10^{-4}	4.61625×10^{-4}

Table 5.5: Transformation strains of the 24 variants [1]

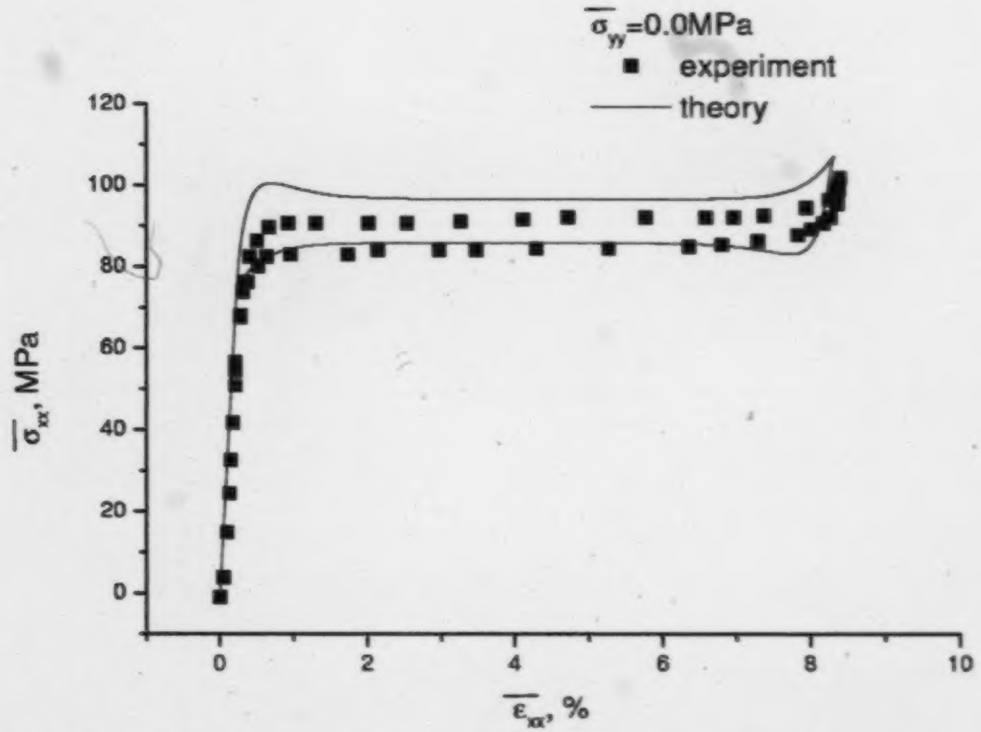

Figure 5.9: Average stress, $\bar{\sigma}_{xx}$, vs. average strain, $\bar{\varepsilon}_{xx}$, comparison with experimental data [1], $\bar{\sigma}_{yy} = 0\ MPa$.

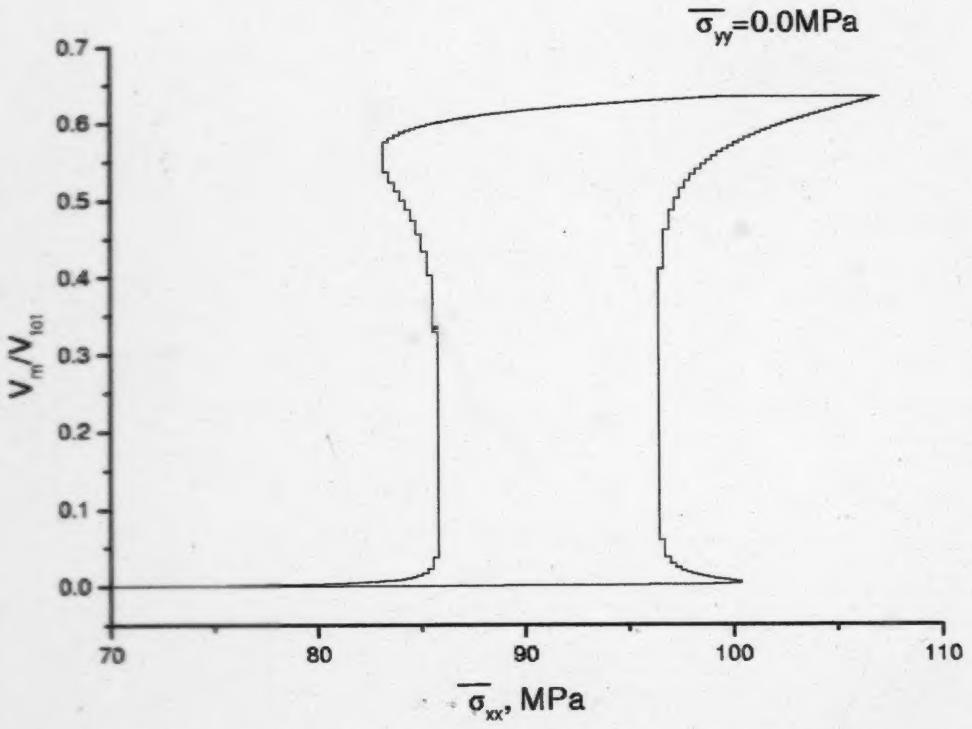

Figure 5.10: Martensitc volume fraction, V_m/V_{tot} as a function of the average stress, $\bar{\sigma}_{xx}$, $\bar{\sigma}_{yy} = 0\ MPa$.

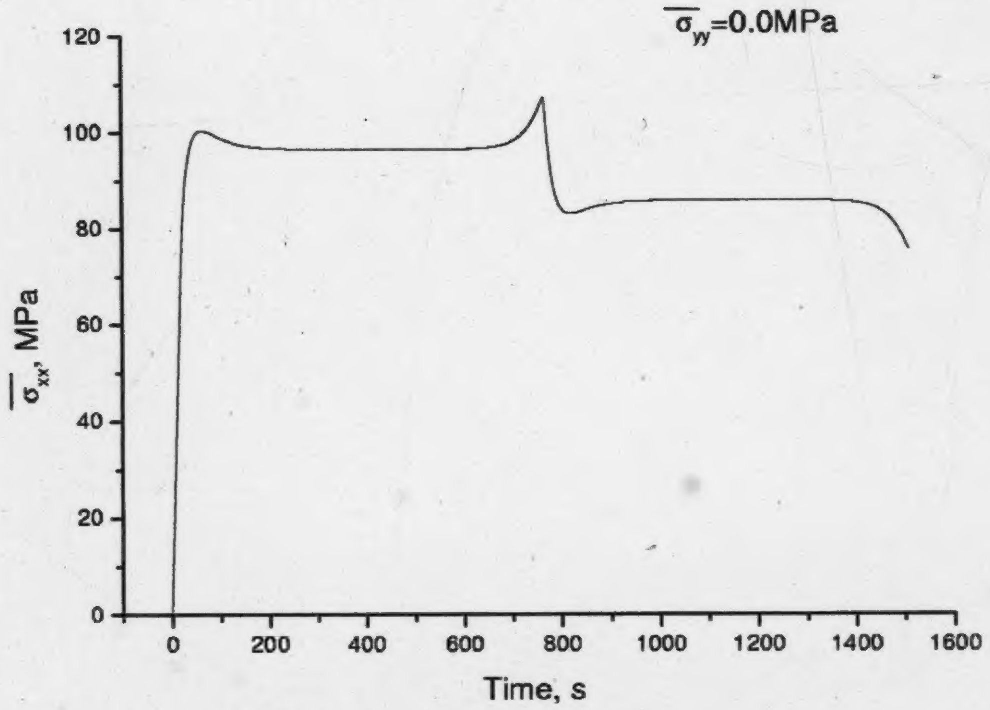

Figure 5.11: Average stress, $\bar{\sigma}_{xx}$, evolution, $\bar{\sigma}_{yy} = 0\ MPa$.

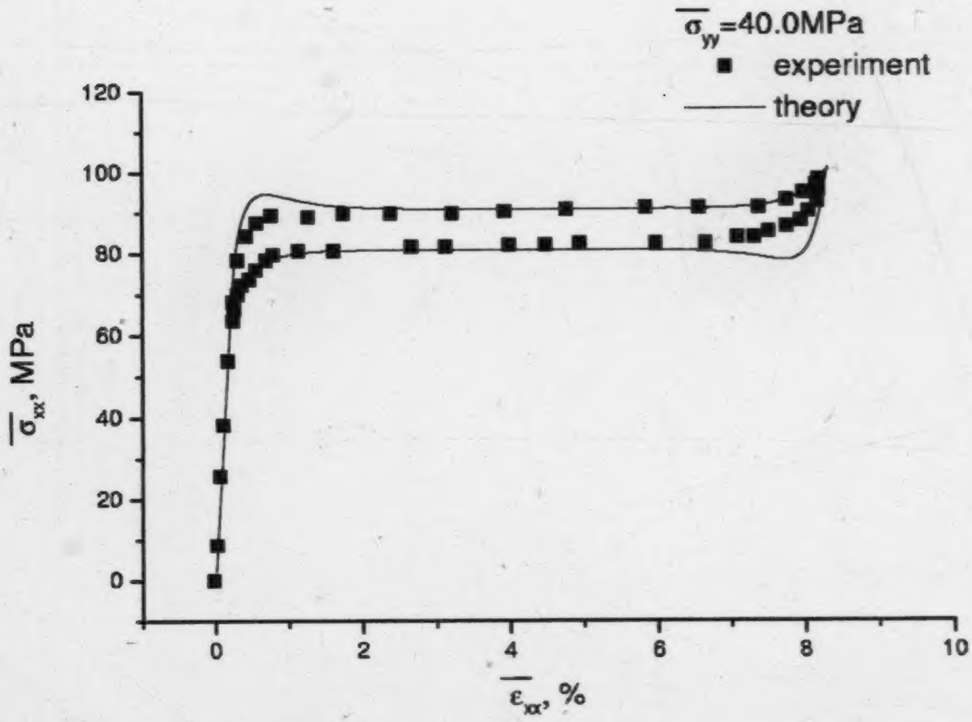

Figure 5.12: Average stress, $\bar{\sigma}_{xx}$, vs. average strain, $\bar{\varepsilon}_{xx}$, comparison with experimental data [1], $\bar{\sigma}_{yy} = 40\ MPa$.

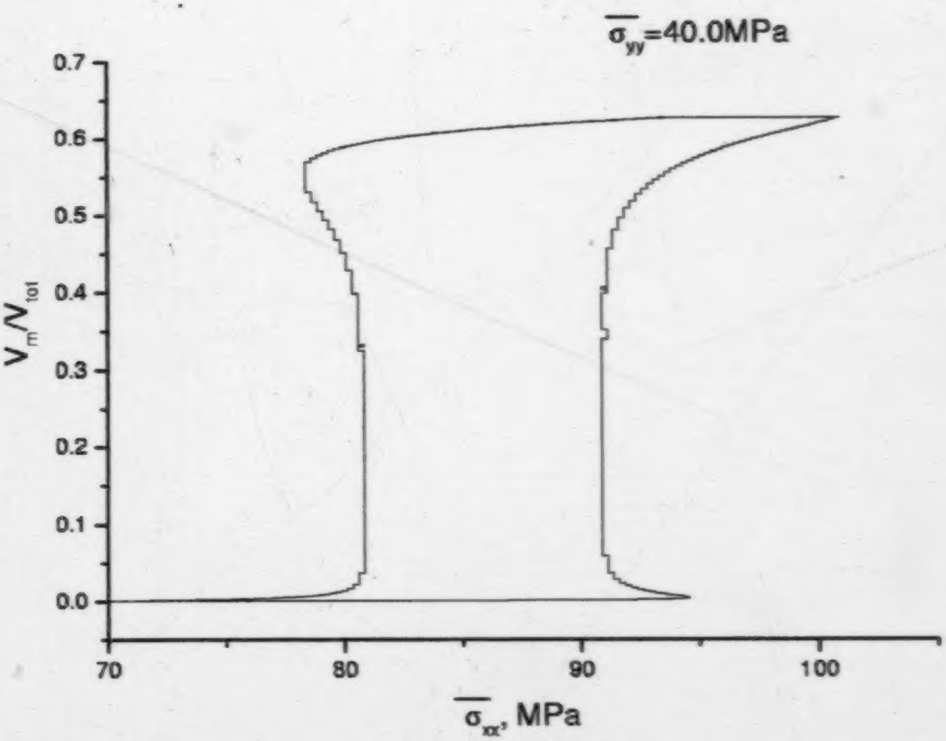

Figure 5.13: Martensitc volume fraction, V_m/V_{tot} as a function of the average stress, $\bar{\sigma}_{xx}$, $\bar{\sigma}_{yy} = 40\ MPa$.

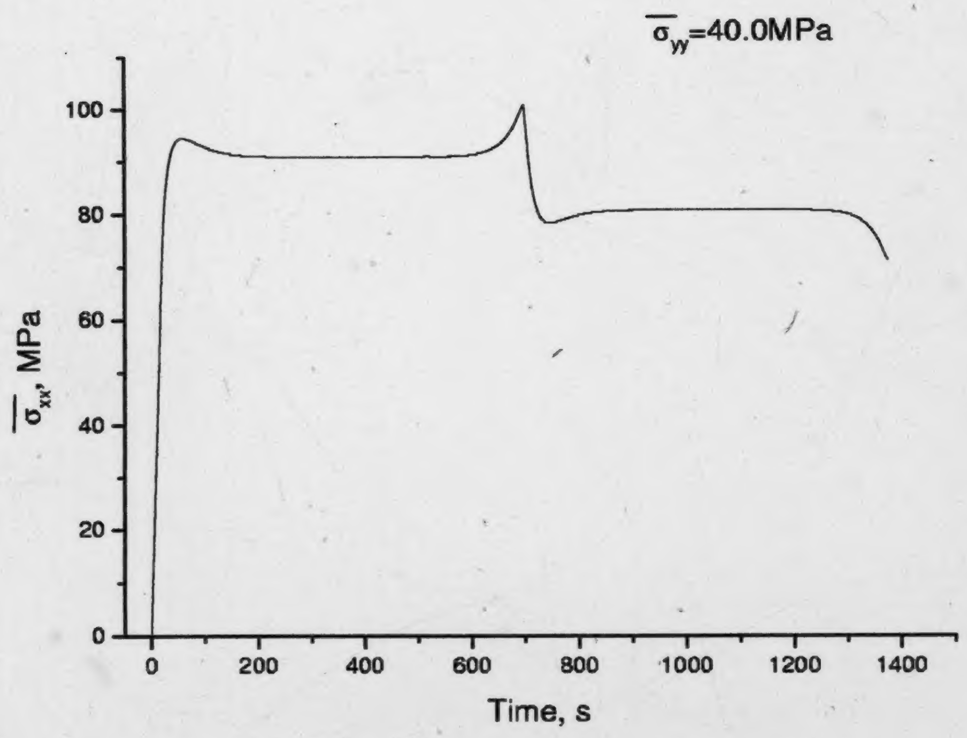

Figure 5.14: Average stress, $\bar{\sigma}_{xx}$, evolution, $\bar{\sigma}_{yy} = 40\ MPa$.

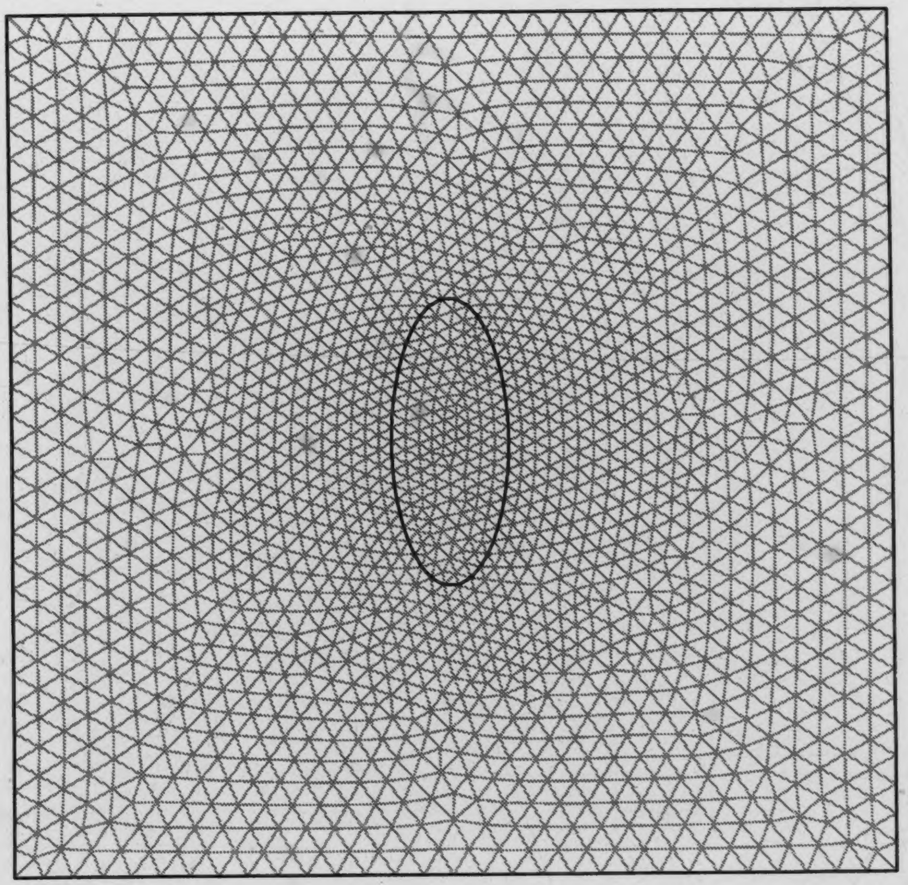

Figure 5.15: Shape of the martensitic inclusion when $\bar{\varepsilon}_{xx} = 1.0\%$ during A→M transformation, $\bar{\sigma}_{yy} = 40\ MPa$.

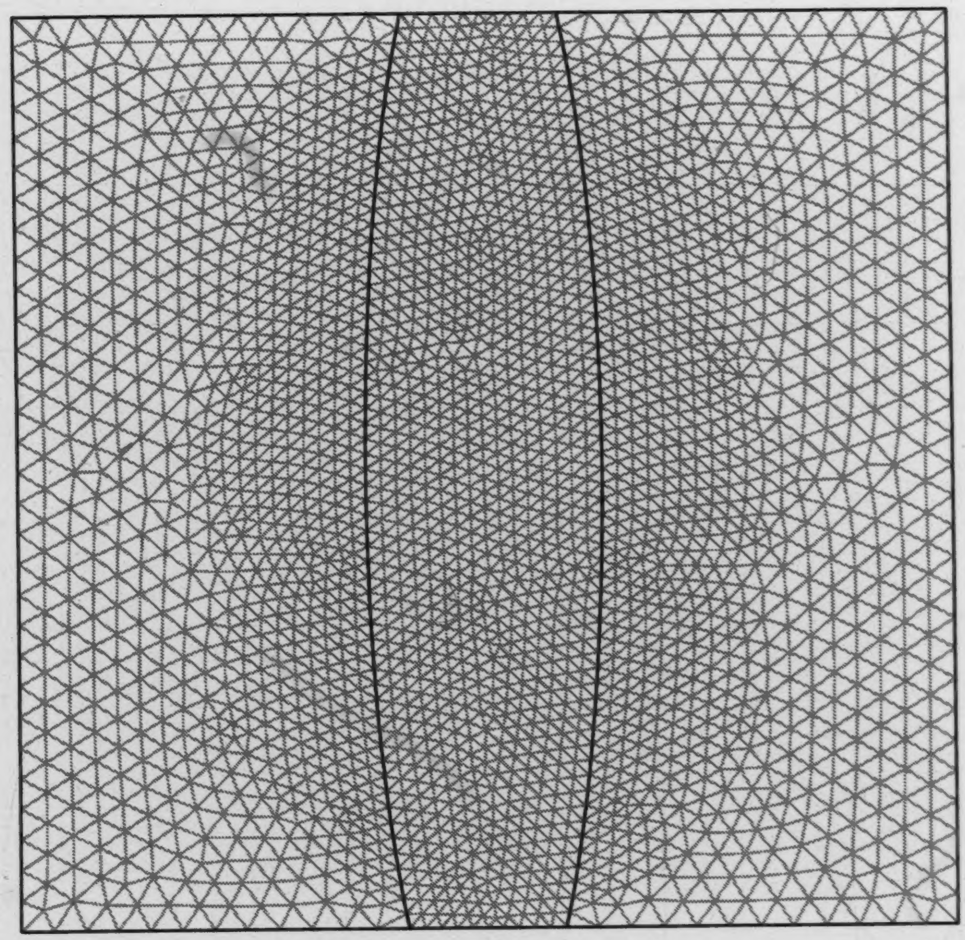

Figure 5.16: Shape of the martensitic inclusion when $\bar{\varepsilon}_{xx} = 3.5\%$ during A→M transformation, $\bar{\sigma}_{yy} = 40\ MPa$.

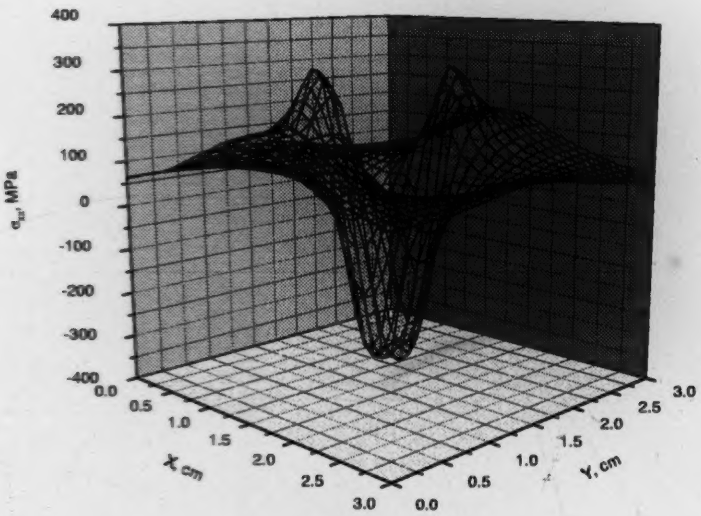

(a) 3D presentation

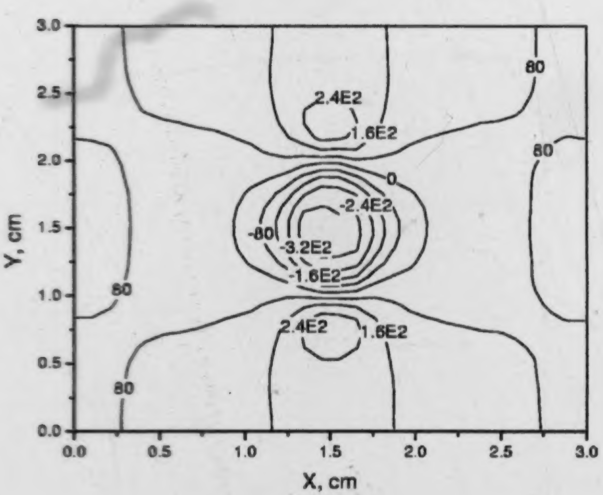

(b) contour plot

Figure 5.17: Distribution of σ_{xx}(MPa) when $\bar{\varepsilon}_{xx} = 1.0\%$ during A→M transformation, $\bar{\sigma}_{yy} = 40\ MPa$.

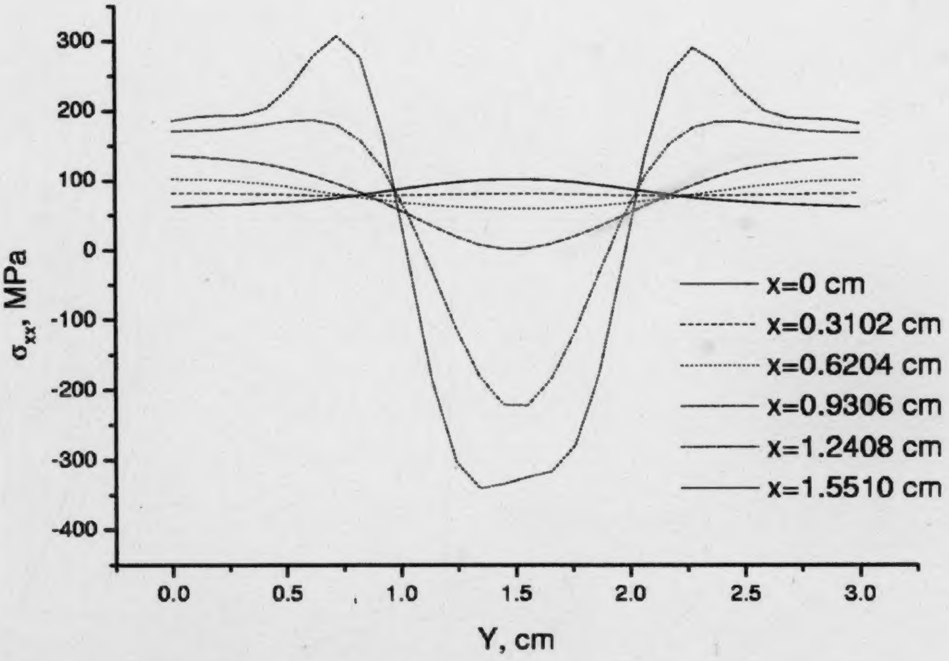

Figure 5.18: Cross-sectional profiles of σ_{xx} when $\bar{\varepsilon}_{xx} = 1.0\%$ during A→M transformation, $\bar{\sigma}_{yy} = 40\ MPa$.

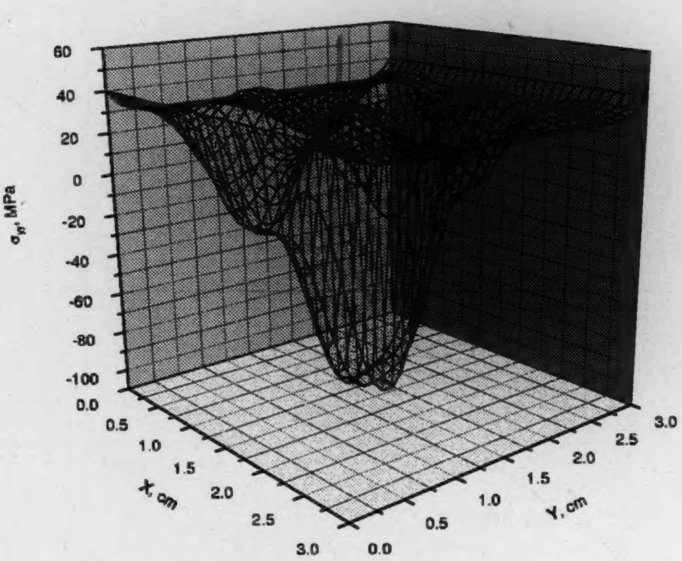

(a) 3D presentation

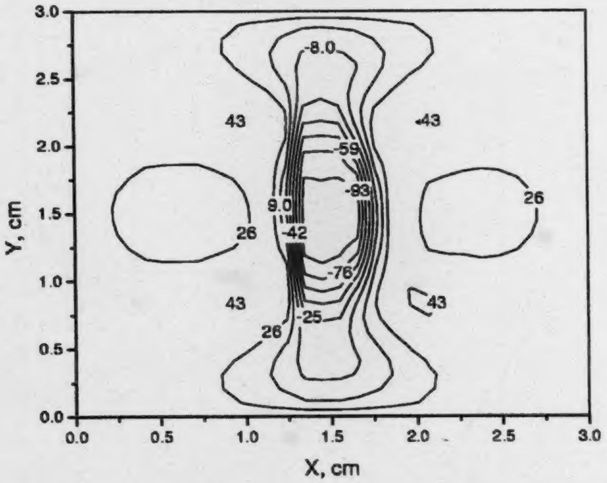

(b) contour plot

Figure 5.19: Distribution of σ_{yy}(MPa) when $\bar{\varepsilon}_{xx} = 1.0\%$ during A→M transformation, $\bar{\sigma}_{yy} = 40\ MPa$.

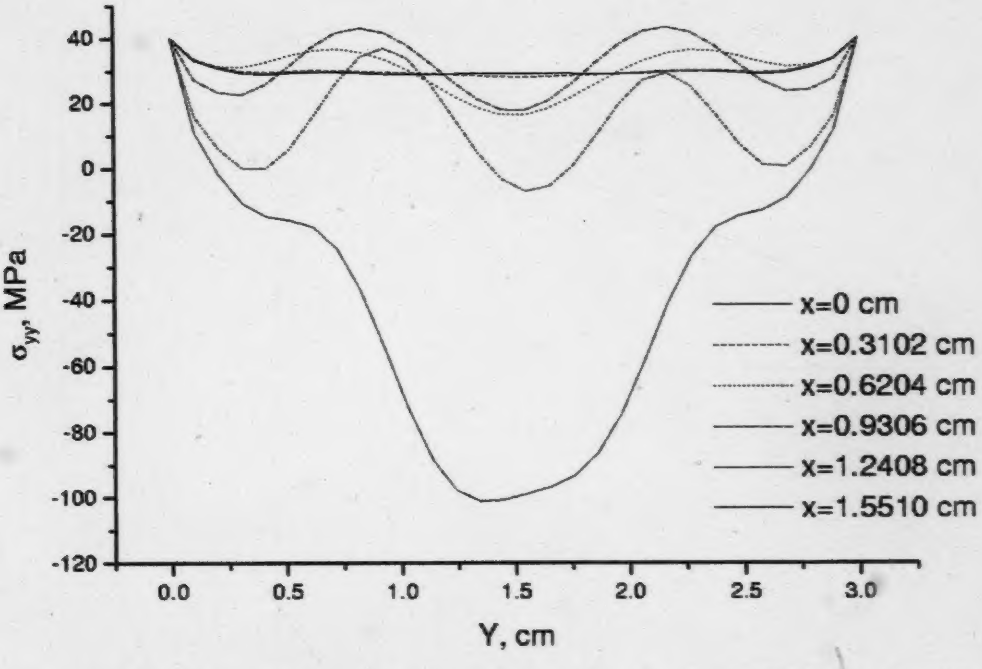

Figure 5.20: Cross-sectional profiles of σ_{yy} when $\bar{\varepsilon}_{xx} = 1.0\%$ during A→M transformation, $\bar{\sigma}_{yy} = 40\ MPa$.

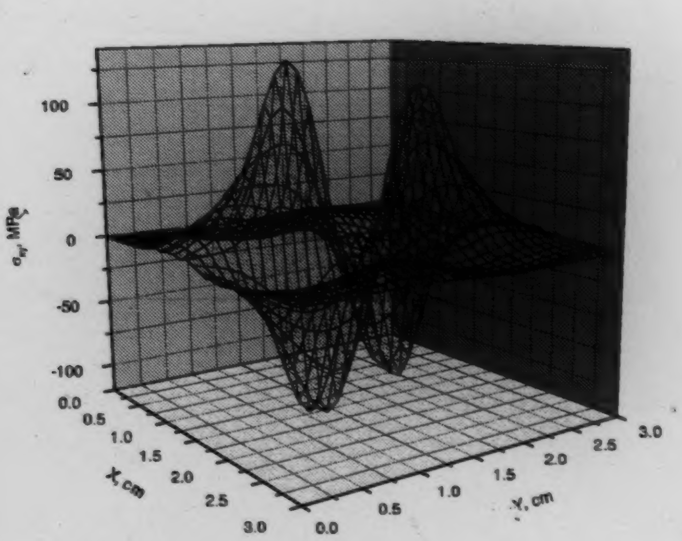

(a) 3D presentation

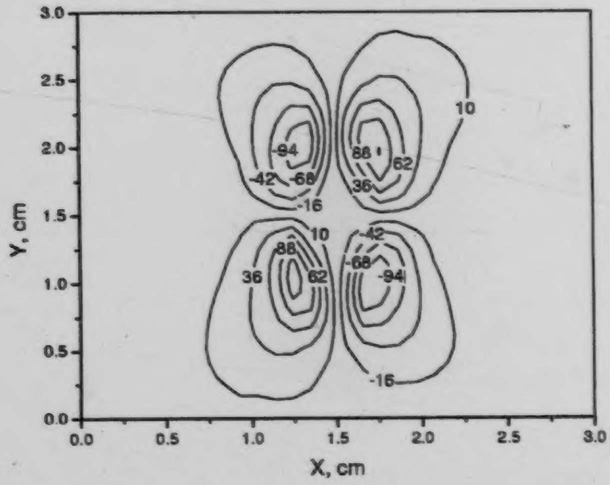

(b) contour plot

Figure 5.21: Distribution of σ_{xy}(MPa) when $\bar{\varepsilon}_{xx} = 1.0\%$ during A→M transformation, $\bar{\sigma}_{yy} = 40\ MPa$.

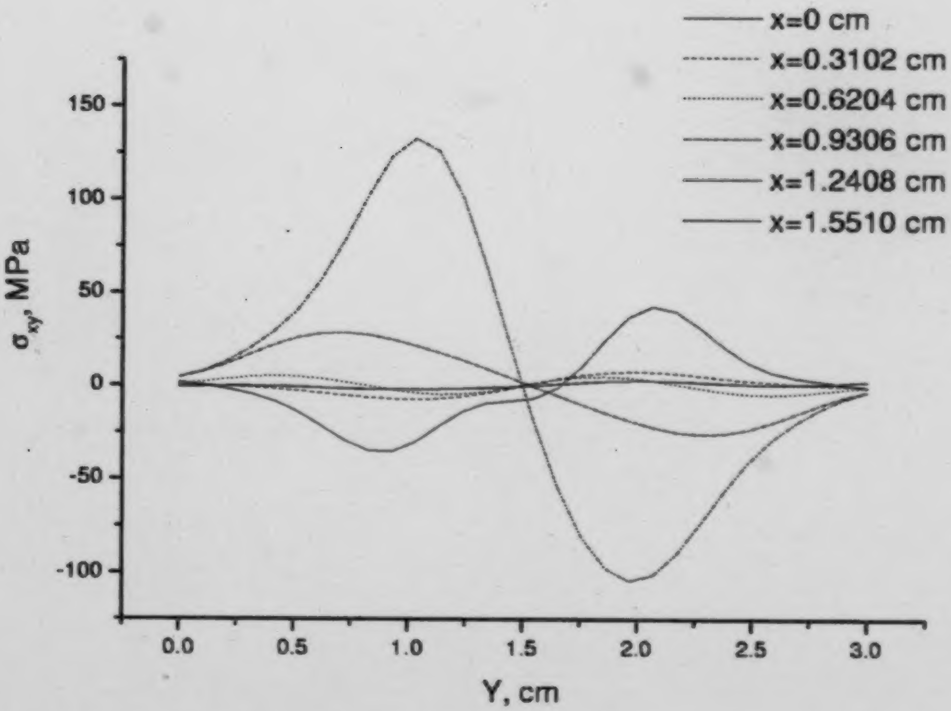

Figure 5.22: Cross-sectional profiles of σ_{xy} when $\bar{\varepsilon}_{xx} = 1.0\%$ during A→M transformation, $\bar{\sigma}_{yy} = 40\ MPa$.

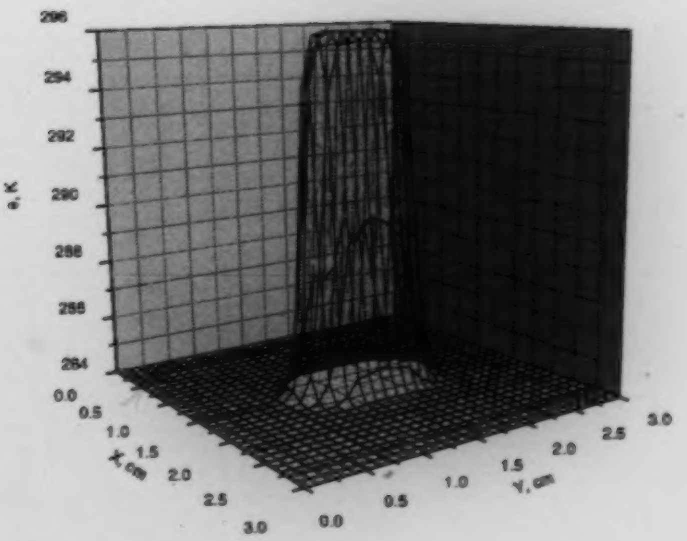

(a) 3D presentation

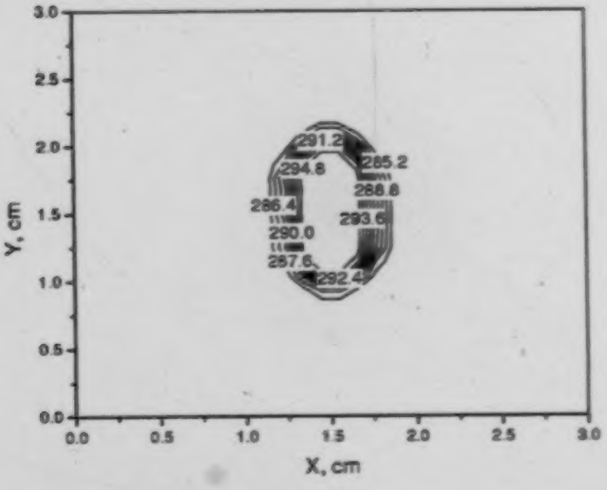

(b) contour plot

Figure 5.23: Temperature, θ, distribution when $\bar{\varepsilon}_{xx} = 1.0\%$ during A→M transformation, $\bar{\sigma}_{yy} = 40\ MPa$.

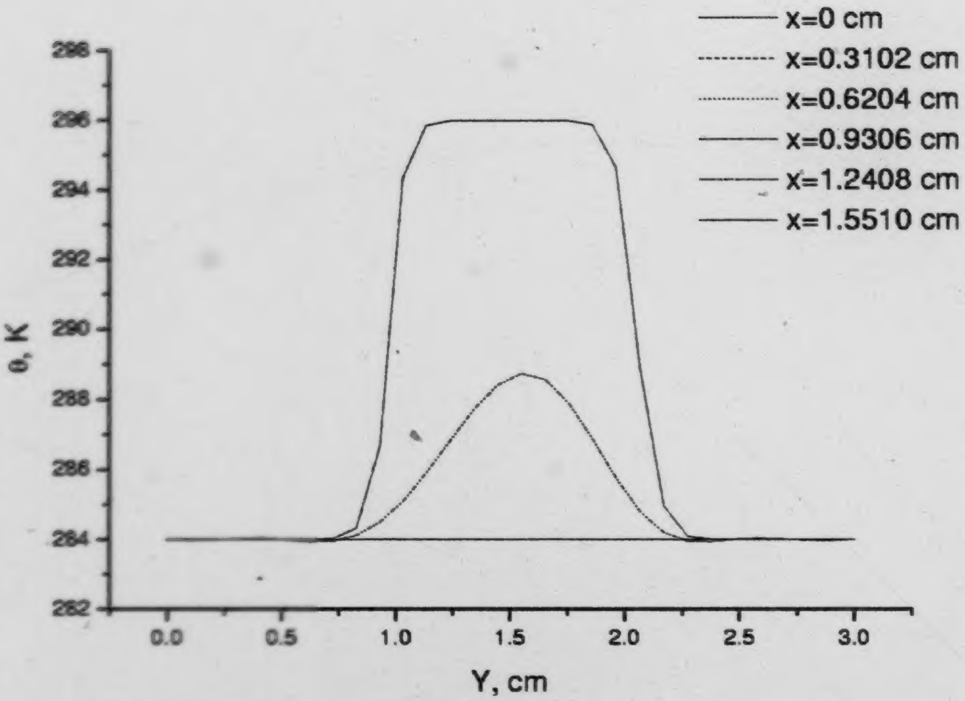

Figure 5.24: Cross-sectional profiles of the temperature, θ, when $\bar{\varepsilon}_{xx} = 1.0\%$ during A→M transformation, $\bar{\sigma}_{yy} = 40\ MPa$.

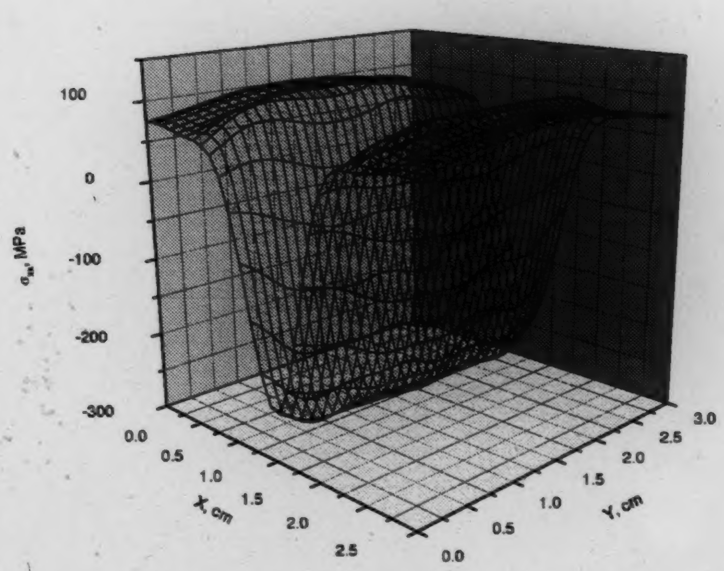

(a) 3D presentation

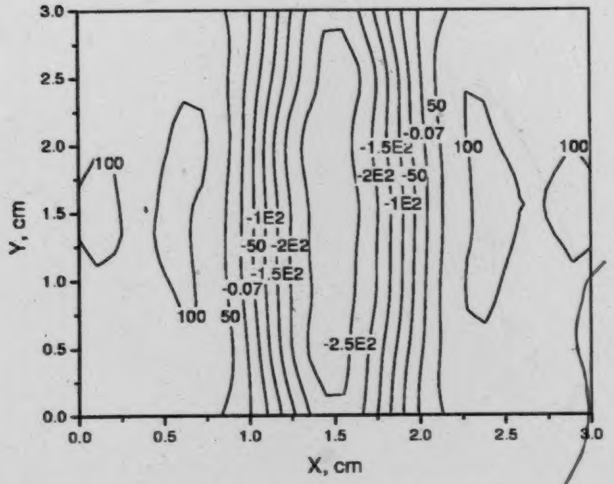

(b) contour plot

Figure 5.25: Distribution of σ_{xx}(MPa) when $\bar{\varepsilon}_{xx} = 3.5\%$ during A→M transformation, $\bar{\sigma}_{yy} = 40\ MPa$.

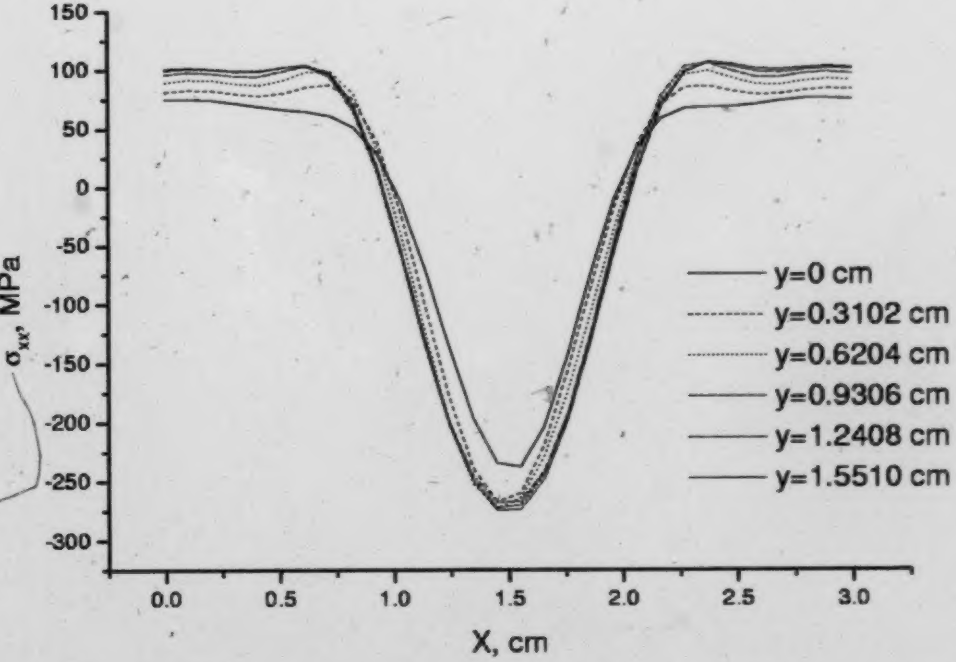

Figure 5.26: Cross-sectional profiles of σ_{xx} when $\bar{\varepsilon}_{xx} = 3.5\%$ during A→M transformation, $\bar{\sigma}_{yy} = 40\ MPa$.

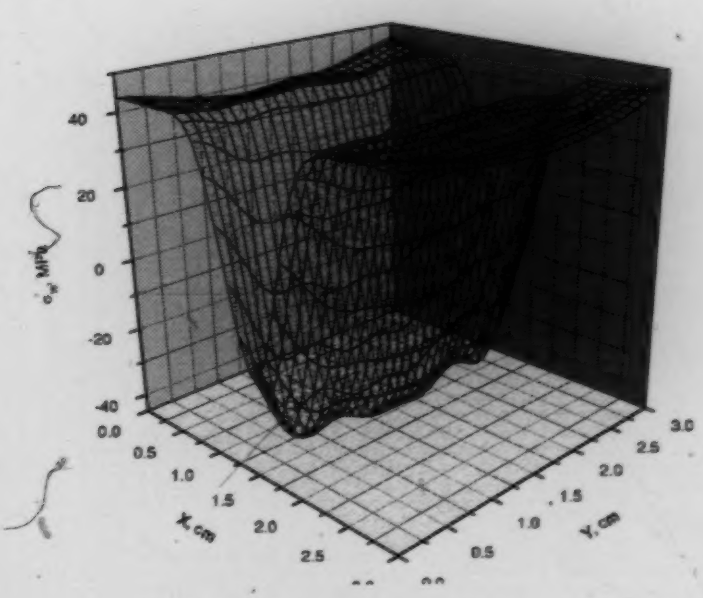

(a) 3D presentation

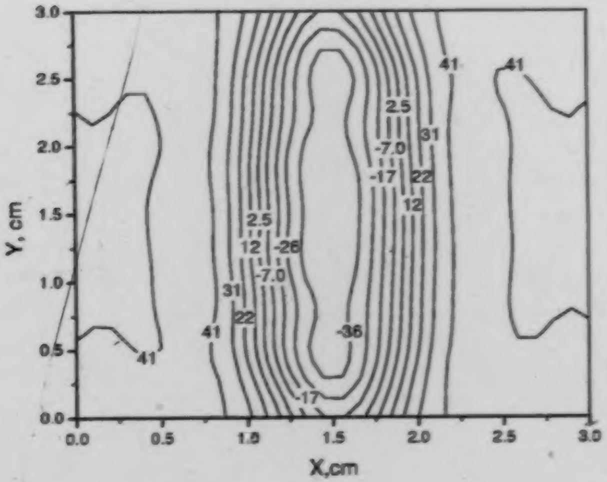

(b) contour plot

Figure 5.27: Distribution of σ_{yy}(MPa) when $\bar{\epsilon}_{xx} = 3.5\%$ during A→M transformation, $\bar{\sigma}_{yy} = 40\ MPa$.

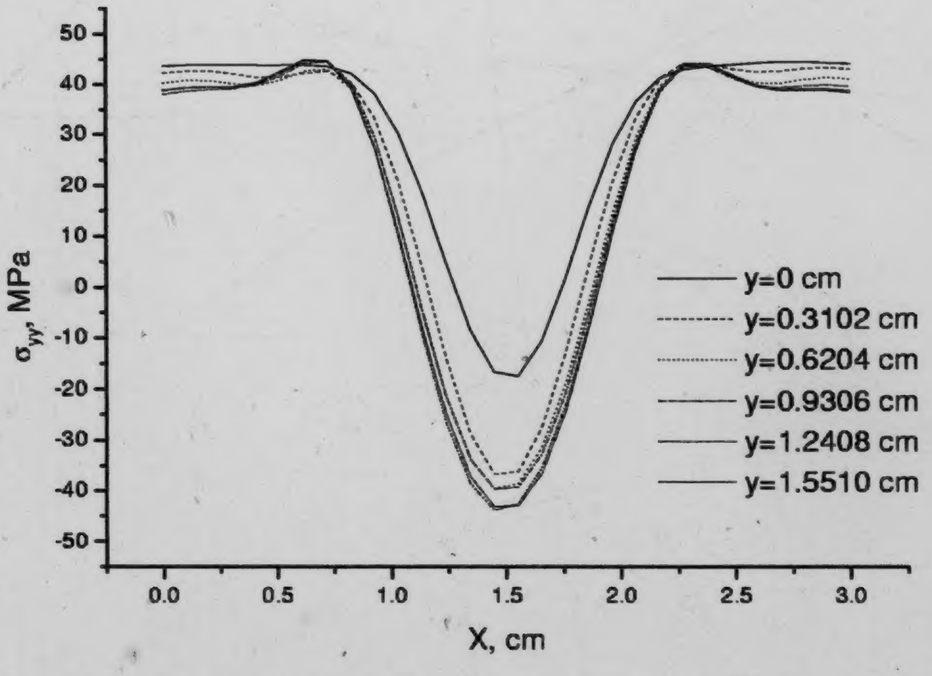

Figure 5.28: Cross-sectional profiles of σ_{yy} when $\bar{\varepsilon}_{xx} = 3.5\%$ during A→M transformation, $\bar{\sigma}_{yy} = 40\ MPa$.

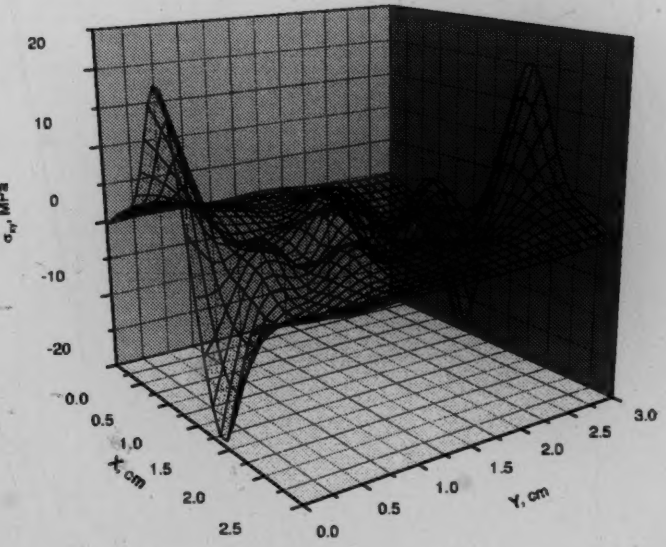

(a) 3D presentation

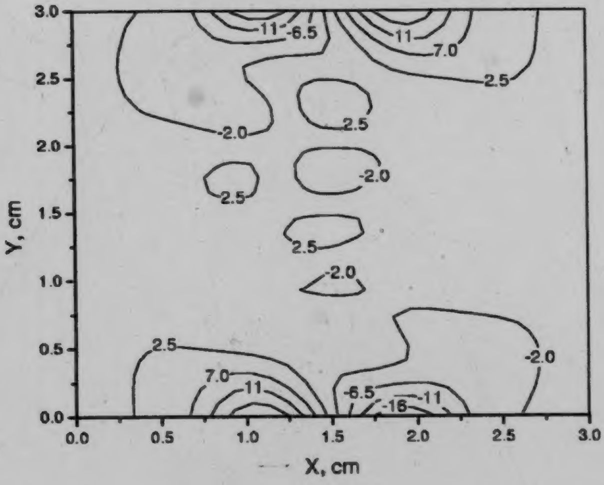

(b) contour plot

Figure 5.29: Distribution of σ_{xy}(MPa) when $\bar{\varepsilon}_{xx} = 3.5\%$ during A→M transformation, $\bar{\sigma}_{yy} = 40\ MPa$.

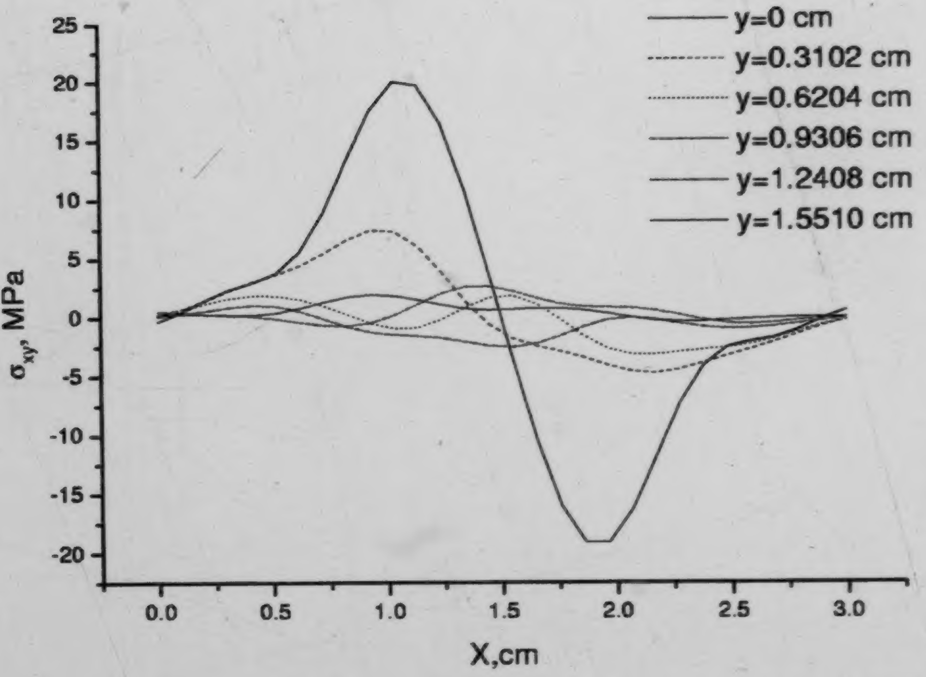

Figure 5.30: Cross-sectional profiles of σ_{xy} when $\bar{\varepsilon}_{xx} = 3.5\%$ during A→M transformation, $\bar{\sigma}_{yy} = 40\ MPa$.

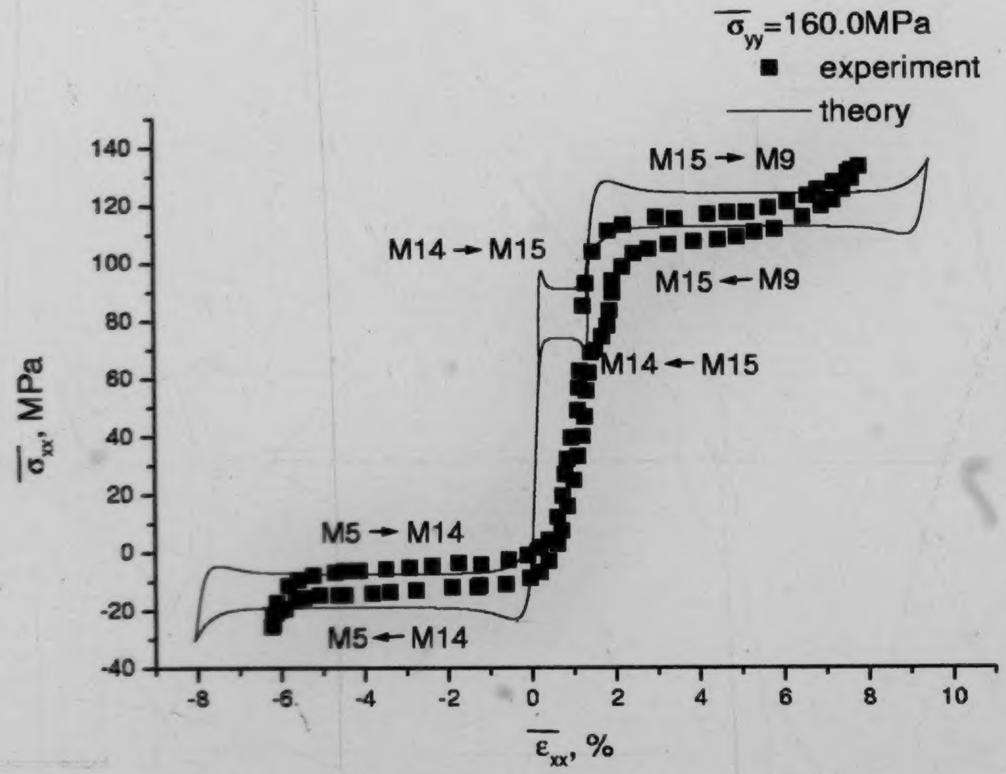

Figure 5.31: Average stress, $\bar{\sigma}_{xx}$, vs. average strain, $\bar{\varepsilon}_{xx}$, comparison with experimental data [1], $\bar{\sigma}_{yy} = 160\ MPa$.

Bibliography

[1] D. Fang, W. Lu, W. Yan, T. Inoue and K. Hwang, "Stress-strain relation of CuAlNi SMA single crystal under biaxial loading-constitutive model and experiments," *Acta Materialia* **47**, pp. 269–280, 1999.

[2] R. Abeyaratne and J. Knowles, "Dynamics of propagating phase boundaries: adiabatic theory for thermoelastic solids," *Physica D* **79**, pp. 269–288, 1994.

[3] R. Abeyaratne and J. Knowles, "A continuum model of a thermoelastic solid capable of undergoing phase transitions," *J. Mech. Phys. Solids* **41**, pp. 541–571, 1993.

[4] R. Abeyaratne and J. Knowles, "On the driving traction acting on the surface of strain discontinuity in a continuum," *J. Mech. Phys. Solids* **38**, pp. 345–360, 1990.

[5] O. P. Bruno, P. H. Leo, and F. Reitich, "Free boundary conditions at austenite-martensite interfaces," *Phys. Rev. Lett.* **74**, pp. 746–749, 1995.

[6] H. B. Callen, *Thermodynamics and introduction to thermostatistics*, Wiley, New York, 1985.

[7] V. Stoilov and A. Bhattacharyya, "A theoretical framework of one-dimensional sharp phase fronts in shape memory alloys," *to appear in Acta Materialia* .

[8] S. Kim, "A continuum model for phase transitions in thermoelastic solids and its application to shape memory alloys," *PhD thesis, MIT, USA* , 1995.

[9] B. Finlayson, *Numerical methods for problems with moving fronts*, Ravenna Park Publishing, Seattle, Washington, USA, 1992.

[10] A. C. Eringen, *Continuum Physics. Vol. 2*, Academic Press, New York, 1975.

[11] G. Dhatt, *The finite element method displayed,* John Wiley, NewYork,USA, 1984.

[12] O. Zienkiewicz and R. Taylor, *The finite element method,* Vol. 1: Basic *Formulation and Linear Problems*, McGraw-Hill, London,UK, 1989.

[13] K. B. J. Batoz and L. Ho, "A study of three-node triangular plate bending elements," *Int. J. Num. Meth. Eng.* **15**, pp. 1771–1812, 1980.

[14] J. von Neumann and R. Richtmyer, "A method for the numerical calculation of hydrodynamic shocks," *J. Appl. Phys.* **21**, pp. 232–247, 1950.

[15] J. Hawley, L. Smar and J. Wilson, "A numerical study of nonspherical black hole accretion. ii. finite differencing and code calibration," *Astrophys. J. Suppl. Ser.* **55**, pp. 211–246, 1984.

[16] J. Yokota and H. Huynh, "A nonoscillatory, characteristically convected, finite volume scheme for multidimensional convection problems," *NASA Technical Memorandum* **102354**, pp. 1–18, 1990.

[17] P. Roe, "Some contributions to the modelling of discontinuous flows, in Large-Scale Computations in Fluid Mechanics," *Lectures in Applied Mathematics* **22**, pp. 163–194, 1985.

[18] W. Press, S. Teukolsky, W. Vetterling and B. Flannery, *Numerical recipes in C: the art of scientific programming*, Cambridge University Press, Cambridge,UK, 1992.

[19] I. Hladik, M. Reed and G. Swoboda, "Robust preconditioners for linear elasticity fem analyses," *Int. J. Numer. Meth. Engng.* **40**, pp. 2109–2127, 1997.

[20] J. K. Dickinson and P. A. Forsyth, "Preconditioned conjugate gradient methods for three-dimensional linear elasticity," *Int. J. Numer. Meth. Engng.* **37**, pp. 2211–2234, 1994.

[21] E. D'Azevedo, P. Forsyth and W. Tang, "Ordering methods for preconditioned conjugate gradient methods applied to unstructured grid problems," *SIAM. J. Matrix Anal. Appl.* **13**, pp. 944–961, 1992.

[22] M. A. Ajiz and A. Jennings, "A robust incomplete choleski conjugate gradient algorithm," *Int. J. Numer. Meth. Engng.* **20**, pp. 949–966, 1984.

[23] M. Shashkov, *Conservative finite-difference methods on general grid*, CRC Press, New York,USA, 1996.

[24] I. Robertson, “Elastic properties of shape memory alloy martensites,” *Scripta Metallurgica et Materialia* **24**, pp. 1947–1952, 1990.

[25] T. Duerig, K. Meiton, D. Stockel, and C. Wayman, *Engineering aspects of shape memory alloys*, Butterworth-Heinemann, New York, 1990.

[26] Q. Jiang, J. Li and J. Tong, “C_p measurements around the martensitic transformation temperature of CuAlNi alloy,” *Mat. Science and Engineering A* **196**, pp. 165–169, 1995.

[27] R. Salzbrenner and M. Cohen, “Thermodynamics of thermoelastic martensitic transformations,” *Acta Metallurgica* **27**, pp. 739–748, 1979.

Chapter 6

Conclusions

This thesis addresses two fundamental issues of modeling the thermodynamical response of single crystal SMAs: a) theoretical description(model) of SMAs with sharp phase fronts; b) numerical method(algorithm) for adequate solution of the corresponding mathematical problem. The theoretical model and the numerical algorithm were initially developed for one dimensional SMA systems(Chapters 2 and 4) and generalized for three dimensional problems in Chapters 5.

The theoretical model consists of two parts: conservation laws(mass, linear momentum, angular momentum and energy) and constitutive relation(Helmholtz free energy). As it has been shown by Abeyaratne and

Knowles [1], this formulation does not render a unique solution for SMA systems with sharp phase fronts. The theoretical model developed in this thesis completes the system of equations describing the phase transformation in SMAs with sharp phase fronts by introducing the notion of continuity of the chemical potential at the phase boundary. The suggested theoretical framework is general enough to incorporate any Helmholtz free energy function of the SMA, and therefore if this function is explicitly known, then so is the entire set of governing equations (including that for the phase boundary evolution). The validity of the developed theoretical model was verified by comparing the theoretical predictions with experimentally measured data in one and two dimensional cases([2],[3]).

The second component of the research involved development of numerical methods/algorithms for solving the mathematical problems arising from the suggested theoretical models. A MBFEM-based numerical approach was developed to address BVPs for SMAs with 1D phase fronts [4]. The algorithm implements front tracking, based on introduction of an additional mesh point at the location of the phase boundary. The nonlinear algebraic system of equations resulting from the FE discretization was solved by invoking Newton-Raphson iterations. The algorithm has been found to be accurate and unconditionally stable when compared to an analytical solution for a purely thermal transformation. The accuracy of the algorithm was also validated in comparison with experimental data [2] and in simulation of the thermomechanical response of linear SMA actuators [5].

The solution of the mathematical problem of phase transformation in SMAs in 2D domains (i.e. SMA thin films) was addressed by developing a new numerical algorithm, which utilizes the finite element method (FEM). In this algorithm the phase front tracking is based on permanent update of the mesh so that the phase boundary always lies on mesh nodes. The data from the "old" is transferred to the "new" by non-oscillatory 2D interpolation(SuperBee [6]). It is shown that the algorithm ($O(h^2, \tau^2)$) is stable and adequately accurate by comparing the predictions of the model with analytical solutions for purely thermal and thermomechanical problems as well as with the experimental results of Fang et. al. ([7]) for the pseudoelasticity in SMA CuAlNi thin films [3].

Bibliography

[1] R. Abeyaratne and J. Knowles, "Dynamics of propagating phase boundaries: adiabatic theory for thermoelastic solids," *Physica D* **79**, pp. 269–288, 1994.

[2] V. Stoilov and A. Bhattacharyya, "A theoretical framework of one-dimensional sharp phase fronts in shape memory alloys," *to appear in Acta Materialia* .

[3] V. Stoilov, A. Bhattacharyya and J. Yokota, "A computational study of evolving phase fronts in shape memory alloy thin films," *Proceedings of 39th Annual Technical Meeting of the Society of Engineering Science* , 2002.

[4] V. Stoilov, O. Iliev, and A. Bhattacharyya, "A moving boundary finite element method-based approach for the solution of one-dimensional prob-

lems in shape memory alloys," *Computer Methods in Applied Mechanics and Engineering* **190**, pp. 1741–1762, 2000.

[5] A. Bhattacharyya, V. Stoilov, and O. Iliev, "Evaluation of structural influence of shape memory alloys linear actuators by sharp phase front-based constitutive models," *Computational Materials Science* **18**, pp. 269–282, 2000.

[6] J. Yokota and H. Huynh, "A nonoscillatory, characteristically convected, finite volume scheme for multidimensional convection problems," *NASA Technical Memorandum* **102354**, pp. 1–18, 1990.

[7] D. Fang, W. Lu, W. Yan, T. Inoue and K. Hwang, "Stress-strain relation of CuAlNi SMA single crystal under biaxial loading-constitutive model and experiments," *Acta Materialia* **47**, pp. 269–280, 1999.

Appendix A

MBFEM

A.1 Non-dimensional variables

The non-dimensional variables (included below with a "tilde") may be obtained by application of the Buckingam π theorem [1]. We give a list below where every non-dimensional variable is preceded by a physical description of the quantity being non-dimensionalized:

- length: $\tilde{x} = \frac{1}{L}x$,
- phase boundary position: $\tilde{x}_{pb} = \frac{1}{L}x_{pb}$,
- displacement: $\tilde{\delta} = \frac{1}{L}\delta$,

- time: $\tilde{t} = \frac{k}{\rho c L^2} t$,
- temperature: $\tilde{\theta} = \frac{1}{\theta_{amb}} \theta$,
- stress: $\tilde{\sigma} = \frac{1}{E} \sigma$,
- coefficient of thermal expansion: $\tilde{\alpha} = \alpha \theta_{amb}$,
- convection coefficients: $\tilde{h} = \frac{PL^2}{Ak} h$,
- latent heat:$\tilde{\lambda}_T = \frac{\rho \lambda_T}{E}$,
- mobility parameter: $\tilde{R} = \frac{\rho c L}{k} R$,
- driving force: $\tilde{f} = \frac{1}{E} f$,
- Boltzman constant: $\widetilde{K} = \frac{r \theta_{amb}}{E} K$,
- martensitic start temperature: $\widetilde{M}_s = \frac{M_s}{\theta_{amb}}$,
- austenitic start temperature: $\tilde{A}_s = \frac{A_s}{\lambda_{amb}}$,
- current density: $\tilde{J} = L \sqrt{\frac{\rho_E}{k \theta_{amb}}} J$.

A.2 Discretization of Eq. 2.29 in absence of the jump condition, Eq. 2.30

The matrices **K**, **M**, $\bar{\mathbf{M}}^*$ and the vector $\vec{F}$ resulted from the discratization of Eq. 2.29 in the absence of the jump condition, Eq. 2.30. We now give their non-vanishing components. The non-zero components of **K** are

$$\begin{aligned} K_{11} = -K_{12} &= \frac{1}{\Delta L}, \\ K_{ee-1} = -\frac{1}{2}K_{ee} = K_{ee+1} &= -\frac{1}{\Delta L}, \quad 2 \leq e \leq N, \\ K_{N+1N} = -K_{N+1N+1} &= -\frac{1}{\Delta L}. \end{aligned} \tag{A.1}$$

The non-zero components of **M** are

$$\begin{aligned} M_{11} = 2M_{12} &= \frac{\Delta L}{3}, \\ M_{ee-1} = \frac{1}{4}M_{ee} = M_{ee+1} &= \frac{\Delta L}{6}, \quad 2 \leq e \leq N, \\ M_{N+1N} = \frac{1}{2}M_{N+1N+1} &= \frac{\Delta L}{6}. \end{aligned} \tag{A.2}$$

The non-zero components of $\bar{\mathbf{M}}^*$ are

$$\begin{aligned} \bar{M}^*_{11} = \frac{\Delta L}{4}\left(\theta^*_1 + \frac{\theta^*_2}{3}\right), \bar{M}^*_{12} &= \frac{\Delta L}{4}\left(\frac{\theta^*_1 + \theta^*_2}{3}\right), \\ \bar{M}^*_{ee-1} = \frac{\Delta L}{4}\left(\frac{\theta^*_{e-1} + \theta^*_e}{3}\right), \bar{M}^*_{ee} &= \frac{\Delta L}{4}\left(\frac{\theta^*_{e-1}}{3} + 2\theta^*_e + \frac{\theta^*_{e+1}}{3}\right), \\ \bar{M}^*_{ee+1} &= \frac{\Delta L}{4}\left(\frac{\theta^*_e + \theta^*_{e+1}}{3}\right), \quad 2 \leq e \leq N, \end{aligned}$$

$$\bar{M}^*_{N+1N} = \frac{\Delta L}{4}\left(\frac{\theta^*_N + \theta^*_{N+1}}{3}\right), \bar{M}^*_{N+1N+1} = \frac{\Delta L}{4}\left(\frac{\theta^*_N}{3} + \theta^*_{N+1}\right). \qquad \text{(A.3)}$$

The components of $\vec{F}$ are

$$F_1 = F_{N+1} = \frac{\Delta L}{2}, \qquad F_e = \Delta L, \quad 2 \le e \le N, \qquad \text{(A.4)}$$

A.3 Modification of Eq. 2.40 due to the jump condition, Eq. 2.30

A.3.1 Phase boundary lies between two nodes

In order to incorporate the effect of the jump condition, the global temperature vector will now have $N+2$ components because the temperature, θ^i_{pb},corresponding to the node at the phase boundary will have to be introduced. This is done by introducing a new teperature vector, $\vec{\Theta}^i$(without the subscript "UN") with $N+2$ components, with the components defined as

$$\Theta^i_k = \Theta^i_{UN,k} \quad (1 \le k \le p),$$

$$\Theta^i_{p+1} = \theta^i_{pb},$$

$$\Theta^i_k = \Theta^i_{Un,k-1} \quad (p+2 \le k \le N+2). \qquad \text{(A.5)}$$

The components of the matrix $\mathbf{A}^i$ are

$$A^i_{km} = A^i_{UN,km} \quad \begin{cases} 1 \le k \le p-1, & 1 \le m \le p, \\ 1 \le k \le p-1, & p+2 \le m \le N+2, \end{cases}$$

$$A^i_{km} = A^i_{UN,k-1m-1} \quad \begin{cases} p+3 \le k \le N+2, & 1 \le m \le p, \\ p+3 \le k \le N+2, & p+2 \le m \le N+2, \end{cases} \tag{A.6}$$

The remaining components of the matrix $\mathbf{A}^i$ follows as

$$\begin{aligned} A^i_{pp-1} = \frac{2\tau w_{p-}}{\Delta L}, \quad A^i_{pp} = [2\tau\left(1+\frac{w_{p-}}{\Delta L}\right) + \\ w_{p-}(w_{p-}+\Delta L)\Bigl[g\frac{d\sigma^i}{dt}+h]\tau + w_{p-}(w_{p-}+\Delta L)(1+\alpha g\theta^*_p)\Bigr], \\ A^i_{pp+1} = 2\tau, \quad A^i_{p+1p} = w_{p+}, \quad A^i_{p+1p+1} = -\Delta L, \quad A^i_{p+1p+2} = w_{p-}, \\ A^i_{p+2p+1} = 2\tau, \quad A^i_{p+2.p+3} = \frac{2\tau w_{p+}}{\Delta L}, \\ A^i_{p+2p+2} = [2\tau\left(1+\frac{w_{p+}}{\Delta L}\right) + w_{p+}(w_{p+}+\Delta L)\left[g\frac{d\sigma^i}{dt}+h\right]\tau + \\ w_{p+}(w_{p+}+\Delta L)(1+\alpha g\theta^*_{p+1})] \;. \end{aligned} \tag{A.7}$$

Any components of $\mathbf{A}^i$ that have not been mentioned in the above list should be zero. The components of vector $\vec{B}^i$ are

$$\begin{aligned} B^i_{kk} &= B^i_{UN,k} \quad (1 \le k \le p-1), \\ B^i_k &= B^i_{UN,k-1} \quad (p+3 \le k \le N+2). \end{aligned} \tag{A.8}$$

The remaining components are

$$B^i_p = -w_{p-}(w_{p-}+\Delta L)\left[\left(1+\alpha g\theta^*_p\right)\theta^i_p + \tau(h+J^2)\right],$$

$$B^i_{p+1} = -w_{p-} w_{p+} \frac{g}{\alpha}(\sigma^i \varepsilon_T + \lambda_T) \frac{dx^i_{pb}}{dt},$$

$$B^i_{p+2} = -w_{p+}(w_{p+} + \Delta L) \left[(1 + \alpha g \theta^*_{p+1}) \theta^i_{p+1} + \tau(h + J^2)\right]. \qquad \text{(A.9)}$$

A.3.2 Phase boundary lies on node

The components of the temperature vector are

$$\Theta^i_k = \Theta^i_{UN,k} \quad (1 \le k \le p, \quad p+2 \le k \le N+1),$$

$$\Theta^i_{p+1} = \theta^i_{pb}. \qquad \text{(A.10)}$$

All components of $\mathbf{A}^i$ and $\vec{B}^i$ are identical to $\mathbf{A}^i_{UN}$ and $\vec{B}^i_{UN}$, respectively, except the following listed below

$$A^i_{p+1p} = \frac{1}{\Delta L}, \; A^i_{p+1p+1} = -\frac{2}{\Delta L}, \; A^i_{p+1p+2} = \frac{1}{\Delta L}, \; B^i_{p+1} = -\frac{g}{\alpha}(\sigma \varepsilon_T + \lambda_T) \frac{dx^i_{pb}}{dt}. \qquad \text{(A.11)}$$

A.4 The components of the Jacobian, $\mathbf{J}^{i(m)}$

The Jacobian, $\mathbf{J}^{i(m)}$, introduced in Eq. 2.49 has components which are developed in the following manner. We first define an auxiliary Jacobian, $\bar{\mathbf{J}}^{i(m)}$, as

$$\bar{\mathbf{J}}^{i(m)} = \tau \mathbf{K} + \mathbf{M} + \tau \left(g \frac{d\sigma^i}{dt} + h\right) \mathbf{M} + \mathbf{N}^{i(m)} \qquad \text{(A.12)}$$

The auxiliary Jacobian , $\bar{\mathbf{J}}^{i(m)}$, may be constructed once matrices **K**, **M** and $\mathbf{N}^{i(m)}$ are known. The component of **K** and **M** are given in Section B.1 of Appendix B whereas the non-zero components of $\mathbf{N}^{i(m)}$ are given bellow

$$\begin{aligned} N_{11}^{i(m)} &= \alpha g \left[\frac{\Delta L}{6}(3\theta_1^{i(m)}) + \theta_2^{i(m)}) - \frac{\Delta L}{12}(3\theta_1^{i-1} + \theta_2^{i-1}) \right], \\ N_{p-1p}^{i(m)} &= \alpha g \left[\frac{\Delta L}{6}(\theta_{p-1}^{i(m)}) + \theta_p^{i(m)}) - \frac{\Delta L}{12}(\theta_{p-1}^{i-1} + \theta_p^{i-1}) \right], \\ N_{pp}^{i(m)} &= \alpha g \left[\frac{\Delta L}{6}(\theta_{p-1}^{i(m)}) + 6\theta_p^{i(m)} + \theta_{p+1}^{i(m)}) - \frac{\Delta L}{12}(\theta_{p-1}^{i-1} + 6\theta_p^{i-1} + \theta_{p+1}^{i-1}) \right], \\ N_{p+1p}^{i(m)} &= \alpha g \left[\frac{\Delta L}{6}(\theta_p^{i(m)}) + \theta_{p+1}^{i(m)}) - \frac{\Delta L}{12}(\theta_p^{i-1} + \theta_{p+1}^{i-1}) \right], \\ N_{N+1N+1}^{i(m)} &= \alpha g \left[\frac{\Delta L}{6}(3\theta_N^{i(m)}) + 3\theta_{N+1}^{i(m)}) - \frac{\Delta L}{12}(\theta_N^{i-1} + 3\theta_{N+1}^{i-1}) \right] \end{aligned} \tag{A.13}$$

Once the auxiliary Jacobian, $\bar{\mathbf{J}}^{i(m)}$, is constructed , the actual Jacobian $\mathbf{J}^{i(m)}$, follows below.

A.4.1 Phase boundary lies between two nodes

When phase boundary lies between two existing nodes, a new node is introduced. The components of the Jacobian in such case are

$$J_{ks}^{i(m)} = \bar{J}_{ks}^{i(m)} \qquad \begin{cases} 1 \le k \le p-1, & 1 \le s \le p, \\ 1 \le k \le p-1, & p+2 \le s \le N+2, \end{cases}$$

$$J_{ks}^{i(m)} = \bar{J}_{k-1s-1}^{i(m)} \qquad \begin{cases} p+3 \le k \le N+2, & 1 \le s \le p, \\ p+3 \le k \le N+2, & p+2 \le s \le N+2, \end{cases}$$

$$\begin{aligned}
J^{i(m)}_{pp-1} &= \frac{2\tau w_{p-}}{\Delta L}, \\
J^{i(m)}_{pp} &= -\Bigg[2\tau\left(1+\frac{w_{p-}}{\Delta L}\right) + w_{p-}(w_{p-1}+\Delta L)\left[g\frac{d\sigma^i}{dt}+h\right]\tau + \\
&\quad w_{p-}(w_{p-}+\Delta L)(1+2\alpha\theta^{i(m)}_p)\Bigg] + w_{p-}(w_{p-}+\Delta L)\alpha g\theta^{i-1}_p, \\
J^{i(m)}_{pp+1} &= 2\tau, J^{i(m)}_{p+1p} = w_{p+}, \\
J^{i(m)}_{p+1p+1} &= -\Delta L, J^{i(m)}_{p+1p+2} = w_{p-}, J^{i(m)}_{p+2p+1} = 2\tau, J^{i(m)}_{p+2p+3} = \frac{2\tau w_{p+}}{\Delta L}, \\
J^{i(m)}_{p+2p+2} &= -\Bigg[2\tau\left(1+\frac{w_{p+}}{\Delta L}\right) + w_{p+}(w_{p+}+\Delta L)\left[g\frac{d\sigma^i}{dt}+h\right]\tau + \\
&\quad w_{p+}(w_{p+}+\Delta L)(1+2\alpha g\theta^{i(m)}_{p+1})\Bigg] + w_{p+}(w_{p+}+\Delta L)\alpha g\theta^{i-1}_{p+1} \ . \qquad (A.14)
\end{aligned}$$

A.4.2 Phase boundary lies on a node

When the phase boundary coincides with an existing node, all the components of the Jacobean are identical to the corresponding components of the auxiliary Jacobean except those listed below

$$J^{i(m)}_{p+1p} = w_{p+} \ , \quad J^{i(m)}_{p+1p+1} = -\Delta L \ , \quad J^{i(m)}_{p+1p+2} = w_{p-} \ . \qquad (A.15)$$

Appendix B

Linear SMA Actuators

B.1 List of relevant non-dimensional parameters

Non-dimensional phase boundary position

$$\bar{s} = \frac{s}{L} .$$

Non-dimensional time

$$\bar{t} = \frac{k}{\rho c L^2} t .$$

Non-dimensional stress

$$\bar{\sigma} = \frac{\sigma}{E \varepsilon_T} .$$

Non-dimensional phase boundary velocity

$$\dot{\bar{s}} = \frac{\rho c L}{k}\dot{s} .$$

Non-dimensional specific energy output

$$\bar{W}_{act} = \frac{W_{act}}{E\epsilon_T^2}$$

Non-dimensional spring stiffness

$$\bar{K}_s = \frac{K_s L}{AE} .$$

Appendix C

A 3D Theoretical Framework

C.1 3D state of stress

The stress and the elastic strain tensors are written in vector form as

$$\vec{T} = \begin{pmatrix} \sigma_{11} \\ \sigma_{22} \\ \sigma_{33} \\ \sigma_{23} \\ \sigma_{13} \\ \sigma_{12} \end{pmatrix} \quad , \vec{E}_{el} = \begin{pmatrix} \epsilon_{11}^{el} \\ \epsilon_{22}^{el} \\ \epsilon_{33}^{el} \\ 2\epsilon_{23}^{el} \\ 2\epsilon_{13}^{el} \\ 2\epsilon_{12}^{el} \end{pmatrix} \tag{C.1}$$

The forth order elasticity tensor, $\mathcal{L}$, has 36 independent components, and is written as a 6x6 matrix. As well, an isotropic thermal expansion tensor is also replaced by a vector. These are

$$\mathcal{L}=\begin{pmatrix} \lambda_{1111} & \lambda_{1122} & \lambda_{1133} & \lambda_{1123} & \lambda_{1113} & \lambda_{1112} \\ & \lambda_{2222} & \lambda_{2233} & \lambda_{2223} & \lambda_{2213} & \lambda_{2212} \\ & & \lambda_{3333} & \lambda_{3323} & \lambda_{3313} & \lambda_{3312} \\ & & & \lambda_{2323} & \lambda_{2313} & \lambda_{2312} \\ & & & & \lambda_{1313} & \lambda_{1312} \\ & & & & & \lambda_{1212} \end{pmatrix}, \quad \vec{A}=\alpha\begin{pmatrix} 1 \\ 1 \\ 1 \\ 0 \\ 0 \\ 0 \end{pmatrix}. \tag{C.2}$$

In SMA crystals wide variety of lattices with different types of symmetries can be observed. The parent phase, austenite, is usually represented by a high order of symmetry lattice(cubic), whereas the order of symmetry of the matensitic variants vary from trigonal to monoclinic[2]. Here we will specify the stiffness matrix only for crystals with cubic and orthorhombic symmetry characteristic for CuAlNi $\beta_1 \rightarrow \gamma_1'$ transformation.

a) orthorhombic symmetry[3]

$$\mathcal{L}^{orth} = \begin{pmatrix} \lambda_{1111} & \lambda_{1122} & \lambda_{1133} & 0 & 0 & 0 \\ & \lambda_{2222} & \lambda_{2233} & 0 & 0 & 0 \\ & & \lambda_{3333} & 0 & 0 & 0 \\ & & & \lambda_{2323} & 0 & 0 \\ & & & & \lambda_{1313} & 0 \\ & & & & & \lambda_{1212} \end{pmatrix} \qquad (C.3)$$

b) cubic symmetry[3]

$$\mathcal{L}^{c} = \begin{pmatrix} \Upsilon & \Pi & \Pi & 0 & 0 & 0 \\ & \Upsilon & \Pi & 0 & 0 & 0 \\ & & \Upsilon & 0 & 0 & 0 \\ & & & \Xi & 0 & 0 \\ & & & & \Xi & 0 \\ & & & & & \Xi \end{pmatrix}, \qquad (C.4)$$

where $\Upsilon = \lambda_{1111} = \lambda_{2222} = \lambda_{3333}$, $\Pi = \lambda_{1122} = \lambda_{2211} = \lambda_{1133} = \lambda_{3311} = \lambda_{2233} = \lambda_{3322}$ and $\Xi = \lambda_{2323} = \lambda_{1313} = \lambda_{1212}$.

The matrices in Eqs. C.3 and C.4 are defined in the coordinate system of the parent phase(austenite). In different coordinate system defined by the correspondence

$$\vec{e}_{n(1)} \leftarrow \vec{e}_{o(1)}$$

$$\vec{e}_{n(2)} \leftarrow \vec{e}_{o(2)}$$

$$\vec{e}_{n(3)} \leftarrow \vec{e}_{o(3)}$$

the components of $\mathcal{L}$(Eq. C.2) must be calculated using the law of transformation of the fourth order tensor

$$\lambda'_{iklm} = \beta_{in}\beta_{kp}\beta_{lr}\beta_{ms}\lambda_{nprs} \ , \tag{C.5}$$

where the transformation tensor $\beta_{ij} = \vec{e}_{n(i)} \cdot \vec{e}_{o(j)}$.

C.2 2D state of stress

The state of plane stress of a body is such that $\sigma_{13} = \sigma_{23} = \sigma_{33} = 0$ and $\sigma_{11} \equiv \sigma_{11}(x_1, x_2)$, $\sigma_{12} \equiv \sigma_{12}(x_1, x_2)$ and $\sigma_{22} \equiv \sigma_{22}(x_1, x_2)$ are taken to depend on the x_1 and x_2 coordinates only. In view of this simplification, the stress and the elastic strain are written as:

$$\vec{T} = \begin{pmatrix} \sigma_{11} \\ \sigma_{22} \\ \sigma_{12} \end{pmatrix} \ , \ \vec{E}_{el} = \begin{pmatrix} \epsilon^{el}_{11} \\ \epsilon^{el}_{22} \\ 2\epsilon^{el}_{12} \end{pmatrix} \ . \tag{C.6}$$

The elastic components ϵ_{33}^{el}, ϵ_{23}^{el} and ϵ_{13}^{el} which are omitted in the elastic strain vector can be obtained as functions of the other three non-zero components, ϵ_{11}^{el}, ϵ_{22}^{el} and ϵ_{12}^{el}. These relations follow from Eq. C.6 and the Hooke's law, $\vec{T} = \mathcal{L} \cdot \vec{E}_{el}$, as

$$\begin{aligned}
\lambda_{3333}\epsilon_{33}^{el} + 2\lambda_{3323}\epsilon_{23}^{el} + 2\lambda_{3313}\epsilon_{13}^{el} &= -\lambda_{3311}\epsilon_{11}^{el} - \lambda_{3322}\epsilon_{22}^{el} - 2\lambda_{3312}\epsilon_{12}^{el} \\
\lambda_{3323}\epsilon_{33}^{el} + 2\lambda_{2323}\epsilon_{23}^{el} + 2\lambda_{2313}\epsilon_{13}^{el} &= -\lambda_{2311}\epsilon_{11}^{el} - \lambda_{2322}\epsilon_{22}^{el} - 2\lambda_{2312}\epsilon_{12}^{el} \\
\lambda_{2333}\epsilon_{33}^{el} + 2\lambda_{1323}\epsilon_{23}^{el} + 2\lambda_{1313}\epsilon_{13}^{el} &= -\lambda_{1311}\epsilon_{11}^{el} - \lambda_{1322}\epsilon_{22}^{el} - 2\lambda_{1312}\epsilon_{12}^{el} \qquad \text{(C.7)}
\end{aligned}$$

Eq. C.7 can be used to determine the 2D analog of Eq. 5.41, where $[\mathcal{M}]$ is replaced by $[S]^{-1}$, and $[S]$ is a 3x3 symmetric matrix.

$$S = \begin{pmatrix} S_{11} & S_{12} & S_{13} \\ & S_{22} & S_{23} \\ & & S_{33} \end{pmatrix} \quad ; \qquad \text{(C.8)}$$

Note that S_{ij} are fourth order polynomials involving the non-zero components of $\mathcal{L}$ in Eq. C.2.

The the vector of thermal expansion coefficients in both symmetries is

$$A_i = \alpha \begin{pmatrix} 1 \\ 1 \\ 0 \end{pmatrix} \qquad \text{(C.9)}$$

C.3 Maxwell Relations

For a particular phase (austenite or martensite) with a volume V and uniform temperature θ the Gibbs free energy (thermomechanical potential) of the phase is defined as [4]

$$G = U - S\theta - V tr(\mathbf{T_R}\mathbf{F}), \tag{C.10}$$

where U and S are total internal energy and entropy of the phase. The differential form of Eq. C.10 is

$$dG = dU - \theta dS - Sd\theta - tr(\mathbf{T_R}d(\mathbf{F}V)) - tr((d\mathbf{T_R})(\mathbf{F}V)). \tag{C.11}$$

A thermodynamical quasistatic process implies [5]:

$$\theta dS = dU - \mu dN - tr(\mathbf{T_R}d(\mathbf{F}V)), \tag{C.12}$$

where μ is the chemical potential and N is the total number of particles in the phase(a "particle" maybe defined as a "subunit" of the phase, such that all particles are identical to one another). With Eq. C.12, Eq. C.11 reduces to

$$dG = \mu dN - Sd\theta - tr((d\mathbf{T_R})(\mathbf{F}V)). \tag{C.13}$$

Since G is a continuous function, following relations can be invoked

$$\partial_{\mathbf{T_R}}\partial_N G = \partial_N\partial_{\mathbf{T_R}} G \quad , \quad \partial_\theta\partial_N G = \partial_N\partial_\theta G. \tag{C.14}$$

Using Eq. C.13 and Eq. C.14, the following partial derivatives are determined

$$\partial_{\mathbf{T_R}}\partial_N G = \partial_{\mathbf{T_R}}\mu \ , \ \partial_\theta\partial_N G = -\mathbf{F}\partial_N V \ ,$$

$$\partial_\theta\partial_N G = \partial_\theta\mu \ , \ \partial_N\partial_\theta G = -\partial_N S \ . \qquad \text{(C.15)}$$

Defining $\partial_N V = V_p$ and $\partial_N S = \eta_p$ as the volume and entropy per particle, Eq. C.15 along with the identities of Eq. C.14 result in

$$\partial_\theta\mu = -\eta_p \ , \ \partial_{\mathbf{T_R}}\mu = -V_p\mathbf{F} \ . \qquad \text{(C.16)}$$

C.4 von Neumann stability analysis

In this section we present the von Neumann linear stability analysis for the 2D linear heat conduction equation with Dirichlet boundary conditions. The finite difference scheme on uniform mesh in x and y directions($h_x = h_y = h$) looks as follows:

$$\frac{C_p}{k}\frac{u^{n+1}_{i,j} - u^n_{i,j}}{\tau} =$$
$$\varrho\left(\frac{u^{n+1}_{i+1,j} - 2u^{n+1}_{i,j} + u^{n+1}_{i-1,j}}{h^2} + \frac{u^{n+1}_{i,j+1} - 2u^{n+1}_{i,j} + u^{n+1}_{i,j-1}}{h^2}\right) +$$
$$(1-\varrho)\left(\frac{u^n_{i+1,j} - 2u^n_{i,j} + u^n_{i-1,j}}{h^2} + \frac{u^n_{i,j+1} - 2u^n_{i,j} + u^n_{i,j-1}}{h^2}\right) . \qquad \text{(C.17)}$$

To find the necessary condition for stability, we will investigate the behavior of particular solution [6]

$$u_{k,l}^n = q^n e^{i(k\varphi + l\psi)} , \qquad \text{(C.18)}$$

where i is the unit imaginary number, q is a complex number, which must be defined, and φ and ψ are arbitrary real numbers. The solution Eq. C.18 will be stable if

$$|q^n e^{i(k\varphi+l\psi)}| < |q^0 e^{i(k\varphi+l\psi)}| = |e^{i(k\varphi+l\psi)}| = 1 .$$

The condition above easily reduces to

$$|q| < 1 . \qquad \text{(C.19)}$$

After substitution of solution Eq. C.18 in the Eq. C.17 and canselation by

$$u_{k,l}^n = q^n e^{i(k\varphi + l\psi)} ,$$

we get

$$\begin{aligned}\frac{C_p}{k}\frac{q-1}{\tau} = \varrho q \left(\frac{e^{i\varphi} - 2 + e^{-i\varphi}}{h^2} + \frac{e^{i\psi} - 2 + e^{-i\psi}}{h^2}\right) + \\ (1-\varrho)\left(\frac{e^{i\varphi} - 2 + e^{-i\varphi}}{h^2} + \frac{e^{i\psi} - 2 + e^{-i\psi}}{h^2}\right) . \qquad \text{(C.20)}\end{aligned}$$

Finally, using trigonometric identities, we obtain

$$q = \frac{1 - (1-\varrho)\frac{4\tau k}{C_p h^2}\left(sin^2\left(\frac{\varphi}{2}\right) + sin^2\left(\frac{\psi}{2}\right)\right)}{1 + \varrho\frac{4\tau k}{C_p h^2}\left(sin^2\left(\frac{\varphi}{2}\right) + sin^2\left(\frac{\psi}{2}\right)\right)} \qquad \text{(C.21)}$$

From Eq. C.21 is clear that q is a real number and the stability condition(Eq. C.19) can be replaced with

$$-1 \le q \le 1\ . \tag{C.22}$$

The right hand side nonequality in Eq. C.22 is trivially satisfied(see Eq. C.21), whereas the left hand side nonequality specifies the required stability condition. Using that

$$-1 \le q = \frac{1-(1-\varrho)\frac{4\tau k}{C_p h^2}\left(sin^2\left(\frac{\varphi}{2}\right)+sin^2\left(\frac{\psi}{2}\right)\right)}{1+\varrho\frac{4\tau k}{C_p h^2}\left(sin^2\left(\frac{\varphi}{2}\right)+sin^2\left(\frac{\psi}{2}\right)\right)} \le \frac{1-(1-\varrho)\frac{8\tau k}{C_p h^2}}{1+\varrho\frac{8\tau k}{C_p h^2}}\ ,$$

the parameter ϱ can be expressed as

$$\varrho \ge \frac{1}{2} - \frac{C_p h^2}{8k\tau} \tag{C.23}$$

Obviously the nonequality in Eq. C.23 is always satisfied for $\varrho \ge \frac{1}{2}$. If $\varrho = 0$ the stability criterion reads

$$\frac{k\tau}{C_p h^2} \le \frac{1}{4}\ . \tag{C.24}$$

Recall that $\varrho = 0$, $\varrho = 0.5$ and $\varrho = 1$ correspond to the three time discretization schemes in Section 5.5.5. Based on the results above the implicit($\varrho = 1$) and Crank-Nicholson ($\varrho = 0.5$) schemes are unconditionally stable, where as the explicit scheme ($\varrho = 0$) must satisfy the condition Eq. C.24 in order to be stable.

Bibliography

[1] E. Buckingham, "On physically similar system illustrations of the use of the dynamical equations," *Phys. Rev.* 4, pp. 345–376, 1914.

[2] K. Bhattacharyya and R. Kohn, "Symmetry, texture and recoverable strain of shape-memory alloy polycrystals," *Acta Metallurgica Materialia* **44**, pp. 529–542, 1995.

[3] J. F. Nye, *Physical properties of crystals, their representation by tensors and matrices.*, Clarendon Press, Oxford, 1957.

[4] C. Truesdell and W. Noll, *Handbuch der Physic III/3*, Springer-Verlag, Berlin, 1965.

[5] C. Kittel, *Thermal Physics*, Wiley & Sons, Inc., New York, 1969.

[6] M. Shashkov, *Conservative finite-difference methods on general grid*, CRC Press, New York,USA, 1996.